9-3-2010

Characterization of the Dynamics of Optically-Injected Nanostructure Lasers

Michael Pochet

Michael C. Pochet
Candidate

Electrical and Computer Engineering
Department

This dissertation is approved, and it is acceptable in quality and form for publication:

Approved by the Dissertation Committee:

Luke F. Lester , Chairperson

Payman Zarkesh-Ha

Marek Osinski

Steven Koch

CHARACTERIZATION OF THE DYNAMICS OF OPTICALLY-INJECTED NANOSTRUCTURE LASERS

BY

MICHAEL C. POCHET

B.S., Electrical Engineering, Virginia Polytechnic Institute and State University, 2001

M.B.A., Business Administration, University of LaVerne, 2003

M.S., Electrical Engineering, Air Force Institute of Technology, 2006

DISSERTATION

Submitted in Partial Fulfillment of the
Requirements for the Degree of
Doctor of Philosophy

Engineering

The University of New Mexico

Albuquerque, New Mexico

August, 2010

The views expressed in this document are those of the author and do not reflect the official policy or position of the United States Air Force, Department of Defense, or the United States Government.

ACKNOWLEDGMENTS

I would like to express my sincere appreciation to my advisor, Prof. Luke F. Lester, for his guidance and support throughout the course of this work. The insight and experience he bestowed on me was certainly appreciated and will benefit my future career.

I am greatly appreciative of my fellow research group member, Nader A. Naderi, for help and collaboration on measurements. I am also thankful for the insight of our group's visiting professor, Prof. Frederic Grillot, in understanding the complexity of the Henry-factor. In addition, I would like to thank Vassilios Kovanis at the Air Force Research Laboratory, Wright-Patterson AFB, Ohio, for pushing my interest in optical-injection.

I am also thankful for the many great discussions and different perspectives offered by my fellow research group members: William Zortman, Jeremy Wright, Yan Li, Chang-Yi Lin, Furqan L. Chiragh, Mohamed A. El-Emawy, Nishant Patel, David Murrell, and Magnus Breivik. I have appreciated their insight on the topics of nanostructure lasers, optical-injection, optical-feedback, the world we live in, and everything in between.

I would like to thank my dissertation committee members Professor Steven Koch, Professor Marek Osinski, and Professor Payman Zarkesh-Ha who gave me great help and insightful comments in completing this dissertation.

Last and most importantly of all, I thank my family.

CHARACTERIZATION OF THE DYNAMICS OF OPTICALLY-INJECTED NANOSTRUCTURE LASERS

BY

MICHAEL C. POCHET

ABSTRACT OF DISSERTATION

Submitted in Partial Fulfillment of the
Requirements for the Degree of

Doctor of Philosophy

Engineering

The University of New Mexico
Albuquerque, New Mexico

August, 2010

CHARACTERIZATION OF THE DYNAMICS OF OPTICALLY-INJECTED NANOSTRUCTURE LASERS

by

Michael C. Pochet

B.S., Electrical Engineering, Virginia Polytechnic Institute and State University, 2001
M.B.A., Business Administration, University of LaVerne, 2003
M.S., Electrical Engineering, Air Force Institute of Technology, 2006
Ph.D, Engineering, 2010

ABSTRACT

The direct-modulation of semiconductor lasers is the simplest and most compact approach to pass data onto an optical fiber; however, their intrinsic limitations under direct-modulation such as wavelength chirp and inherent relaxation oscillation frequency constraints impede their high-speed and long-distance capabilities. The injection-locking of semiconductor lasers improves the injected laser's operational characteristics under direct-modulation, attracting a large degree of interest over the past decade. These improvements include increasing the modulation bandwidth through the enhancement of the resonance frequency, suppressing nonlinear distortion, and reducing relative intensity noise, mode-hopping, and chirp. The nonlinear dynamics associated with optically-injected semiconductor lasers has also attracted great interest due to potential applications

including: all-optical amplitude-modulation to frequency-modulation conversion, chaotic-communication, and photonic microwave generation.

In this dissertation, the optical-injection of quantum-dash and quantum-dot Fabry-Perot semiconductor lasers is investigated in the context of modeling the impact of their characteristically large nonlinear gain component. The impact of the large degree of gain compression on the differential and nonlinear carrier relaxation rates observed in nanostructure lasers under large operational photon densities is also investigated under strong optical-injection conditions.

A novel small-signal microwave modulation response function is derived and shown to improve upon current models at modeling the microwave modulation response under optical-injection. The nonlinear dynamics observed under weak injection strengths are theoretically analyzed using a novel dimensionless rate equation model where including the impact of the nonlinear carrier relaxation rate is shown to improve the agreement with experimentally collected data.

The novel tools derived to analyze the operation of the optically-injected system encompass the physical nature of the injected laser in a more complete manner than previously derived approaches. Theoretical predictions derived here show that large nonlinear carrier relaxation rates, along with suitably small linewidth enhancement parameter values of nanostructure lasers suppress the instability of the optically-injected system. The quantum-dash laser's potential for implementation as a tunable photonic oscillator for use in radio-over-fiber applications or directly-modulated slave laser in a coherent optical communication system is described, along with the quantum-dot laser's highly stable operation under optical-injection.

TABLE OF CONTENTS

LIST OF FIGURES

LIST OF TABLES

GLOSSARY OF TERMS

The following parameters are associated with the free-running (solitary) laser:

γ_n: differential carrier relaxation rate in Hz

γ_p: nonlinear carrier relaxation rate in Hz

γ_s: spontaneous carrier relaxation rate in Hz

γ_c: cavity photon decay rate in Hz

τ_p: photon lifetime in seconds, s

α: linewidth enhancement parameter (alpha-factor, Henry-factor), unitless

γ_{fr}: overall relaxation oscillation frequency damping rate rad/s, ($\gamma_{fr} = \gamma_n + \gamma_p + \gamma_s$)

Ω_{fr}: angular relaxation oscillation frequency, rad/s, ($\Omega_{fr}^2 = \gamma_n\gamma_c + \gamma_p\gamma_s$)

f_{fr}: relaxation oscillation frequency in Hz

Γ: optical confinement factor

g: gain coefficient implicitly incorporating the group velocity v_g, in Hz

g_{th}: gain at threshold implicitly incorporating the group velocity v_g, in Hz

$g_{n,s}$: differential gain parameter implicitly incorporating the group velocity v_g, cm^3/s

$g_{p,s}$: nonlinear gain parameter characterizing the effect of gain compression due to the saturation of gain by the intra-cavity photon density implicitly incorporating the group velocity v_g, cm^3/s

g_n: differential gain parameter normalized to field strength implicitly incorporating the group velocity v_g, cm^3/s

g_p: nonlinear gain parameter characterizing the effect of gain compression due to the saturation of gain by intra-cavity photons normalized to field strength implicitly incorporating the group velocity v_g, cm^3/s

ε_p: nonlinear gain compression coefficient

τ_t: parasitic RC carrier transport time in seconds, s

γ_t: inverse parasitic RC carrier transport time ($\gamma_t = 1/\tau_t$) in Hz

n_g: group index of the active region

v_g: group velocity in the active region in m/s

The following parameters are associated with the optically-injected system:

Δf: detuning frequency in GHz defined as $\Delta f = f_{master} - f_{slave} = f_{inj} - f_{slave}$

f_{master}: frequency of the master laser

f_{slave}: frequency of the free-running slave laser

$\Delta\omega$: angular detuning frequency defined as $\Delta\omega = \omega_{master} - \omega_{slave}$

ω_{master}: angular frequency of the master laser

ω_{slave}: angular frequency of the slave laser

k_c: coupling coefficient in Hz

R_{FE}: field enhancement factor defined as A_o/A_{fr}, unitless

A_o: steady-state field magnitude of the slave laser under optical-injection

A_{fr}: steady-state field magnitude of the free-running slave laser

A_{inj}: steady-state field magnitude of the injected master laser

θ_o: steady-state phase offset between the injected master laser field and free-running slave laser field

η_o: maximum injection strength in Hz define as

$$\eta_o = k_c \frac{A_{inj}}{A_{fr}} = \frac{c}{2n_g L} \frac{(1-R)}{\sqrt{R}} \sqrt{\frac{P_{inj,external}}{P_{FR,total}}}$$

η: injection strength in Hz defined as $\eta = k_c \frac{A_{inj}}{A_o} = \frac{\eta_o}{R_{FE}}$

η_{ratio}: injected field ratio defined as $\eta_o = \frac{c}{2n_g L} \frac{(1-R)}{\sqrt{R}} \sqrt{\frac{P_{inj,external}}{P_{FR,total}}}$, unitless

γ_{th}: threshold gain shift defined as $\gamma_{th} = 2\eta\cos(\theta_o)$

J: bias current density

J_{th}: bias current density at threshold

Publications Associated with this Work Investigating Nanostructure Lasers:

Pochet, M., Naderi, N.A., Li, Y., Kovanis, V., and Lester, L.F., "Tunable Photonic Oscillators Using Optically Injected Quantum-Dash Diode Lasers", *IEEE Photonic Tech Letters* 22(11), 763-784 (2010).

Pochet, M., Naderi, N.A., Terry, N., Kovanis, V., and Lester, L.F., "Linewidth Enhancement Factor and Dynamical Response of an Injection-Locked Quantum-Dot Fabry-Perot Laser at 1310nm", *Proceedings of SPIE - The International Society for Optical Engineering* 7616, 76160F-1—76160F-12 (2010).

Pochet, M., Naderi, N.A., Kovanis, V., and Lester, L.F., "Optically Injected Quantum-dash Lasers at 1550nm Employed as Highly Tunable Photonic Oscillators", *Conference Proceedings - Conference on Lasers and Electro-Optics* CTuZ6, 1-3 (2010).

Naderi, N. A., Pochet, M., Kovanis, V., Lester, L. F., "Bandwidth Enhancement in an Injection-Locked Quantum-dot Laser Operating at 1.31-μm", *Proceedings of SPIE - The International Society for Optical Engineering* 7597, 759719-1—791719-12 (2010).

Pochet, M., Naderi, N. A., Terry, N., Kovanis, V., and Lester, L. F., "Dynamic behavior of an injection-locked quantum-dash Fabry Perot laser at zero-detuning," *Optics Express* 17(23), 20623-20630 (2009).

Pochet, M., Naderi, N.A., Terry, N., Kovanis, V., and Lester, L.F., "Operational Behavior of an Injection-Locked Quantum-Dash Fabry-Perot Laser at Zero-Detuning", *Conference Proceedings* - Frontiers in Optics, Laser Science Conference LSTuA7 (2009).

Pochet, M., Naderi, N.A., Grillot, F., Terry, N., Kovanis, V., and Lester, L.F., "Methods for Improved 3-dB bandwidth in an Injection-Locked QDash Fabry Perot Laser @ 1550nm", *Conference Proceedings - Conference on Lasers and Electro-Optics* CTuQ4 (2009).

Pochet, M., Naderi, N.A., Grillot, F., Terry, N., Kovanis, V., and Lester, L.F., "Modulation response of an injection locked quantum-dash Fabry Perot laser at 1550nm", *Proceedings of SPIE - The International Society for Optical Engineering* 7211, 721107-1—721107-9 (2009).

Grillot, F., Lin, C.-Y., Naderi, N.A., Pochet, M., and Lester, L.F., "Optical feedback instabilities in a monolithic InAs/GaAs quantum-dot passively mode-locked laser", *Applied Physics Letters* 94(15), 153503-1—153503-3 (2009).

Grillot, F., Naderi, N.A., Pochet, M., Lin, C.-Y., and Lester, L.F., "Systematic investigation of the alpha parameter influence on the critical feedback level in QD lasers", *Proceedings of SPIE - The International Society for Optical Engineering Physics and Simulation of Optoelectronic Devices XVII*, 7211 (2009).

Grillot, F., Naderi, N. A., Pochet, M., Lin, C. Y., and Lester, L.F., "Influence of the Linewidth Enhancement Factor on the Critical Feedback in a Quantum-dash Laser", *Conference Proceedings - Conference on Lasers and Electro-Optics* (2009).

Grillot, F., Lin, C. Y., Naderi, N. A., Pochet, M., and Lester, L.F., "Effects of Optical Feedback in InAs/GaAs Monolithic Quantum-dot Passively Mode-Locked Lasers", *Conference Proceedings - Conference on Lasers and Electro-Optics* (2009).

Grillot, F., Naderi, N. A., Pochet, M., Lin, C. Y., Besnard, P., and Lester, L.F., "Tuning the critical feedback level in 1.55-μm quantum-dash semiconductor laser diodes", *The Institution of Engineering and Technology* 3(6), 242-247 (2009).

Naderi, N.A., Pochet, M., Grillot, F., Li, C.-Y., and Lester, L.F., "Temperature Effects on the Modulation Response of an Injection-Locked InAs/InP Quantum-Dash Laser", *Conference Proceedings - The 21st Conference on Indium Phosphide and Related Materials (IPRM)* (2009).

Naderi, N., Pochet, M., Grillot, F., Terry, N., Kovanis, V., and Lester, L.F, "Modeling the Injection-Locked Behavior of a Quantum-dash Semiconductor Laser", *IEEE Journal of Selected Topics in Quantum Electronics* 15(3), 563-571 (2009).

Terry, N.B, Naderi, N.A., Pochet, M., Moscho, A.J., Lester, L.F., and Kovanis, V., Bandwidth enhancement of injection-locked 1.3 μm quantum-dot DFB laser", *Electronics Letters* 44(15), 904-905 (2008).

Terry, N., Naderi, N., Pochet, M., Lester, L.F, and Kovanis, V., "3-dB bandwidth enhancement via strong optical injection-locking of a quantum-dot DFB @ 1310 nm", *Conference Proceedings - Lasers and Electro-Optics Society Annual Meeting-LEOS*, 683-684 (2008).

Naderi, N.A., Pochet, M., Grillot, F., Terry, N., Kovanis, V., and Lester, L.F., "Extraction of operating parameters from an injection-locked quantum-dash fabry-perot laser at 1.55m", *Conference Proceedings - Lasers and Electro-Optics Society Annual Meeting-LEOS*, 475-476 (2008).

Grillot, F., Naderi, N.A., Pochet, M., Lin, C.Y., and Lester, L.F., "Variation of the critical feedback level in a 1550nm quantum-dash fabry-perot semiconductor laser", *Conference Proceedings - Lasers and Electro-Optics Society Annual Meeting-LEOS*, 677-678 (2008).

Grillot, F., Naderi, N.A., Pochet, M., Lin, C.-Y., and Lester, L.F., "Variation of the feedback sensitivity in a 1.55 μm InAs/InP quantum-dash Fabry-Perot semiconductor laser", *Applied Physics Letters* 93(19), 191108-1—191108-3 (2008).

Characterization of the Dynamics of Optically-Injected Nanostructure Lasers

Chapter 1. Introduction

Due to their low propagation loss and immunity to electromagnetic interference, optical fibers have become the medium of choice over copper wire in the telecommunications industry. The direct modulation of semiconductor lasers is the simplest and most compact approach to pass data onto an optical fiber; however, drawbacks such as wavelength chirp and inherent relaxation oscillation frequency limits impede the high-speed and long-distance capabilities of such systems [1], [2]. The limitations of directly-modulated semiconductor lasers have narrowed their application to low-frequency, short-haul systems in the ~10 Gb/s range, leading to the implementation of external modulation architectures as the primary means of passing data onto an optical fiber for long-haul communications at 40 Gb/s and above [1], [2].

In external modulation, the optical source is operated continuously and its output light is modulated using an optical external modulator. Although more complicated in design, the zero-chirp operation and higher bandwidth capabilities (~40 Gb/s) of external modulators has motivated their large-scale use in fiber-optic systems [3]. Along with external modulation techniques, wavelength division multiplexing is commonly used to multiply the available transmission capacity through an optical fiber by adding new channels, where each channel is on a different wavelength [2]. The drawback to

implementing wavelength division multiplexing is the increase in transmitting and receiving equipment, leading to increased system cost and complexity.

Improvements in the capabilities of strained quantum-well lasers in the near-IR [4], [5], tunnel injection and the introduction of nanostructure lasers in the late 1990's has increased the modulation bandwidth and materials complexity of directly-modulated semiconductor lasers [6]. The novelty of the nanostructure laser is its high characteristic temperature, its low threshold current when compared to quantum-well lasers and most importantly its low linewidth enhancement parameter (chirp parameter) [6]. One practical limitation to the 3-dB bandwidth of directly-modulated semiconductor lasers is their relaxation oscillation frequency, driven largely by device heating and gain compression [7], [8].

The injection-locking of semiconductor lasers has been shown to improve the injected laser's operational characteristics under direct modulation, attracting a large degree of interest over the past decade. These improvements include increasing the modulation bandwidth through the enhancement of the resonance frequency, suppressing nonlinear distortion, and reducing relative intensity noise, mode hopping, and chirp [9]-[13]. The nonlinear dynamics associated with optically-injected semiconductor lasers has also attracted great interest due to potential applications including all-optical amplitude-modulation (AM) to frequency-modulation (FM) conversion, chaotic-communication, and photonic microwave generation [14]-[16].

The objective of this dissertation is to provide a thorough investigation of optically-injected nanostructure lasers. Specifically, the optical-injection of a quantum-dash Fabry-Perot semiconductor laser emitting at 1.55-μm and a quantum-dot Fabry-

Perot semiconductor laser emitting at 1.3-μm is detailed in the context of modeling the impact of their large nonlinear carrier relaxation and overall damping rates, along with the impact of gain compression on the differential and nonlinear carrier relaxation rates. The nonlinear dynamics observed under weak injection strengths and the bandwidth enhancement characteristics observed under strong injection are studied. The small-signal modulation response function and the dimensionless rate equation model derived in this work, which invoke non-linear gain in the small-signal response for the first time, are shown to improve upon the current approaches used in predicting the behavior of nanostructure semiconductor lasers under optical-injection.

The intrinsic properties of semiconductor lasers are unique based on their material properties and structural design. This work aims to understand the dependence of the dynamic behavior of the optically-injected system on free-running slave laser parameters, with a specific focus on the slave laser's nonlinear carrier relaxation rate. Theoretical predictions derived here show that large nonlinear carrier relaxation rates, along with suitably small linewidth enhancement parameter values of nanostructure lasers suppress the instability of the coupled system.

1.1. Overview of Optical-Injection

Optical-injection of semiconductor lasers involves two optical sources referred to as the master and slave lasers as seen in Figure 1. The master laser, typically a high-power single-mode narrow-linewidth tunable laser, is injected into the slave laser, thereby affecting the operation and inherent free-running characteristic parameters of the slave laser. An isolator is placed between master and slave lasers to eliminate reflected light coupling back to the master laser. Under stable injection-locking of semiconductor

lasers, which occurs when the strength of the injected master laser light and frequency difference between the master and slave fall within a certain range, the slave's lasing wavelength is pulled/locked to the injected master laser's wavelength. Stable injection-locking provides several improvements to directly-modulated lasers [9], [10]. These improvements include increasing the modulation bandwidth, suppressing nonlinear distortion, and reducing relative intensity noise, mode hopping, and chirp [9]-[13]. A basic example of the spectral improvements under stable injection-locking for a multi-mode Fabry-Perot quantum-dash slave laser is shown in Figure 2. An example of the modulation bandwidth enhancement for the injection-locked Fabry-Perot quantum-dash semiconductor laser is shown in Figure 3. The characteristics of the modulation response curves in Figure 3 are observed to vary as a function of the detuning frequency between the master and slave lasers for a fixed injection strength.

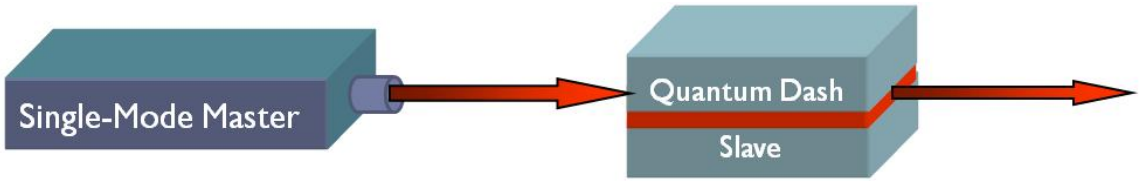

Figure 1. Basic cartoon describing optical-injection.

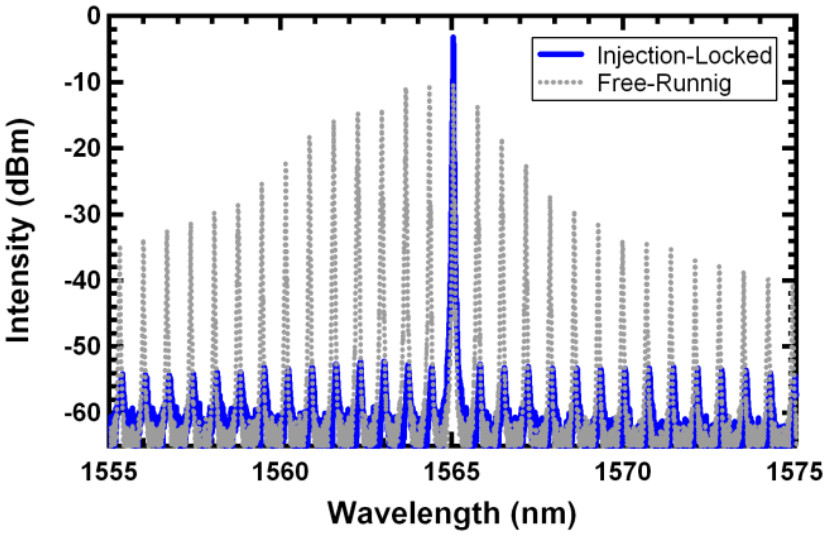

Figure 2. Optical spectra of an injection-locked multi-mode quantum-dash Fabry-Perot laser.

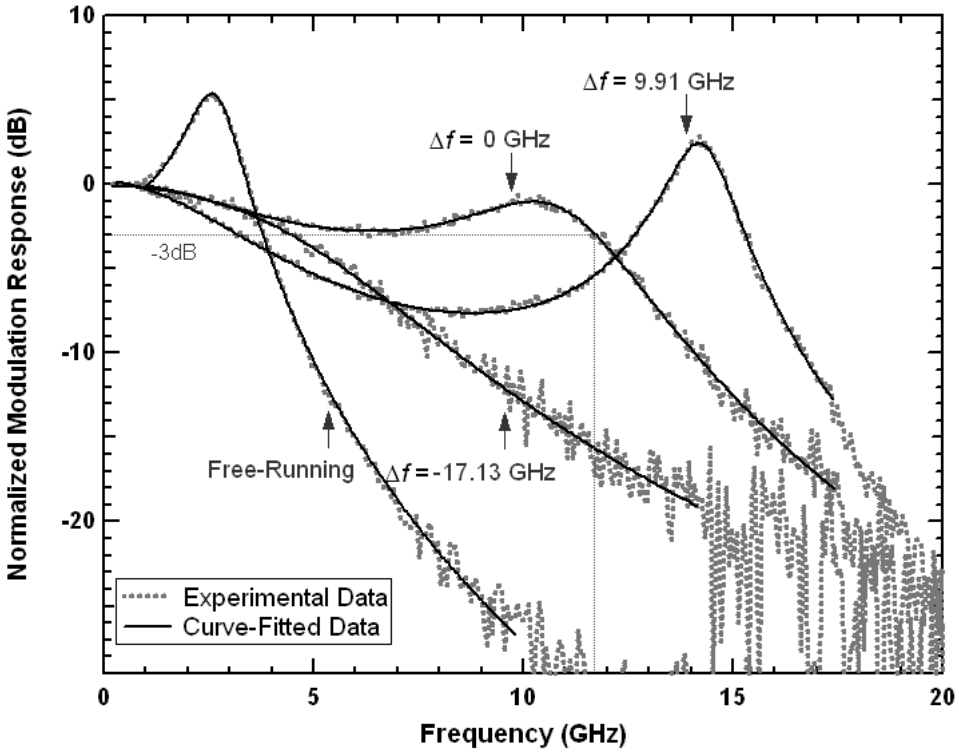

Figure 3. Modulation response of the injection-locked quantum-dash laser for varied frequency detuning (Δf) conditions.

Besides the stable injection-locking regime, the optically-injected system demonstrates a dynamic behavior whereby the optical spectra are characterized by the appearance of relaxation oscillation sidebands and coherence collapse [17]-[23]. The optical power spectra associated with the dynamic states exhibited by a diode laser under optical-injection are referred to as period-one, period-doubling, four-wave mixing, and coherence-collapse, and are illustrated in Figure 4. The optical spectra shown in Figure 4 are unique in nature due to the high resolution of the spectrometer used in data collection (maximum resolution = 1 MHz), which allowed extreme detail of the optically-injected quantum-dash laser's behavior to be observed. In Figure 4 and throughout this work, the detuning frequency is defined as: $\Delta f = f_{master} - f_{slave}$.

An unlocked system, where either the injected signal strength is weak and/or the frequency difference is too large resulting in the master laser field having no impact on the slave laser, is shown in Figure 4(a) [19], [23]. The period-one state, illustrated in Figure 4(b), is characterized by the presence of undamped relaxation oscillation sidebands. Figure 4(c) shows the period-doubling state which is similar to the period-one state, but with additional relaxation oscillation side-bands associated with a second periodic-oscillator at roughly half the slave laser's characteristic relaxation oscillation frequency [19], [23]. Stable locking is shown in Figure 4(d) and is characterized by single mode operation with a significant degree of side mode suppression (defined here as > 30-dB), where the single locked-mode has a narrow linewidth, reduced chirp and noise compared to the slave laser's free running characteristics. The small side modes (side mode suppression > 40 dB) in Figure 4(d) are attributed to feedback in the experimental setup. The coherence-collapse state pictured in Figure 4(e) is characterized by a large

broadening of the coupled system's linewidth. Four-wave-mixing is shown in Figure 4(f) and is a described as a pseudo-unlocked state where two additional frequencies are generated due to optical non-linearities in the device. Under four-wave mixing, the slave laser's operating frequency is unaffected by the injected power. For a fixed injected master power, the coupled system will progress from the period-one state to four-wave-mixing for increased detuning frequencies and a clear boundary is typically difficult to quantitatively determine. The microwave modulation response under period-one, period-doubling, and coherence collapse are normally considered undesirable for use in high-speed coherent optical communication systems where the slave laser is directly-modulated.

With the optical power spectral descriptions describing the operational states (stable-locking, period-one, period-doubling, coherence collapse, four-wave-mixing), stability maps characterizing the dynamic state as a function of the maximum injection strength and detuning frequency can be constructed for a given slave laser. An example is illustrated in Figure 5 for the quantum-dash Fabry-Perot slave laser. The relatively stable operation under zero frequency-detuning conditions and the large period-one oscillation state parameter space open the quantum-dash laser to possible applications as a tunable photonic oscillator or directly-modulated slave laser in a coherent optical communication system. These potential applications are discussed in the next section.

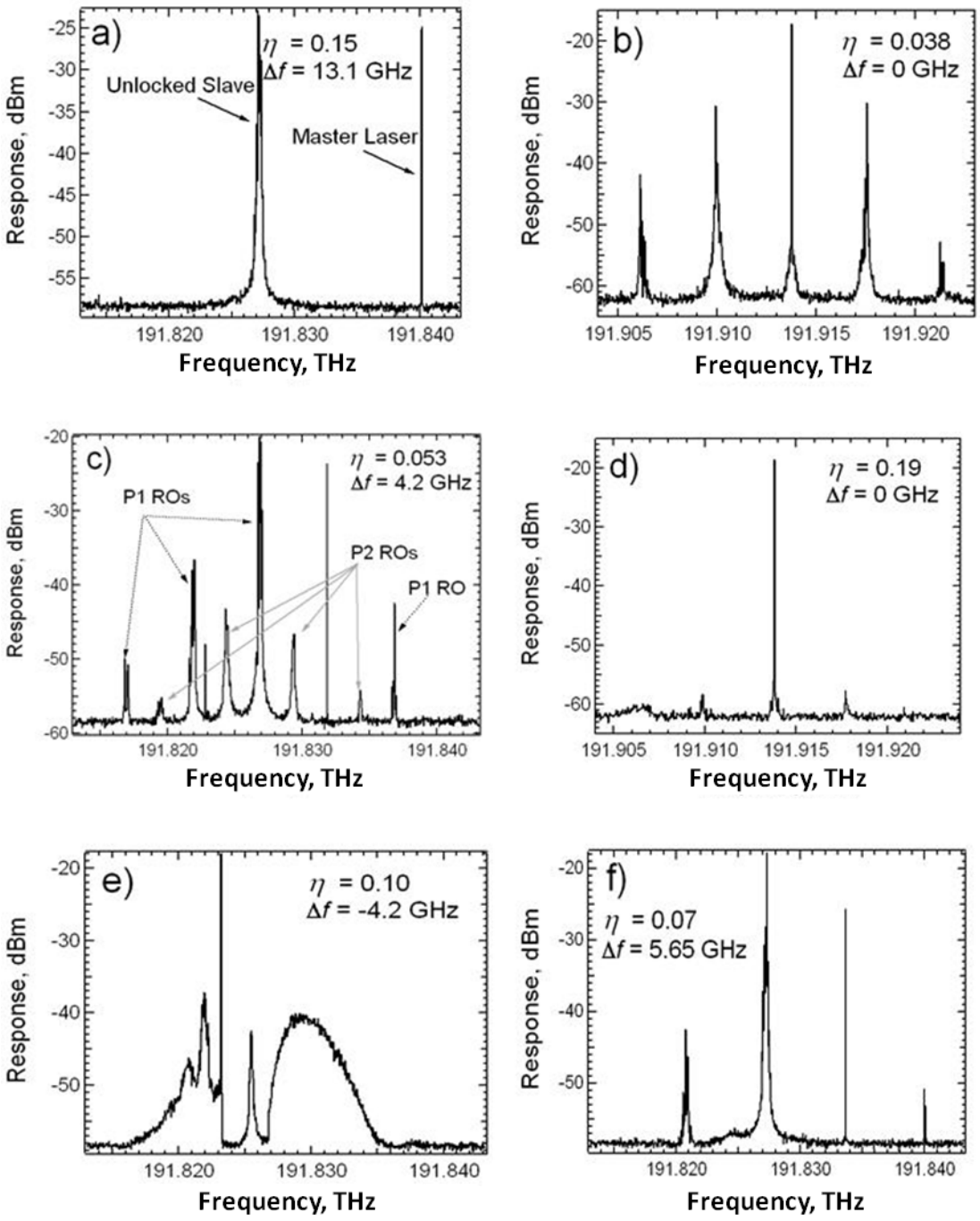

Figure 4. Behavioral states of a quantum-dash laser subject to optical-injection. The injection strength and detuning frequency are indicated on the individual figures. (a) Illustrates the unlocked case; (b) the period-one oscillation state; (c) period-doubling; (d) stable-locking; (e) coherence collapse; and (f) four-wave-mixing.

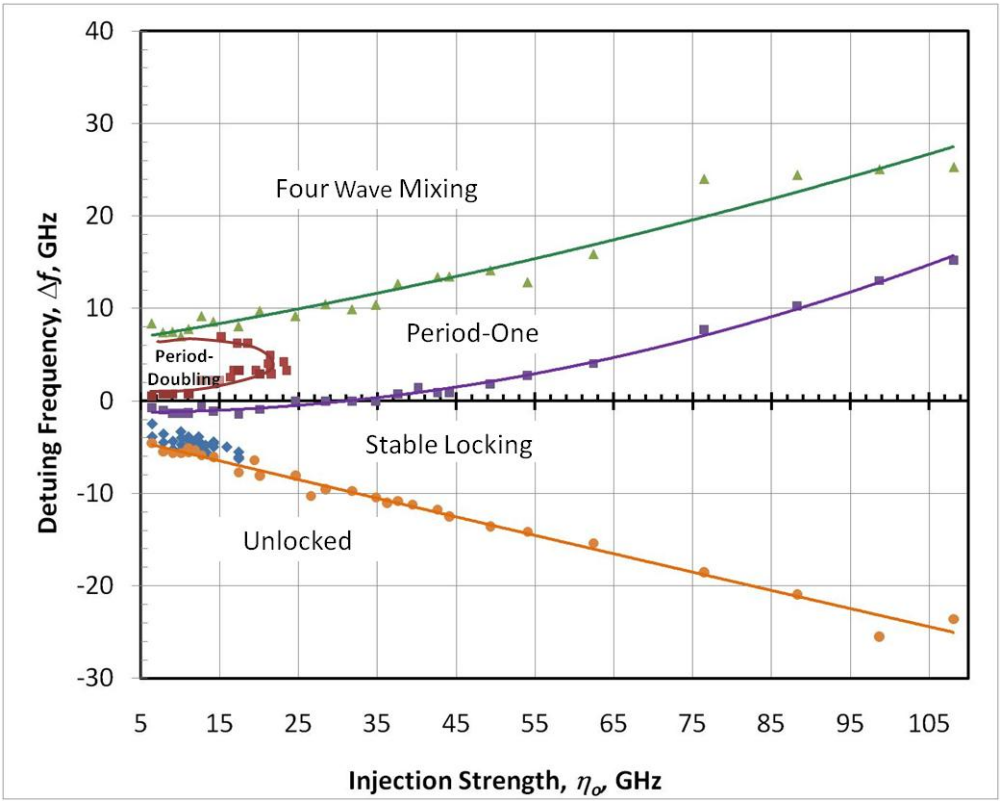

Figure 5. Stability map for the optically-injected quantum-dash slave laser at a bias current of 65 mA showing only stable and period-one operation at zero-detuning and a large period-one parameter space as the injection strength and/or detuning frequency are varied. The blue diamonds at negative detuning indicate chaotic (coherence collapse) operation. The trendlines have been added as a visual aid only.

1.2. Applications of Optically-Injected Lasers

Communication applications of optically-injected semiconductor lasers have predominantly focused on the stable locking state achieved under strong injection where desirable high frequency modulation characteristics have been exhibited [12], [24], [25]. Recently, however, the complex nonlinear dynamical states resulting from the optical-injection of semiconductor lasers have generated increased interest for many novel applications [14]-[16]. Potential applications based on their rich nonlinear dynamics

include: chaotic communications, chaotic lidar, chaotic radar, photonic microwave generation, dual-frequency precision radar/lidar, all-optical AM-to-FM conversion, and single-sideband radio-over-fiber transmission [16]. In this section, the applications of the period-one operational state are discussed.

The period-one state is described as the condition where the slave laser is locked to the injected field and the coupled system oscillates at the injected frequency (f_{inj}) with sidebands at frequencies of $f_{inj} \pm f_r$, where f_r is the resonance frequency of the optically-injected laser as illustrated in Figure 6 [14]-[15]. The resultant electric field of the optically-injected slave laser oscillates without being damped towards a steady-state value as in a free-running or stable-locked semiconductor laser. The period-one resonance frequency is tunable based on the injection strength and/or detuning frequency between the master and slave laser, generating a microwave modulation on the laser output in an all-optical manner [15], [26]-[28].

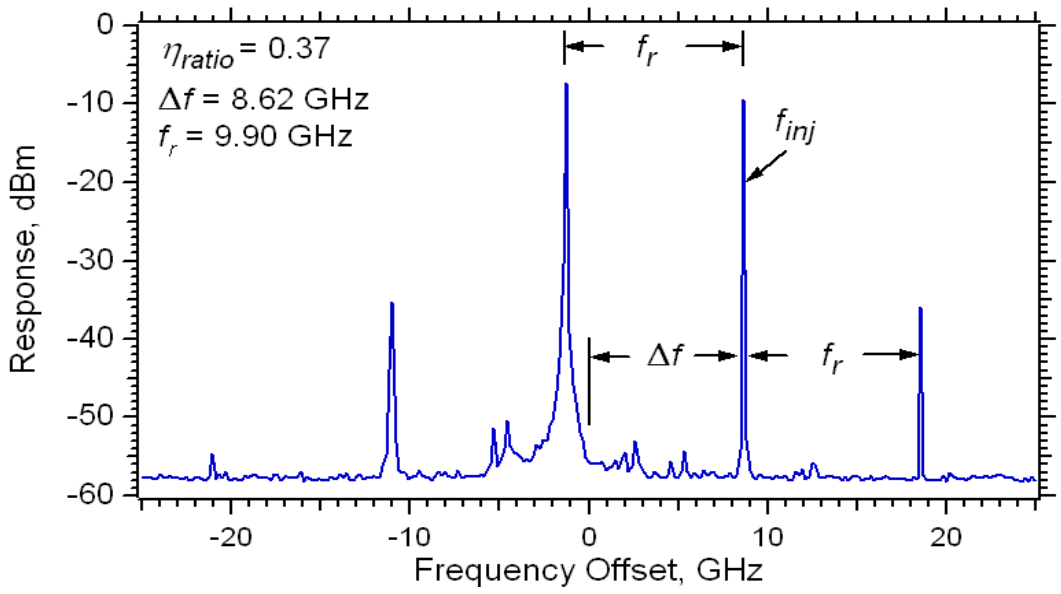

Figure 6. Optical power spectra of the optically-injected quantum-dash laser under a bias of 65 mA in the period-one oscillation state. The injected field ratio and detuning frequency are indicated on each plot. f_r is the measured resonance frequency. Δf is the detuning frequency.

Compared with direct modulation, external modulation, mode-locking, self pulsation, and optical phase-lock loops, the period-one approach presents several advantages in microwave generation [14]-[16]. The primary advantage identified is that the all-optical approach of optical-injection avoids the limitations of microwave electronics and electrical parasitics. In this regard, the system is controlled using the DC injection current of the master laser to modulate its output power resulting in a tunable resonance frequency varying from the free-running laser's natural relaxation oscillation frequency to up to six times this value [14]. Chan et al. and Hwang et al. report the generation of period-one microwave frequencies up to 60 GHz, making the period-one optical-injection system an ideal radio-over-fiber source [14], [15].

Radio-over-fiber technology uses optical fibers to transmit information between central locations and base stations, where the data is transmitted via a microwave signal carrier on an optical wave taking advantage of the efficient, low-loss and electromagnetic interference-free signal transportation offered by optical fibers; conversely, traditional electrical systems using coaxial cables and metallic waveguides have extremely large attenuation and are complex and expensive. The advantage of radio-over-fiber is the location of expensive microwave components at a centralized base station, simplifying the data conversion at the individual base stations [29]. In conventional narrowband communication systems, radio-frequency signal processing functions (frequency up-conversion, carrier modulation, and multiplexing) are performed at each base stations that receive transmitted data via an amplitude-modulated optical signal. The frequency tunability of the period-one resonance frequency based on the strength of the injected signal opens the possibility of all-optical AM-to-FM conversion, enabling the integration of the optical-injection architecture into radio-over-fiber systems.

In the AM-to-FM conversion application, the input amplitude modulated signal is used to drive the master laser injecting the slave laser under a condition that results in the period-one oscillation state; the amplitude modulated signal injecting the slave laser will then be converted to a frequency modulated microwave signal. The optical-injection based AM-to-FM frequency modulation conversion increases bandwidth capabilities, and reduces signal distortion, electronic noise, and power consumption [25]. A depiction of the radio-over-fiber architecture using optical-injection to perform the AM-to-FM conversion is given in Figure 7.

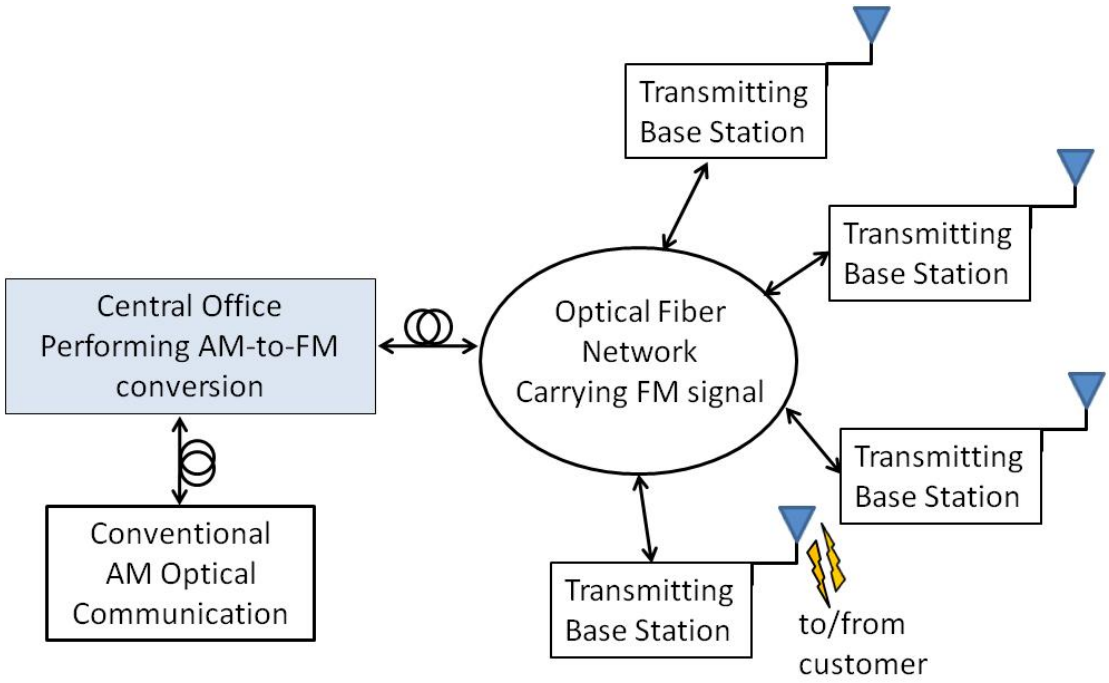

Figure 7. Generic depiction of the radio-over-fiber architecture. The AM-to-FM conversion is performed at the central office and the FM modulated optical signal is transmitted to the base stations simplifying base station processing requirements.

1.3. Nanostructure Lasers

In this dissertation, nanostructure lasers (referring to quantum-dot and quantum-dash lasers) under optical-injection are investigated due to their theoretically superior free-running lasing characteristics compared to quantum-well lasers resulting from their delta-function density of states. The theoretically superior properties arising from their three-dimensional carrier confinement include the following: low-threshold current densities, temperature insensitivity of the threshold current, ultra-high differential gain, increased cutoff frequency, and chirp free operation under direct modulation [30], [31]. Quantum-dot lasers are also attractive in that by varying the dot size and composition, emission wavelengths are achievable over wider ranges on given substrates since the

three dimensional structure of the dots helps to relax the strain from the lattice mismatch while minimizing dislocation formation [31]. The density of states for increased degrees of carrier confinement in bulk, quantum-well, quantum-wire, and quantum-dot semiconductor materials is depicted in Figure 8 [32].

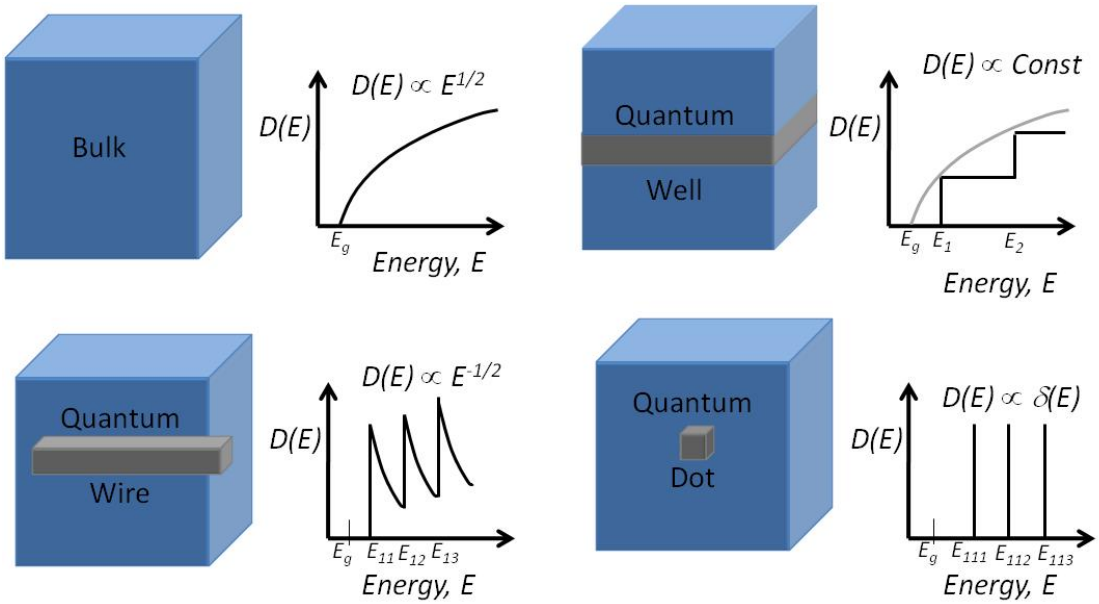

Figure 8. Cartoon of the basic structure and the associated density of states of bulk, quantum-well, quantum-wire, and quantum-dot semiconductor material.

Of particular interest in the modeling of the stability of an optically-injected semiconductor laser is its linewidth enhancement parameter [17], [21]. Previous theoretical and experimental work has highlighted a strong correlation between nonlinear operation and the linewidth enhancement parameter [21]. It is the high degree of stability predicted for low linewidth enhancement parameter lasers that attracts interest in optically-injected nanostructure lasers. The three-dimensional carrier confinement

exhibited by quantum-dot lasers and their delta function density of states predicts a symmetric gain spectrum based on the Kramers-Kronig relation. The symmetric gain spectrum of a quantum-dot laser theoretically yields a linewidth enhancement parameter of zero at the peak gain because the index of refraction will not change with carrier density. Experimental investigations have proven this theoretical concept, as Newell et al., Kondratko et al., and Fathpour et al. have reported near zero linewidth enhancement parameters for quantum-dot lasers at or near threshold [33], [34], and [6].

Along with the linewidth enhancement parameter, the impact of the relatively large nonlinear carrier relaxation rate of a nanostructure laser in modeling its stability is of strong interest. Nanostructure lasers are known to be more strongly damped than quantum-well and hetero-junction lasers, and this strong damping leads to a sizeable nonlinear carrier relaxation rate. Previous works have discussed the effect of nonlinear gain in suppressing the instability of the system [21]; this work aims to quantify the impact of the nonlinear carrier relation rate in both the small-signal microwave modulation response and the nonlinear dynamics observed in the coupled system.

This work focuses on two nanostructure laser types: a quantum-dash Fabry-Perot laser emitting at 1.55-μm grown on an n^+-InP substrate, and a quantum-dot Fabry Perot laser emitting at 1.31-μm grown on an n^+-GaAs substrate. Both lasers were obtained from Zia Laser, a company that commercialized quantum-dot products based on the "dots-in-a-well" (DWELL) design. In the DWELL structure, the active region is similar to that of a quantum-well; however, the well contains an embedded layer of pyramid-shaped indium-arsenide dots. Additional details describing the quantum-dot and quantum-dash lasers will be presented in Chapter 4.

1.4. Document Organization

This work provides a thorough investigation of optically-injected quantum-dash and quantum-dot nanostructure lasers. Chapter 2 derives a predictive model to investigate the small-signal microwave modulation response of an optically-injected nanostructure laser. The function derived is unique in that it accounts for both the nonlinear carrier relaxation rate parameter and the saturation of this parameter under considerably strong injection conditions. In Chapter 3 a normalized approach is described that theoretically evaluates the behavioral state as a function of the injected field ratio and/or the detuning frequency for varied slave laser bias cases. Chapter 4 gives a detailed device characterization of the nanostructure lasers under test and highlights their characteristic parameters that make them ideal for implementation in optically-injected architectures. Chapter 5 and Chapter 6 describe the experimental validation of the theory described in Chapter 2 and Chapter 3. Additionally, Chapter 5 and Chapter 6 present experimental data characterizing the steady-state microwave modulation response under varied degrees of detuning, with a focus on the zero-detuning and the positive frequency detuning edge conditions. A stability map describing the operation of the quantum-dash laser under optical-injection is presented in Chapter 5. Chapter 7 summarizes the work and suggests future topics of study related to optical-injection.

Chapter 2. Modulation Response of the Optically-Injected Nanostructure Laser

As introduced in Chapter 1, optical-injection enhances the 3-dB bandwidth and resonance frequency of a diode laser. The purpose of this chapter is to theoretically derive a predictive model to investigate the microwave modulation response of an optically-injected nanostructure laser. The function derived is unique in that it for the first time accounts for the nonlinear carrier relaxation rate parameter and the saturation of this parameter under considerably strong injection conditions. Pervious works have dismissed the necessity to consider the impact of these parameters. This work shows that when modeling nanostructure lasers, these parameters play a sizable role in the coupled system's response.

The dynamic parameters describing the microwave modulation response are also used to describe the stability limits in frequency detuning and injection strength parameter space. In Chapter 5 and Chapter 6, the function derived here is shown to increase the level of accuracy in predicting experimental results over models where the nonlinear carrier relaxation rate is not considered.

2.1. Rate Equations Describing Optically-Injected Diode Lasers

The resonance frequency and microwave modulation response of an optically-injected diode laser is investigated by performing a small-signal analysis of the single mode rate equations. The rate equations describing optically-injected diode lasers are given in equations (1) – (3), which are based on the conventional equations describing diode lasers in the absence of optical-injection (free-running) with terms introduced to describe the impact of the injected light [35], [36]. As in the free-running rate equation

model, the field magnitude and phase equations given in (1) and (2) arise from the fundamental complex field rate equation [36].

$$\frac{dA(t)}{dt} = \frac{1}{2}\Gamma g A(t) - \frac{1}{2}\gamma_c A(t) + k_c A_{inj}\cos(\theta(t)) \tag{1}$$

$$\frac{d\theta(t)}{dt} = \frac{\alpha}{2}\Gamma g - \frac{\alpha}{2}\gamma_c - \Delta\omega - k_c \frac{A_{inj}}{A(t)}\sin(\theta(t)) \tag{2}$$

$$\frac{dN(t)}{dt} = J(t) - \gamma_s N(t) - gA^2(t) \tag{3}$$

where $A(t)$ and $N(t)$ are the electric field magnitude and carrier density of the injected slave, respectively. A_{inj} is the magnitude of the injected field. $\theta(t)$ is the phase offset between the master and slave laser. $\Delta\omega$ is the detuning frequency between the master and slave laser defined by $\Delta\omega = \omega_{master} - \omega_{slave}$. J is the bias current density, γ_s is the spontaneous carrier relaxation rate, γ_c is the cavity photon decay rate given by: $\gamma_c = \Gamma g_{th}$, where $\gamma_c = 1/\tau_p$ and τ_p is the photon lifetime [37]. Γ is the optical confinement factor, g is the gain coefficient, and g_{th} is the gain at threshold. α is the slave laser linewidth enhancement parameter. The coupling coefficient, k_c, is dependent on the internal cavity round trip time.

The rate equations describing a diode laser under optical-injection have been thoroughly analyzed in various works, most recently in a manner to derive an expression modeling the absolute small-signal microwave frequency modulation response [38]-[40]. The small-signal modulation response models in Lau et al. and Naderi et al. do not directly account for the nonlinear carrier relaxation rate, γ_p, nor the gain compression characteristic of diode lasers, as their impact in most diode lasers is considered relatively

small [39], [40]; nanostructure lasers, however, have been shown to a possess a large damping rate driven by a large nonlinear carrier relaxation rate when compared to quantum-well lasers [41]-[43] as well as gain compression coefficients roughly an order magnitude larger than quantum-well lasers [8]. The purpose of the derivation presented here is to determine the small-signal modulation response where the nonlinear carrier relaxation rate parameter, γ_p, and its compression (along with the differential carrier relaxation rate parameter) under strong injection is considered in order to more effectively model optically-injected nanostructure lasers.

Under the dynamical perturbation of a small-signal current modulation, the free-running gain coefficient can deviate from g_{th} due to the variations in the carrier and photon densities [37]. Based on this free-running dependence of the gain coefficient on a small-signal perturbation, it is inferred that it will also be impacted by the external optically-injected perturbation. The dependence of the gain coefficient on the carrier and photon densities is defined in (4) [37]:

$$g = g_{th} + g_n(N - N_{th}) + g_{p,s}\left((S + S_{inj}) - S_{fr}\right) \tag{4}$$

where g_n (> 0) is the differential gain parameter and $g_{p,s}$ (< 0) is the nonlinear gain parameter characterizing the effect of gain compression due to the saturation of gain by intra-cavity photons, where S is the photon density resulting from the small-signal current perturbation. g_{th}, N_{th}, and S_{fr} are the gain at threshold, carrier density and photon density at steady-state under free-running operation, respectively [35], [37]. S_{inj} is the injected photon density. In (4), g_{th}, g_n, and $g_{p,s}$ implicitly incorporate the group velocity. Next, (4) is adjusted to reflect the relationship between the normalized field and the photon density given by: $A^2(t) = S(t)$, yielding the relationship given in (5) [37].

$$g = g_{th} + g_n(N - N_{th}) + g_p\left((A^2 + A_{inj}^2) - A_{fr}^2\right) \tag{5}$$

where A_{fr} is the steady-state free-running normalized field and A_{inj} is the injected field strength.

The rate equations are re-written in (6) – (8) to reflect the expanded gain coefficient definition in (5) and the time dependence is dropped for simplification purposes ($A(t) \rightarrow A$, $\theta(t) \rightarrow \theta$, $N(t) \rightarrow N$).

$$\frac{dA}{dt} = \frac{1}{2}\Gamma\left(g_{th}A + g_n(N - N_{th})A + g_p\left((A^2 + A_{inj}^2) - A_{fr}^2\right)A\right) - \frac{1}{2}\gamma_c A + k_c A_{inj}\cos(\theta) \tag{6}$$

$$\frac{d\theta}{dt} = \frac{\alpha}{2}\Gamma\left(g_{th} + g_n(N - N_{th}) + g_p\left((A^2 + A_{inj}^2) - A_{fr}^2\right)\right) - \frac{\alpha}{2}\gamma_c - k_c\frac{A_{inj}}{A}\sin(\theta) - \Delta\omega \tag{7}$$

$$\frac{dN}{dt} = J - \gamma_s N - g_{th}A^2 - g_n(N - N_{th})A^2 - g_p\left((A^2 + A_{inj}^2) - A_{fr}^2\right)A^2 \tag{8}$$

2.2. Steady-state solutions to rate equations:

The steady-state solutions of (6), (7), and (8) are found in order to simplify the resultant small-signal, differential analysis results [35], [36]. The steady-state solutions also yield important relationships between parameters under stable-locking conditions and parameter range limits that are useful in modeling various detuning conditions that will be described in detail later.

The steady-state solution of the field magnitude rate equation in (6) is the following expression:

$$0 = \frac{1}{2}\Gamma\left(g_n(N_o - N_{th})A_o + g_p\left((A_o^2 + A_{inj}^2) - A_{fr}^2\right)A_o\right) + k_c A_{inj}\cos(\theta_o) \tag{9}$$

N_o is given by $\Delta N + N_{th}$, where N_o and A_o are the steady-state modified carrier density and enhanced field magnitude, respectively, under optical-injection. ΔN is the shift in carrier density from threshold. Rearranging (9) and defining the threshold gain shift parameter, γ_{th}, as $2\eta\cdot\cos(\theta_o)$, and the injection-strength as $\eta = k_c(A_{inj}/A_o)$ yields (10) and (11), which will be used later in simplifying the differential analysis based small-signal modulation response:

$$0 = \Gamma g_n \Delta N + \Gamma g_p \left(A_o^2 + A_{inj}^2 - A_{fr}^2\right) + \gamma_{th} \tag{10}$$

$$\Delta N = \frac{-\gamma_{th}}{\Gamma g_n} - \frac{g_p}{g_n}\left(A_o^2 + A_{inj}^2 - A_{fr}^2\right) \tag{11}$$

The steady-state solution of the phase-offset rate equation in (7) under **zero-detuning** is the following expression:

$$0 = \frac{\alpha}{2}\Gamma\left(g_n(N_o - N_{th}) + g_p\left((A^2 + A_{inj}^2) - A_{fr}^2\right)\right) - k_c\frac{A_{inj}}{A_o}\sin(\theta) \tag{12}$$

Replacing $(\Gamma g_n \Delta N + \Gamma g_p(A_o^2 + A_{inj}^2 - A_{fr}^2))$ from (10) with $-\gamma_{th}$ yields:

$$0 = -\alpha\eta\cos(\theta_o) - \eta\sin(\theta_o) \tag{13}$$

Expression (13) leads to the following phase-to-linewidth enhancement parameter relationship under zero-detuning conditions:

$$\theta_o = -\tan^{-1}(\alpha) \tag{14}$$

For cases away from the zero-detuning condition, (12) is modified to include the detuning frequency yielding the result in (15).

$$\Delta\omega = \frac{\alpha}{2}\left(\Gamma g_n \Delta N + \Gamma g_p \left((A^2 + A_{inj}^2) - A_{fr}^2\right)\right) - \eta \sin(\theta_o) \tag{15}$$

Replacing $[\Gamma g_n \Delta N + \Gamma g_p (A_o^2 + A_{inj}^2 - A_{fr}^2)]$ from (10) with $-\gamma_{th}$ yields the relationship between detuning frequency and the injection strength, steady-state phase offset between the master and slave lasers, and linewidth enhancement parameter shown here:

$$\Delta\omega = -\alpha\eta \cos(\theta_o) - \eta \sin(\theta_o) \tag{16}$$

Simplifying (16) results in the commonly used expression relating the detuning frequency to the injection strength, steady-state phase offset between the master and slave laser, and linewidth enhancement parameter [9], [38], [40]:

$$\Delta\omega = -\eta\left(1 + \alpha^2\right)^{1/2} \sin\left(\theta_o + \tan^{-1}(\alpha)\right) \tag{17}$$

Expression (17) is used to determine the constraints to the phase offset between the master and slave fields under stable locking conditions. By manipulating (17) into the form given in (18), it is found that a real solution for the phase can only be obtained if the argument of the inverse-sine function is ≤ 1, leading to the expression given in (19), which was originally introduced by Mogensen et al. as the locking half-width [9]. This locking half-width leads to the injection-locking approach for measuring the slave laser's linewidth enhancement parameter under strong injection, discussed later in the work [44]. The locking half-width is shown to approximate the experimentally measured negative frequency detuning boundary. Returning to (18), the maximum and/or minimum value of the inverse-sine function is $\pm\pi/2$, simplifying (18) to the expression given in (20) and

leading to a set of constraints for the steady-state phase offset that will be used later in applying parameter limits to the small-signal microwave modulation response function.

$$\pm \sin^{-1}\left(\frac{-\Delta\omega}{\eta \cdot \sqrt{1+\alpha^2}}\right) - \tan^{-1}(\alpha) = \theta_o \tag{18}$$

$$\Delta\omega \le \eta\left(1+\alpha^2\right)^{1/2} \tag{19}$$

$$-\frac{\pi}{2} - \tan^{-1}(\alpha) \le \theta_o \le +\frac{\pi}{2} - \tan^{-1}(\alpha) = \cot^{-1}(\alpha) \tag{20}$$

From the steady-state solution of the electric field rate equation given in (9), a second constraint on the stead-state phase offset is determined based on theory stating that the carrier number cannot be above N_{th}, the threshold value [45]. Under this constraint, the change in carrier density, ΔN, will be a negative value. Rearranging (9) yields the expression shown in (21). The negative value of ΔN and the nonlinear gain parameter, g_p, and positive value of the change in field magnitude, $\Delta A^2 = A_o^2 + A_{inj}^2 - A_{fr}^2$, due to optical-injection makes the left hand side of (21) a positive quantity under all stable-locking conditions leading to θ_o being constrained to values yielding in a positive cosine argument, as given in (22).

$$\frac{-\Gamma v_g g_n}{2\eta}\left(\Delta N + \frac{g_p}{g_n}\Delta A^2\right) \le \cos(\theta_o) \tag{21}$$

$$-\frac{\pi}{2} \le \theta_o \le \frac{\pi}{2} \tag{22}$$

The constraints on θ_o given in (20) and (22) can then be combined, keeping the most restrictive parameter limits to give the important result shown in (23). Note that the constraints in (23) are based on a ***positive*** linewidth enhancement parameter, α. For cases

where α is negative, the inverse-tangent value is negative, making the lower constraint of θ_o greater than $-\pi/2$.

$$-\frac{\pi}{2} \le \theta_o \le \cot^{-1}(\alpha) \tag{23}$$

Inserting the steady-state phase offset constraints for stable-locking in (23) into (17) yields the detuning boundaries originally presented by Mogensen et al. given in expression (24) [9]. The simplification in (24) is based on the trigonometric identities: $\tan^{-1}(x) + \cot^{-1}(x) = \pi/2$ and $\sin(-\pi/2 + x) = -\cos(x)$.

$$-\eta\left(1+\alpha^2\right)^{1/2} \le \Delta\omega \le \eta \tag{24}$$

An additional stability constraint is determined through the analysis of the poles of the small-signal microwave modulation response, discussed later in section 2.8 [11], [36].

Next, the steady state solution of the carrier density rate equation given in (8) is found to be given by the following expression:

$$0 = J - \gamma_s(\Delta N + N_{th}) - \frac{\gamma_c}{\Gamma}A_o^2 - g_n(\Delta N)A_o^2 - g_p\left((A^2 + A_{inj}^2) - A_{fr}^2\right)A_o^2 \tag{25}$$

Substituting for ΔN as given in (11) results in:

$$0 = J - (\gamma_s + g_n A_o^2)\left(\frac{-\gamma_{th}}{\Gamma g_n} - \frac{g_p}{g_n}\left((A^2 + A_{inj}^2) - A_{fr}^2\right)\right) - \gamma_s N_{th} - \frac{\gamma_c}{\Gamma}A_o^2 - g_p\left((A^2 + A_{inj}^2) - A_{fr}^2\right)A_o^2 \tag{26}$$

Expression (26) is then expanded and solved for A_o^2, yielding expression (27):

$$A_o^2 = \frac{J - \gamma_s N_{th} + \frac{\gamma_s \gamma_{th}}{\Gamma g_n} + \gamma_s \frac{g_p}{g_n}(A_o^2 + A_{inj}^2 - A_{fr}^2)}{\left(\frac{\gamma_c - \gamma_{th}}{\Gamma}\right)} \tag{27}$$

Manipulating (27) and given that the steady-state free-running (η = 0) field magnitude density (ΔA^2 = 0) is described by: $A_{fr}^2 = \frac{J - \gamma_s N_{th}}{\gamma_c / \Gamma} = \Gamma(J - J_{th})/\gamma_c$ results in the following equation [35], [40]:

$$A_o^2 = \frac{A_{fr}^2 + \frac{\Gamma\gamma_s}{\gamma_c}\left(\frac{\gamma_{th}}{\Gamma g_n} + \frac{g_p}{g_n}(A_o^2 + A_{inj}^2 - A_{fr}^2)\right)}{\left(1 - \frac{\gamma_{th}}{\gamma_c}\right)} = \frac{\gamma_c A_{fr}^2 + \Gamma\gamma_s\left(\frac{\gamma_{th}}{\Gamma g_n} + \frac{g_p}{g_n}(A_o^2 + A_{inj}^2 - A_{fr}^2)\right)}{(\gamma_c - \gamma_{th})} \tag{28}$$

Multiplying both sides of expression (28) by g_n yields a form similar to that presented in previous works, however, here the result shown in expression (29) includes the nonlinear carrier relaxation rate component interacting with the varies intra-cavity field components [40].

$$g_n A_o^2 = \frac{\gamma_c g_n A_{fr}^2 + \gamma_s\gamma_{th} + \Gamma\gamma_s g_p\left(A_o^2 + A_{inj}^2 - A_{fr}^2\right)}{(\gamma_c - \gamma_{th})} \tag{29}$$

Given that A_o^2 is the enhanced slave field magnitude, a field enhancement factor is introduced to quantitatively define the resultant degree of enhancement. As introduced in [40], the field enhancement factor, R_{FE}, is defined by $R_{FE} = A_o/A_{fr}$.

The injection strength is then manipulated into a ratio of the injected field magnitude to the free-running slave field magnitude using the field enhancement factor, R_{FE}, resulting in what is referred to as the maximum injection strength, η_o, defined in (30).

$$\eta = k_c \frac{A_{inj}}{A_o} = \frac{\eta_o}{R_{FE}} \rightarrow \text{ where } \eta_o = k_c \frac{A_{inj}}{A_{fr}} \tag{30}$$

In order to simplify expression (29), the free-running differential carrier relaxation rate, γ_n, and nonlinear carrier relaxation rate, γ_p, are defined per (31) and (32), respectively [37].

$$\gamma_n = g_{n,s} S_{fr} = g_n A_{fr}^2 \tag{31}$$

$$\gamma_p = -\Gamma g_{p,s} S_{fr} = -\Gamma g_p A_{fr}^2 \tag{32}$$

The free-running relaxation oscillation frequency is defined here as $\Omega_{fr}^2 = \gamma_c \gamma_n + \gamma_s \gamma_p$ [37]. Substituting (30) - (32) into (29) and substituting for γ_{th} results in the following expression:

$$\gamma_n R_{FE}^2 \left(\gamma_c - 2 \frac{\eta_o}{R_{FE}} \cos(\theta_o) \right) = \Omega_{fr}^2 + 2\gamma_s \frac{\eta_o}{R_{FE}} \cos(\theta_o) - \gamma_p \gamma_s R_{FE}^2 - \gamma_s \gamma_p \frac{A_{inj}^2}{A_{fr}^2} \tag{33}$$

Manipulating (33) results in a cubic that can be solved for the field enhancement factor, R_{FE}, based on the maximum injection strength, η_o, free-running relaxation oscillation frequency, Ω_{fr}, spontaneous carrier relaxation rate, γ_s, and the differential carrier relaxation rate, γ_n.

$$\Omega_{fr}^2 R_{FE}^3 - 2\gamma_n \eta_o \cos(\theta_o) R_{FE}^2 - \Omega_{fr}^2 R_{FE} + \gamma_s \gamma_p \frac{\eta_o^2}{k_c^2} - 2\gamma_s \eta_o \cos(\theta_o) = 0 \tag{34}$$

Solving for the roots of (34) yields two complex and one real solution for R_{FE}. The complex and/or negative roots can be ignored, while the real, positive root is used to quantitatively describe the enhancement of the steady-state locked slave field. For cases close to the negative frequency detuning edge, where the steady-state phase offset is

shown to be approximately -π/2, the roots are reduced to +/- 1, indicating that at this detuning condition, the internal slave field will be minimally enhanced regardless of the injection strength.

2.3. Differential analysis of the rate equations given in (6) - (8):

In order to determine the dynamic response to a small-signal current modulation, the time derivatives of the rate equations are examined [35]. Starting with the field magnitude rate equation from (6):

$$\frac{d}{dt}(dA) = dA\left(\frac{1}{2}\Gamma g_n \Delta N + \frac{3}{2}\Gamma g_p A_o^2 - \frac{1}{2}\Gamma g_p A_{fr}^2\right) + d\theta\left(-\eta A_o \sin(\theta)\right) + dN\left(\frac{1}{2}\Gamma g_n A_o\right) \quad (35)$$

Substituting for ΔN based on (11) and $2\eta\cdot\cos(\theta_o)$ for the threshold gain shift term, γ_{th}, and collecting like terms yields:

$$\frac{d}{dt}(dA) = dA\left(-\eta\cos(\theta) + \Gamma g_p A_o^2\right) + d\theta\left(-\eta A_o \sin(\theta)\right) + dN\left(\frac{1}{2}\Gamma g_n A_o\right) \quad (36)$$

Differential analysis of the rate equation describing the field phase offset as given in (7) results in the following:

$$\frac{d}{dt}(d\theta) = dA\left(\frac{\eta\sin(\theta_o)}{A_o} - \alpha\Gamma g_p A_o\right) + d\theta\left(-\eta\cos(\theta)\right) + dN\left(\frac{\alpha}{2}\Gamma g_n\right) \quad (37)$$

The differential analysis of the carrier density rate equation given in (8) yields:

$$\begin{aligned}\frac{d}{dt}(dN) = {} & dJ - dN\left(\gamma_s + g_n A_o^2\right) \\ & - dA\left(2g_{th}A_o - 2g_n \Delta N A_o - 4g_p A_o^3 + 2g_p A_o A_{fr}^2\right)\end{aligned} \quad (38)$$

Substituting for ΔN based on the steady-state relationship given in (11) results in:

$$\frac{d}{dt}(dN) = dJ + dN\left(-\gamma_s - g_n A_o^2\right) + dA\left(-\frac{2A_o\gamma_c}{\Gamma} + \frac{2A_o\gamma_{th}}{\Gamma} - 2g_p A_o^3\right) \tag{39}$$

2.4. Deriving the relative small-signal modulation response:

In order to derive the small-signal microwave modulation response, the differential analysis results from (36), (37), and (39) are used to define a set of rate coefficients given in (40). In (40), the field enhancement parameter, (31) and (32) are used to simplify the resultant coefficient terms.

$$m_{AA} = \eta\cos(\theta_o) + \gamma_p R_{FE}^2 \qquad m_{A\theta} = \eta A_o R_{FE}\sin(\theta_o) \qquad m_{AN} = -\frac{1}{2}\frac{\Gamma\gamma_n R_{FE}^2}{A_o R_{FE}}$$

$$m_{\theta A} = +\alpha\frac{\gamma_p R_{FE}^2}{A_o R_{FE}} - \eta\frac{1}{A_o R_{FE}}\sin(\theta_o) \quad m_{\theta\theta} = \eta\cos(\theta_o) \qquad m_{\theta N} = -\frac{\alpha}{2}\Gamma\frac{\gamma_n R_{FE}^2}{A_o^2 R_{FE}^2} \tag{40}$$

$$m_{NA} = \frac{2A_o R_{FE}\left(\gamma_c - \gamma_{th} - \gamma_p R_{FE}^2\right)}{\Gamma} \qquad m_{N\theta} = 0 \qquad m_{NN} = \gamma_s + \gamma_n R_{FE}^2$$

The rate coefficients allow for the differential rate equations to be expressed in a compact matrix form:

$$\frac{d}{dt}\begin{pmatrix} dA \\ d\theta \\ dN \end{pmatrix} = \begin{pmatrix} -m_{AA} & -m_{A\theta} & -m_{AN} \\ -m_{\theta A} & -m_{\theta\theta} & -m_{\theta N} \\ -m_{NA} & 0 & -m_{NN} \end{pmatrix}\begin{pmatrix} dA \\ d\theta \\ dN \end{pmatrix} + \begin{pmatrix} 0 \\ 0 \\ dJ \end{pmatrix} \tag{41}$$

Using the small-signal frequency response approach described in Coldren et al. and setting d/dt equal to $j\omega$ yields [35]:

$$\begin{pmatrix} m_{AA} + j\omega & m_{A\theta} & m_{AN} \\ m_{\theta A} & m_{\theta\theta} + j\omega & m_{\theta N} \\ m_{NA} & 0 & m_{NN} + j\omega \end{pmatrix}\begin{pmatrix} dA \\ d\theta \\ dN \end{pmatrix} = \begin{pmatrix} 0 \\ 0 \\ dJ \end{pmatrix} \tag{42}$$

Cramer's rule is used to solve for the small-signal photon density response in terms of modulation current given by $H(\omega) = \Delta A_o/\Delta J$:

$$H(\omega) = \frac{Det\begin{pmatrix} 0 & m_{A\theta} & m_{AN} \\ 0 & m_{\theta\theta} + j\omega & m_{\theta N} \\ dJ & 0 & m_{NN} + j\omega \end{pmatrix}}{Det\begin{pmatrix} m_{AA} + j\omega & m_{A\theta} & m_{AN} \\ m_{\theta A} & m_{\theta\theta} + j\omega & m_{\theta N} \\ m_{NA} & 0 & m_{NN} + j\omega \end{pmatrix}} \tag{43}$$

The denominator is given in (44).

$$\begin{aligned} \text{Denominator} &= -j\omega^3 - \omega^2\left(\gamma_n R_{FE}^2 + \gamma_p R_{FE}^2 + \gamma_s + \gamma_{th}\right) \\ &+ j\omega\left(\gamma_n\gamma_c R_{FE}^2 + \gamma_p\gamma_s R_{FE}^2 + \eta^2 + \gamma_s\gamma_{th} + \gamma_p R_{FE}^2\eta\cos(\theta_o) - \gamma_p R_{FE}^2\alpha\eta\sin(\theta_o)\right) \\ &+ \left(\eta^2\left(\gamma_n R_{FE}^2 + \gamma_s\right) - \eta\left(\alpha\sin(\theta_o) - \cos(\theta_o)\right)\left(\gamma_n R_{FE}^2\gamma_c + \gamma_p R_{FE}^2\gamma_s - \gamma_n R_{FE}^2\gamma_{th}\right)\right) \end{aligned} \tag{44}$$

Expression (44) is then simplified by defining a set of parametric elements A, B, and C, allowing the system determinant to be expressed in the form $Det = -j\omega^3 - \omega^2 A + j\omega B + C$, where the coefficients A, B, and C are given by:

$$A = \gamma_n R_{FE}^2 + \gamma_p R_{FE}^2 + \gamma_s + \gamma_{th} \tag{45}$$

$$B = \gamma_n\gamma_c R_{FE}^2 + \gamma_p\gamma_s R_{FE}^2 + \eta^2 + \gamma_s\gamma_{th} - Z\gamma_p R_{FE}^2 \tag{46}$$

$$C = \eta^2\left(\gamma_n R_{FE}^2 + \gamma_s\right) - Z\left(\gamma_n\gamma_c R_{FE}^2 + \gamma_p\gamma_s R_{FE}^2 - \gamma_n\gamma_{th} R_{FE}^2\right) \tag{47}$$

$$Z = \alpha\eta\sin(\theta) - \eta\cos(\theta) \tag{48}$$

Based on (45) - (48), the simplified small-signal field magnitude modulation response is given by:

$$H(\omega) = \frac{-\Gamma\gamma_n(j\omega + Z)}{-j\omega^3 - \omega^2 A + j\omega B + C} \tag{49}$$

The relative modulation response can be defined by:

$$H(\omega) = \frac{H(\omega)}{H(0)} = \frac{(C/Z)(j\omega + Z)}{-j\omega^3 - \omega^2 A + j\omega B + C} \xrightarrow{j\omega = S} \frac{(C/Z)(S + Z)}{S^3 + S^2 A + SB + C} \tag{50}$$

The absolute, relative modulation response, $|H_R(\omega)|^2$, is defined by multiplying (49) by its complex conjugate and is given by:

$$\left|H(\omega)\right|^2 = \frac{(C/Z)^2(\omega^2 + Z^2)}{(C - A\omega^2)^2 + (B\omega - \omega^3)^2} \tag{51}$$

For the limit of $\eta = 0$ (free-running), the coefficients A, B, and C, and the relative small-signal modulation response are reduced as given in (52) – (56), where (56) is the equivalent free-running modulation response [35], [37]. The relaxation oscillation frequency and overall damping rate of the free-running system are observed to be equivalent to the B and A coefficients, respectively.

$$A_{\eta=0} = \gamma_n + \gamma_p + \gamma_s \tag{52}$$

$$B_{\eta=0} = \gamma_n\gamma_c + \gamma_p\gamma_s \tag{53}$$

$$C_{\eta=0} = 0 \tag{54}$$

$$Z_{\eta=0} = 0 \tag{55}$$

$$H_{R,\eta=0}(\omega) = \frac{H_{FR}(\omega)}{H_{FR}(0)} = \frac{B_{\eta=0}}{B_{\eta=0} - \omega^2 + j\omega A_{\eta=0}} \tag{56}$$

Analysis of the A, B, and C coefficients in (45) - (47) shows that the damping rate given in A is increased by the injected field via the enhancement of γ_n and γ_p with R_{FE}^2, as well as by the threshold gain shift, γ_{th}. The resonance frequency driving term, $B^{1/2}$, is dependent on the enhanced free-running resonance frequency given by $\Omega_{fr}^2 = (\gamma_n\gamma_c + \gamma_p\gamma_s)R_{FE}^2$, the square of the injection strength, η^2, and the interaction between the threshold gain shift and the spontaneous carrier relaxation rate. The nonlinear carrier relaxation rate, γ_p, impacts the resonance frequency through its interaction with the Z coefficient, which is a function of the steady-state phase offset between the master and slave fields, the slave laser linewidth enhancement parameter, and the injection strength.

With the absolute, relative modulation response function described in (51), along with the A, B, and C coefficients defined in (45) - (47), the modulation response of the optically-injected diode laser can be effectively modeled. Likewise, the function presented can be verified by least-square fitting experimentally collected microwave modulation response data.

2.5. Resonance frequency of the coupled system:

The resonance frequency of the coupled system is analyzed using the determinant of the matrix introduced in (43), $Det = -j\omega^3 - \omega^2 A + j\omega B + C$, which is put into a more common representation by replacing $j\omega$ with S, yielding:

$$Det = S^3 + AS^2 + BS + C \tag{57}$$

Under stable-locking conditions, the roots of (57) will be a pair of complex conjugate roots and a real, negative root [11], [52]. As with a free-running laser, the resonance frequency is equivalent to the absolute value of the complex root. However,

solving for the roots of a cubic as in (57) is not as simple as in the quadratic free-running case. One approximation, as discussed in Lau et al. is to assume that for modulation frequencies in the GHz range, the *C* coefficient can be neglected, reducing (57) to[45]:

$$Det = S(S^2 + AS + B) \tag{58}$$

Replacing *S* with $j\omega$ in (58) results in:

$$Det = j\omega(-\omega^2 + j\omega A + B) \tag{59}$$

The $(-\omega^2 + j\omega A + B)$ portion matches that of the free-running diode laser as described in Lau et al., whereby two complex conjugate poles will be found, along with a pole at 0 [35]. For the $C = 0$ case in (59), the resonance frequency is related to the *B* coefficient given: $\Omega_r^2 = B$, and the damping rate given by $\gamma = A$ [35].

2.6. Key Detuning Cases under Stable Locking:

Based on the small-signal microwave modulation response function derived above, and the phase-detuning frequency constraints described in (23) and (24), the γ_{th} and *Z* parameters can be simplified at the positive frequency detuning edge where $\theta_o = -\pi/2$. Likewise, based on relationship between the linewidth enhancement parameter and steady-state phase offset under zero-detuning given in (14), the γ_{th} and *Z* parameters can be simplified to eliminate their dependence on θ_o. Both the positive wavelength detuning boundary for stable-locking and the zero-detuning conditions play an important role in analyzing experimentally collected small-signal modulation response data and in predicting the optically-injected behavior at these two operational conditions for varied slave laser structures and bias conditions. The interest in the zero-detuning condition is motivated by its relatively flat microwave modulation response, observed both

theoretically and experimentally under moderate injection strength, making this detuning condition ideal for broad-band applications. The positive frequency detuning edge is attractive due to the resonance frequency's direct proportionality to the maximum injection strength, giving the system the maximum resonance frequency and maximum possible 3-dB bandwidth. The drawback associated with the positive detuning edge is the large pre-resonance sag observed in the modulation response, which can be explored using the model described here. The simplifications to the γ_{th} and Z parameters are discussed in the next two sub-sections.

Simplification of the A, B, and C coefficients at zero-detuning

At the zero-detuning condition, the steady-state solution of expressions (6) and (7) yield the relationship between the linewidth enhancement parameter and phase given in (14): $\theta_o = -\tan^{-1}(\alpha)$. The γ_{th} and Z parameters can be simplified using the trigonometric identities: $\sin[-\tan^{-1}(\alpha)] = \alpha/(1+\alpha^2)^{1/2}$ and $\cos[-\tan^{-1}(\alpha)] = 1/(1+\alpha^2)^{1/2}$, resulting in:

$$\gamma_{th}=2\eta\cdot\cos(\theta_o) = 2\eta\cdot\cos(-\tan^{-1}(\alpha)) = 2\eta/(1+\alpha^2)^{1/2} \tag{60}$$

$$Z = \eta(\alpha\sin(\theta_o) - \cos(\theta_o)) = \eta(\alpha\cdot\sin(-\tan^{-1}(\alpha))) - \cos(-\tan^{-1}(\alpha)))) = -\eta(1+\alpha^2)^{1/2} \tag{61}$$

The importance of the simplification in (60) and (61) is that the steady-state phase offset can be determined based on the linewidth enhancement parameter of the slave laser, which can be measured experimentally using the injection-locking setup or various other methods [44], [46]-[48].

Simplification of the A, B, and C coefficients at the positive detuning edge

At the positive frequency detuning edge of stable-locking, the steady-state phase offset has been shown to be approximately $-\pi/2$. The field enhancement factor, R_{FE}, is approximately 1 under this detuning case. This phase offset reduces γ_{th} and Z as given in (62) and (63). Assuming a strong injection condition such that $\eta_o^2 >> \Omega_{fr}^2$ & γ_p, the A, B, and C coefficients given in (45) - (47) are reduced to those given in (64)– (66):

$$\gamma_{th}=2\eta\cdot\cos(\theta_o) = 0 \tag{62}$$

$$Z = \eta(\alpha\cdot\sin(\theta_o) - \cos(\theta_o)) = -\alpha\eta \tag{63}$$

simplifying the A, B, and C coefficients to:

$$A_{\theta=-\pi/2} = \gamma_n + \gamma_p + \gamma_s = \gamma_{fr} \tag{64}$$

$$B_{\theta=-\pi/2} = \Omega_{fr}^2 + \eta_o^2 + \alpha\eta_o\gamma_p \approx \eta_o^2 \tag{65}$$

$$C_{\theta=-\pi/2} = \eta_o^2(\gamma_n + \gamma_s) + \alpha\eta_o\,\Omega_{fr}^2 \approx \eta_o^2\gamma_{fr} + \alpha\eta_o\,\Omega_{fr}^2 \tag{66}$$

As it was previously shown that the resonance frequency of the coupled system is characterized by: $\Omega_r^2 = B$ in section 2.6, we see in (65) that B is approximately equal to η_o^2, thereby $\Omega_r^2 \approx \eta_o^2$ at the positive frequency detuning boundary of stable-locking where $\eta_o^2 >> \Omega_{fr}^2$. The large resonance peak experimentally observed in the small-signal modulation response at the positive frequency detuning boundary can then be used to verify the maximum injection strength value calculated based on the facet reflectivity, internal cavity round trip time, coupling efficiency of the master laser to the slave laser facet and the measured master and slave laser powers as described in the next section.

The theoretical small-signal response for varied bias current values for the quantum-dash Fabry-Perot laser studied in this work is plotted in Figure 9 to exemplify

the strong dependence of the resonance peak on the maximum injection strength, η_o, at the positive frequency detuning edge. Figure 9 shows that for varied slave laser bias currents (and hence different free-running damping rates and linewidth enhancement parameter), the resonance peak remains relatively constant. The positive frequency detuning edge of the injection-locked system is attractive due to the resonance frequency's direct proportionality to the maximum injection strength under this condition, giving the system a large 3-dB bandwidth and/or resonance frequency enhancement that is controlled mainly by the external master laser.

In Figure 9, the maximum injection strength, η_o, is fixed at 100 GHz for each case, leading to a resonance peak at 100 GHz/2π = 15.91 based on $\Omega_r = B^{1/2}$. As discussed in [49], the drawback of the positive frequency detuning edge is the large pre-resonance sag which typically limits the 3-dB bandwidth as in Figure 9. Noting the cubic frequency dependence of (51), the extraction of a simple 3-dB equation that accounts for the low-frequency sag in the response is problematic. In order to simplify the analysis of the sag, the two competing resonant frequencies, $B^{1/2}$ and $(C/A)^{1/2}$, are reduced to the following forms using (64) - (66): $B = \eta_o^2$ and $(C/A) = \eta_o^2 + (\Omega_{fr}^2/\gamma_{fr})(\alpha \cdot \eta^2)$ [49]. When the two resonances coincide with one another, a large resonance peak and pre-resonance sag are observed. As the $(C/A)^{1/2}$ pole increases beyond the $B^{1/2}$ pole due to an increase in $(\Omega_{fr}^2/\gamma_{fr})$ and/or the linewidth enhancement parameter α for various pumping scenarios, the sag decreases in severity. When the $(C/A)^{1/2}$ pole is adequately increased beyond the pole, the sag remains above the 3-dB threshold as shown in the 80 mA case of Figure 9.

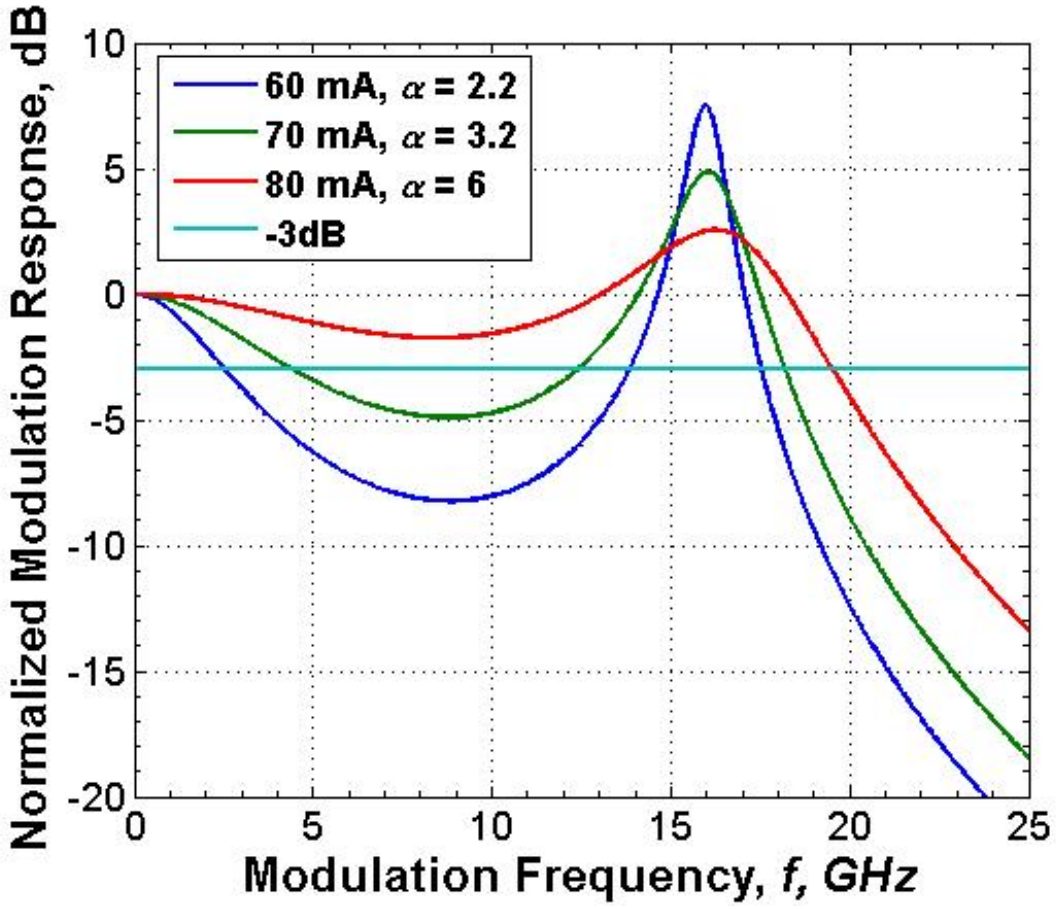

Figure 9. Theoretical modulation response at the positive frequency detuning edge where the steady-state phase offset is fixed to -π/2 using the simplified parametric terms given in (64) - (66).

For comparison purposes, the full model using the parametric terms given in (45)-(47) at the negative frequency detuning edge where the steady-state phase offset is fixed to -π/2 is plotted in Figure 10. The free-running parameters in both Figure 9 and Figure 10 are equivalent. The full model in Figure 10 shows that the B parameter is enhanced by the Ω_{fr}^2 and $\alpha\eta_o\gamma_p$ products, leading to an increase in the resonance peak as the individual Ω_{fr}, α, and γ_p terms increase with the bias current. Based on this finding, it is found that

the free-running slave laser terms should not be ignored under strong injection when analyzing the response at the positive detuning edge beyond a first order approximation.

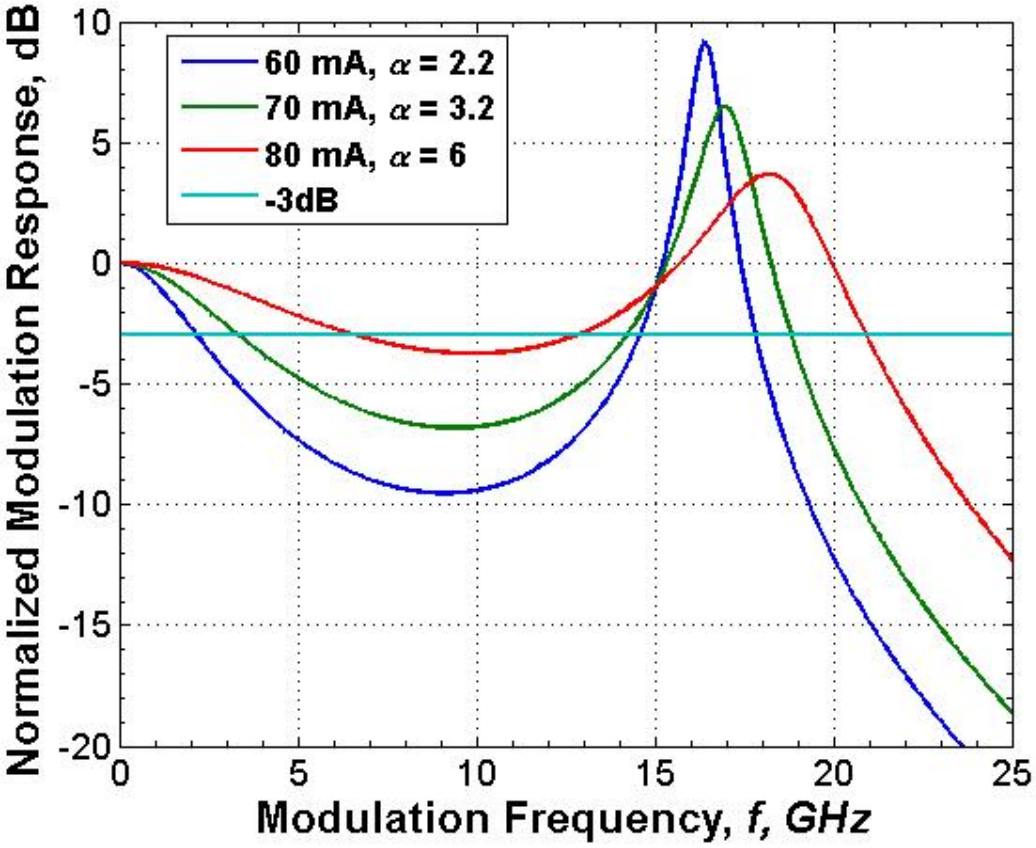

Figure 10. Theoretical modulation response at the positive detuning edge where the steady-state phase offset is fixed to -π/2 using the full coefficients given in (45) - (47).

2.7. Calculation of the Coupling Coefficient, k_c:

The maximum injection strength, η_o, introduced in (30) describes the rate at which the injected master laser field adds to the slave laser's free-running electric field. The value of the coupling coefficient, k_c, can be determined using several methods found in

the literature. Chrostowski summarizes the various methods, highlighting how the various approaches differ in the manner the injected field adds to the slave field with regards to the reflectivity of the slave laser facets [50]. The generic representation given by Chrostowski is $k_c = \tau_{rt}^{-1}\varepsilon_f$ where τ_{rt} is the internal round-trip time, and ε_f is the field transmission coefficient [50]. The internal cavity round trip time is given by: $\tau_{rt} = 2n_gL/c$, where c is the speed of light in vacuum, L is the length of the laser cavity, and n_g is the group index. The field transmission coefficient, ε_f, translates the measured external power ratio to an internal ratio. In this work where the optically-injected characteristics of Fabry-Perot diode lasers are analyzed, ε_f is determined in a manner similar to that given in Lau et al., where the internal power ratio is determined using the ratio of co-directionally propagating waves just inside the injected slave laser facet [39]. An illustration of the approach taken in [39] is given in Figure 11. In Figure 11, $P_{FR,F}$ and $P_{FR,R}$ are the free-running internal forward and reverse propagating wave power levels, respectively, and are both taken just within the injected facet. $P_{FR,ext}$ is the externally measured free-running slave laser power out of an injected slave laser facet measured using a wide area detector. The external and internal injected powers are given by $P_{inj,ext}$ and $P_{inj,int}$, respectively. The relationship between the internal and external, forward and reverse propagating waves are given in expressions (67) – (69), where R is the Fabry-Perot facet reflectivity. The relationship between the internal and external power ratios is given in (70).

$$P_{FR,ext} = P_{FR,R}(1 - R) \tag{67}$$

$$P_{FR,R}(R) = P_{FR,F} \tag{68}$$

$$P_{inj,ext}(1-R) = P_{inj,int} \tag{69}$$

$$R_{int} = R_{ext}\frac{(1-R)^2}{R} \tag{70}$$

where R_{ext} is given by: $R_{ext} = P_{inj,ext}/P_{FR,ext,single\text{-}facet}$.

Figure 11. Illustration of the approach taken in [39] to determine the external to internal injected power ratio at a single slave laser facet. The internal power ratio is taken just within the slave laser facet under optical-injection using the forward traveling waves. The internal power ratio is given by: $R_{int} = P_{inj,int}/P_{FR,F}$.

The drawback of using (70) in determining the external-to-internal power ratio is that only a portion of the slave laser's total output (that of a single slave laser facet) is considered. A portion of the experimental investigations in this work was on diode lasers with cleaved facets, where equal power is output from the front and back facets [51]. In order to account for the total slave laser free-running output power, the internal power ratio is taken at the mid-point of the slave laser cavity, as illustrated in Figure 12. In Figure 12, the power ratio is then taken not as the ratio of forward propagating waves, but as the total power ratio. In this fashion, the total free-running slave laser power is

accounted for, yielding the relationship between external and internal power ratios given in (70), where R_{ext} is given by: $R_{ext} = P_{int,ext}/P_{FR,ext,total}$ under the premise that the left and right facet reflectivity are equal ($P_{FR,ext,total} = P_{FR1,ext} + P_{FR2,ext}$. Given that the injected optical field and the forward traveling free-running slave laser field at the facet under injection travel in parallel, they each experience identical gain traveling in the diode laser's optical waveguide. Likewise, the forward-traveling free-running slave laser field (after reflection off the left facet) and the reverse-traveling free-running slave laser field (after reflection off the right facet) will be identical at the mid-point of the optical cavity's length, as illustrated in Figure 12.

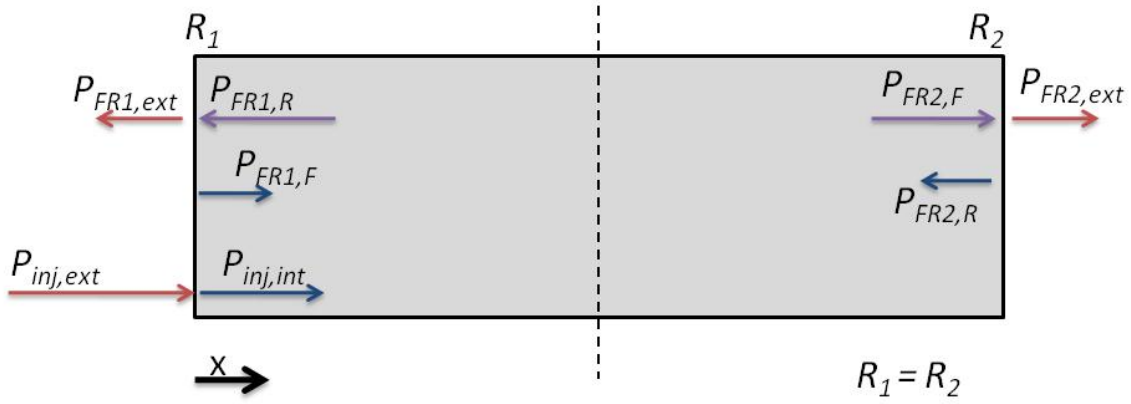

Figure 12. Illustration of the approach taken to calculate the external to internal injected power ratio where the output at both slave laser emitting facets is considered. The internal power ratio is taken at the center of the slave laser cavity, indicated by the dotted line. The internal power ratio is given by: $R_{int} = P_{inj,int}/(P_{FR1,F} + P_{FR2,R})$.

Using the relationships described in (67) – (69) to determine the appropriate relationship between the external slave laser free-running power at each facet and internal

power strengths $P_{FR1,F}$ and $P_{FR2,R}$, the complete representation of the external to internal power ratio is given in (71).

$$\frac{P_{inj,internal}}{P_{FR,internal}} = \frac{P_{inj,external}(1-R_1)}{P_{FR1,F}+P_{FR1,R}} = \frac{P_{inj,external}(1-R_1)}{\frac{P_{FR1,extnal}R_1}{(1-R_1)}+\frac{P_{FR2,extnal}R_2}{(1-R_2)}} \tag{71}$$

Given symmetric mirror reflectivities at the left and right facets, (71) simplifies to:

$$\frac{P_{inj,internal}}{P_{FR,internal}} = \frac{P_{inj,external}(1-R)^2}{P_{FR,total}R} \longrightarrow R_{int} = R_{ext}\frac{(1-R)^2}{R} \tag{72}$$

where R_{ext} is given by: $P_{inj,external}/(P_{FR,ext,total})$. Experimentally, the externally measured injected power accounts for the coupling efficiency between the lensed fiber and the slave laser facet. The coupling efficiency is based on the ratio between the slave laser free-running power measured using a wide area detector and the power measured out of the lensed fiber (in experiments, this number typically rangers from 40 – 50%). The total representation of the maximum injection strength is given in (73) [51]. Based on the measured microwave modulation response at the positive frequency detuning edge of stable-locking, where the maximum resonance frequency enhancement is observed, the frequency of the resonance peak is used to verify the maximum injection strength, η_o, using the approach described here. This approach was observed to be in good agreement with the experimentally measured data [51], discussed later in this work.

$$\eta_o = k_c\sqrt{\frac{S_{inj}}{S_{fr}}} = k_c\sqrt{\frac{P_{inj}}{P_{fr}}} = \frac{c}{2n_gL}\sqrt{\frac{P_{inj,external}(1-R)^2}{P_{FR,total}R}} = \frac{c}{2n_gL}\frac{(1-R)}{\sqrt{R}}\sqrt{\frac{P_{inj,external}}{P_{FR,total}}} \tag{73}$$

The significance of (73) is the correlation between both facet reflectivity and cavity length on the coupling coefficient, generating a means to examine changes to a slave laser cavity's dimensions and facet properties on the efficiency of the optical-injection process. The resonance frequency enhancement is directly correlated to the maximum injection strength, η_o. In turn, η_o is inversely related to the mirror reflectivity and the cavity length.

2.8. Stability Analysis of the Coupled System at Zero-Detuning:

The microwave modulation response can be analyzed based on the poles and zeros of the small-signal transfer function given in (51). Murakami et al. discusses the complex pole-zero plot relationship as a function of injection-ratio and detuning frequency, primarily under strong injection [36]. Additionally, both Simpson et al. and Murakami at al. detail the stability analysis of an optically-injected diode laser based on (57), with a focus on the case where the phase offset is 0 [11], [36]. Simpson et al. and Murakami at al. also focus on the relatively weak injection regime, where the coupled system is dominated by nonlinear dynamics [11], [36]. In this section, the poles of the transfer function polynomial are used to investigate the impact of the slave laser's linewidth enhancement parameter and nonlinear carrier relaxation rate on the coupled system's stability under zero-detuning as a function of the maximum injection strength, η_o.

One approach to determine if the coupled system operates in a stable or unstable manner is to examine the sign of the real part of the complex roots of (57) [36]. For cases where the real part of the root is negative, a stable damped oscillation exists and the system operates in the stable regime [36], [45]. For cases where the real part is positive,

the system moves toward the unstable regime, in which the system exhibits periodic fluctuations. Figure 13 illustrates the trend of the real part of the complex root as a function of the maximum injection strength, η_o, under zero-detuning. Figure 13 also shows the stability analysis's dependence on the slave laser linewidth enhancement parameter. It is in Figure 13 that the attractiveness of optically-injected nanostructure lasers is exhibited, since their characteristically low linewidth enhancement parameters is shown to inhibit unstable operation. In Figure 13, completely stable behavior is observed assuming operational parameters for the quantum-dash laser biased at 70 mA for a linewidth enhancement parameter of ~2 or below at zero-detuning.

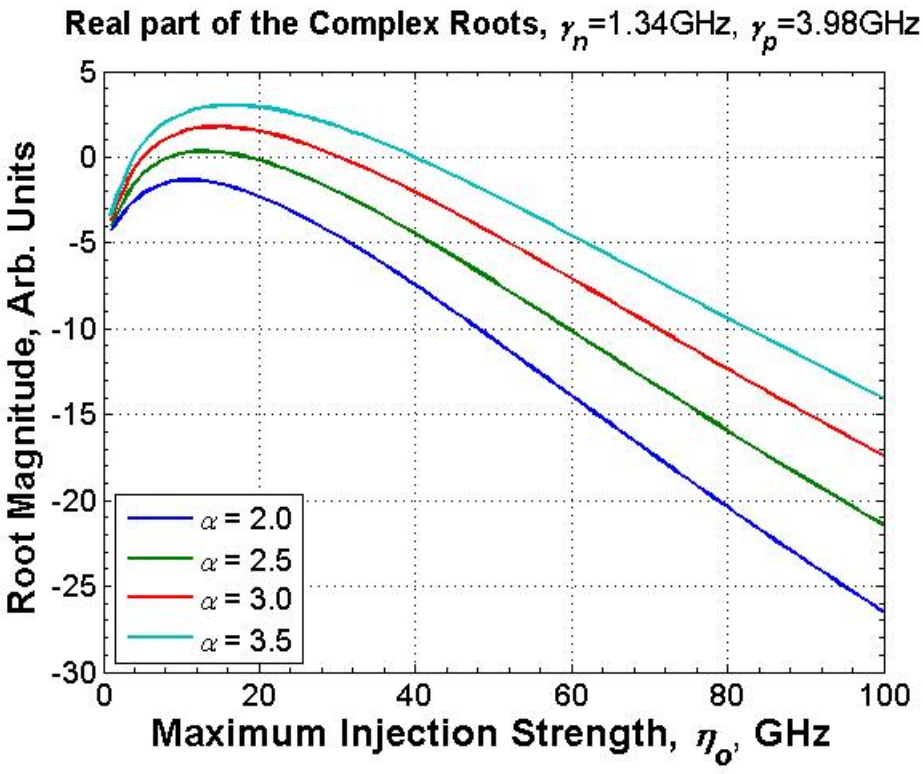

Figure 13. Progression of the real part of the complex root of the polynomial function found in (57) at zero-detuning emphasizing the impact of the slave laser linewidth enhancement parameter. Negative values are a sign of stable-locking conditions and positive values are a sign of undamped oscillations indicative of unstable-locking. The free-running laser values are for the quantum-dash laser under a bias current of 70 mA.

Figure 14 shows the impact of the nonlinear carrier relaxation rate, γ_p, on the real part of the complex poles as a function of injection strength at zero-detuning. In the figure, it is observed that the nonlinear carrier relaxation rate parameter reduces the size of the unstable operation region. This will be analyzed in greater detail using a dimensionless, normalized rate equation model in Chapter 3.

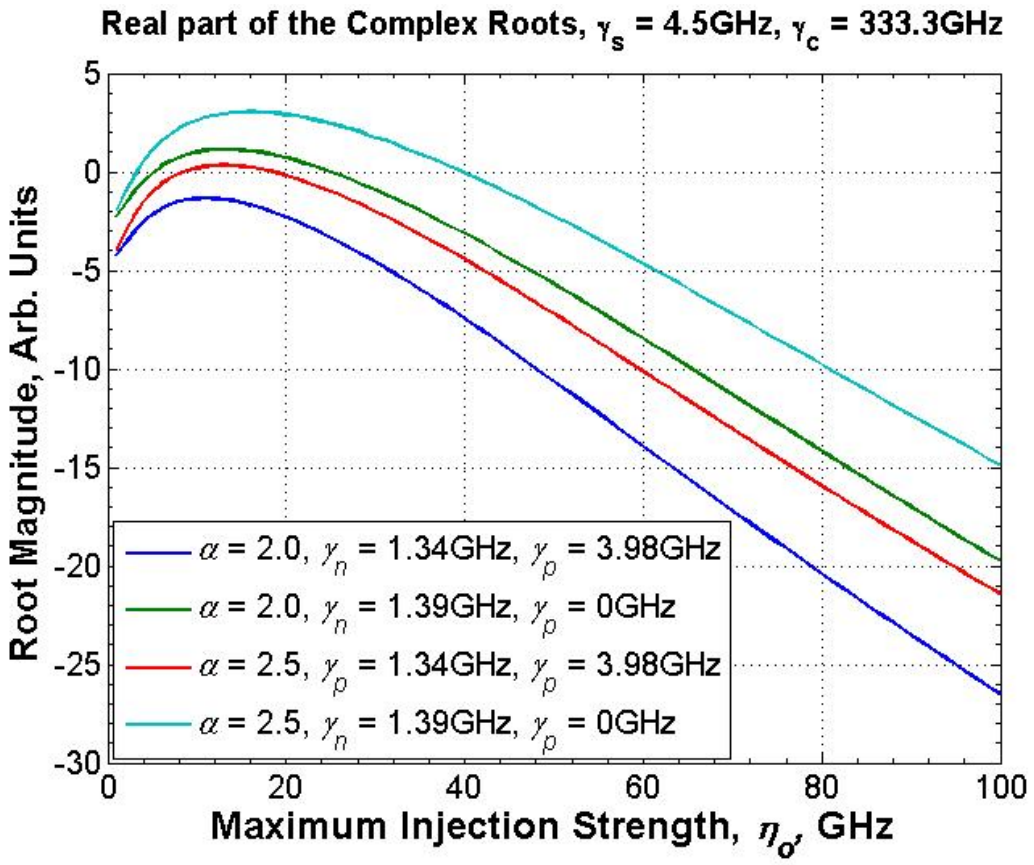

Figure 14. Impact of the nonlinear carrier relaxation rate on the real part of the complex root of the polynomial function found in (57) at zero-detuning. The free-running laser parameters (γ_n, γ_p) are for the quantum-dash laser under a bias current of 70 mA. When the real part of the root is negative, a stable damped oscillation exists and the system operates in the stable regime

Where Figure 13 plots the real part of the complex pole as a function of the maximum injection strength, η_o, at zero-detuning, a corresponding plot (Figure 15) can be used to determine the steady state phase offset limit to stable-locking for a given maximum injection strength. This analysis yields a phase offset constraint further limiting the stable-locking phase region given in (23), and is the mechanism for generating stability maps as given in Lau et al. and Murakami et al. [38], [36]. Solving for the steady-state phase offset limit of stable-locking can be used to determine the field

enhancement factor using expression (17) and the experimentally measured frequency detuning edge. The real part of the complex root of (57) is plotted as a function of phase offset in Figure 15, where the stable-boundary is observed to be -1.529 radians. **The significance here is that the positive frequency detuning edge of stable-locking, which is typically approximated to be -π/2, deviates only slightly from this value (under strong injection conditions)**. Once the steady-state phase offset is determined at this boundary, the field enhancement factor can then be determined using (17). The field enhancement factor is typically approximated to be 1 at the positive frequency detuning edge of stable-locking [40], and the plot shown here affirms this assumption as it is found to be 1.05 (indicated on Figure 15(bottom)).

The drawback to the stability analysis of examining the sign of the real part of the complex root in the transfer function polynomial is that it merely indicates that undamped oscillations occur, not the specific behavior of the unstable operation. The nature of the undamped, unstable operation is examined in greater detail in Chapter 3 using a newly derived normalized rate equation model based on the approach detailed by Erneux et al. and Gavrielides et al. [17], [20]. The utility of the stability analysis depicted in Figure 13 and Figure 15 is its simplicity in evaluating a laser's stability under optical-injection based on its free-running parameters.

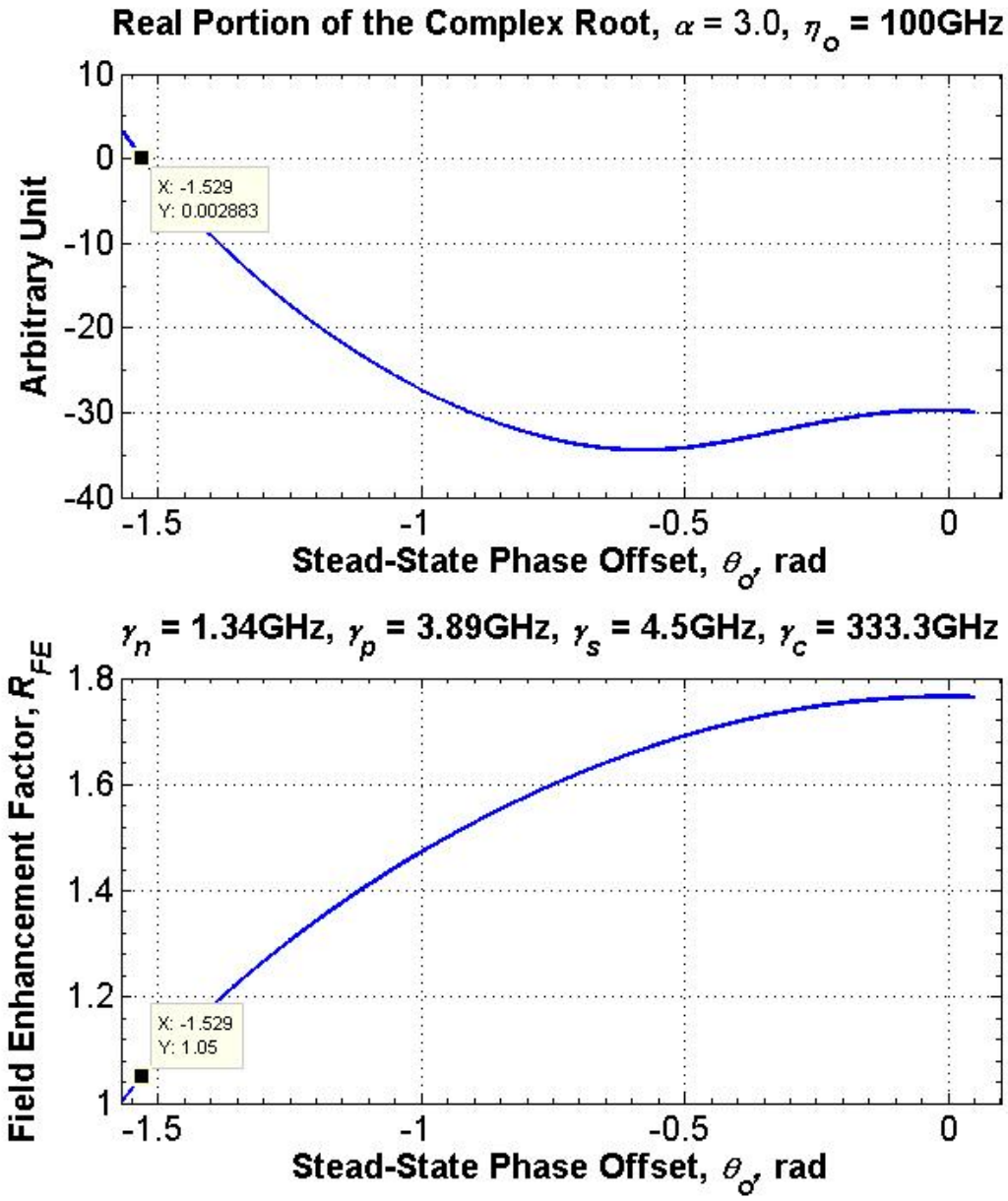

Figure 15. (top) Progression of the real part of the complex root of (57) as a function of steady-state phase offset for a fixed maximum injection strength of 100 GHz. Negative values are a sign of stable-locking conditions and positive values are a sign of undamped oscillations indicative of unstable-locking. (bottom) The corresponding field enhancement factor based on the phase offset. The free-running laser parameters are based on the quantum-dash laser biased at 70 mA. Takeaway: the steady-state phase offset boundary of stable-locking is approximately -π/2. The corresponding field enhancement factor is ~1.

2.9. Pole-Zero Analysis at Zero-Detuning

This section analyzes the poles and zeros of the small-signal transfer function given in (51) at zero-detuning in order to give a complete picture of the modulation response's dependence on the maximum injection strength parameter, η_o. The impact of the nonlinear carrier relaxation rate of the nanostructure lasers is compared with the model where it is not included in the derivation.

Increasing the injection strength modifies the poles and zeros of the small-signal transfer function, resulting in an increased overall damping of the modulation response under zero-detuning conditions. The progression of the transfer function poles and zeros as a function of maximum injection strength, η_o, at zero-detuning is illustrated in Figure 16. In Figure 16, it is noted that the absolute value of the complex roots indicate the resonance frequency of the coupled system. The field enhancement factor, R_{FE}, which increases with the maximum injection strength η_o, decreases the proportionality between the resonance frequency of the coupled system (given by the absolute value of the complex roots) and the maximum injection strength η_o, leading to a sub-linear relationship. The relationship between the injection strength, $\eta = \eta_o / R_{FE}$, and the resonance frequency of the coupled system is illustrated in Figure 16 by the purple and dark blue lines, respectively.

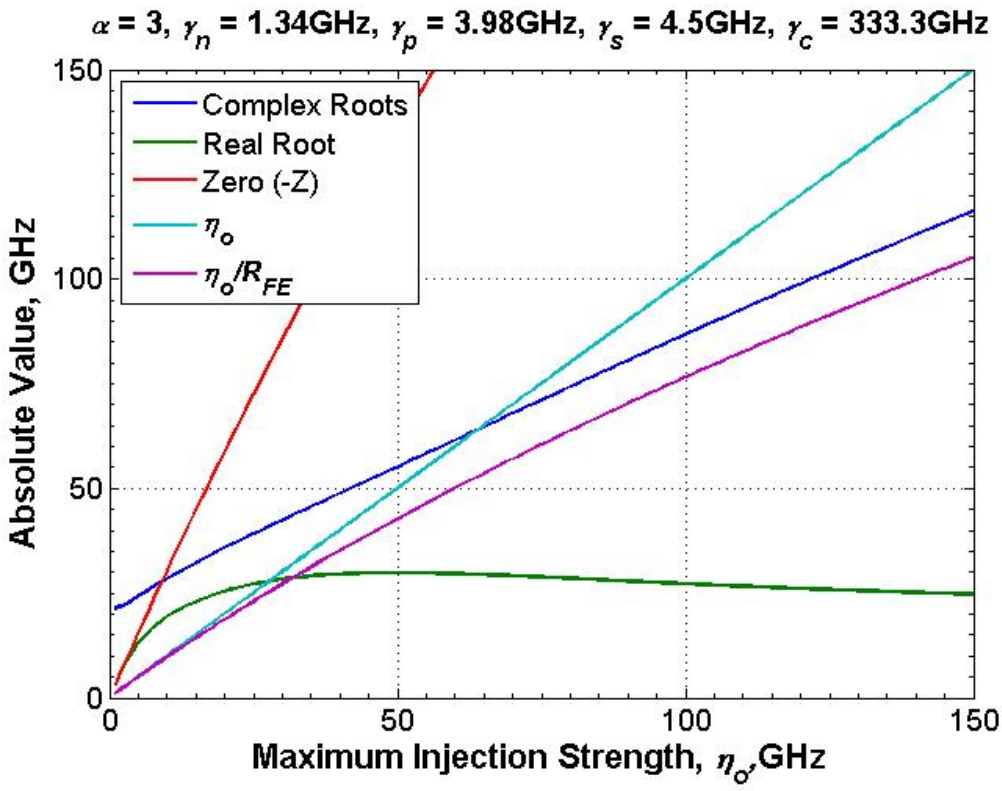

Figure 16. Absolute value of the roots/pole of the transfer function in (51) at zero-detuning; $\alpha = 3$. The field enhancement factor, R_{FE}, which increases with the maximum injection strength η_o, decreases the proportionality between the resonance frequency of the coupled system (given by the absolute value of the complex roots) and the maximum injection strength η_o, leading to a sub-linear relationship. The free-running laser parameters are based on the quantum-dash laser biased at 70 mA.

The third, real root of the transfer function's denominator results in a low frequency roll-off that is relatively constant as the maximum injection strength is increased. The zero increases at a faster rate than either of the transfer function's poles. This relationship will cause the pole to have little impact at lower modulation frequencies such that it does not offset the impact of the low frequency poles under strong injection conditions.

The impact of the slave laser linewidth enhancement parameter on the zero, as given in (48), is illustrated in Figure 17. The decreased zero will result in its offsetting a pole in the transfer function, leading to a greater damping of the modulation response. The decrease in the linewidth enhancement parameter, α, is also shown to decrease the resonance frequency of the coupled system. At zero-detuning, the steady-state phase offset between the master and slave is given by the relationship in (14). As α is decreased, θ_o decreases in magnitude; given that the real root of (34) yields the value of R_{FE} and is dependent on the cosine of the phase offset θ_o, this relationship results in an increase in R_{FE} which decreases the injection strength $\eta = \eta_o / R_{FE}$. The overall impact of the linewidth enhancement parameter on the small-signal modulation response is illustrated in Figure 18 and Figure 19.

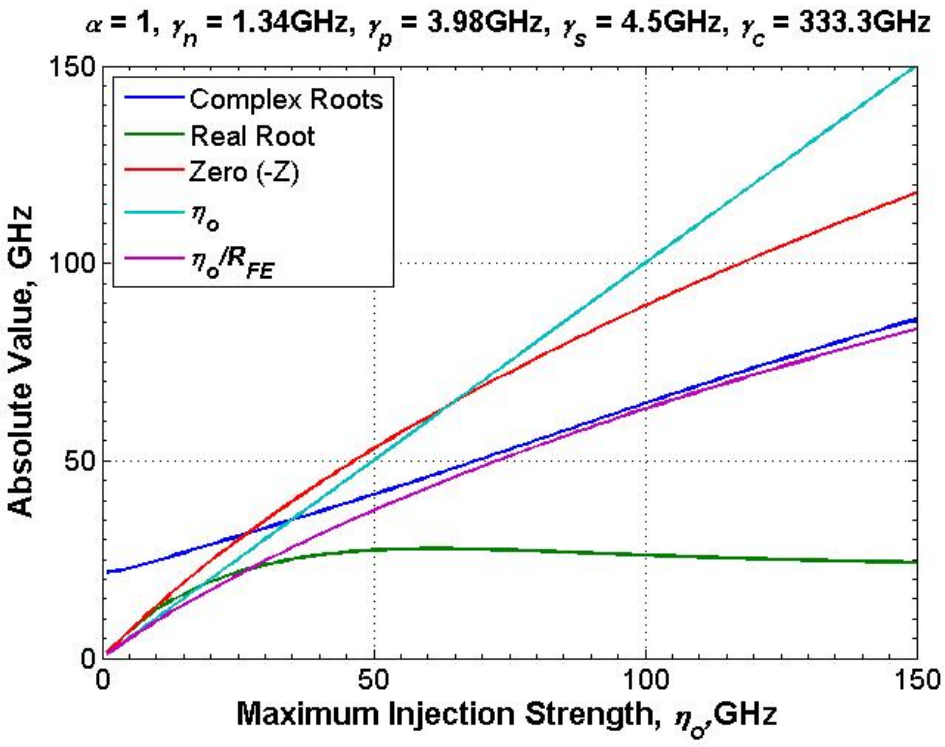

Figure 17. Absolute value of the roots/pole of the transfer function in (50) at zero-detuning; $\alpha = 1$. Compared with Figure 16, the zero increases at a much smaller rate and a weaker relationship exists between the maximum injection strength η_o and resonance frequency of the coupled system (given by the absolute value of the complex roots). The decreased zero will result in its offsetting a pole in the transfer function, leading to a greater damping of the modulation response. The free-running laser parameters are based on the quantum-dash laser biased at 70 mA.

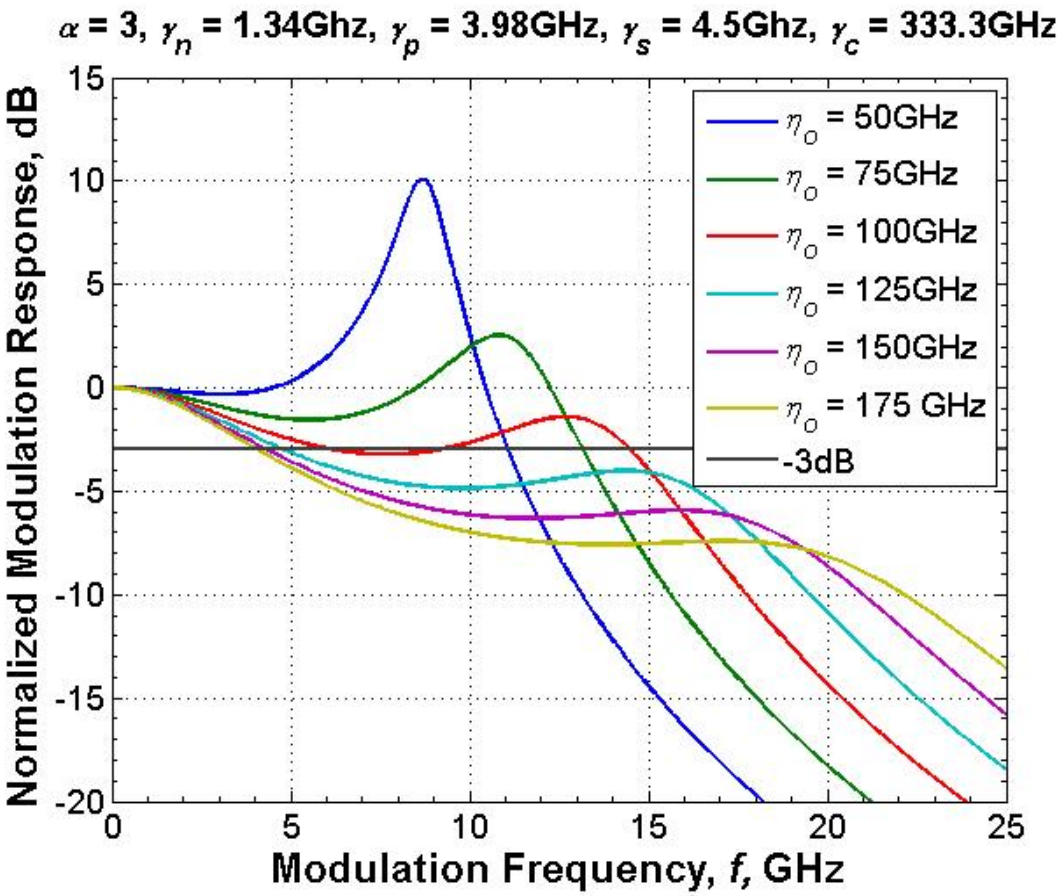

Figure 18. Modulation response as a function of maximum injection strength at zero-detuning, $\alpha = 3$. The free-running laser parameters are based on the quantum-dash laser biased at 70 mA.

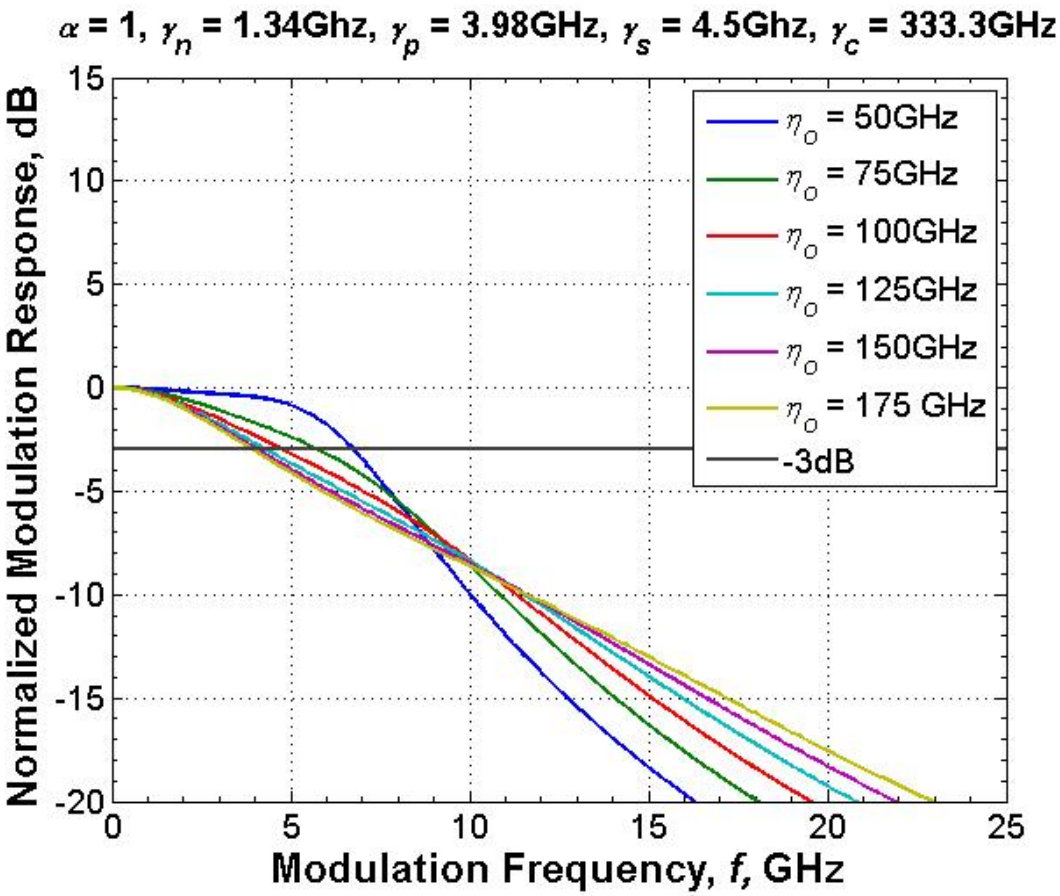

Figure 19. Modulation response as a function of maximum injection strength at zero-detuning, $\alpha = 1$. Compared with Figure 18, the response is more strongly damped. The free-running laser parameters are based on the quantum-dash laser biased at 70 mA.

The impact of the linewidth enhancement parameter α on the modulation transfer function is also examined using the A, B, and C coefficients defined in (45) - (47). Figure 20 and Figure 21 show the A, B, and C coefficients as a function of the maximum injection strength, η_o, for $\alpha = 3$, and $\alpha = 1$, respectively. The $\alpha = 1$ case shows that the damping rate driven by the A coefficient increases at a faster rate than the resonance frequency approximated by the B coefficient, leading to the damped response at increased maximum injection strengths observed in Figure 19. Recall that for a free-running diode laser, the damping rate is linearly dependant on the laser output power and the resonance

frequency is proportional to the square root of the output power [37]. For the case of the optically-injected diode laser at zero-detuning, the θ_o-α-R_{FE} inter-relationship modifies the observed behavior between maximum injection-strength (proportional to the square root of the injected power), damping rate, and resonance frequency.

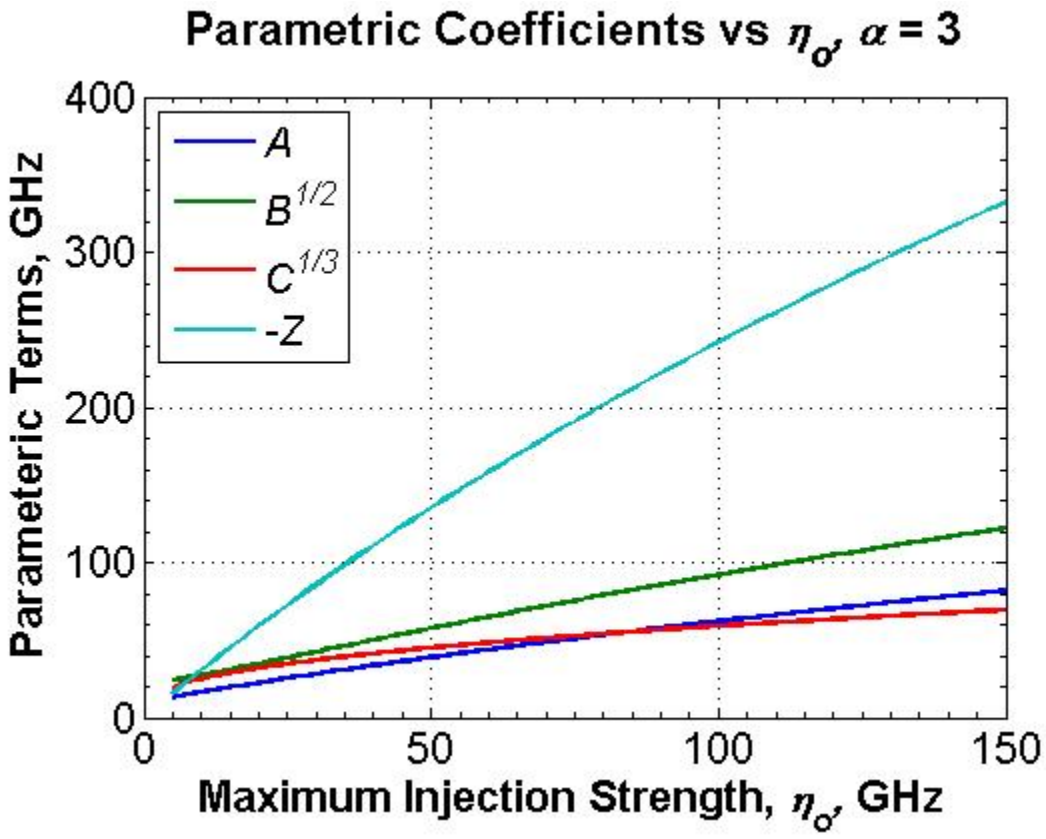

Figure 20. *A*, *B*, and *C* coefficients as a function maximum injection strength at zero-detuning, $\alpha = 3$. Notice that the resonance frequency driving term, $B^{1/2}$, remains larger than the damping rate driving term, *A*. The free-running laser parameters are based on the quantum-dash laser biased at 70 mA (γ_n = 1.34 GHz, γ_p = 3.98 GHz, γ_s = 4.5 GHz, γ_c = 333.3 GHz).

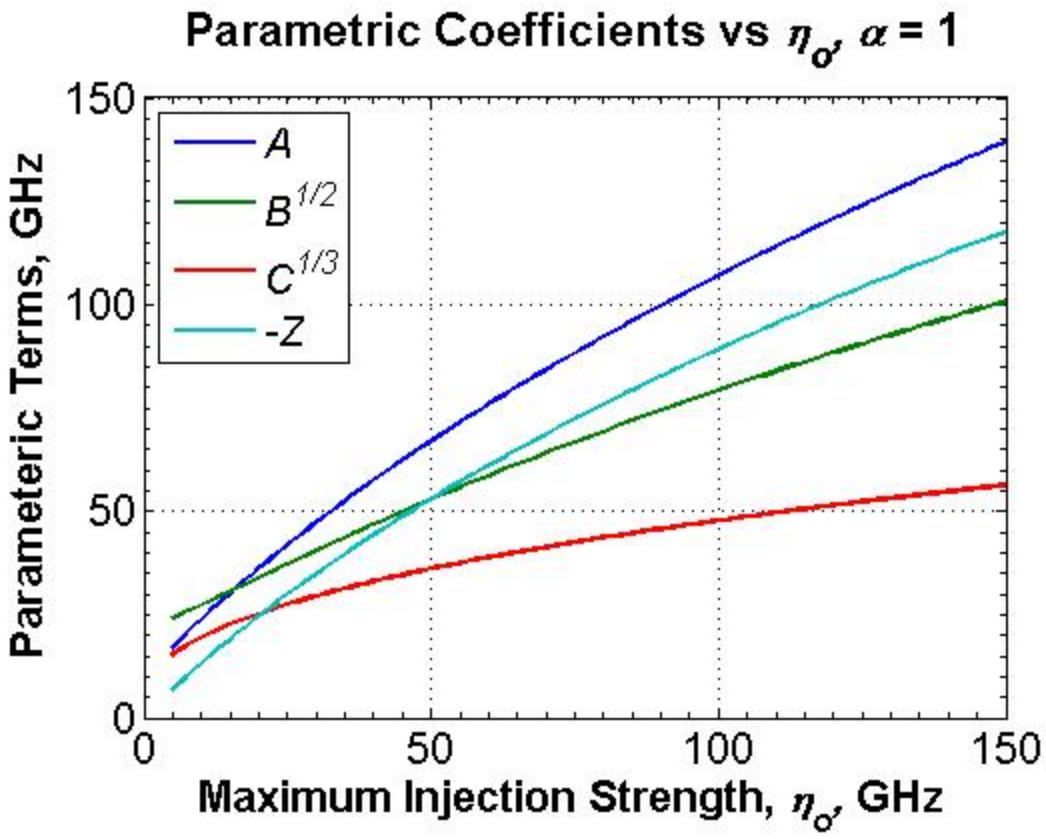

Figure 21. *A*, *B*, *C* and *Z* coefficients as a function maximum injection strength at zero-detuning, $\alpha = 1$. Notice that the resonance frequency driving term, $B^{1/2}$, remains smaller than the damping rate driving term, *A*, contrasting with the results in Figure 20. The larger damping rate term leads to the damped response observed in Figure 19. The free-running laser parameters are based on the quantum-dash laser biased at 70 mA (γ_n = 1.34 GHz, γ_p = 3.98 GHz, γ_s = 4.5 GHz, γ_c = 333.3 GHz).

The impact of the nonlinear carrier relaxation rate, γ_p, is examined in Figure 22, where the *A*, *B*, and *C* coefficients with and without γ_p are plotted as function of the maximum injection strength. In the case where the contribution of γ_p is neglected, γ_n has been adjusted such that $\Omega_{fr}^2 = \gamma_c\gamma_n$ (as opposed to $\Omega_{fr}^2 = \gamma_c\gamma_n + \gamma_p\gamma_s$). Figure 22 illustrates the relatively linear increase in both *A* and *B* coefficients to larger magnitudes when γ_p is considered. The impact of the nonlinear carrier relaxation rate, γ_p, on the modulation

transfer function is given in Figure 23, where the microwave modulation response is plotted for increased maximum injection strengths under zero-detuning with the nonlinear carrier relaxation rate excluded. As expected, Figure 23 illustrates that the nonlinear carrier relaxation rate increases the degree of damping exhibited in the modulation response. Counter-intuitively, the nonlinear carrier relaxation rate is also observed to increase the resonance frequency of the coupled system, observable in Figure 22 and Figure 23.

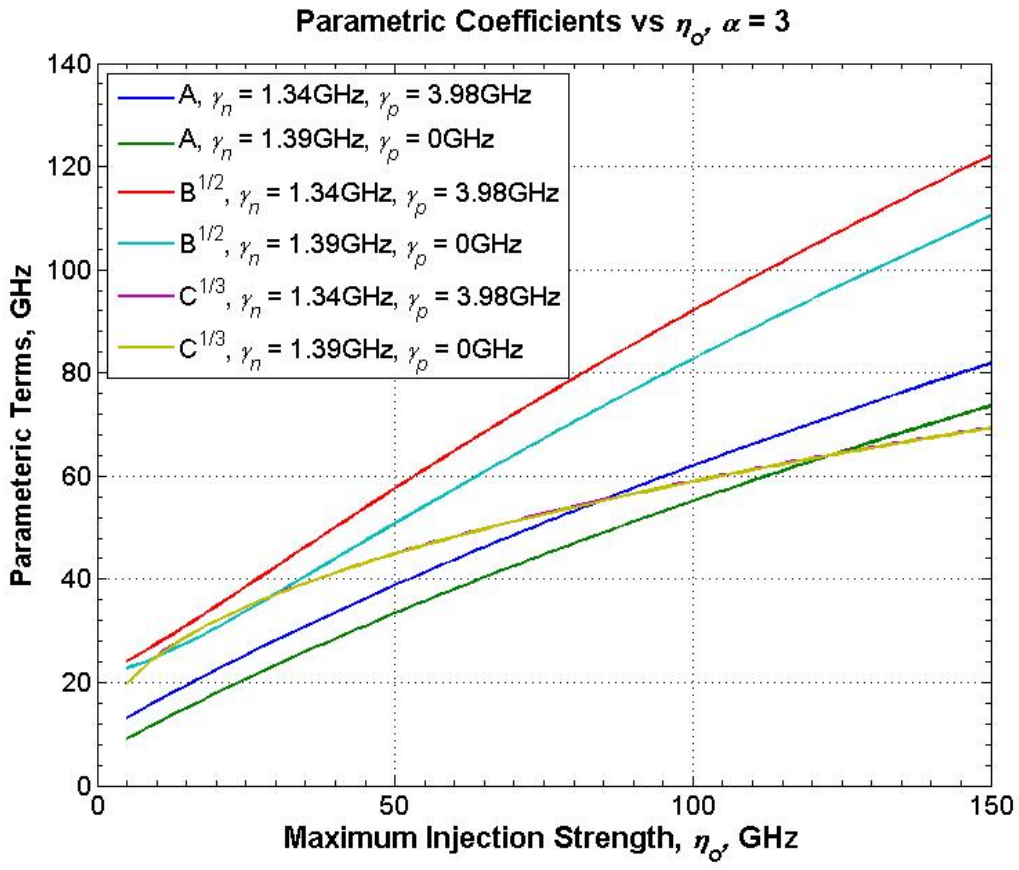

Figure 22. *A*, *B*, and *C* coefficients comparing their values with and without the inclusion of the nonlinear carrier relation rate as a function maximum injection strength at zero-detuning; $\alpha = 3$. Notice that the resonance frequency driving term, $B^{1/2}$, increases with the inclusion of the nonlinear carrier relaxation rate γ_p in the simulation. Additionally, the damping rate term is also observed to increase with the inclusion of γ_p. The free-running laser parameters are based on the quantum-dash laser biased at 70 mA. The impact of γ_p on the *C* term is negligible.

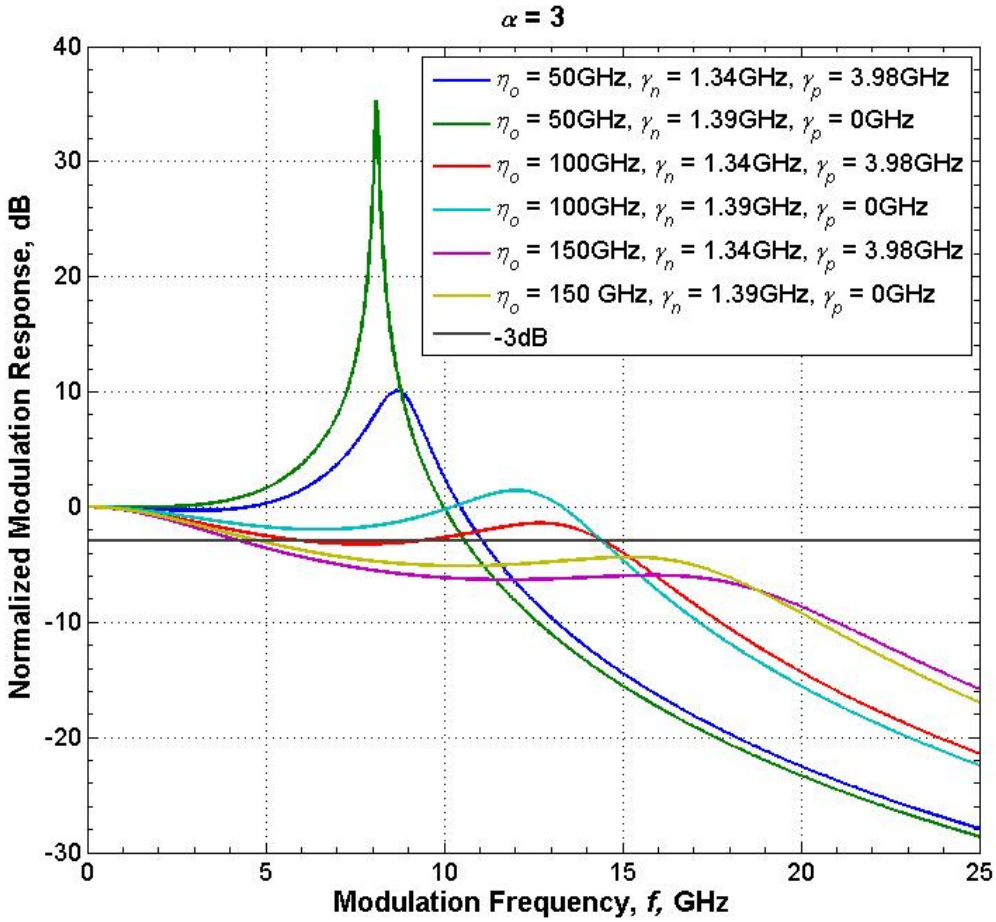

Figure 23. Microwave modulation response plotted both with and without the consideration of the nonlinear carrier relation rate as a function maximum injection strength at zero-detuning; $\alpha = 3$. Notice that simulating the response with the nonlinear carrier relaxation rate γ_p increases both the resonance frequency and damping of the coupled system. The free-running laser parameters are based on the quantum-dash laser biased at 70 mA.

2.10. Impact of Gain Compression

The next step in modeling the optically-injected nanostructure laser is to account for the gain compression observed under strong injection. Among the intrinsic dynamical parameters (γ_n, γ_p, γ_c, and γ_s) describing free-running diode lasers, γ_c and γ_s are constants

independent of the laser power while γ_n and γ_p are linearly proportional to the laser power [37]. The nonlinear carrier relaxation rate, γ_p, is defined as $-\Gamma g_{p,s} S_{fr}$ in (32), where $g_{p,s}$ is the nonlinear gain parameter characterizing the effect of gain compression due to the saturation of gain by intra-cavity photons [37]. Likewise, the differential carrier relaxation rate, γ_n, is defined as $g_{n,s} S_{fr}$ in (31), where $g_{n,s}$ is the differential gain parameter characterizing the dependence of the gain parameter on the carrier density as described in (4) [37]. For most quantum-well and heterostructure lasers, the impact of gain compression can be neglected and both $g_{n,s}$ and $g_{p,s}$ can be considered constant over large ranges of carrier and photon density levels [35], [37]. This is not the case, however, for the nanostructure lasers investigated in this work, where γ_n and γ_p are found to be compressed at large free-running laser output powers. This compression or roll-off as regards the quantum-dash device investigated in this work is illustrated in Figure 24, where Ω_{fr}^2, γ_n, and γ_p are plotted as a function of total output power.

The takeaway from Figure 24 is that γ_p and γ_n are observed to lose their linear proportionality to the laser output power as the output power is increased beyond ~8 mW. In section 2.2, the field enhancement factor R_{FE} was introduced to quantify the enhancement of the steady-state field of the optically-injected slave laser (and likewise the enhanced steady-state photon density, S_o) and used to scale γ_p and γ_n under optical-injection. This scaling with R_{FE} assumes that the linear relationship holds regardless of the magnitude of the injected field. To account for the roll-off of the differential and nonlinear carrier relaxation rates induced by the injected photons (or injected field), the gain compression coefficient is introduced into the gain function in the standard way as discussed by Coldren at al. [35].

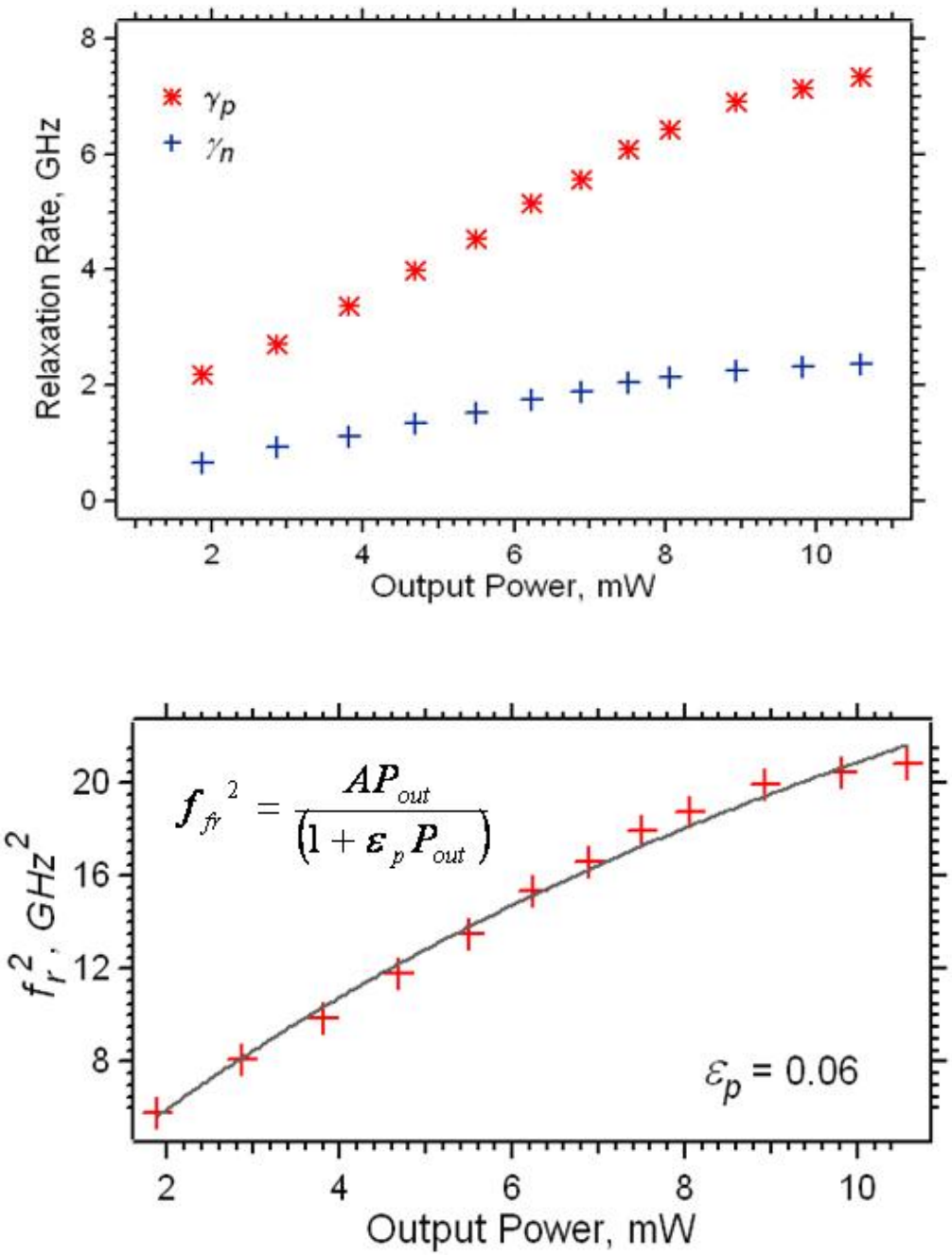

Figure 24. (top) Illustration of free-running nonlinear carrier relaxation rate and differential carrier relaxation rate saturation with increased laser output power. (bottom) Saturation of the relaxation oscillation frequency squared with increased laser output power. Data shown was collected on the quantum-dash Fabry Perot laser.

Coldren et al. describes relationship of the laser gain to carrier density using (74), where a coefficient describing the compression of gain at high photon densities is defined by ε_p [35]. The laser gain is then described by [35]:

$$g(N,S) = \frac{g_o}{(1+\varepsilon_p S)} \ln\left(\frac{N+N_s}{N_{tr}+N_s}\right) \tag{74}$$

Where g_o is the nominal, unsaturated gain coefficient, N_{tr} is the transparency current density, N_s is a term introduced for force the natural logarithm to be finite at $N = 0$, and S is the photon density [35]. At threshold, $N = N_{th}$, and $g(N_{th}, 0) = g_{th}$, the threshold gain value. Based on (74), the gain derivative with respect to both carrier and photon density is given by (75) and (76).

$$\frac{\partial g}{\partial N} = \frac{g_o}{(1+\varepsilon_p S)} \frac{1}{(N+N_s)} \tag{75}$$

$$\frac{\partial g}{\partial S} = \frac{-\varepsilon_p g_o}{(1+\varepsilon_p S)^2} \ln\left(\frac{N+N_s}{N_{tr}+N_s}\right) = \frac{-\varepsilon_p g(N,S)}{(1+\varepsilon_p S)} \tag{76}$$

Changes in carrier and photon density from both small-signal current perturbations and/or optical-injection on the gain are reflected by the differential expression in (77). The change in gain, along with carrier density and photon density, taken in reference to the free-running, steady-state threshold value where $\Delta N = N_o - N_{th}$ and $\Delta S = S_o + S_{inj} - S_{fr}$ yields (78).

$$\partial g(N,S) = \frac{g_o}{(1+\varepsilon_p (S+S_{inj}))} \frac{1}{(N+N_s)} \partial N + \frac{-\varepsilon_p g_o}{(1+\varepsilon_p (S+S_{inj}))^2} \ln\left(\frac{N+N_s}{N_{tr}+N_s}\right) \partial S \tag{77}$$

$$g = g_{th} + \frac{g_o}{(1+\varepsilon_p(S_o+S_{inj}))}\frac{1}{(N_o+N_s)}(N_o - N_{th}) + \frac{-\varepsilon_p g_o}{(1+\varepsilon_p(S_o+S_{inj}))^2}\ln\left(\frac{N_o+N_s}{N_{tr}+N_s}\right)(S_o+S_{inj}-S_{fr,SS}) \tag{78}$$

Defining $g_{n,S}$ and $g_{p,S}$ using (79) and (80) where S_{total} is the total photon density in the slave laser cavity simplifies (78) to the expression given in (81) using (79) and (80), as previously defined in (4). Although $g_{n,s}$ and S_{fr} (likewise $g_{p,s}$ and S_{fr}) cannot be individually determined using the approach used, the $(1 + \varepsilon_p S_{fr})$ portion in the denominator of $g_{n,S}$ and $g_{p,S}$ can be determined. Quantifying $\varepsilon_p S_{fr}$ allows the gain compression term to be scaled with the injection strength, resulting in the differential and nonlinear carrier relaxation rates defined in (82) and (83) where gain compression and the scaling of S_{fr} due to optical-injection is included.

$$g_{n,S} = \frac{\partial g}{\partial N} = \frac{g_o}{(1+\varepsilon_p S_{total})}\frac{1}{(N+N_s)} \tag{79}$$

$$g_{p,S} = \frac{\partial g}{\partial S} = \frac{-\varepsilon_p g_o}{(1+\varepsilon_p S_{total})^2}\ln\left(\frac{N+N_s}{N_{tr}+N_s}\right) \tag{80}$$

$$g = g_{th} + g_{n,s}(N - N_{th}) + g_{p,S}\left((S+S_{inj}) - S_{fr}\right) \tag{81}$$

The effect of the compression on the microwave modulation response at zero-detuning for increasing maximum injection strengths is illustrated in Figure 25. Although the impact of gain compression on the overall modulation response is relatively small, it is shown to reduce the resonance frequency enhancement, thereby limiting the potential 3-dB bandwidth enhancement. The impact of gain compression on the *A*, *B*, and *C* parametric terms is given in Figure 26, where each parameter is reduced compared to the

'uncompressed' value. Figure 26 also shows that the impact of gain compression increases with the maximum injection strength.

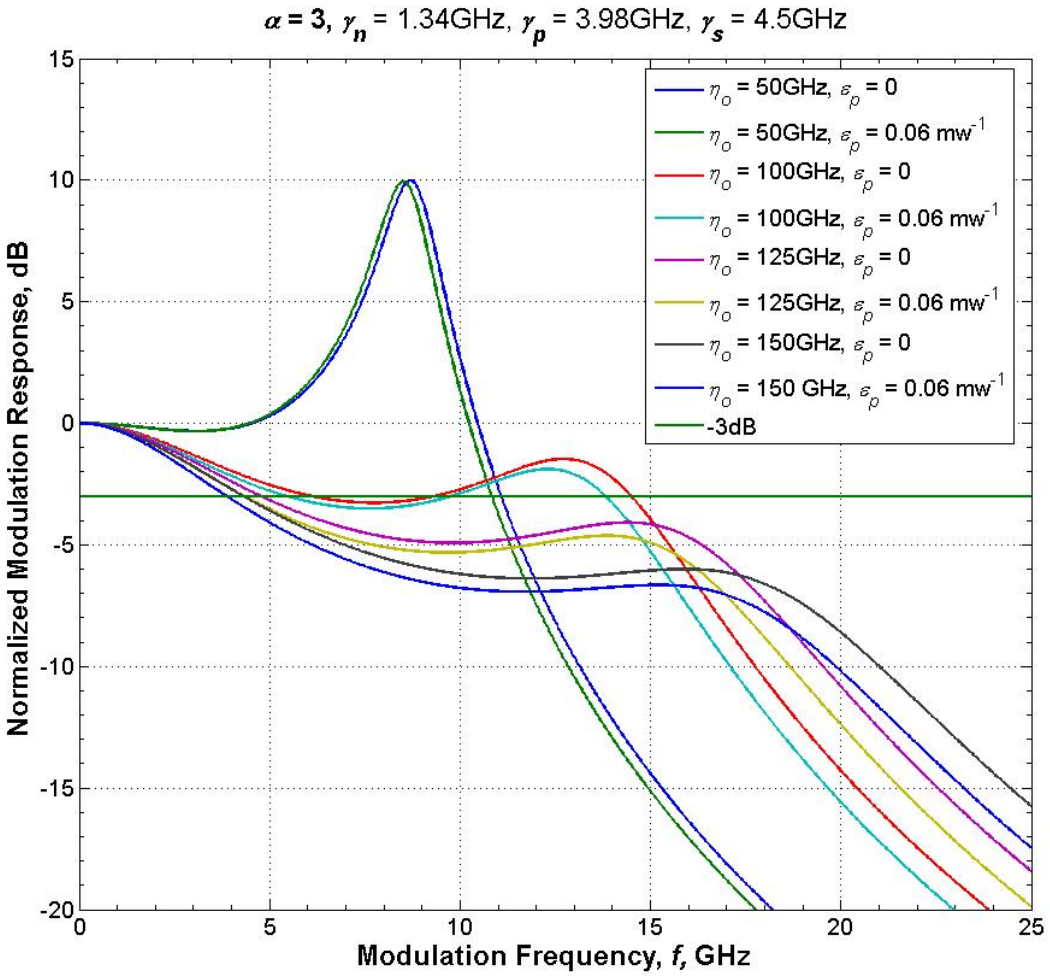

Figure 25. Microwave modulation response plotted both with and without the consideration of the gain compression coefficient shown in eqn. (74) on the differential and nonlinear carrier relation rate at zero-detuning; $\alpha = 3$. The free-running laser parameters are based on the quantum-dash laser biased at 70 mA, and the gain compression coefficient is 0.06 mW^{-1}.

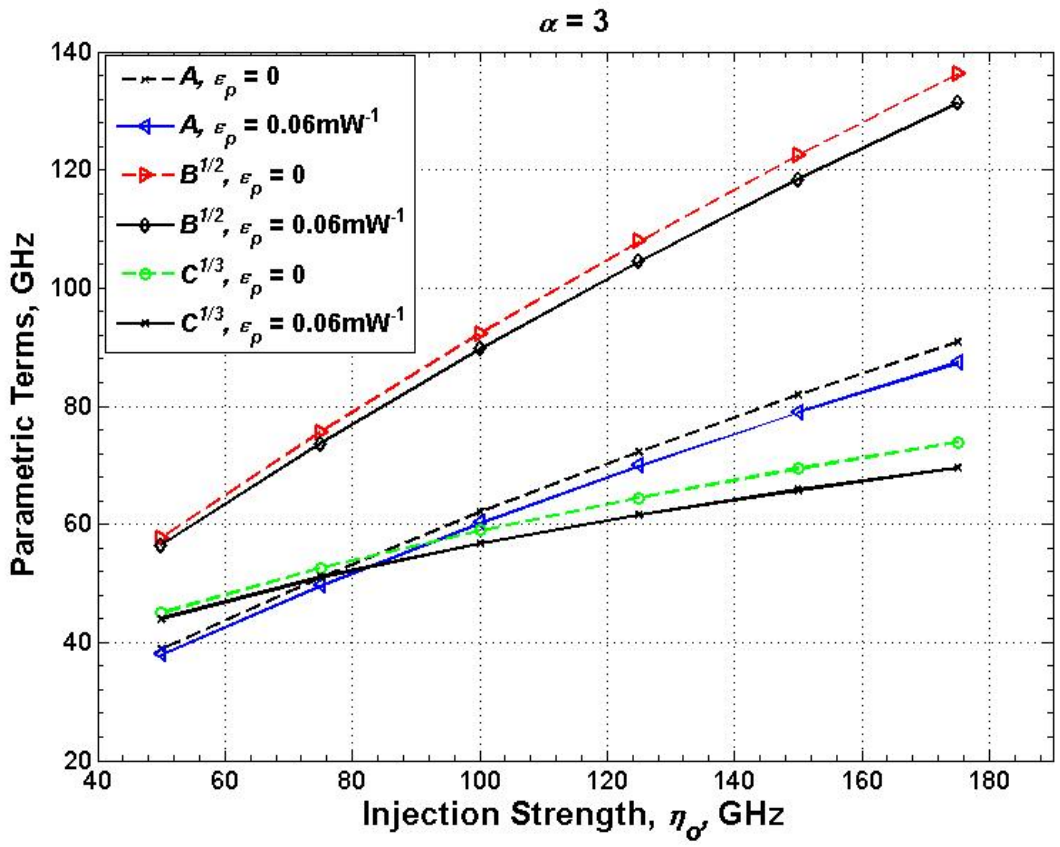

Figure 26. *A*, *B*, and *C* parametric terms plotted both with and without the consideration of the gain compression effect on the differential and nonlinear carrier relation rates plotted as a function of maximum injection strength at zero-detuning; $\alpha = 3$. The free-running laser parameters are based on the quantum-dash laser biased at 70 mA, and the gain compression coefficient is 0.06 mW^{-1}.

In both Figure 25 and Figure 26, the impact of gain compression on γ_n and γ_p is given in (82) and (83). Essentially, the approach used here to illustrate the impact of gain compression on γ_n and γ_p re-normalize the gain compression to the scaled free-running slave power. The R_{FE}^2 factor in (82) and (83) scales the value based on the slave field enhancement as described in Section 2.2.

$$\gamma_{n,comp} = \gamma_n R_{FE}^2 \frac{(1+\varepsilon_p P_{fr})}{\left(1+\varepsilon_p (P_{fr} R_{FE}^2 + P_{inj})\right)} \tag{82}$$

$$\gamma_{p,comp} = \gamma_p R_{FE}^2 \frac{(1+\varepsilon_p P_{fr})^2}{\left(1+\varepsilon_p (P_{fr} R_{FE}^2 + P_{inj})\right)^2} \tag{83}$$

2.11. Overall Modulation Response Function

Overall, the modulation response function derived in this chapter expands upon the approach analyzed by Murakami et al. and Lau et al. by including the impact of the nonlinear carrier relaxation rate, γ_p, and the gain compression coefficient's impact on both the differential and nonlinear carrier relaxation rates [36], [38]. In the previous sections, the impact of the nonlinear carrier relaxation rate was illustrated by comparing the modulation response with and without its consideration (Figure 23). The impact of gain compression was then added to account for the usual sub-linear dependence of the free-running relaxation frequency with optical power (Figure 25). The normalized relative modulation response function in (51) is illustrated in Figure 27, where the physical effects of gain compression and the nonlinear carrier relaxation rate on the modulation response under optical-injection are exhibited through the parametric terms in (45) - (47). In Figure 27, the complete physical model shows more damped response compared to the basic model where γ_p and ε_p equal 0, while the resonance frequency enhancement remains largely unchanged. In Chapter 5 and Chapter 6, this model will be used as a predictive tool data and used to least-square-fit experimental data.

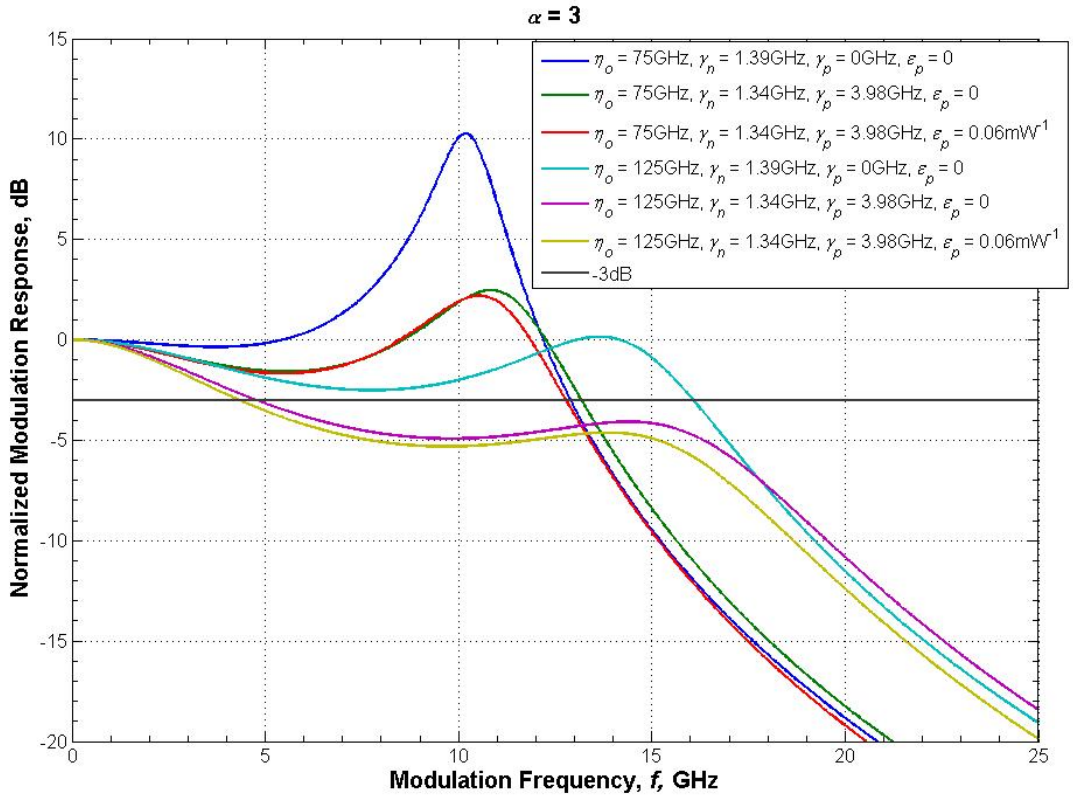

Figure 27. Modulation response function incorporating the physical effects of the nonlinear carrier relaxation rate and gain compression under optical-injection. The free-running laser parameters are based on the quantum-dash laser biased at 70 mA, $\alpha = 3$.

Chapter 3. Dynamic Operation of Optically-Injected Nanostructure Diode Lasers

In the previous chapter, the microwave modulation response of an optically-injected nanostructure laser was theoretically analyzed. Based on the dynamic parameters describing the modulation response under steady-state conditions, the frequency detuning and injection strength limits for stable-locking were derived. The drawback of the stability limits described in Chapter 2 is that the nature of the unstable/nonlinear operation cannot be described in detail. In this chapter, a dimensionless normalized approach to theoretically evaluate the behavioral state (i.e. stable locking, period-one, period-doubling, or chaos) as a function of the injected field ratio and/or the detuning frequency for varied slave laser bias cases is described [17], [20]. The normalized model reformulates the rate equations in (6) - (8) into a dimensionless form; this approach is largely due to the relatively small value of the photon lifetime of the semiconductor laser [17]. The normalized model is advantageous compared with other methods due to its fundamental parameter scaling approach that facilitates the comparison of one laser to another. The model derived here is unique in that it includes the impact of the nonlinear carrier relaxation rate, γ_p. The slave laser linewidth enhancement parameter and γ_p are shown to have a strong impact on the level of stability exhibited by the optically-injected laser at low injected field ratios.

3.1. The Normalized Rate Equations

The normalized approach presented here differs from the model previously published in that the impact of the nonlinear carrier relaxation rate is included. The expanded rate equations given Chapter 2 are reiterated below as a starting point:

$$\frac{dA}{dt} = \frac{1}{2}\Gamma\left(g_{th}A + g_n(N - N_{th})A + g_p(A^2 - A_{fr}^2)A\right) - \frac{1}{2}\gamma_c A + k_c A_{inj}\cos(\theta) \tag{6}$$

$$\frac{d\theta}{dt} = \frac{\alpha}{2}\Gamma\left(g_{th} + g_n(N - N_{th}) + g_p(A^2 - A_{fr}^2)\right) - \frac{\alpha}{2}\gamma_c - k_c\frac{A_{inj}}{A}\sin(\theta) - \Delta\omega \tag{7}$$

$$\frac{dN}{dt} = J - \gamma_s N - g_{th}A^2 - g_n(N - N_{th})A^2 - g_p(A^2 - A_{fr}^2)A^2 \tag{8}$$

The time-scale in (6) - (8) is normalized to the cavity decay rate such that: $t = \tau/\gamma_c$, simplifying the time-step used in solving the coupled differential equations [17], [20]. Next, substitutions are made based on the following parameter definitions given in (84) – (87), yielding the normalized rate equations given in (88) – (90).

$$\Delta N = (N - N_{th}) \longrightarrow d\Delta N = dN \tag{84}$$

$$N_{th} = \frac{J_{th}}{\gamma_s} \tag{85}$$

$$Z = \frac{1}{2}\frac{\Gamma g_n}{\gamma_c}\Delta N \longrightarrow \Delta N = Z\frac{2\gamma_c}{\Gamma g_n} \longrightarrow d\Delta N = dZ\frac{2\gamma_c}{\Gamma g_n} \tag{86}$$

$$Y^2 = \frac{g_n}{2\gamma_s}A^2 \longrightarrow Y = \sqrt{\frac{g_n}{2\gamma_s}}A \longrightarrow dY = \sqrt{\frac{g_n}{2\gamma_s}}dA \tag{87}$$

$$\frac{dY}{d\tau} = ZY - \varepsilon Y(Y^2 - P) + \eta_N\cos(\theta) \tag{88}$$

$$\frac{d\theta}{d\tau} = \alpha Z - \alpha\varepsilon(Y^2 - P) - \frac{\eta_N}{Y}\sin(\theta) - \Delta\Omega \tag{89}$$

$$T\frac{dZ}{d\tau} = P - Z - Y^2(1 + 2Z - 2\varepsilon Y^2 + 2\varepsilon P) \tag{90}$$

In the normalized model given in (88) – (90), Y is described as the dimensionless/normalized field magnitude, and Z is the normalized carrier density. The normalized model is dependent on four parameters derived from the free-running slave laser: P, T, ε, and α. The T-parameter is the ratio of the cavity decay rate, γ_c, to the spontaneous carrier relaxation rate, γ_s, such that $T = (\gamma_c / \gamma_s)$. Both γ_s and γ_c are independent of slave laser output power, making T constant for a slave laser regardless of the bias current. P is proportional to the pumping current above threshold, and is calculated using $P = (1/2)(\gamma_n/\gamma_s) \propto (J - J_{th})/J_{th}$, where J is the injected current density and J_{th} is the threshold current density. The free-running relaxation rate, normalized to the cavity decay rate is given by $\Omega_{fr}^2 = [2P(1+\varepsilon)]/T = \gamma_n\gamma_c + \gamma_p\gamma_s$, and the normalized free-running damping rate is given by $\gamma_{fr} = [(1+2P)/T + 2P\varepsilon] = \gamma_s + \gamma_n + \gamma_p$. ε accounts for the nonlinear carrier relaxation rate and is defined as: $\varepsilon = \gamma_p\gamma_s/(\gamma_c\gamma_n)$. Thus, the P-, T-, and ε parameters are calculated for a given slave laser bias current knowing the free-running damping rate, and relaxation oscillation frequency, along with the constant photon lifetime and spontaneous carrier lifetime values. In solving the coupled, normalized differential equations, the normalized field magnitude Y is not at steady-state, and is thus represented as a dependant term in the normalized field magnitude and phase rate equations. The detuning parameter, $\Delta\Omega$, is normalized to the cavity decay rate such that $\Delta\Omega = \Delta\omega/\gamma_c$.

Contrary to the definition for the injection strength, η, defined in Chapter 2, the normalized injection strength in (88) and (89) is purely derived from the injected power

and is defined as: $\eta_N = (k_c / \gamma_c) Y_{inj} = \sqrt{\frac{g_n}{2\gamma_s}} \frac{k_c A_{inj}}{\gamma_c}$. Recall that η was defined as $\eta = k_c(A_{inj}/A_o)$ in Chapter 2, where A_o is the steady-state photon density under optical-injection. Multiplying the numerator and denominator by A_{fr}, $\eta_N = \sqrt{\frac{g_n}{2\gamma_s}} \frac{k_c A_{inj}}{\gamma_c}$ becomes $\eta_N = \sqrt{P} \frac{k_c A_{inj}}{\gamma_c A_{fr}}$, which is rearranged to yield the previously defined expression for the maximum injection strength based on η_N: $\eta_o = \frac{\eta_N}{\sqrt{P}} \gamma_c = \frac{k_c A_{inj}}{A_{fr}}$.

3.2. Simulating the Nanostructure Laser

To simulate the nanostructure laser's behavior under optical-injection, the coupled normalized differential equations in (88) - (90) are solved in the time domain, and qualitative changes can be observed in the normalized field magnitude solution. The stability of this solution is examined by introducing a small perturbation to the field amplitude. Using this new field amplitude as an initial condition (along with the unperturbed phase and normalized carrier density), the rate equations are solved and allowed to come to a new equilibrium-state. The stability of the system is characterized by the number of extrema in the new equilibrium-state. A single extrema observed is indicative of a stable-locking state; a large number of extrema in the equilibrium-state solution is indicative of an unsettled, chaotic response. For this work, the electric field solution is analyzed as the injection strength, η_N, is varied for a constant detuning frequency, as well as for a fixed injection strength as the detuning frequency is varied. Together, the two means of analysis: fixed injection strength/varied detuning and vice

versa are able to generate two dimensional stability maps as given in Simpson et al., Hwang et al., Wieczorek et al., and most recently Bonatto et al. [19], [21], [54], [55]. The extrema to the normalized photon density solution's time response is plotted as a function of the maximum injection strength, η_o, or detuning frequency and are referred to as bifurcation diagrams as they indicate the transition between operational states as the maximum injection strength is varied [53].

Bifurcation diagrams for representative quantum-dash slave laser bias conditions are given in Figure 28, where the y-axis is normalized to the free-running steady-state field magnitude (equivalent to R_{FE} in the stable-locking regime). The x-axis in Figure 28 is translated from the injection-strength, η_N, to an injection strength ratio, η_o, given the relationship: $\eta = \eta_N \gamma_c Y_{fr}^{-1} = \eta_N \gamma_c P^{-1/2}$. The free-running normalized field magnitude, Y_{fr}, is equal to the square root of the pumping term, $P^{1/2}$, based on the free-running steady-state solution of (88).

The *P*- and *T*-terms and linewidth enhancement parameter, α, values in Figure 28 are representative of varied slave laser bias conditions for the quantum-dash Fabry-Perot slave laser. The quantum-dash devices investigated in the course of this work have been found to possess a linewidth enhancement parameter,α, that increases with increased bias currents [56]. Specifically, the quantum-dash devices have demonstrated an α-factor that increases from ~1 to ~14 as the bias current is increased from threshold to approximately twice the threshold value [56].

The bifurcation diagrams in Figure 28 show that as the linewidth enhancement parameter and *P*-term increase with bias current, larger injection strengths are necessary to achieve stable-locking; stable locking is characterized in the diagrams by a single

extrema value observed in the electric field solution. Additionally, the numerical simulations in Figure 28 show that as the linewidth enhancement parameter is increased from 2.2 to 6.0, more chaotic states are observed in the solution at lower injection strengths. Figure 28 also shows that the 'bubble' indicating operational states other than stable locking increases in size as the linewidth enhancement parameter and *P*-term increase with bias current. The quantum-dash laser is unique in allowing examination of dynamics over a large range of linewidth enhancement parameter values within a single device. In Figure 28, the maximum injection strength, η_o, associated with the stable-locking (single-extrema) to period-one or period-doubling (multiple extreme) transition is referred to as the Hopf-bifurcation point. Likewise, the injection strength associated with the period-one (two-extreme) to stable-locking (single extrema) transition is referred to as the reverse-Hopf-bifurcation point. The theoretical bifurcation diagrams in Figure 28 will be compared with experimentally collected data in Chapter 5. The Matlab code used to generate the diagrams is included in Appendix AA.

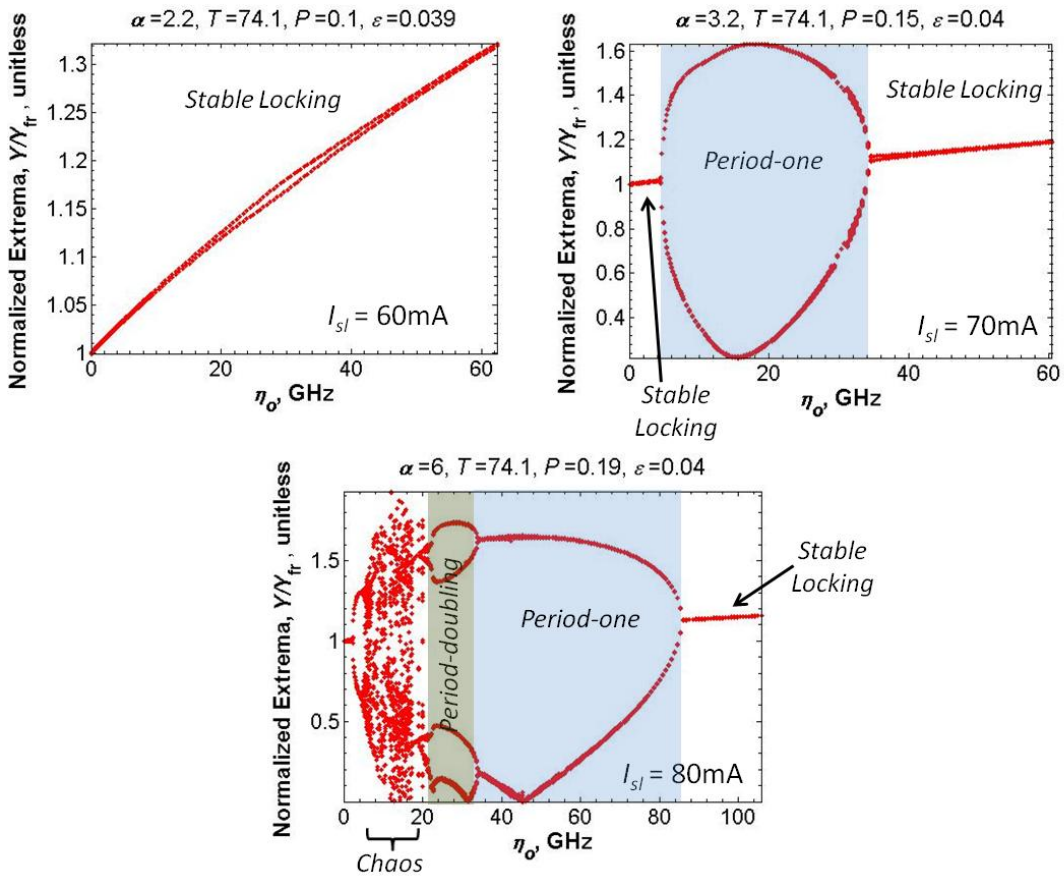

Figure 28. Bifurcation diagrams showing theoretical solutions to the normalized rate equations in (88) - (90) for zero-detuning conditions. The four cases correspond to respective P, T, and α-factor values for 60, 70, and 80 mA slave bias conditions of the quantum-dash slave laser.

Next, the impact of the nonlinear carrier relaxation rate, γ_p, on the stability of the coupled system in analyzed where the free-running parameters of the quantum-dash laser biased at 70 mA are used as baseline values. Recall from Figure 14 in section 2.8 that the nonlinear carrier relaxation rate was shown to suppress the emergence of unstable operation based on the real part of the complex pole of the small-signal modulation response. In Figure 29, the impact on the size of the unstable regions at zero-detuning is illustrated by plotting the extrema of the normalized electric field solution as a function

of maximum injection strength for cases where γ_p is and is not included. The single extreme is a sign of stable optical-injection, whereas the two extrema solutions illustrated by the 'bubble' in Figure 29(right) is a sign of undamped relaxation oscillations over that range of maximum injection strengths, η_o. The theoretical values, and specifically the linewidth enhancement parameter, were chosen to coincide with the values analyzed in Figure 14, where the simulation results are in good agreement with one another. The results of each model where the nonlinear carrier relaxation rate is not included shows that a small window of unstable operation for maximum injection strengths from 5 GHz to 25 GHz will occur.

Although Figure 14 and Figure 29 are in strong agreement in predicting if the coupled system operates in a stable or unstable manner, the more basic approach used in Figure 14 is limited in its application. The approach used in Figure 14 to examine the stability of the semiconductor laser's operation under optical-injection only confirms stable or unstable operation; solving the dimensionless, normalized rate equations given in (88) – (90), however, gives an indication regarding the nature of the unstable operation based on the **number of extrema** observed in the electric field solution of the coupled rate equation.

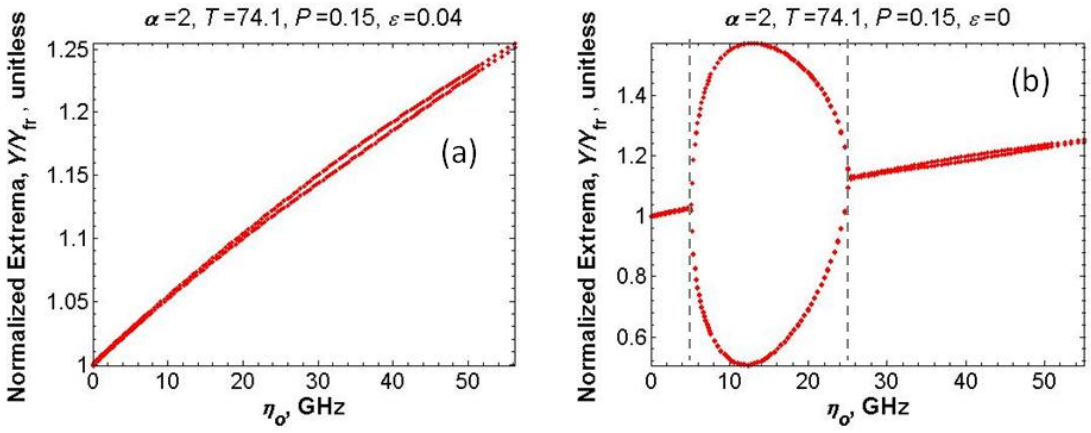

Figure 29. Bifurcation diagrams predicting the stability at zero-detuning where the nonlinear carrier relaxation rate parameter is (a) and is not considered (b) in the numerical simulation.

The impact of the nonlinear carrier relaxation rate in suppressing the multi-extrema indicative of chaotic operation is illustrated also in Figure 30. In Figure 30(a), the coupled system is predicted to exhibit only stable and period-one operation. In Figure 30(b), however, a small region of chaotic operation is expected at maximum injection strengths of approximately 10 GHz. With all parameters held constant minus the nonlinear carrier relaxation rate, its impact is highlighted here to have a strong influence on the dynamical characteristics of the coupled optically-injected system.

Next, Figure 31 illustrates the impact of the linewidth enhancement parameter on the stability of the optically-injected system. With all other parameters held constant, the increased linewidth enhancement parameter is shown to move the system from completely stable (Figure 29(a)) to one a case where undamped period-one (Figure 31(a)) and period-doubling (Figure 31(b)) oscillations will be generated.

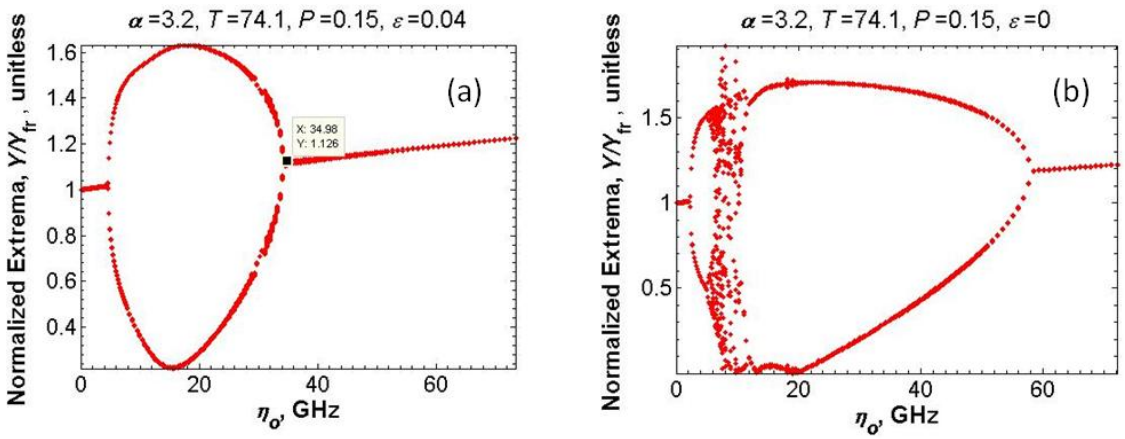

Figure 30. Bifurcation diagrams predicting the stability at zero-detuning where the nonlinear carrier relaxation rate parameter is (a) and is not considered (b) in the normalized rate equations.

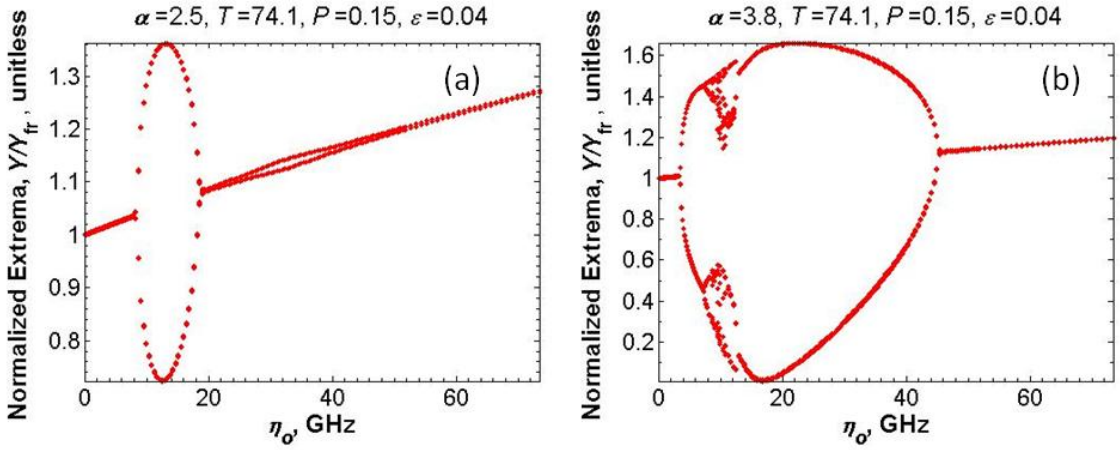

Figure 31. Bifurcation diagrams predicting the stability at zero-detuning for different values of the linewidth enhancement parameter: (a) 2.5 (b) 3.8.

Chapter 4. Free-Running Nanostructure Characterization

In this chapter, the free-running operation of the quantum-dot and quantum-dash nanostructure lasers is studied. The free-running operational parameters are critical in validating the theoretical models derived in Chapter 2 and Chapter 3 with the experimental data presented in Chapter 5 and Chapter 6.

For testing, each nanostructure laser device is mounted on a gold-coated copper heat sink using indium solder. Because the bottom side of the laser device serves as the ground plane, a ground pad with the same thickness as the laser device is mounted adjacent to the laser to bring it up to the same height as the top/signal contact pad. A two-finger RF signal/ground probe was used to contact the signal and ground pads of the device in order to minimize high frequency parasitics. The laser output was coupled to a lensed fiber mounted on a piezoelectric-controlled stage, and coupling efficiencies of approximately 50% were reached. Once coupled to the lensed fiber, the laser output was either converted to an electrical signal using a 40 GHz photodiode to measure the modulation response or directly to an optical spectral analyzer to observe the optical response. The experimental study of the free-running microwave modulation response (S_{21}) of both nanostructure lasers was accomplished using an HP8722D network analyzer, and the response data was then used to extract the relaxation oscillation frequency and damping rate as a function of laser bias current. A high-resolution (10 pm / 1.75 GHz @ 1310-nm and 1.25 GHz at 1550-nm) optical spectrum analyzer (OSA) (Yokogawa AQ6319) was also used to monitor the optical response of the laser devices. For a portion of the characterization of the quantum-dash laser, an Agilent high resolution spectrometer (Agilent 83453B) with a maximum resolution of 1 MHz was used in place

of the OSA; its operating wavelength span, however, did not cover the 1310-nm output wavelength of the quantum-dot Fabry-Perot device investigated in this work. An illustration of the experimental setup used to characterize the free-running laser parameters is given in Figure 32. The temperature of the copper heat sink was maintained using a thermo-electric cooler. In order to measure the light-current characteristics of the laser devices, an integrating sphere replaces the lensed fiber in Figure 32.

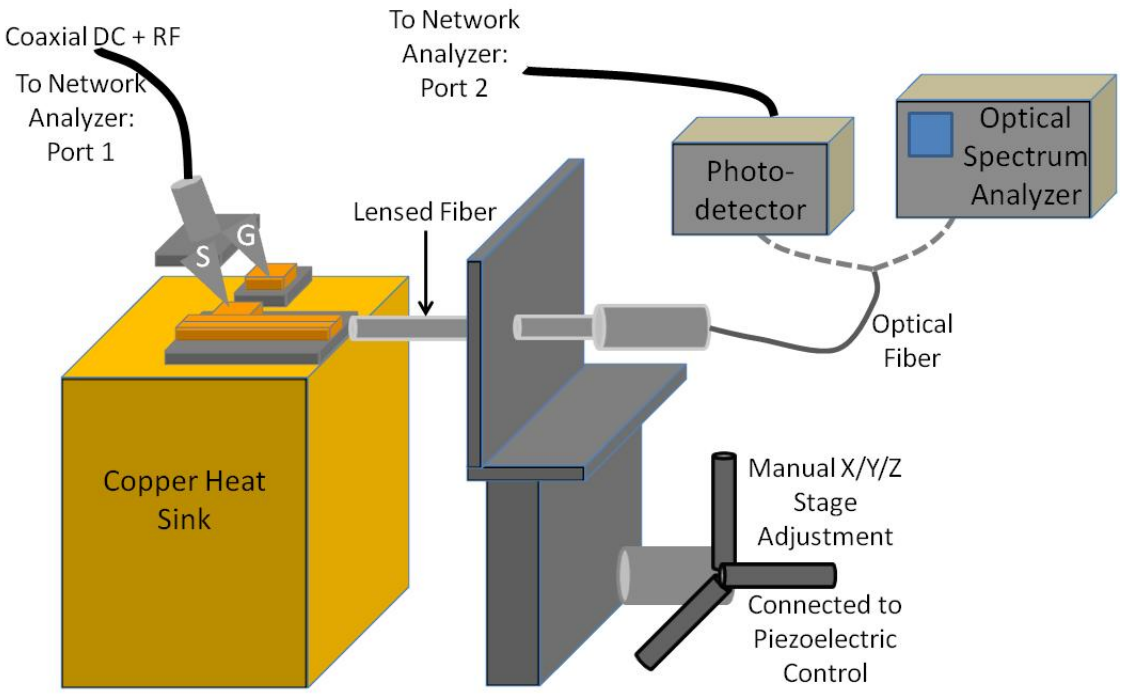

Figure 32. Illustration of the experimental setup used to characterize the free-running laser parameters. The optical fiber feeding from the lensed fiber can be connected to either the optical spectrum analyzer or the photodetector; a 50/50 coupler is not used. Note: not to scale.

The above threshold linewidth enhancement parameter was measured for each device using the injection-locking approach, which is based on the asymmetry of the

stable-locking region as the master laser is detuned from the slave laser [44]. The relationship of the linewidth enhancement parameter to the positive and negative frequency detuning boundaries of stable locking is given by (91):

$$\alpha = \sqrt{\left(\frac{\Delta f_{neg}}{\Delta f_{pos}}\right)^2 - 1} = \sqrt{\left(\frac{\Delta \lambda_{pos}}{\Delta \lambda_{neg}}\right)^2 - 1} \tag{91}$$

where Δf_{pos} and Δf_{neg} are the positive and negative frequency detuning boundaries of stable locking, respectively [Liu01]. The detuning convention is described by: $\Delta f = f_{master} - f_{slave}$ ($\Delta\lambda = \lambda_{master} - \lambda_{slave}$).

4.1. Description of the Quantum-dot Fabry-Perot slave laser

The quantum-dot slave laser was grown using solid source molecular beam epitaxy on an n^+-GaAs substrate. The dots-in-a-well active region consists of 6 layers of InAs quantum-dots embedded in compressively-strained $In_{0.15}Ga_{0.85}As$ quantum-wells separated by 30-nm undoped GaAs spacers. A 45-nm layer of undoped GaAs was added on each side of the active region. The epitaxial structure is shown in Figure 33. The lasers have 3-μm wide ridge waveguides and 300 μm cavity lengths. The front and back cleaved facets were HR coated to have a reflectivity of 80% and 95%, respectively, to enable the device to lase at the ground state. The light-current characteristic is shown in Figure 34, from which a threshold current of 1.9 mA (J_{th} = 211.1 A/cm^2) was found.

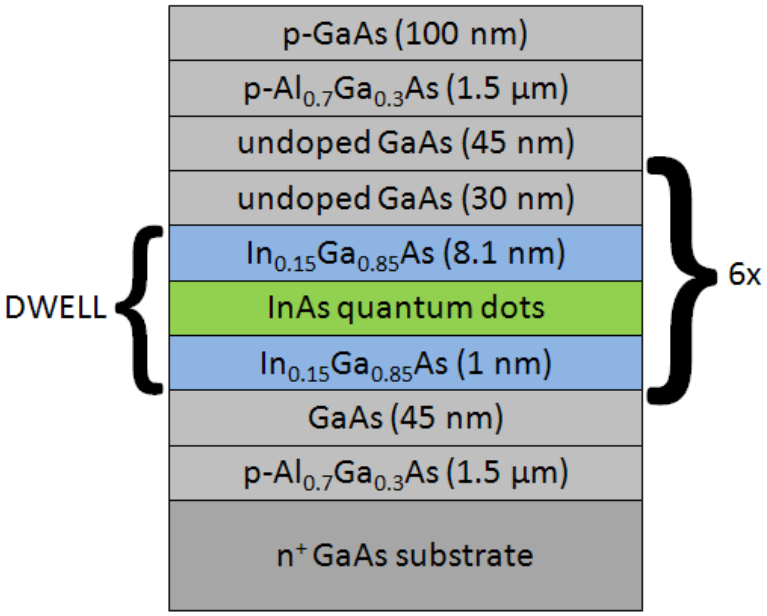

Figure 33. Epitaxial layer composition of the quantum-dots-in-a-well laser structure.

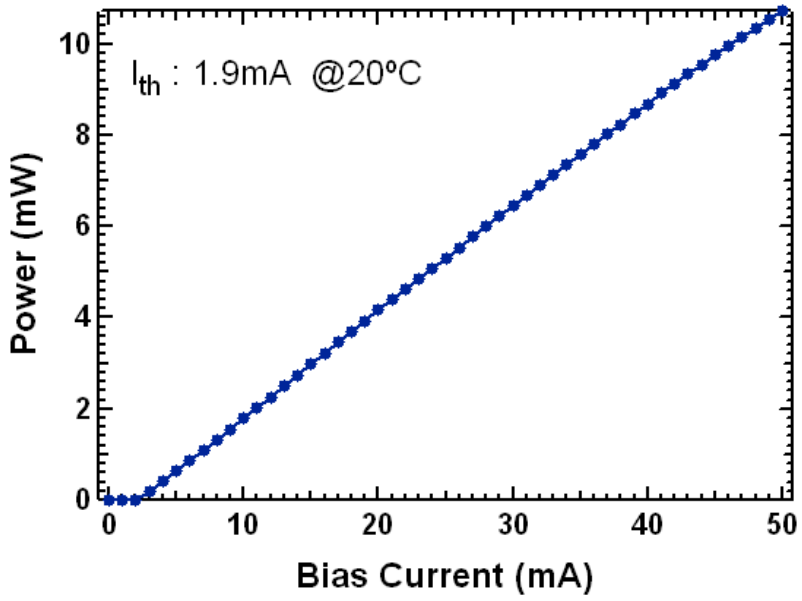

Figure 34. Light-current characteristics of the quantum-dot Fabry-Perot laser showing a measured threshold current of 1.9 mA at 20°C.

The optical response at a bias current of 5 mA is shown in Figure 35. The average group index of the gain region was calculated to be 3.706 based on an average Fabry-Perot free-spectral-range (FSR) of 134.68 GHz (~770pm) across the 30-nm span shown ($n_{g,avg} = c/(2\Delta\nu_{avg} L)$) in Figure 35. The 30-nm span illustrated in Figure 35 was also used to calculate the group index of the gain region as a function of Fabry-Perot mode and is plotted in Figure 36. The group index of the active region, as a function of Fabry-Perot mode was calculated using: $n_g = \lambda^2/(2L\Delta\lambda)$, where λ is the mode wavelength and $\Delta\lambda$ is the FSR. The FSR was taken as the average FSR measured between the two adjacent modes. The jaggedness illustrated in Figure 36 is likely due to a non-uniform variation of the measured FSR. The facet reflectivity values, group index and internal loss (4-cm^{-1}) of the device, yield a photon lifetime of 14.4 ps.

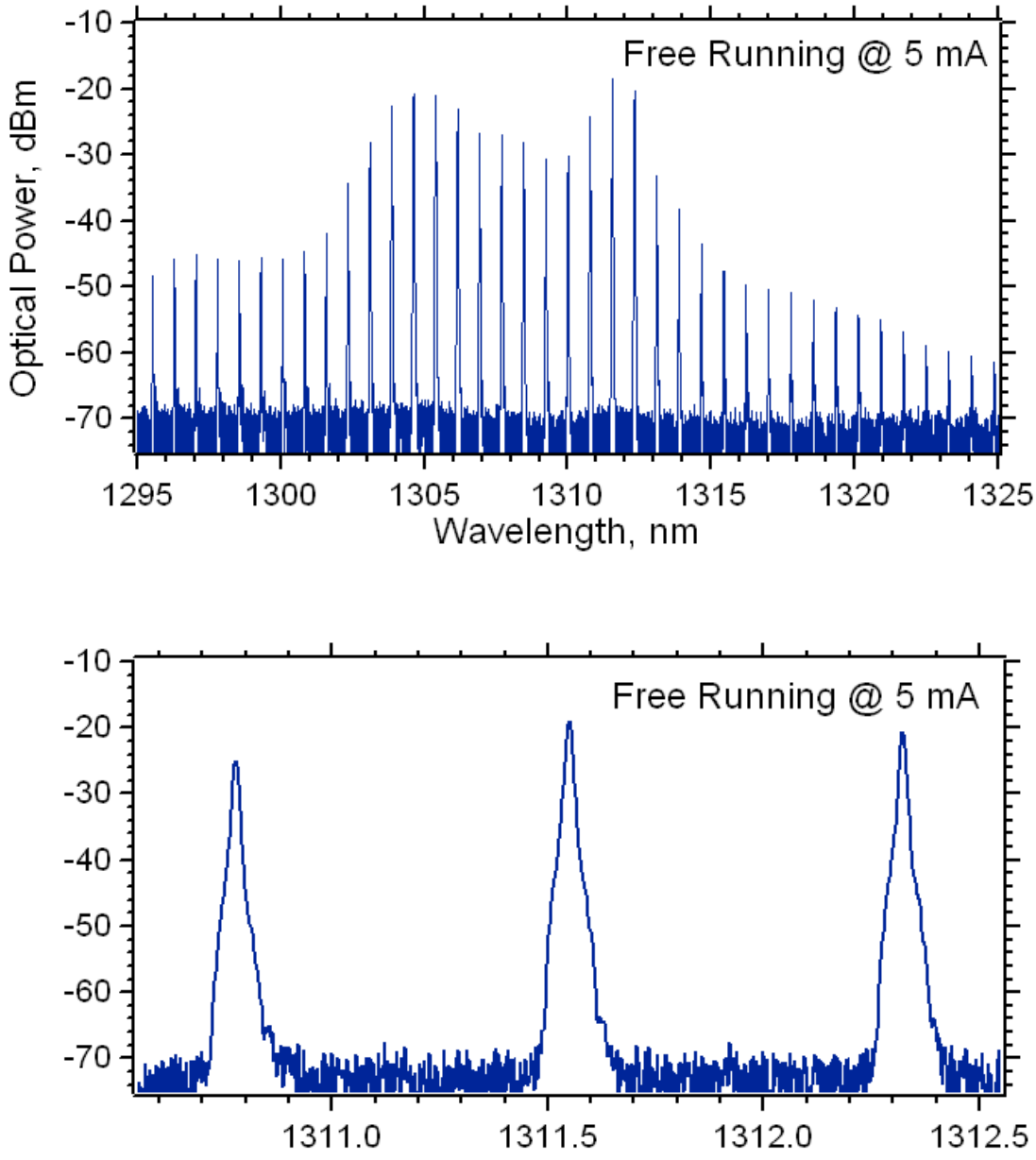

Figure 35. Optical spectra of the free-running quantum-dot laser observed under a bias current of 5mA. Top: 30-nm span. Bottom: 2-nm span.

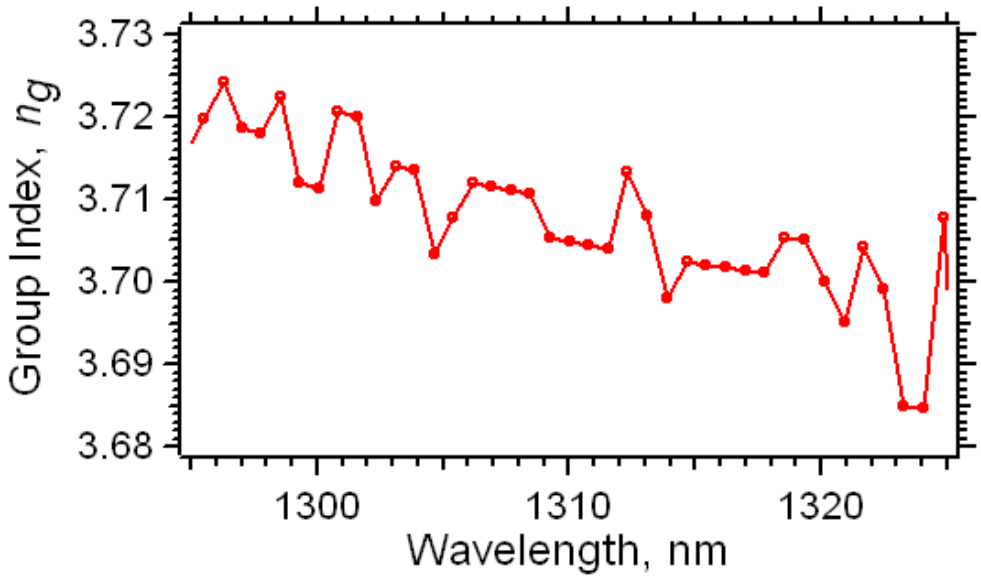

Figure 36. Group index of the active region as a function of Fabry-Perot mode at a bias current of 5 mA. The free-spectral range ($\Delta\lambda$) was averaged between each two adjacent modes, and calculated using $n_g = \lambda^2/(2L\Delta\lambda)$.

The relaxation oscillation frequency, Ω_{fr}, overall damping rate, γ_{fr}, and parasitic carrier transport time, τ_t, ($\tau_t = 1/\gamma_t$) are determined by least-squares fitting of the free-running modulation response for different bias currents as shown in Figure 37 using the standard model in (92) [31]. Figure 37 shows typical free-running modulation response of the quantum-dot laser under test. The highly damped nature of the device tested here is similar to other nanostructure lasers characterized in the literature [42], [43].

$$\left|H_R(\omega)\right|^2 = \frac{\Omega_{fr}^4}{\left((\Omega_{fr}^2 - \omega^2)^2 + \gamma_{fr}^2\omega^2\right)\left(1 + (\omega/\gamma_t)^2\right)} \tag{92}$$

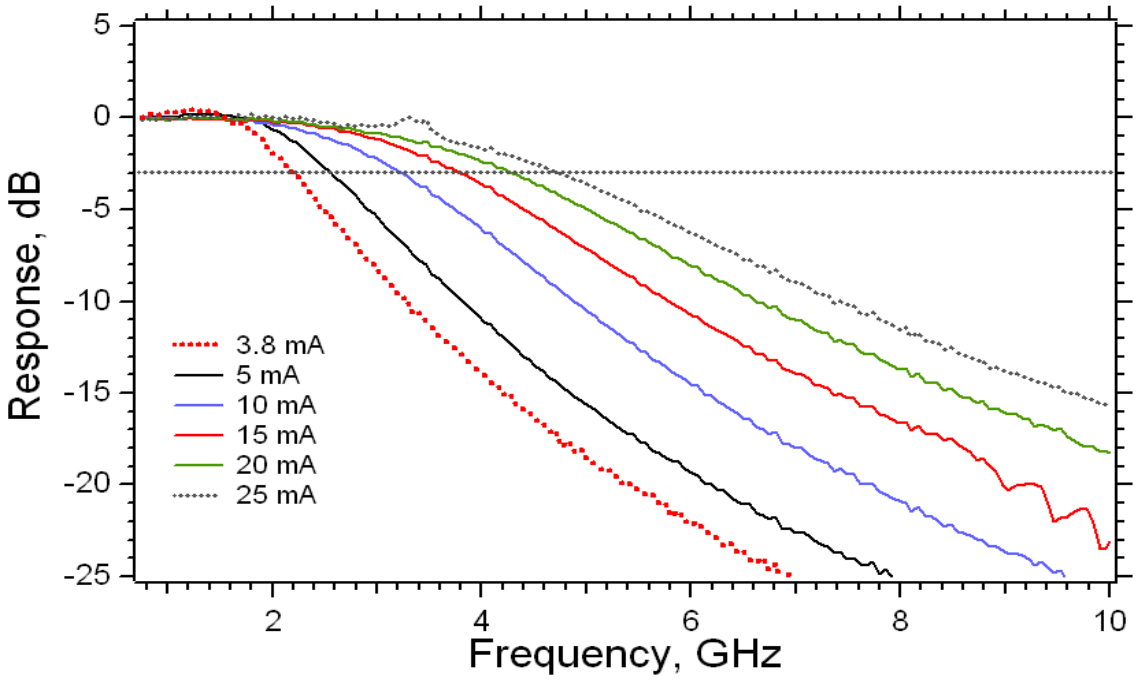

Figure 37. Free-running modulation responses of the quantum-dot laser. The current indicated in the legend is the applied DC bias current.

The slave laser damping rate plotted as a function of f_{fr}^2 ($\Omega_{fr} = 2\pi f_{fr}$) is used to extrapolate the value of the spontaneous carrier relaxation rate, γ_s, given: $\gamma_{fr} = Kf_{fr}^2 + \gamma_s$. γ_{fr} plotted as a function of f_{fr}^2 is shown in Figure 38, where γ_s is 7.5 GHz. The γ_s value is significantly larger compared to quantum-well lasers, where the typical value reported for quantum-well devices is 1-2 GHz [37].

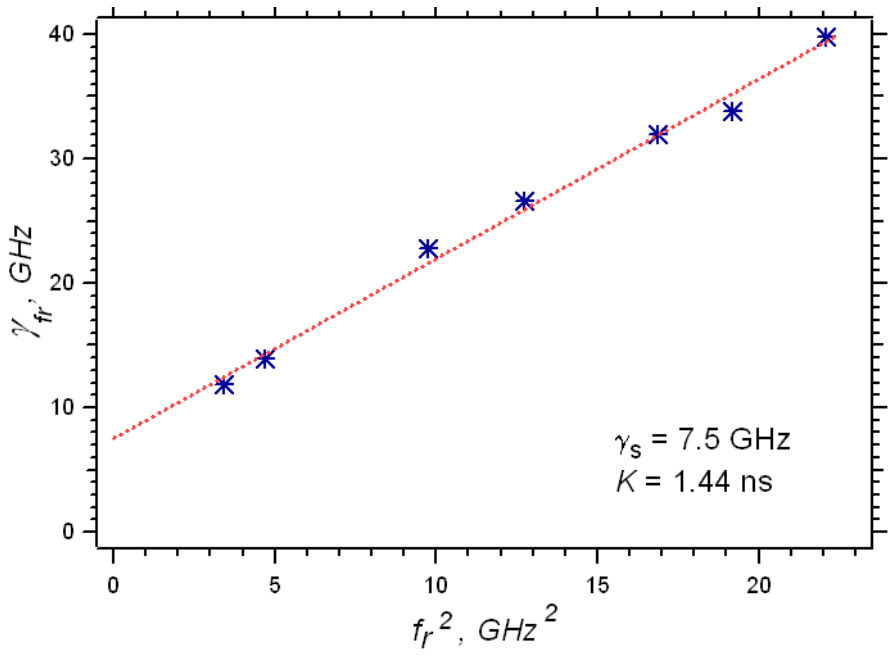

Figure 38. Free-running damping rate (γ_{fr}) as a function of the relaxation oscillation frequency squared (f_{fr}^2). The dotted red line is a least-squares linear fit to the data points, which is extrapolated to determine the spontaneous carrier relaxation rate, γ_s.

The impact of the non-linear gain compression coefficient on the free-running relaxation oscillation frequency was evaluated using the following relation:

$$f_{fr}^{\ 2} = \frac{AP_{out}}{\left(1+\varepsilon_p P_{out}\right)} = \frac{AP_{out}}{\left(1+P_{out}/P_{sat}\right)} \tag{93}$$

where ε_p is the gain compression coefficient related to the total output power P_{out} and A is a fitting constant [Wong, Takahashi, Su]. A plot of the square of the measured relaxation oscillation frequency as a function of power is given in Figure 39, where the gain compression coefficient is extracted to be 0.155 mW^{-1}. This value is more than 2X the value measured for a quantum-dash Fabry-Perot laser with cleaved facets (see next

section), where ε_p was measured to be 0.06 mW^{-1}, and is approximately 10X the value reported for quantum-well lasers [8].

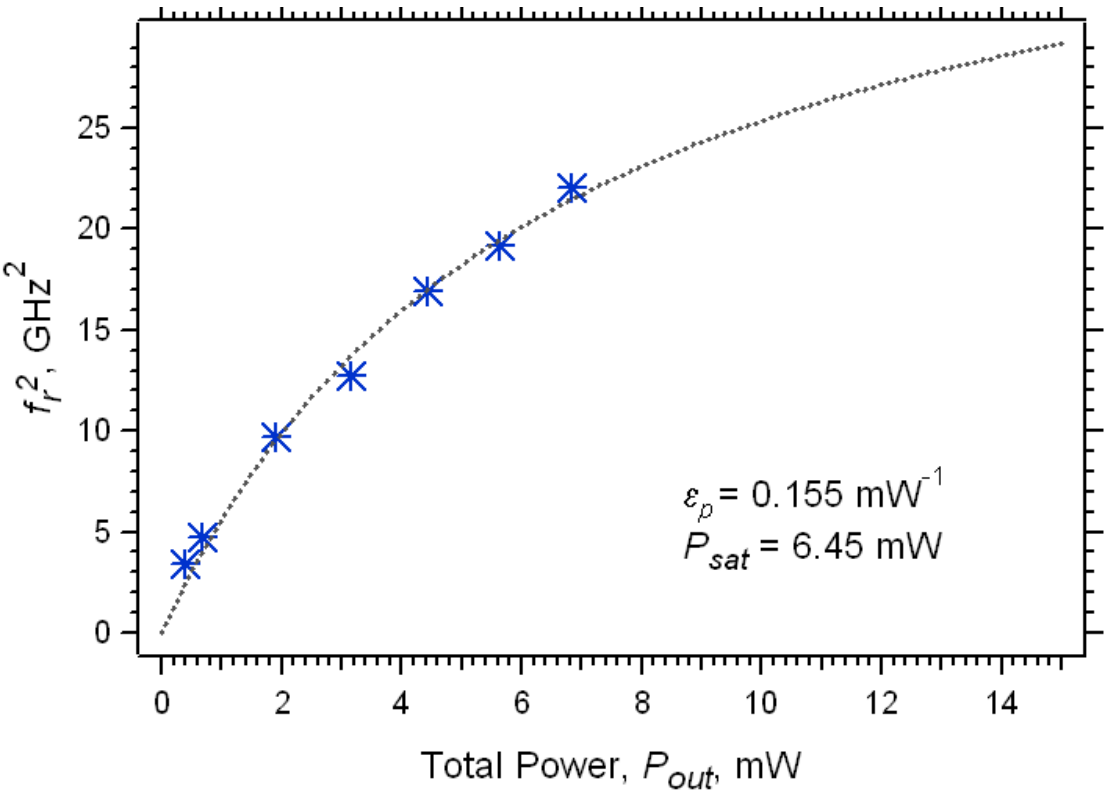

Figure 39. Quantum-dot laser free-running relaxation oscillation (f_{fr}^2) as a function of the total output power (P_{out}). The dotted line is a least squares linear fit using expression (93), where the gain compression coefficient is found to be 0.155 mW^{-1}. In each plot, the experimental values (blue asterisks) correspond to laser bias currents of 3.8, 5, 10, 15, 20, 25, and 30 mA.

The linewidth enhancement parameter measured using the injection-locking technique for various slave laser bias currents is shown in Table 1, where the linewidth enhancement parameter for each bias current is averaged over several injected master strengths (minimum of 3 injection strength levels). The measured linewidth enhancement parameter was fairly consistent as the injection ratio was increased, as indicated in Table

1. It has been suggested that the linewidth enhancement parameter can be manipulated to higher values at large injected power levels due to the semiconductor lasers' nonlinear gain [59]; the measured results showed no trend with increasing injected power levels, suggesting that the master powers used were not high enough to induce either gain compression effects or to shift the threshold carrier density significantly [59]. The linewidth enhancement parameter was not measured at bias currents above 8 mA, as the available master laser power was limited to 30 mW. For bias currents above 8 mA, the stable-locking detuning ranges were too small to yield reliable measurements due to the resolution of the OSA.

Table 1. Quantum-dot laser linewidth enhancement parameter measured using the injection-locking technique for varied slave laser bias currents. The linewidth enhancement parameter is averaged over several injection strengths.

Slave Laser Bias Current (mA)	α	Standard Deviation
2	0.9	0.2
2.5	0.6	0.1
3	1.2	0.4
4	1.6	0.2
5	2.0	0.2
6	2.7	0.4
7	4.6	0.5

Below-threshold amplified spontaneous emission (ASE) measurements were performed to measure the material linewidth enhancement parameter, also referred to as the Hakki-Paoli technique [33]. The net modal gain, *g*, was extracted from the peak-to-valley ratio of sub-threshold Fabry-Perot oscillations using the relationship in (94):

$$g = \frac{1}{L} Ln\left(\frac{1}{r} \frac{\left(x^{1/2} - 1\right)}{\left(x^{1/2} + 1\right)} \right) \tag{94}$$

where L is the laser cavity length, x is the ratio of the peak-to-valley power levels, and r is the facet reflectivity given by $(R_{front} \cdot R_{back})^{1/2}$, and R_{front} and R_{back} are the front and back facet reflectivity, respectively. The differential gain was calculated using the relationship $\Delta g/\Delta I$, where ΔI is the current increment. The differential index was calculated using [33]: $\Delta n/\Delta I = -(n/\lambda)\Delta\lambda/\Delta g$. The linewidth enhancement parameter is calculated using the differential gain and differential index results [33]:

$$\alpha = -\left(\frac{4\pi n}{\lambda}\right) \frac{dn/dN}{dg/dN} = -\left(\frac{4\pi n}{\lambda^2}\right) \Delta\lambda/\Delta g = -\left(\frac{4\pi n}{\lambda^2}\right) \frac{\Delta\lambda/\Delta I}{\Delta g/\Delta I} \tag{95}$$

Temperature effects were excluded from the $\Delta\lambda/\Delta I$ measurement by operating the current source (ILX LPD-3871) in pulsed mode [60]. Heating effects in the laser cavity resulting from increased bias currents can offset the wavelength decrease resulting from increased bias currents, as shown in Figure 40(b). Specifically, the quantum-dot laser was biased using 20 μs pulse widths while the duty cycle was operated at different levels: 1%, and 10% increments from 10% to 100%. The observed optical mode was then least-squares-fit using a Gaussian function and its wavelength peak recorded for each duty cycle increment. For each sub-threshold bias current, the modal peak wavelength was plotted as a function of duty cycle, as shown in Figure 40(a). This data was then extrapolated to 0% duty cycle and the results for each current step (0.1 mA increments) were used to calculate $\Delta\lambda/\Delta I$. The lower limit of operational pulse widths was constrained by the sensitivity of the optical spectrum analyzer, which was unable to resolve the

optical signal for 1% duty cycles and pulse widths below 20 μs. Figure 41(a) depicts the ASE spectra for a slave laser bias of 1.8 mA (I_{th} measured to be 1.9 mA), where the modal peaks and valleys have been extracted to calculate the net modal gain as a function of wavelength (Figure 41(b)). The ASE spectrum was measured for bias currents ranging from 1.0 mA to 2.0 mA in 0.1 mA increments. From 1311-nm to 1316-nm, the gain was relatively flat for each current increment, as observed in Figure 41(b). At a bias current of 1.9 mA, the peak net modal gain was measured to be 4-cm^{-1}. The linewidth enhancement parameter was calculated using expression (3) and the results are reported in Table 2. The modal gain reported in Table 2 was taken as the average from 1311-nm to 1316-nm. At 1.9 mA, the linewidth enhancement parameter fictitiously drops to 0.5 as the bias current approaches threshold and the differential gain and $\Delta\lambda/\Delta I$ are observed to drastically decrease. The highest bias current that gives a reliable linewidth enhancement parameter using the ASE technique is 1.8 mA. The injection-locking method for determining the linewidth enhancement parameter is in reasonable agreement at bias currents just above threshold with the Hakki-Paoli method, which is a below-threshold measurement.

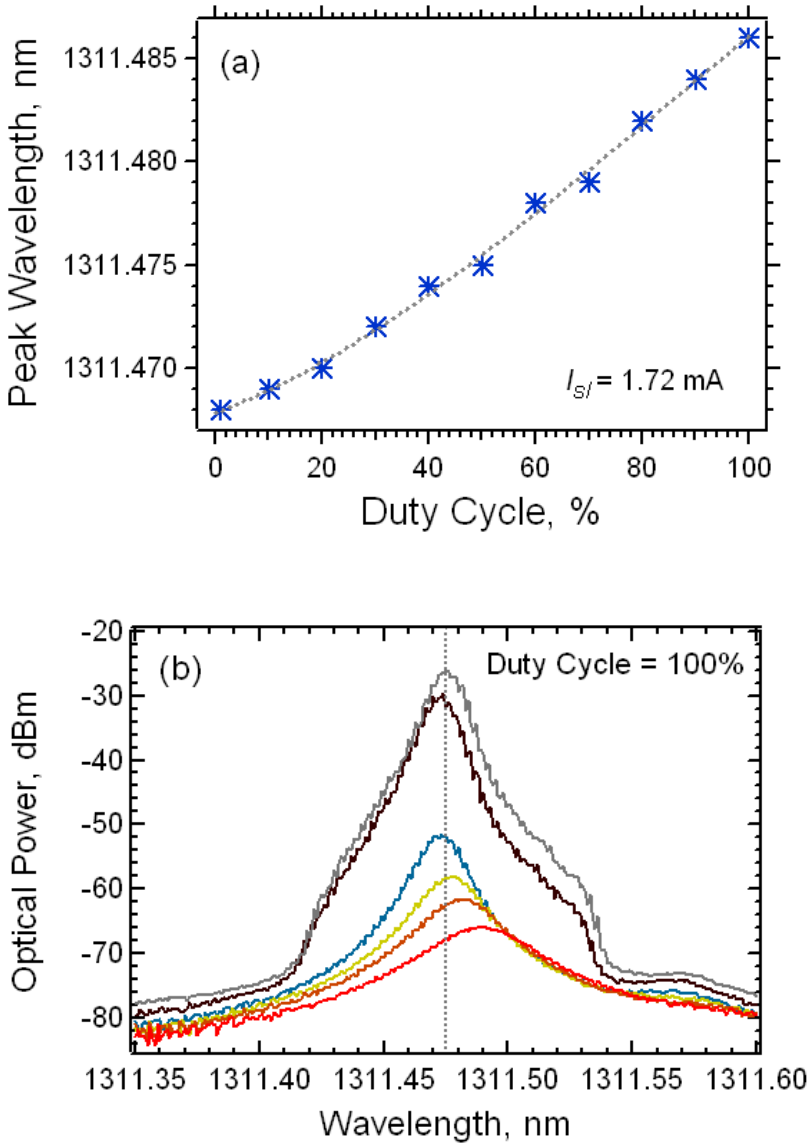

Figure 40. Quantum-dot laser: (a) Peak modal wavelength as a function of duty cycle. The pulse width was 20μs. (b) Optical power response for subthreshold bias currents at 100% duty cycle. The bias currents correspond to 1.1 mA (red), 1.3 mA, 1.5 mA, 1.7 mA, 1.9 mA, and 2.0 mA (gray).

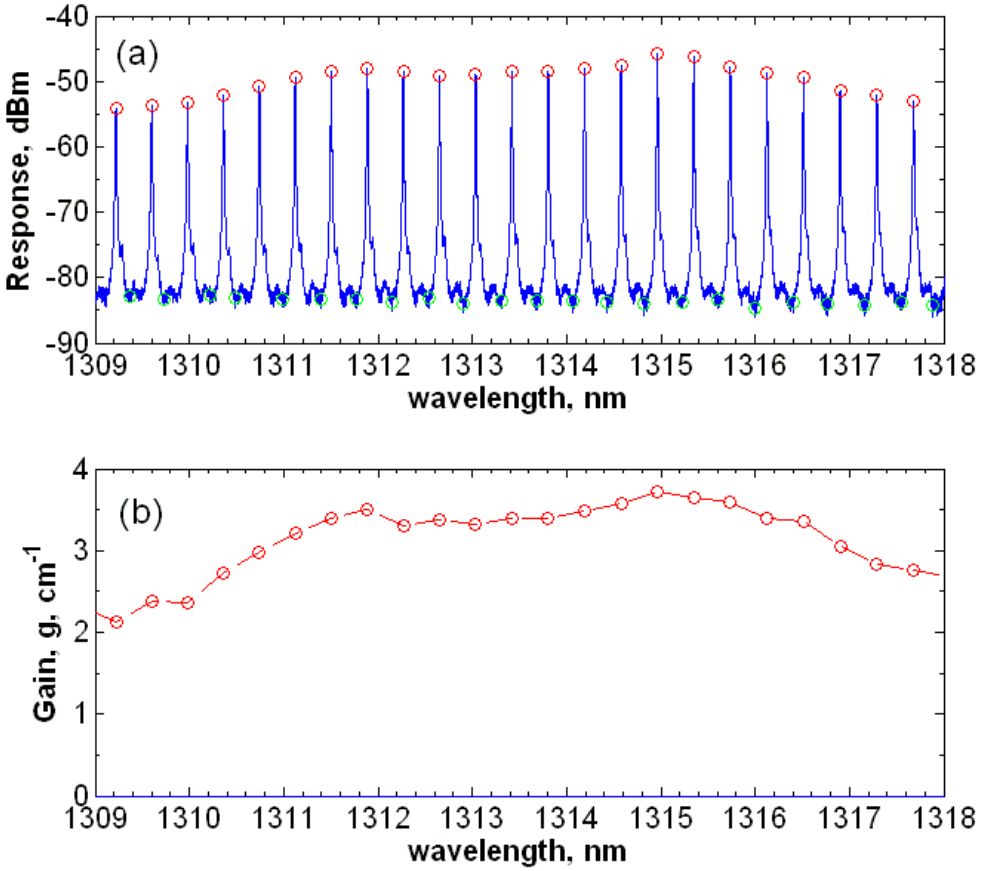

Figure 41. Quantum-dot laser (a) amplified spontaneous emission spectra at 1.8 mA where the modal peaks and valleys have been highlighted; (b) net modal gain calculated using the peak-to-valley ratio measured from the ASE spectra.

Table 2. Calculation of the sub-threshold linewidth enhancement parameter using the ASE approach for the quantum-dot laser.

Bias Current (mA)	$\Delta\lambda/\Delta I$ (pm/mA)	$\Delta g/\Delta I$ (cm^{-1}/mA)	α
2.1	-6.0	0.1	32.5
2.0	-5.1	0.0	42.3
1.9	-7.8	4.6	0.5
1.8	-32.0	6.7	1.3
1.7	-25.0	4.8	1.4
1.6	-38.0	6.6	1.5
1.5	-43.0	8.6	1.4
1.4	-45.9	8.6	1.4

4.2. Description of the Quantum-Dash Fabry-Perot slave laser

The quantum-dash laser was grown on an n^+-InP substrate. The active region consists of 5 layers of InAs quantum-dashes embedded in compressively-strained $Al_{0.20}Ga_{0.16}In_{0.64}As$ quantum-wells separated by 30-nm of undoped tensile-strained $Al_{0.28}Ga_{0.22}In_{0.50}As$ spacers. Lattice-matched $Al_{0.30}Ga_{0.18}In_{0.52}As$ waveguide layers of 105-nm are added on each side of the active region. The p-cladding layer is step-doped AlInAs with a thickness of 1.5-μm to reduce free carrier loss. The n-cladding layer is 500-nm thick AlInAs. The laser structure is capped with a 100-nm InGaAs layer. The epitaxial layer structure is given in Figure 42. The lasers were designed to have 4-μm wide ridge waveguides and 500-μm cleaved cavity lengths. From the light-current characteristic curve in Figure 43, the threshold current was measured to be 47 mA (J_{th} = 2350 A/cm^2), with a slope efficiency of 0.16 W/A (considering both laser facets).

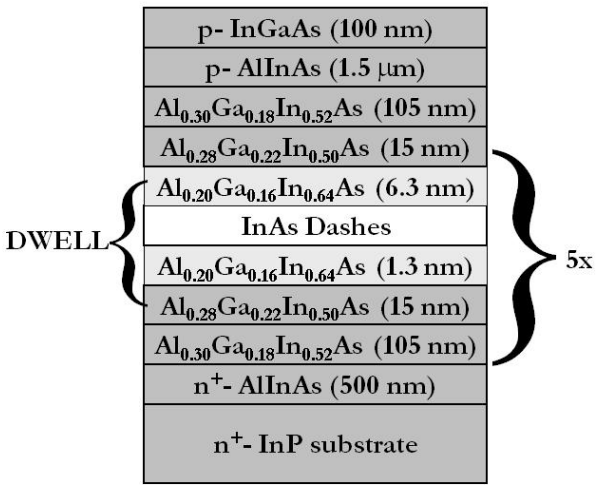

Figure 42. Epitaxial layer composition of the quantum-dashes-in-a-well laser structure.

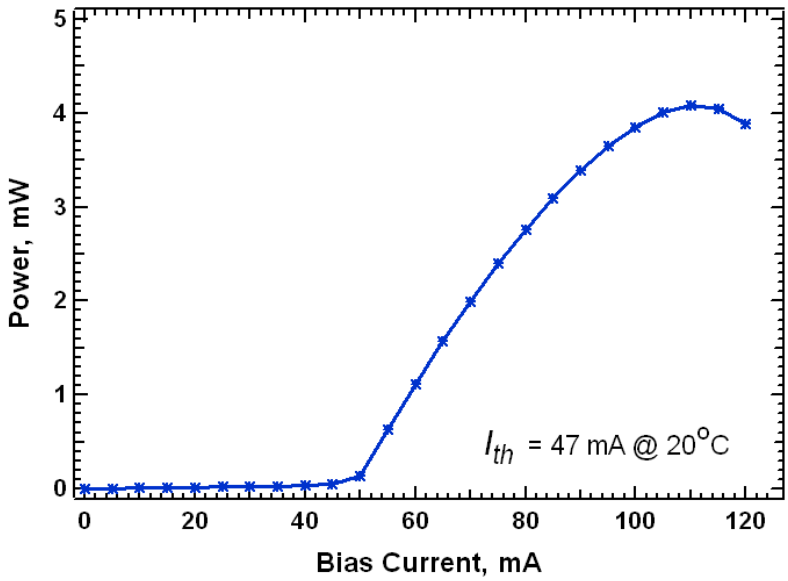

Figure 43. Light-current characteristics of the quantum-dash Fabry-Perot laser showing a measured threshold current of 47 mA at 20°C; power indicated is from a single-facet.

The optical spectral response at a bias current of 65 mA is shown in Figure 44. The average group index of the gain region was calculated to be 3.53 based on a measured average Fabry-Perot free-spectral-range (FSR) of 85.1 GHz (~698pm) across the 30-nm span shown ($n_{g,avg} = c/(2\Delta\nu_{avg} L)$) in Figure 44. The 30-nm span illustrated in Figure 44 was also used to calculate the group index of the gain region as a function of Fabry-Perot mode and is plotted in Figure 45. The group index of the active region, as a function of Fabry-Perot mode was calculated using: $n_g = \lambda^2/(2L\Delta\lambda)$, where λ is the mode wavelength and $\Delta\lambda$ is the FSR. The FSR was taken as the average free-spectral range measured between the two adjacent modes. The jaggedness illustrated in Figure 45 is likely due to a non-uniform variation of the measured FSR. The facet reflectivity values, group index and internal loss (15-cm^{-1}) of the device lead to a calculated photon lifetime of ~3 ps.

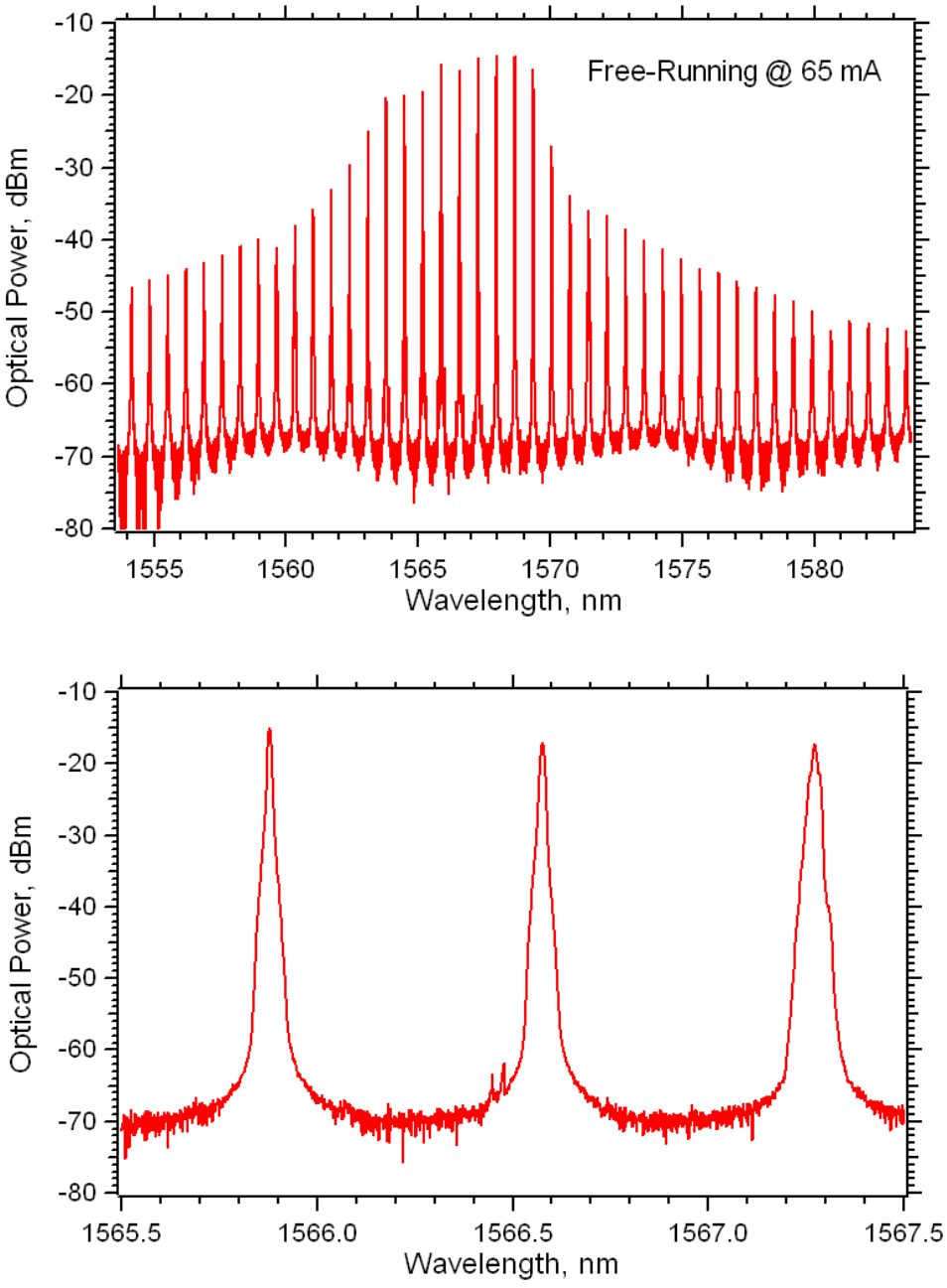

Figure 44. Optical spectra of the free-running quantum-dash laser observed under a bias current of 65 mA; Top: 30-nm span; Bottom: 2-nm Span.

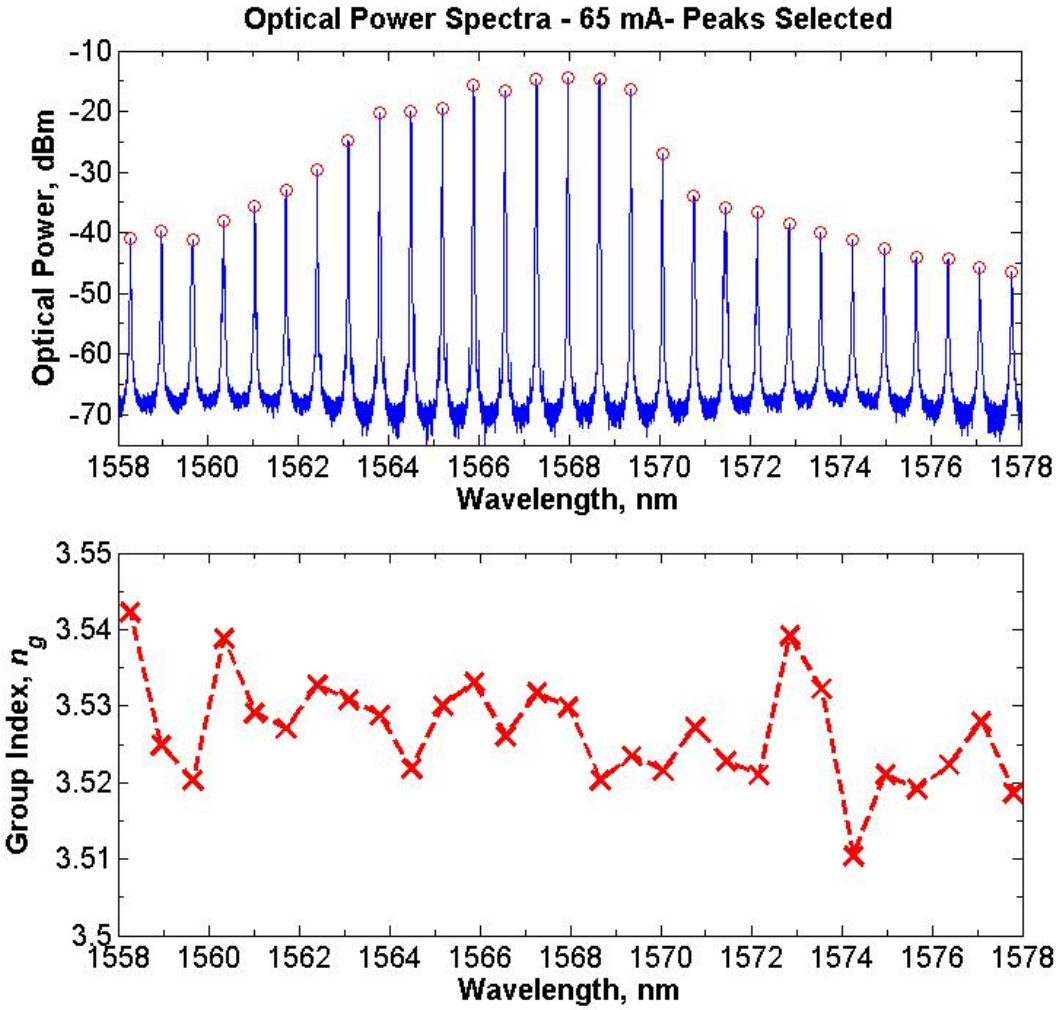

Figure 45. Group index of the active region as a function of Fabry-Perot mode at a bias current of 65 mA. The free-spectral range ($\Delta\lambda$) was averaged between each two adjacent modes, and calculated using $n_g = \lambda^2/(2L\Delta\lambda)$.

The relaxation oscillation frequency, Ω_{fr}, overall damping rate, γ_{fr}, and parasitic carrier transport time, τ_t, ($\tau_t = 1/\gamma_t$) are determined by least-squares fitting the free-running modulation response for varied bias currents as shown in Figure 46 using the standard model in (92) (page 83) [31]. Compared with the highly damped modulation

response of the quantum-dot laser in Figure 37, the quantum-dash modulation response in Figure 46 is not as strongly damped and a resonance peak is clearly identifiable.

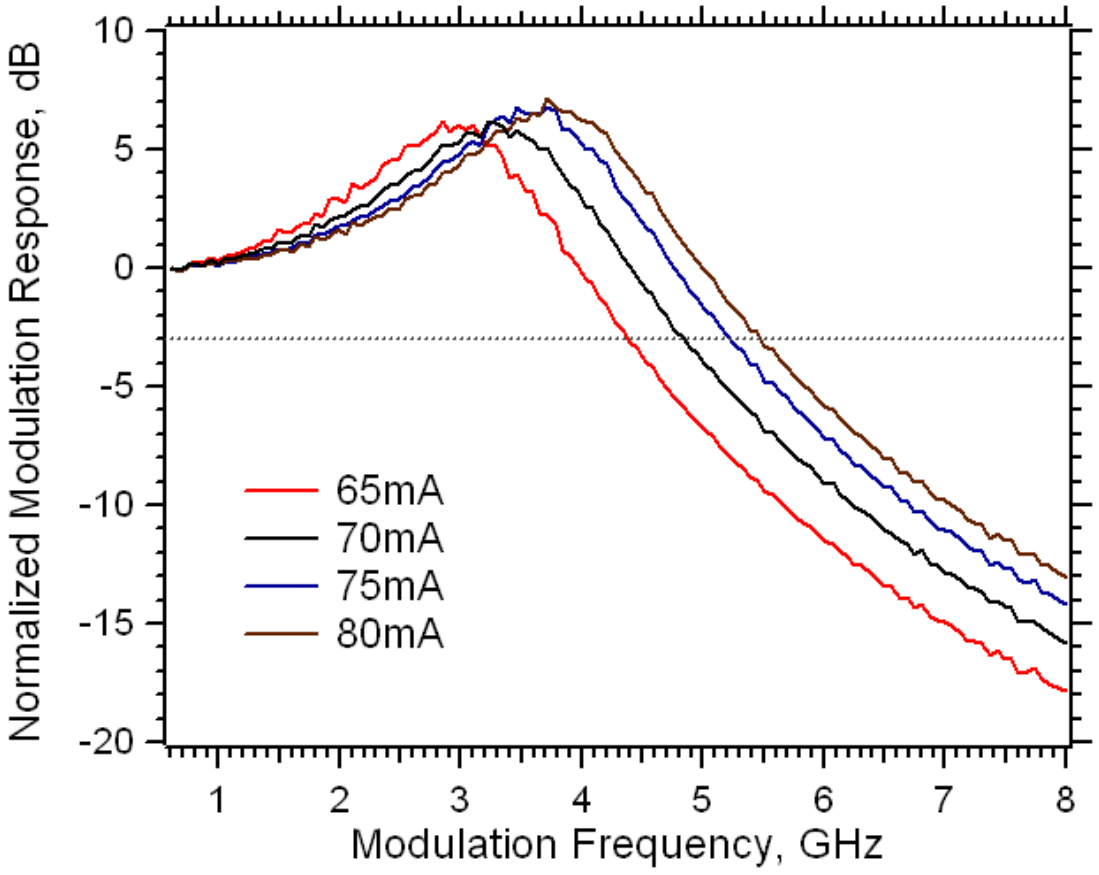

Figure 46. Free-running modulation response of the quantum-dash laser. The current indicated in the legend is the applied DC bias current.

The slave laser damping rate plotted as a function of f_{fr}^2 ($\Omega_{fr} = 2\pi f_{fr}$) is used to extrapolate the value of the spontaneous carrier relaxation rate, γ_s, given: $\gamma_{fr} = K \cdot f_{fr}^2 + \gamma_s$. γ_{fr} plotted as a function of f_{fr}^2 is shown in Figure 47, where γ_s is 4.5 GHz and $K = 0.45$ ns. As in the quantum-dot laser, the γ_s value is generally higher compared to quantum-well lasers, whereby the typical value reported for quantum-well devices is 1-2 GHz [37].

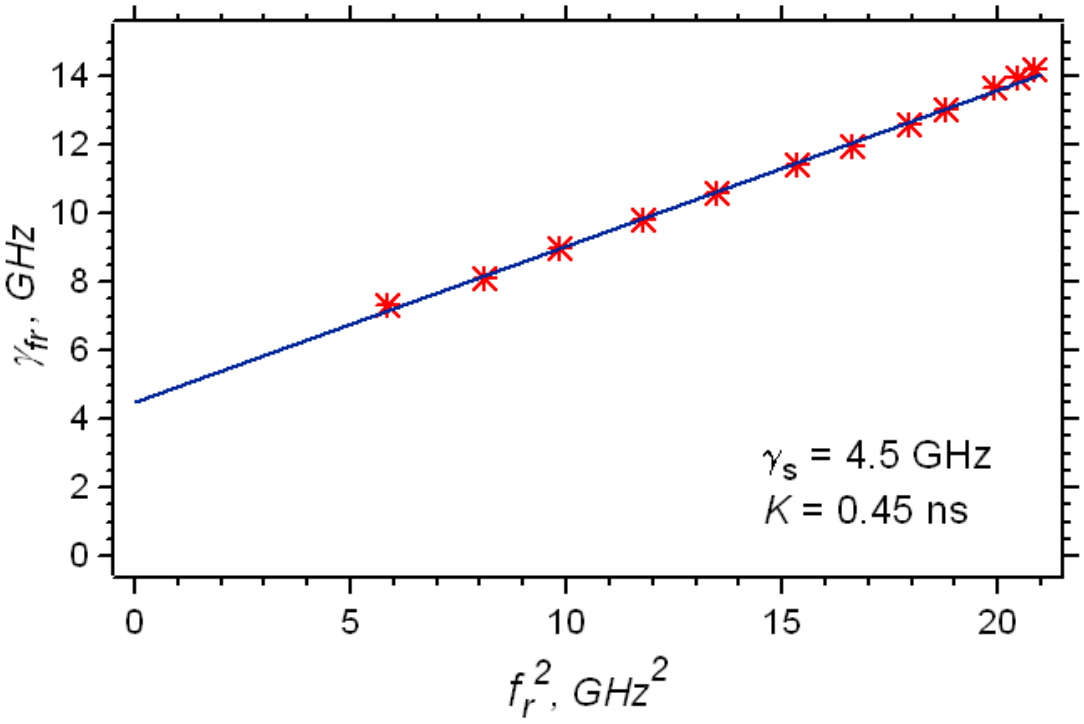

Figure 47. Free-running damping rate (γ_{fr}) as a function of the relaxation oscillation frequency squared (f_{fr}^2). The blue line is a least squares linear fit to the data points, which is then extrapolated to determine the spontaneous carrier relaxation rate, γ_s.

The impact of non-linear gain compression on the free-running relaxation oscillation frequency was evaluated using the relation in (93) (page 85). A plot of the square of the measured relaxation oscillation frequency as a function of power is given in Figure 48, where the gain compression coefficient, ε_p, is extracted to be 0.06 mW^{-1}. Although this value is less than its corresponding value for the quantum-dot laser studied, it remains an order of magnitude greater than typical quantum-well lasers [8].

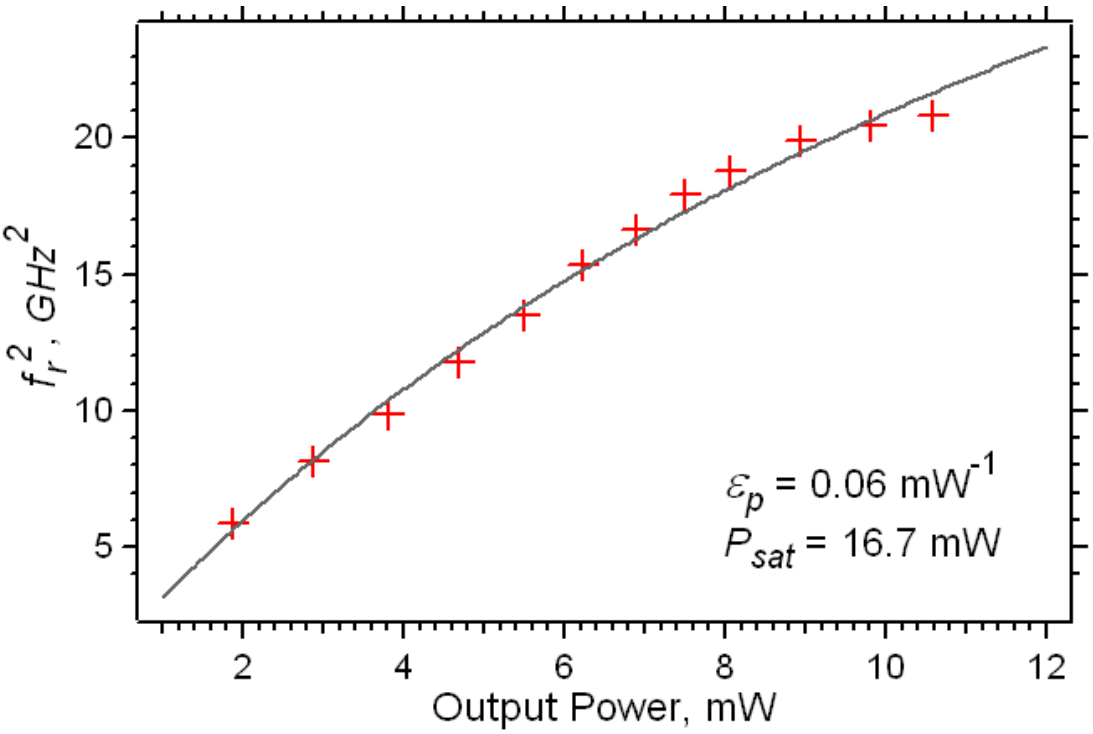

Figure 48. Quantum-dot laser free-running relaxation oscillation (f_{fr}^2) as a function of the total output power (P_{out}, both laser facets). The dotted line is a least squares linear fit using expression (93).

The linewidth enhancement parameter's measurement using the injection-locking technique for the quantum-dash laser differed from those found for the quantum-dot laser. Where the measured linewidth enhancement parameter for the quantum-dot laser was found to be relatively constant as a function of injected master laser power, the quantum-dash laser's measured linewidth enhancement parameter showed a dependence on the injected master laser power. The linewidth enhancement parameter was observed to decrease as the injected power was increased, as illustrated in Table 3 showing measured values at bias current of 65 mA and varied injected powers. Table 4 and Table 5 show corresponding linewidth enhancement parameter data for bias currents of 75 mA

and 85 mA, respectively. For fixed injection strengths, the linewidth enhancement parameter is observed to increase as the laser bias current is increased.

Table 3. Quantum-dash laser linewidth enhancement parameter measured using the injection-locking technique for varied injected master laser powers at 65mA bias current.

$P_{master}(mW)$	$\eta_o(GHz)$	α
8	124	1.0
6	107	1.2
5	98	1.7
4	87	1.9
3	76	2.2

Table 4. Quantum-dash laser linewidth enhancement parameter measured using the injection-locking technique for varied injected master laser powers at 75mA bias current.

$P_{master}(mW)$	$\eta_o(GHz)$	α
8	102	2.3
7	95	2.0
6	88	2.4
5	80	2.2
4	72	2.9

Table 5. Quantum-dash laser linewidth enhancement parameter measured using the injection-locking technique for varied injected master laser powers at 85mA bias current.

$P_{master}(mW)$	$\eta_o(GHz)$	α
9	99	2.8
8	94	3.4
6	81	3.2

The lower current limit in measuring the linewidth enhancement parameter is limited by the observance of period-one oscillations under positive frequency detuning conditions. The measured values shown in Table 3 and Table 4 are for injected power levels where the coupled system transitions from stable-locking to four-wave-mixing at the positive frequency detuning edge and from stable-locking to unlocked operation at the negative frequency detuning edge. Injected power levels where period-one operation was observed as the master laser was positively detuned from the slave laser yielded unrealistic/irrational values. It is noted that in Table 3 and Table 4, the injection strength value, η_o, is in Grad/s.

The upper limit is constrained by the Fabry-Perot mode spacing, measured for the quantum-dash laser to be approximately 85 GHz. Dividing this value in half (master will begin to couple to the adjacent mode past the mode spacing mid-point), stable-locking observed at a detuning of +42.5 GHz results in continuous stable-locking as further detuning causes the master laser to lock to the next Fabry-Perot mode. This detuning of ~42.5 GHz equates to an injection strength of $\sim 2 \cdot 42.5 \cdot \pi = 267$ GHz. The observance of continuous stable-locking under strong injection is further enhanced by the asymmetry of the stable-locking region as given in (24), where the detuning range is given by $-\eta(1 + \alpha^2)^{1/2} \leq \Delta\omega \leq \eta$. An illustration of the continuously locked case is illustrated in Figure 49. An example takeaway from Figure 49 is that for an injection strength of 125 GHz, if the linewidth enhancement parameter is > 3.11, then continuous locking will be observed between adjacent Fabry-Perot modes of the quantum-dash slave laser.

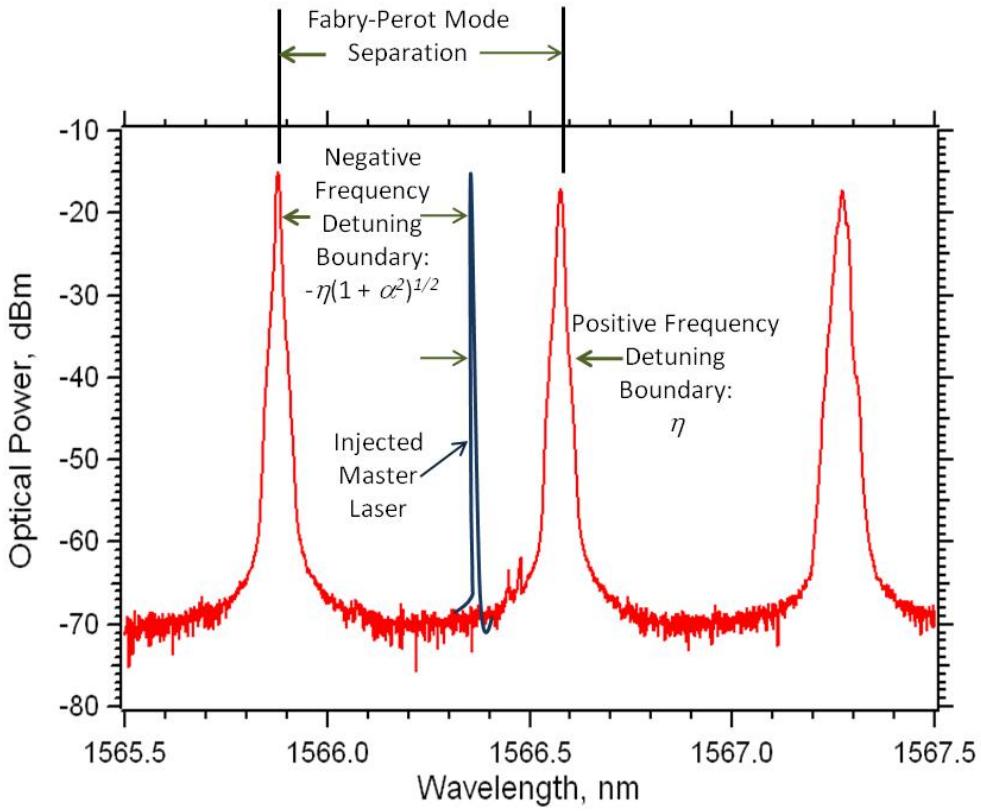

Figure 49. Illustration of the upper injection strength limit experienced when measuring the linewidth enhancement parameter with the injection-locking technique in the quantum-dash Fabry-Perot laser.

Chapter 5. Optically-Injected Quantum-Dash Lasers: Experimental Findings

This chapter investigates the behavior of the optically-injected quantum-dash Fabry-Perot laser as the injected field strength is increased from near-zero to levels resulting in stable locking. First, the microwave domain modulation response of the injection-locked quantum-dash laser is analyzed using the small-signal modulation response derived in Chapter 2. The newly derived modulation response, where the nonlinear carrier relaxation rate and compression of the differential and nonlinear carrier relaxation rates are incorporated, is used to least-squares-fit data collected on the injection-locked system with a focus on the zero-detuning and positive frequency detuning boundary conditions. The extracted values are then compared with theoretically expected values under the given detuning conditions. The correlation between the frequency of the resonance peak of the modulation response at the positive frequency detuning edge and a pole in the modulation response function under this detuning condition is illustrated in order to validate the maximum injection strength, η_o, calculation introduced in (73). The newly derived modulation response function is shown to accurately simulate the injection-locked behaviors and predict operating conditions ideal for high-performance optical communication links.

Second, the free-running characterization in section 4.2 is used to theoretically simulate the dynamic response (stable locking, period-one, period-doubling, or chaos) in the context of the normalized, dimensionless single-mode rate equations described in Chapter 3. This theoretical examination is verified with experimental results obtained using a high resolution spectrometer (1 MHz), yielding a unique data set showing extreme detail of the coupled system's optical power spectra. Experimentally, stability

maps where the dynamic state is characterized as a function of injection strength and detuning frequency are generated for varied slave laser bias conditions. The experimental setup used to characterize the quantum-dash laser at 1550-nm under optical-injection is given in Figure 50.

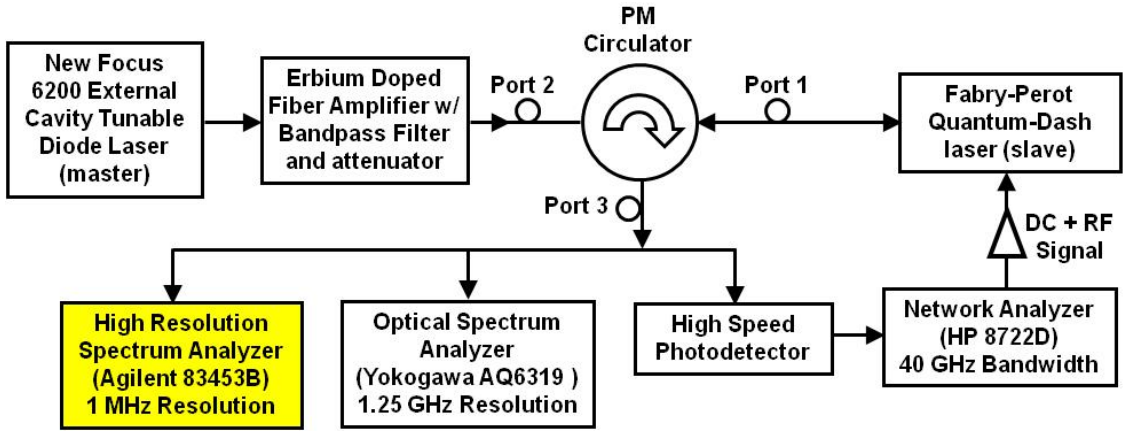

Figure 50. Experimental setup used to characterize the optically-injected quantum-dash laser.

5.1. Microwave modulation response of the injection-locked quantum-dash laser at the positive detuning edge of stable locking

In this section, the microwave modulation response is examined at the positive frequency detuning edge of stable-locking using the microwave modulation response derived in Chapter 2. The transfer function is reiterated here for clarity and to add in a parasitic carrier transport rate, γ_t, as shown in (96). Expressions (97) – (102) show the terms used, where $\eta = \eta_o/R_{FE}$. Based on the free-running characterization of the quantum-dash laser presented in section 4.2, the number of unknowns in (96) – (102) is reduced

from 10 (γ_n, γ_p, γ_c, γ_s, γ_t, ε_p, η_o, R_{FE}, α, θ_o) to 3 (η_o, R_{FE}, θ_o). In (96), γ_t is the inverse parasitic carrier transport time and is determined by least-squares fitting the free-running modulation response. The free-running slave parameters γ_n, γ_p, γ_c, and γ_s are carrier forward from the free-running characterization and considered constant in the response function; γ_n and γ_p are scaled using R_{FE} and compressed via ε_p based on the injected power, as expressed in (103) and (104). The field enhancement factor, R_{FE}, is ideally calculated by solving for the real root of (34) based on the free-running relaxation rates, maximum injection-strength η_o, and phase-offset between the master and slave. This relationship between R_{FE} and the coupled system's operating parameters essentially reduces the number of fitting parameters to 2 (η_o and θ_o).

$$\left|H(\omega)\right|^2 = \frac{(C/Z)^2(\omega^2+Z^2)}{(C-A\omega^2)^2+(B\omega-\omega^3)^2}\frac{1}{\left(1+(\omega/\gamma_t)^2\right)} \tag{96}$$

$$A = \gamma_{n,inj} + \gamma_{p,inj} + \gamma_s + \gamma_{th} \tag{97}$$

$$B = \gamma_{n,inj}\gamma_c + \gamma_{p,inj}\gamma_s + \eta^2 + \gamma_s\gamma_{th} - Z\gamma_{p,inj} \tag{98}$$

$$C = \eta^2(\gamma_{n,inj} + \gamma_s) - Z(\gamma_{n,inj}\gamma_c + \gamma_{p,inj}\gamma_s - \gamma_{n,inj}\gamma_{th}) \tag{99}$$

$$Z = \eta\left(\alpha\sin(\theta_o) - \cos(\theta_o)\right) \tag{100}$$

$$\gamma_{th} = 2\eta\cos(\theta_o) \tag{101}$$

$$\eta_o = \frac{c}{2n_g L}\frac{(1-R)}{\sqrt{R}}\sqrt{\frac{P_{inj,external}}{P_{FR,total}}} \tag{102}$$

$$\gamma_{n,inj} = \gamma_n R_{FE}^2 \frac{(1+\varepsilon_p P_{fr})}{(1+\varepsilon_p (P_{fr} R_{FE}^2 + P_{inj})} \tag{103}$$

$$\gamma_{p,inj} = \gamma_p R_{FE}^2 \frac{(1+\varepsilon_p P_{fr})^2}{(1+\varepsilon_p (P_{fr} R_{FE}^2 + P_{inj})^2} \tag{104}$$

Section 2.6 discussed the importance of the positive frequency detuning edge of stable-locking, where the steady-state phase offset has been shown to be approximately $-\pi/2$ and the field enhancement factor, R_{FE}, is approximately 1 reducing γ_{th} and Z as given in (62) and (63). In Figure 51 the modulation response is shown for three cases at the positive frequency detuning edge of stable-locking, where further detuning resulted in the side mode suppression ratio falling below 30 dB as the injected power was held constant. Constraining the fitting function such that there are only 2 freely varying fitting parameters (η_o and θ_o) yields the fitting results shown in Figure 51, where the fit only weakly agrees with the experimentally observed resonance peak. These poor fitting results are a result of the highly constrained nature of the fitting model. The extracted parameters (η_o and θ_o) and the free-running values carried forward are given in Table 6. The takeaway from Figure 51 and Table 6 is that to adequately fit the experimental response curves, the parameters in the fitting function will need to be more loosely constrained. The error in η_o in the far right column of Table 6 indicates the deviation between the value calculated based on (102) using the externally measured power levels and the value extracted by least-squares-fitting.

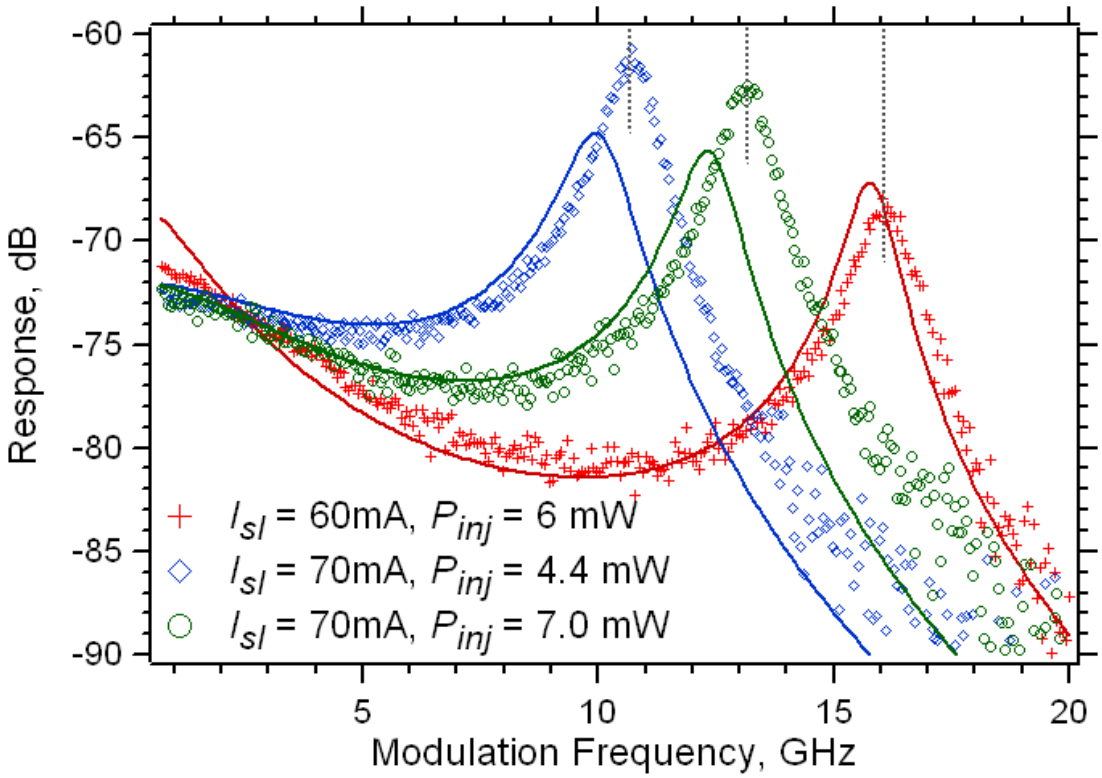

Figure 51. Modulation response at the positive frequency detuning edge of stable locking. Markers indicate the experimental data; solid lines are the least-squares-fitting results with the expressions given in (96) - (104) where only η_o and θ_o are allowed to freely vary as fitting parameters. R_{FE} is calculated by solving for the real root of (34) based on the free-running relaxation rates, least-squares-fit value of the injection-strength η_o and phase-offset between the master and slave. α is constrained based on the free-running measured value.

Table 6. Extracted operating parameters obtained by least-squares-fitting the experimental data in Figure 51 with the expressions given in (96) - (104). The columns in yellow were freely varying fitting parameters; gray columns were held constant; green columns were tightly constrained within 5% of there free-running value.

γ_c = 333.3 GHz, γ_s = 4.5 GHz, ε_p= 0.06											
I_{slave} (mA)	P_{inj} (mW)	Slave Power (mW)	Calculated max Injection Strength, η_o (GHz)	γ_n (GHz)	γ_p (GHz)	η_o (GHz)	θ_o	α	R_{FE}	γ_t (GHz)	error in η_o (%)
60	6	2.23	94.3	0.926	2.7	104	-1.52	1.50	1.07	76.92	10.29
70	4.5	3.98	66.0	1.34	3.98	58.2	-1.49	3.50	1.06	90.91	11.82
70	7	3.98	82.4	1.34	3.98	75.1	-1.53	3.50	1.04	90.91	8.86

Next, the least-squares-fitting constraints are loosened such that the real root of (34) was not used to determine the value of the field enhancement factor and the linewidth enhancement parameter was allowed to vary in a greater degree; the resultant fitting results are shown in Figure 52. Table 7 shows the extracted parameter values for the least-squares-fit curves in Figure 52, along with the maximum injection strength, η_o, calculated based on the externally measured slave power, injected master power, and coupling efficiency from the lensed fiber to the slave facet. The error in η_o in the 2nd from far right column of Table 7 indicates the deviation between the value calculated based on (102) using the externally measured power levels and the value extracted by least-squares-fitting.

The fitting results in Figure 52 and Table 7 show that the newly derived modulation response function can adequately model the experimental data. While (34) was not used in the fitting function (cubic equation used to determine the steady-state phase offset), it was used to calculate the field enhancement using the extracted parameters (value given in the right column of Table 7). The calculated field enhancement factor is generally close to the extracted value; however, using (34) in the fitting function to determine the field enhancement factor impedes the quality of the fit as the function becomes overly constrained.

The maximum injection strength, steady-state phase offset and field enhancement factor are each extracted to be in strong agreement with predicted theoretical values. The linewidth enhancement parameter is found to be larger than expected for all three cases, especially for the 60 mA case where it was measured to be in the range of 1.5 per Table 3 in section 4.2. This deviation from the expected value obtained by measuring the

asymmetry of the stable-locking regime leads one to conclude that the linewidth enhancement parameter varies as a function of the detuning frequency; this conclusion is based on suggestions in Nguyen et al. that the linewidth enhancement parameter is dependent on the injected power [59] and the trend reported in [40]. It is also noted that the gain compression coefficient was extracted to be either negligible or much smaller than the value obtained from characterizing the free-running laser; this finding indicates that the injected photon density may not result in gain compression in the same manner as the free-running inter-cavity photons.

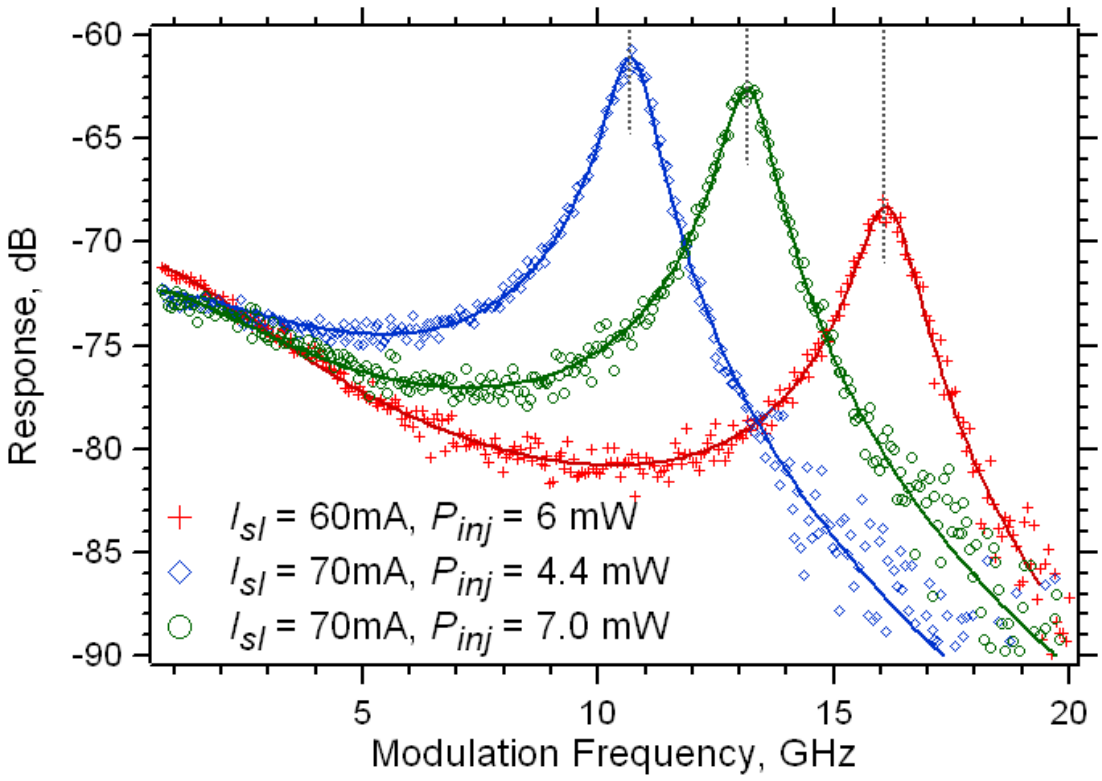

Figure 52. Modulation response at the positive frequency detuning edge of stable locking for 3 different injected powers. Markers indicate the experimental data; solid lines are the least-squares-fitting results with the expressions given in (96) - (104).

Table 7. Extracted operating parameters obtained by least-squares-fitting the experimental data in Figure 52 with the expressions given in (96) - (104). The columns in yellow were freely varying fitting parameters; gray columns were held constant.

γ_c = 333.3 GHz, γ_s = 4.5 GHz													
I_{slave} (mA)	P_{inj} (mW)	Slave Power (mW)	Calculated max Injection Strength, η_o (GHz)	γ_n (GHz)	γ_p (GHz)	η_o (GHz)	θ_o	α	R_{FE}	ε_p (mw^{-1})	γ_t (GHz)	error in η_o (%)	R_{FE} BASED ON (34)
60	6	2.23	94.3	0.926	2.704	98	-1.57	3.82	1.05	0.000	71.43	3.92	1.04
70	4.5	3.98	66.0	1.34	3.98	62	-1.44	3.94	1.15	0.000	100.00	6.06	1.11
70	7	3.98	82.4	1.34	3.98	81	-1.5	3.67	1.10	0.008	100.00	1.70	1.06

Based on the extracted parameter values in Table 7, the *B*-term in (98) is calculated and compared with the resonance peak of the modulation response. Additionally, the absolute value of the complex root of (96) is calculated and compared to the measured resonance frequency; the results are in Table 8. The calculated resonance frequency values compare well with the measured value. The takeaway is that the *B*-term yields a strong approximation of the resonance frequency of the coupled system.

Table 8. Resonance peak of the positive detuning modulation response functions calculated using the *B*-term and from the absolute value of the polynomial transfer function's roots based on the extracted parameters in Table 7.

I_{sl} (mA)	P_{inj} (mW)	*Measured Resonance Peak*	$B^{1/2}/(2\pi)$ (GHz)	Absolute Value of the Polynomial Root
60	6	16	16.4	15.7
70	4.5	10.7	10.5	10.7
70	7	13.2	13.1	12.7

Next, the impact of the nonlinear carrier relaxation rate is excluded and the least-squares-fitting is repeated. Ignoring the contribution of the nonlinear carrier relaxation rate, the least-squares-fitting results of the data shown in Figure 52 are given in Table 9.

The least-square-fit results give an equally tight modeling of the experimental data as those given in Figure 52 where the nonlinear carrier relaxation rate is considered. The results indicate the drawback of the multi-parameter fitting function, as essentially an infinite number of possible solutions exist. The extracted parameters for the cases with and without the inclusion of the nonlinear carrier relaxation rate point out that at this detuning condition (positive frequency detuning edge), the function is dominated primarily by the maximum injection strength. All additional parameters have only a minor impact on the coupled system's small-signal modulation response.

Table 9. Extracted operating parameters close to the positive frequency detuning edge where the nonlinear carrier relaxation rate is not included.

γ_c = 333.3 GHz, γ_s = 4.5 GHz, ε_p= 0, γ_p = 0 GHz										
I_{slave} (mA)	P_{inj} (mW)	Slave Power (mW)	Calculated max Injection Strength, η_o (GHz)	γ_n (GHz)	η_o (GHz)	θ_o	α	R_{FE}	γ_t (GHz)	error in η_o (%)
60	6	2.23	94.3	0.926	97.9	-1.561	3.49	1.00	76.92	3.82
70	4.5	3.98	66.0	1.34	66.44	-1.34	1.56	1.12	76.92	0.67
70	7	3.98	82.4	1.34	85	-1.449	2.20	1.06	100.00	3.16

The takeaway from comparing Table 8 and Table 9 is that the nonlinear carrier relaxation rate and gain compression have a minimal impact on modeling the modulation response at the positive frequency detuning edge where the steady-state phase offset approaches $-\pi/2$ and R_{FE} approaches 1. The approximate A, B, and C parameters at the positive frequency detuning edge of stable locking are given here ($\theta_o = -\pi/2$, $R_{FE} = 1$):

$$\gamma_{th} = 2\eta\cos(\theta_o) = 0 \tag{105}$$

$$Z = \eta\left(\alpha \sin(\theta_o) - \cos(\theta_o)\right) = -\alpha\eta \tag{106}$$

Simplifying the *A*, *B*, and *C* coefficients to the following as given in section 2.6:

$$A_{\theta=-\pi/2} = \gamma_n + \gamma_p + \gamma_s = \gamma_{fr} \tag{107}$$

$$B_{\theta=-\pi/2} = \Omega_{fr}^2 + \eta_o^2 + \alpha\eta_o\gamma_p \tag{108}$$

$$C_{\theta=-\pi/2} = \eta_o^2(\gamma_n + \gamma_s) + \alpha\eta_o\,\Omega_{fr}^2 \tag{109}$$

Therefore we see that the nonlinear carrier relaxation will have no impact on the *C*-term, and at strong injection strengths, will have a marginalized impact on the *B*-term. The takeaway found here is that the resonance peak of the modulation response at the positive frequency detuning edge of stable locking is strongly dependant on the maximum injection strength as given in (102). The experimentally measured resonance peak can therefore be used to validate the approach used to calculate the maximum injection strength based on the facet reflectivity, internal cavity round-trip time, and externally measured master and slave powers. The results show the importance of accounting for the *total* slave laser output power in determining the maximum injection strength η_o, versus the approach in [39] where only the slave output power at the injected facet is taken into account. In the next section, the modulation response under zero-detuning is analyzed using the full model derived in Chapter 2.

Using the verified small-signal modulation response transfer function, semiconductor laser design properties yielding a 1 THz resonance frequency can be theoretically determined. For this design case, a detuning at the positive frequency detuning edge is chosen due its maximum degree of resonance frequency enhancement for a given injection strength. First, it is assumed that the following laser parameters (γ_n,

γ_p, γ_c, γ_s, α) remain constant and are equivalent to the quantum-dash laser values under a bias current of 70 mA reported in this work. It is also assumed that the RC parasitic damping rate does not limit operation at high frequencies (γ_t). The key design parameter is taken to be the cavity length of the laser in order to modify the internal cavity round trip time, given its impact on the injection strength calculation as given in (102). As the laser cavity length is decreased, it is assumed that the device continues to lase for fixed cleaved facet reflectivity values.

$$\eta_o = \frac{c}{2n_g L}\frac{(1-R)}{\sqrt{R}}\sqrt{\frac{P_{inj,external}}{P_{FR,total}}} \tag{102}$$

Given the direct correlation between the *B*-term (in radian frequency) and the resonance peak at the positive frequency detuning condition, the maximum injection strength, η_o, necessary to yield a 1 THz resonance peak is 6280 GHz. To reach this large value, the cavity length is decreased to enhance the $c/2n_gL$ term in (102), while the injected power is increased. Assuming no heating effects at the laser facet and a 50% coupling efficiency between the injected power and the slave laser facet, an injected power of 87.5 mW is necessary for a cavity length of 25-μm. This cavity length and injected power condition is simulated in Figure 53. In Figure 53, cases where the inverse parasitic carrier transport time (γ_t) is and is not considered are included. The figure shows that when γ_t is considered, an enhanced resonance frequency is achievable; however, the modulation efficiency will be highly degraded. The dashed lines adjacent to each solid line illustrate the modification to the small-signal response when gain compression is considered (ε_p is taken to be equal to the free-running extracted value of 0.06 mw^{-1}). The enhanced resonance frequency is essentially unchanged due to gain compression, as the

B-term is dominated by the maximum injection strength, η_o, at the positive frequency detuning edge and therefore the compression of γ_n and γ_p under strong injection has a negligible impact.

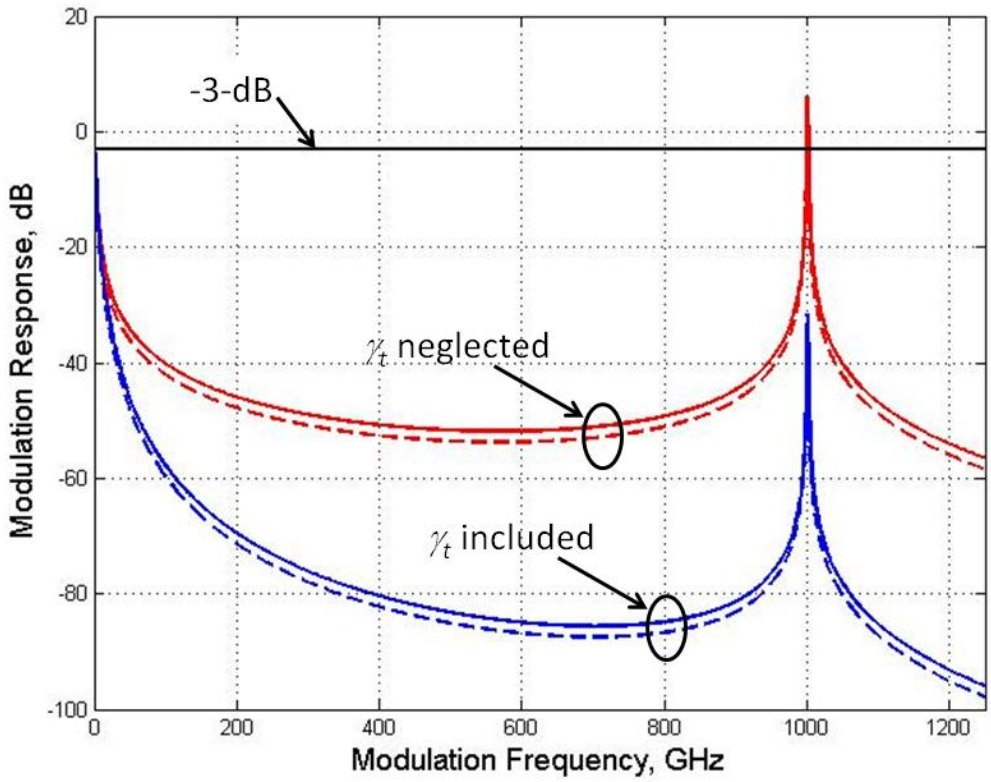

Figure 53. Theoretically simulated small-signal modulation response at the positive frequency detuning edge for a short cavity device (25 μm) under strong injection (P_{inj} = 87.5 mW) to show a 1 THz resonance frequency. Cases where the inverse parasitic carrier transport time (γ_t) is and is not considered are included. The dashed lines illustrate the impact of gain compression on the response.

5.2. Microwave modulation response of the injection-locked quantum-dash laser under zero-detuning and stable locking

The interest in the zero-detuning condition is motivated due to several reasons. First, it simplifies both theoretical predictions and experimental efforts. Second, its microwave modulation response has been observed experimentally and theoretically to be relatively flat in comparison to positive frequency detuning conditions, making this detuning condition ideal for broad-band applications. Lastly, the zero-detuning condition will simplify the implementation of the optical-injection architecture into photonic systems, as the master and slave may be packaged together with a common frequency locker to maintain the detuning condition. From the modeling perspective, the attractiveness of zero-detuning was highlighted in section 2.6, where the steady-state phase to linewidth enhancement parameter relationship was given by: θ_o = -tan^{-1}(α), reducing the Z and γ_{th} terms as given here:

$$\gamma_{th} = \frac{2\eta}{(1+\alpha^2)^{1/2}} \tag{110}$$

$$Z = -\eta(1+\alpha^2)^{1/2} \tag{111}$$

The modulation response function described in (96) - (104), along with the simplifications given in (110) and (111), is used to model experimental modulation response curves collected under the zero-detuned condition as a function of the slave laser bias and injection strength. The modulation response curves under zero-detuning, shifted to a DC modulation efficiency of 0-dB, for 65 mA, 70 mA, 75 mA, 80 mA, and 85 mA slave bias conditions are given in Figure 54 to Figure 58, respectively.

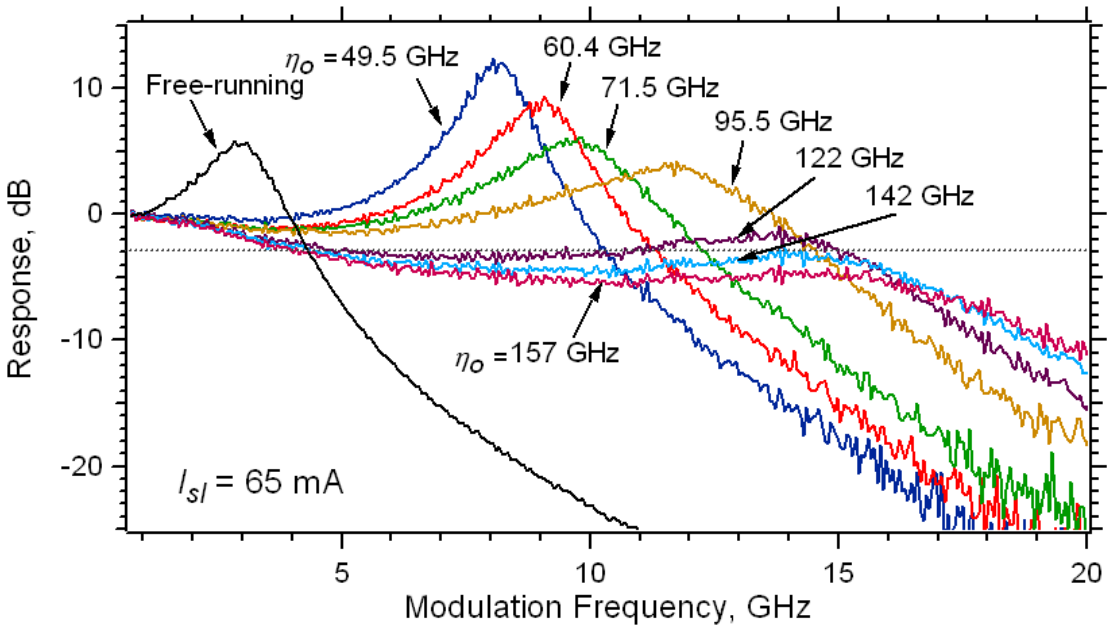

Figure 54. Normalized microwave modulation response under zero-detuning for increased injection strengths; slave bias is 65 mA.

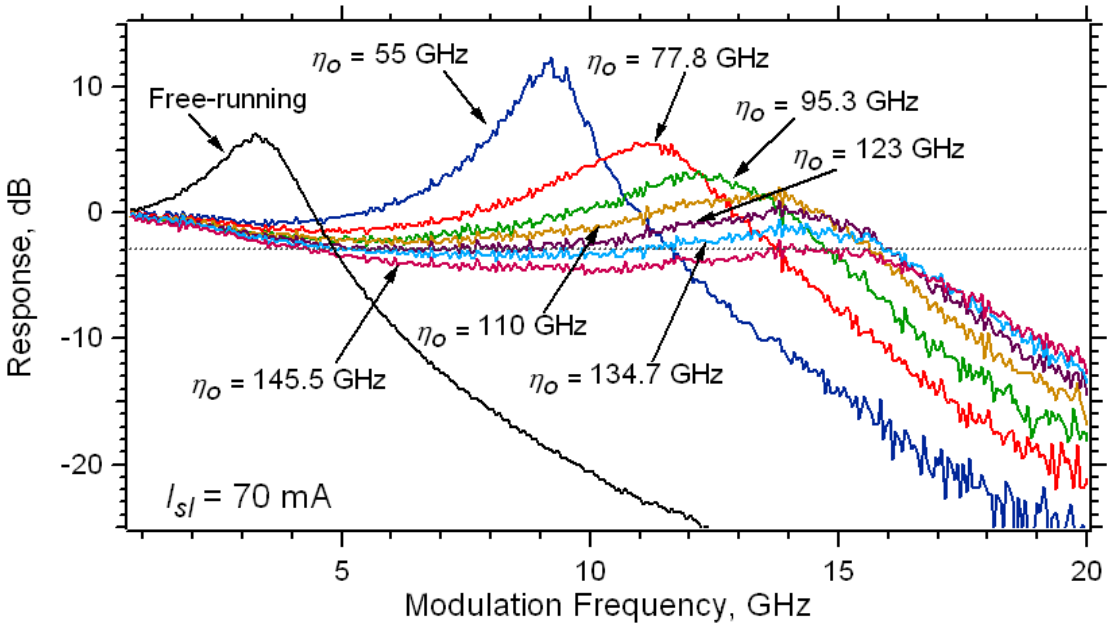

Figure 55. Normalized microwave modulation response under zero-detuning for increased injection strengths; slave bias is 70 mA.

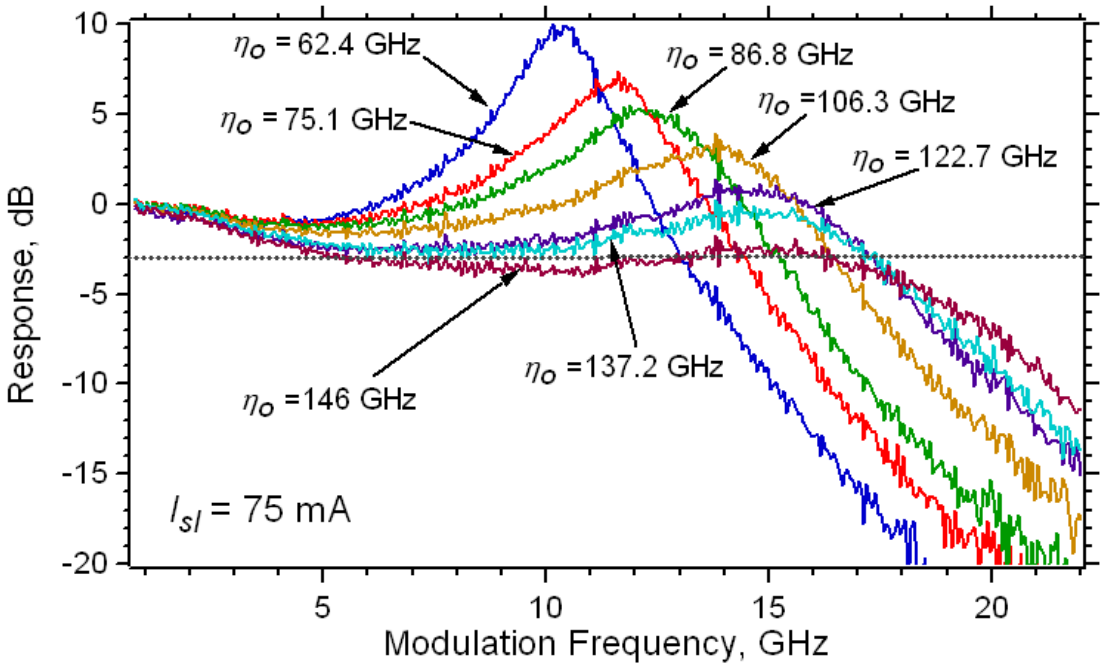

Figure 56. Normalized microwave modulation response under zero-detuning for increased injection strengths; slave bias is 75 mA.

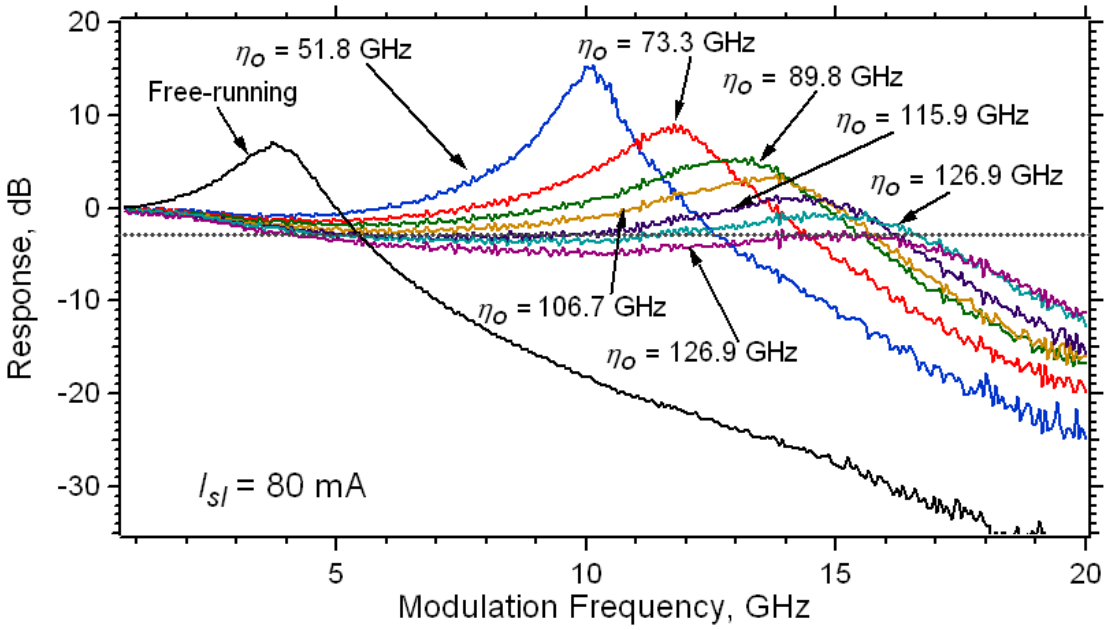

Figure 57. Normalized microwave modulation response under zero-detuning for increased injection strengths; slave bias is 80 mA.

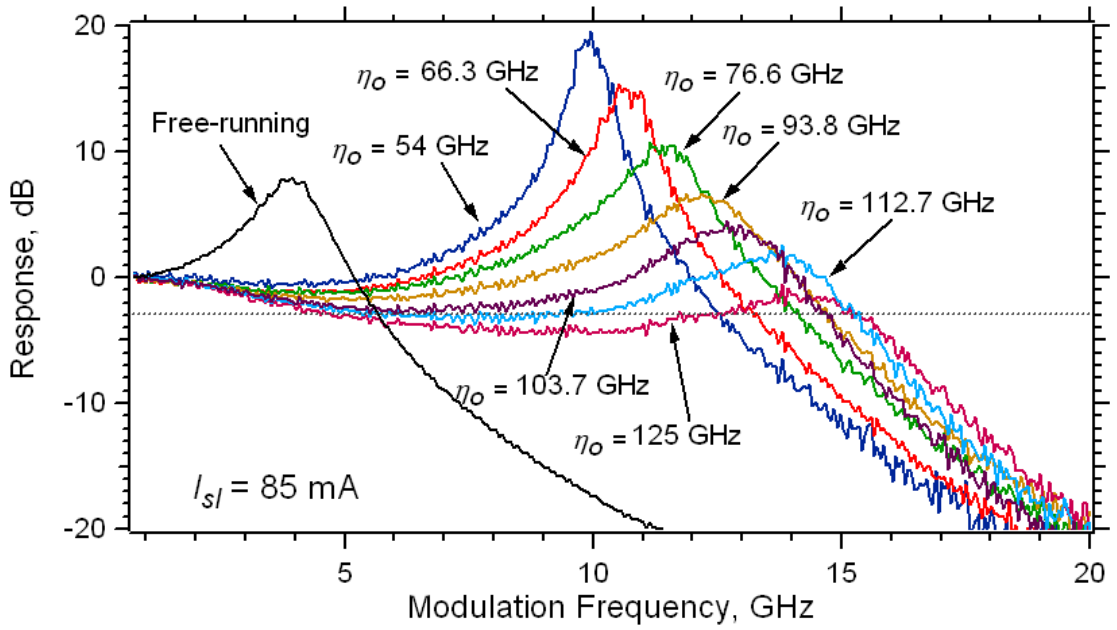

Figure 58. Normalized microwave modulation response under zero-detuning for increased injection strengths; slave bias is 85 mA.

As in section 5.1, the least-square-fitting of the experimental zero-detuning modulation curves with the function derived in Chapter 2 holds the free-running slave parameters (γ_n, γ_p, γ_c, and γ_s) constant. The nonlinear carrier and differential carrier relaxation rates (γ_p, γ_n) are scaled using R_{FE} and compressed based on the injected power using ε_p per expression (103) and (104).

Least-squares-fitting results are illustrated for the injection-locked modulation response curves for a slave laser bias of 70 mA in Figure 59, with the extracted parameters listed in Table 10. In the curve-fitting function, the maximum injection strength was restricted to be within 10% of the value calculated using (102) based on the measured injected power. The extracted linewidth enhancement parameter averages 2.9 and is reasonable for the quantum-dash laser at a bias current of 70 mA. What is not

observed in the extracted parameters is a systematic decrease in the linewidth enhancement parameter with increased injection strengths, as suggested in [59] and experimentally reported in section 4.2. The Matlab code used to perform the least-squares-fitting is found in Appendix A.

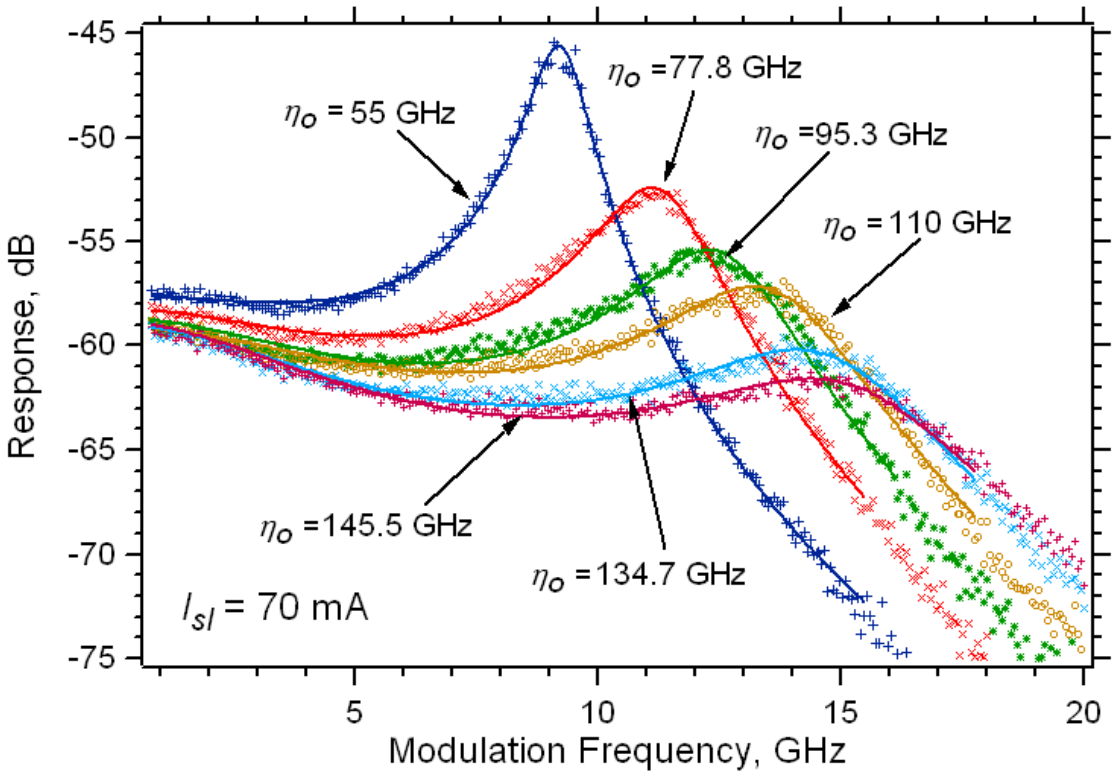

Figure 59. Least-square-fit microwave modulation response under zero-detuning for increased injection strengths; slave bias is 70 mA. Markers indicate experimental data; solid lines are the least-squares-fit results.

Table 10. Extracted parameters (yellow) from the curve fit illustrated in Figure 59 for a quantum-dash bias current of 70 mA.

I_{sl} = 70 mA, θ_o = -tan$^{-1}(\alpha)$, γ_c = 333.3 GHz, γ_s = 4.5 GHz										
P_{inj} (mW)	Slave Power (mW)	Calculated Injection Strength, η_o (GHz)	γ_n (GHz)	γ_p (GHz)	η_o (GHz)	α	R_{FE}	ε_p (mW^{-1})	γ_t (GHz)	error in η_o (%)
2	3.98	55.0	1.34	3.98	56.9	3.00	1.42	0.001	83.33	3.44
4	3.98	77.8	1.34	3.98	81.5	3.10	1.49	0.001	83.33	4.76
6	3.98	95.3	1.34	3.98	99.8	3.10	1.64	0.001	83.33	4.75
8	3.98	110.0	1.34	3.98	115	3.10	1.73	0.001	83.33	4.53
10	3.98	123.0	1.34	3.98	129	3.10	1.84	0.001	83.33	4.88
12	3.98	134.7	1.34	3.98	141	3.00	1.91	0.001	83.33	4.64
14	3.98	145.5	1.34	3.98	153	2.90	1.93	0.001	83.33	5.15
16	3.98	155.6	1.34	3.98	163	2.90	1.94	0.001	83.33	4.76
18	3.98	165.0	1.34	3.98	173	2.90	1.96	0.002	76.92	4.83

Additional least-square-fitting results are reported in Table 11 – Table 14 for the 65 mA, 75 mA, 80 mA, and 85 mA slave bias cases, respectively. In each case, the starting value for the linewidth enhancement parameter was based on the measured values reported in section 4.2. The first takeaway from the extracted parameters for the varied slave laser bias conditions is that the linewidth enhancement parameter remains relatively constant at ~3 over the entire range of slave laser bias currents. This finding contrasts with the highly variable nature of the linewidth enhancement parameter reported by Grillot et al., where the feedback sensitivity of a quantum-dash laser with the same design as the device investigated in this work was examined [56] (likewise, reference [40] examines the same laser device; the author of this work is a co-author of both). It is noted that although identical in design, the operating characteristics of the quantum-dash laser used in [56] and [40] were slightly different; most notably, the output

power and slope efficiency (0.2 mW/mA versus 0.16 mW/mA) were slightly higher for the device in [56] and [40].

In [56] and [40], it was reported that the quantum-dash Fabry-Perot laser's linewidth enhancement parameter was approximately 3.2 at 70 mA bias current and 8.0 at a bias current of 85 mA. Given that the linewidth enhancement factor is dependent on the output power (equally the inter-cavity photon density) as discussed in [8] and [62], the quantum-dash device investigated in this work exhibiting slightly lower output power levels will have lower linewidth enhancement parameter values at identical bias currents compared with [40] and [56]. Secondly, the linewidth enhancement parameter measurement is known to have a high degree of experimental error, as discussed by Melnik et al. in [47].

The second takeaway is in regards to gain compression: it was found that only under the high bias current condition (85 mA) that the gain compression approaches the value determined by characterizing the free-running operation of the quantum-dash as reported in section 4.2 (page 98), where ε_p was found to be 0.06 mW^{-1}. This finding is visually explained using Figure 48 (page 98) where the gain compression coefficient is determined, showing that gain compression does not have a prominent impact until the total output power reaches 4 mW, a power level that corresponds to a bias current above ~95 mA. Based on this finding, it is not surprising to see that gain compression does not affect the modulation response as indicated in Table 11 – Table 14.

Table 11. Extracted parameters (yellow) from the curve fit for the injection-locked quantum-dash laser's modulation response at zero-detuning and 65 mA bias current.

I_{sl} = 65 mA, θ_o = -tan$^{-1}(\alpha)$, γ_c = 333.3 GHz, γ_s = 4.5 GHz										
P_{inj} (mW)	Slave Power (mW)	Calculated Injection Strength, η_o (GHz)	γ_n (GHz)	γ_p (GHz)	η_o (GHz)	α	R_{FE}	ε_p (mw^{-1})	γ_t (GHz)	error in η_o (%)
1.34	3.140	49.5	1.12	3.38	49.4	3.00	1.32	0.001	90.91	0.12
2	3.140	60.4	1.12	3.38	60.4	3.00	1.38	0.001	90.91	0.04
2.8	3.140	71.5	1.12	3.38	71.5	3.00	1.42	0.001	100.00	0.00
5	3.140	95.5	1.12	3.38	95.5	3.30	1.54	0.001	100.00	0.04
5.4	3.140	99.3	1.12	3.38	99.2	3.30	1.57	0.001	100.00	0.09
8.15	3.140	122.0	1.12	3.38	122	3.10	1.64	0.001	100.00	0.02
11	3.140	141.7	1.12	3.38	142	3.30	1.67	0.001	100.00	0.20
13.5	3.140	157.0	1.12	3.38	157	3.20	1.74	0.001	100.00	0.01

Table 12. Extracted parameters (yellow) from the curve fit for the injection-locked quantum-dash laser's modulation response at zero-detuning and 75 mA bias current.

I_{sl} = 75 mA, θ_o = -tan$^{-1}(\alpha)$, γ_c = 333.3 GHz, γ_s = 4.5 GHz										
P_{inj} (mW)	Slave Power (mW)	Calculated Injection Strength, η_o (GHz)	γ_n (GHz)	γ_p (GHz)	η_o (GHz)	α	R_{FE}	ε_p (mw^{-1})	γ_t (GHz)	error in η_o (%)
3.1	4.8	62.4	1.53	4.55	62.6	3.30	1.25	0.001	100.00	0.38
4.5	4.8	75.1	1.53	4.55	77.4	3.30	1.35	0.001	100.00	3.01
6	4.8	86.8	1.53	4.55	88.8	3.30	1.45	0.001	100.00	2.35
9	4.8	106.3	1.53	4.55	107	3.40	1.55	0.001	100.00	0.70
12	4.8	122.7	1.53	4.55	126	3.30	1.65	0.001	100.00	2.69
15	4.8	137.2	1.53	4.55	138	3.10	1.75	0.001	100.00	0.60
17	4.8	146.0	1.53	4.55	157	3.00	1.85	0.001	100.00	7.51

Table 13. Extracted parameters (yellow) from the curve fit for the injection-locked quantum-dash laser's modulation response at zero-detuning and 80 mA bias current.

I_{sl} = 80 mA, θ_o = -tan$^{-1}(\alpha)$, γ_c = 333.3 GHz, γ_s = 4.5 GHz										
P_{inj} (mW)	Slave Power (mW)	Calculated Injection Strength, η_o (GHz)	γ_n (GHz)	γ_p (GHz)	η_o (GHz)	α	R_{FE}	ε_p (mw^{-1})	γ_t (GHz)	error in η_o (%)
2.5	5.6	51.8	1.75	5.16	54.3	3.40	1.19	0.001	100.00	4.83
5	5.6	73.3	1.75	5.16	76.8	3.10	1.49	0.001	90.91	4.77
7.5	5.6	89.8	1.75	5.16	94.1	3.10	1.66	0.001	83.33	4.79
9	5.6	98.3	1.75	5.16	103	3.10	1.68	0.003	83.33	4.78
10	5.6	106.7	1.75	5.16	109	3.20	1.66	0.008	76.92	2.16
12.5	5.6	115.9	1.75	5.16	121	3.10	1.76	0.005	71.43	4.40
15	5.6	126.9	1.75	5.16	133	3.00	1.80	0.002	76.92	4.81
17.5	5.6	137.1	1.75	5.16	144	2.90	1.85	0.001	71.43	5.03
19	5.6	142.9	1.75	5.16	150	2.90	1.90	0.002	55.56	4.97

Table 14. Extracted parameters (yellow) from the curve fit for the injection-locked quantum-dash laser's modulation response at zero-detuning and 85 mA bias current.

I_{sl} = 85 mA, θ_o = -tan$^{-1}(\alpha)$, γ_c = 333.3 GHz, γ_s = 4.5 GHz										
P_{inj} (mW)	Slave Power (mW)	Calculated Injection Strength, η_o (GHz)	γ_n (GHz)	γ_p (GHz)	η_o (GHz)	α	R_{FE}	ε_p (mw^{-1})	γ_t (GHz)	error in η_o (%)
3	6.2	54.0	1.90	5.55	56.6	3.30	1.30	0.022	83.33	4.81
4.5	6.2	66.3	1.90	5.55	69.3	3.20	1.44	0.025	83.33	4.52
6	6.2	76.6	1.90	5.55	80	3.10	1.55	0.016	83.33	4.44
9	6.2	93.8	1.90	5.55	98	3.10	1.63	0.021	76.92	4.48
11	6.2	103.7	1.90	5.55	108	3.20	1.68	0.026	50.00	4.15
13	6.2	112.7	1.90	5.55	118	3.20	1.71	0.019	50.00	4.70
16	6.2	125.0	1.90	5.55	131	3.20	1.72	0.020	50.00	4.80

Next, a linewidth enhancement parameter focused sensitivity analysis of the microwave modulation response curves under zero-detuning at the 85 mA slave bias condition is performed; the response curves are least-squares fit while the linewidth

enhancement parameter is constrained to larger values ($5 < \alpha < 8$). Figure 60 shows the fitting results, where the linewidth enhancement parameter restricted to larger values inhibits the fitting process and yields weaker results (compared to the extracted results reported in Table 14. The fitting approach allowed the maximum injection strength to vary ±15% from the value calculated using expression (102), as tighter constraints led to less adequate fitting results. For the low injection strength cases ($\eta_o < 76.5$ GHz, $P_{inj} < 6$ mW) , the extracted parameters showed that the linewidth enhancement parameter trended to the smallest value within the allowed range ($5 < \alpha < 8$), as given in Table 15. Under higher injection strengths, the least-squares-fitting resulted in larger linewidth enhancement parameter values; however, repeating fitting results showed that at high injection strengths, the function becomes less dependent on the α-parameter value. For visual simplification, only four injection strength cases were included in Figure 60. The fitting results in Table 15 also show that the gain compression coefficient fit tightly to the predicted free-running value. This was in contrast to the values extracted for a freely varying linewidth enhancement parameter in the fitting constraints, where the gain compression coefficient was observed to have a negligible impact on the fitting results.

A similar approach to the 65 mA slave laser bias case resulted in less adequate fitting results for cases when the linewidth enhancement parameter was restricted based on the values in Table 3: $1 < \alpha < 2.2$. In this case, however, the gain compression coefficient trended toward values less than 0.01 as correspondingly reported in Table 11.

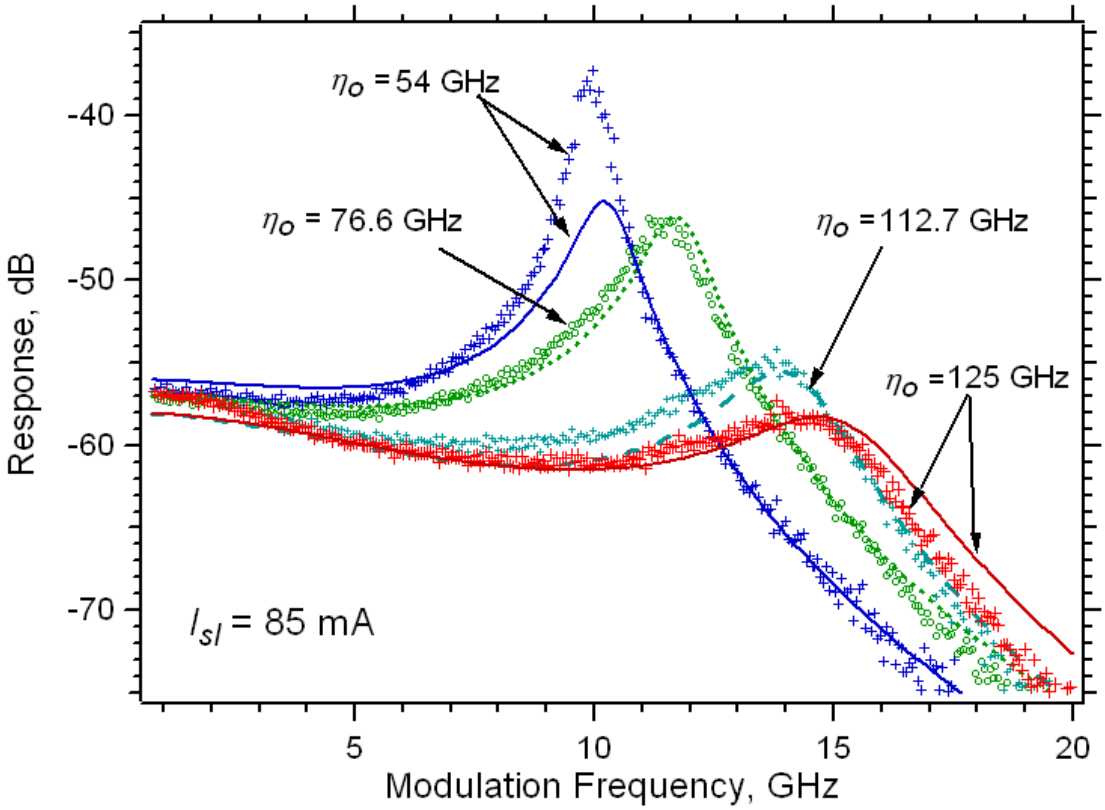

Figure 60. Least-square-fit modulation response under zero-detuning for increased injection strengths; slave bias is 85 mA. The linewidth enhancement parameter is restricted to: $5 < \alpha < 8$. Markers indicate experimental data; the fitting results are given by the solid and dashed lines.

Table 15. Extracted parameters (yellow) from the curve fit for the injection-locked quantum-dash laser's modulation response at zero-detuning and 85 mA bias current.

I_{sl} = 85 mA, θ_o = -tan$^{-1}(\alpha)$, γ_c = 333.3 GHz, γ_s = 4.5 GHz										
P_{inj} (mW)	Slave Power (mW)	Calculated Injection Strength, η_o (GHz)	γ_n (GHz)	γ_p (GHz)	η_o (GHz)	α	R_{FE}	ε_p (mW^{-1})	γ_t (GHz)	error in η_o (%)
3	6.2	54.0	1.90	5.55	47.4	5.00	1.05	0.063	90.91	12.22
4.5	6.2	66.3	1.90	5.55	56.1	5.00	1.09	0.063	50.00	15.38
6	6.2	76.6	1.90	5.55	70.6	5.00	1.32	0.063	100.00	7.83
9	6.2	93.8	1.90	5.55	79.3	5.80	1.32	0.056	83.33	15.46
11	6.2	103.7	1.90	5.55	87.7	6.00	1.39	0.063	50.00	15.43
13	6.2	112.7	1.90	5.55	95.3	6.80	1.41	0.063	50.00	15.44
16	6.2	125.0	1.90	5.55	106	7.90	1.52	0.063	50.00	15.20

Curve-fitting the experimental data with the modulation response function where the nonlinear carrier relaxation rate is excluded (γ_p = 0 GHz) yields similar fitting results due to the multi fitting-parameter nature of the response function. Without the nonlinear carrier relaxation rate, the fitting results give a small increase in the extracted linewidth enhancement parameter and a small decrease in the extracted field enhancement factor.

The overall takeaway from this section is that regardless of the slave laser bias conditions, the linewidth enhancement parameter extracted by least-squares-fitting the modulation response curves remains relatively constant at ~3. Additionally, the drawback of the multi-parameter function in modeling strong injection-locking conditions is apparent with the nonlinear carrier relaxation rate providing only a slight improvement in the modeling capabilities. Essentially, removing the nonlinear carrier relaxation rate from the fitting function results in other parameters (η_o,α, and/or R_{FE}) varying slightly to compensate for its contribution. In the next two sections, the impact of the nonlinear carrier relaxation rate is analyzed for a weakly injected system. Under relatively weak injection, the nonlinear carrier relaxation rate is observed to have a more significant impact on the characteristics of the coupled system.

5.3. Stability map of the optically-injected quantum-dash laser

In this section, stability maps characterizing the dynamic state (stable-locking, period-one, period-doubling, coherence collapse, and four-wave-mixing) as a function of maximum injection strength and detuning frequency are given for varied slave laser bias conditions. The data set is unique in that it was obtained using a high resolution spectrometer (1 MHz) giving extreme detail of the coupled system's optical power spectra.

Stability maps for the 65 mA and 85 mA cases are displayed in Figure 61 and Figure 62, respectively. Overall, the stability maps illustrate that the quantum-dash laser has potential for implementation as a tunable photonic oscillator due to the maps' large regions of period-one parameter space. Additionally, the experimental results demonstrate that only small parameter space regions of period doubling and coherence collapse are observed. In contrast to the 85 mA stability map, the 65 mA case shows only period-one and stable locking under zero-detuning conditions. The notion of only period-one and stable locking under zero-detuning invokes interest in a packaged system where the period-one state is used to generate a microwave frequency for implementation as a tunable photonic oscillator. Under such a system, a frequency locker can be implemented to hold the detuning frequency at zero and the unstable nature of the period-doubling domain can be avoided by operating the injected slave laser under the proper bias conditions.

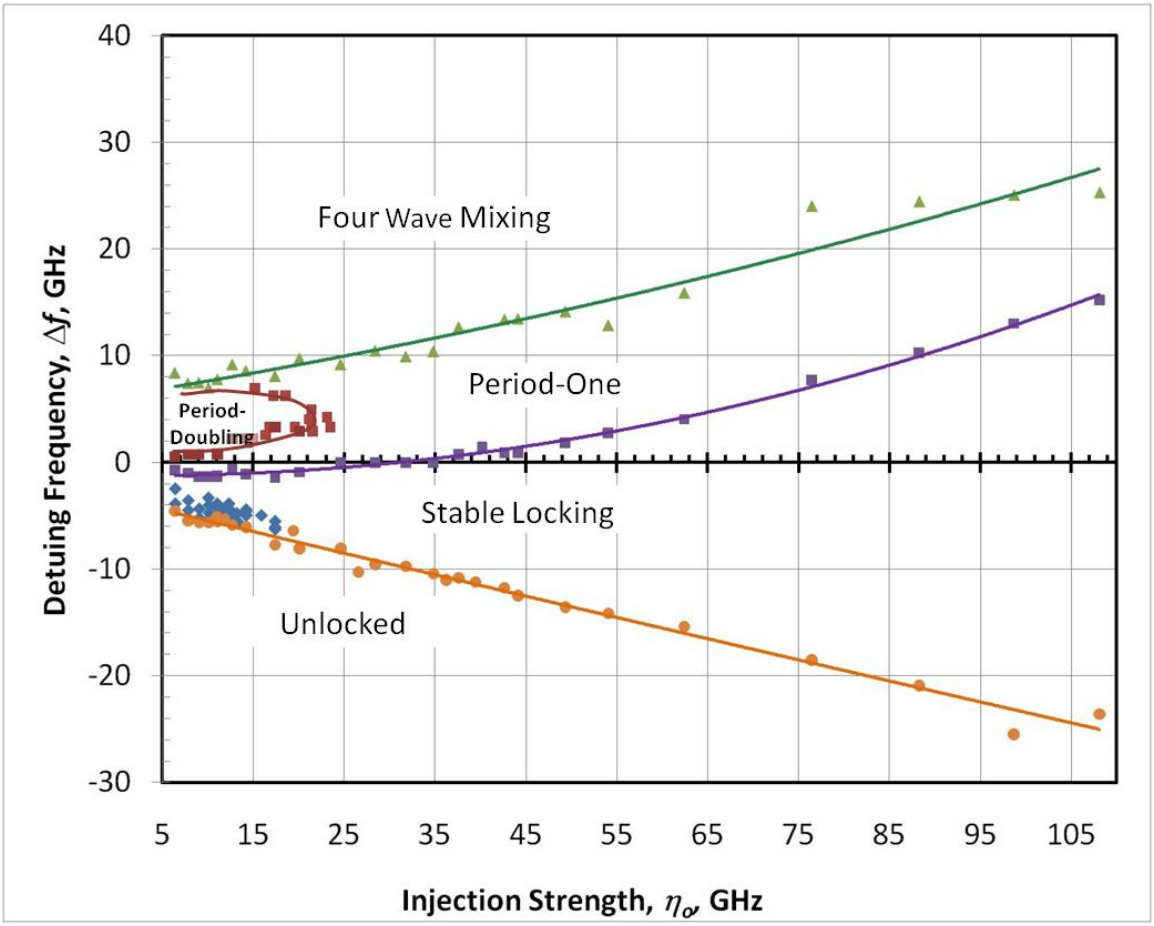

Figure 61. Stability map for the optically-injected quantum-dash slave laser at a bias current of 65 mA. The blue diamonds at negative detuning indicate chaotic (coherence collapse) operation. The trendlines have been added as a visual aid only.

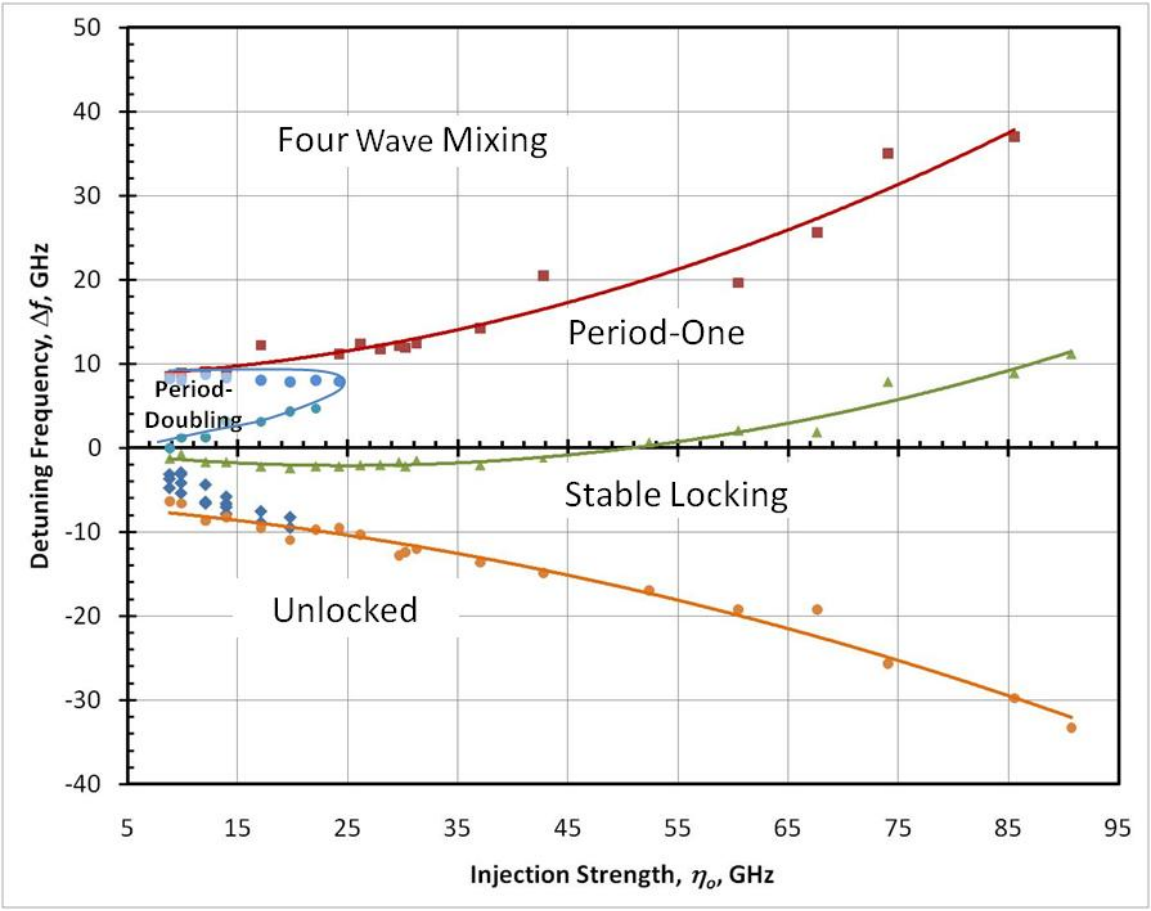

Figure 62. Stability map for the optically-injected quantum-dash slave laser at a bias current of 85 mA. The blue diamonds at negative detuning indicate chaotic (coherence collapse) operation. The trendlines have been added as a visual aid only.

Optical spectra illustrating the detuning series for a fixed maximum injection strength, η_o, of 14.2 GHz where the quantum-dash laser is biased at 65 mA are shown in Figure 63 and Figure 64. The figures depict the progression from an unlocked state at a large negative frequency detuning to four-wave-mixing at a large positive detuning frequency. Specifically, an unlocked state is observed at a detuning of -5.87 GHz (Figure 64); coherence collapse at -4.83 GHz (Figure 64); stable locking at -1.28 GHz (Figure 64); period-one oscillations at 0 GHz (Figure 63); the onset of period-doubling

oscillations at 2.2 GHz (Figure 63) and strengthened period-doubling oscillations at 2.9 GHz and 3.85 GHz (Figure 63); the suppression of the period doubling oscillations at 6.4 GHz (Figure 63); and four-wave-mixing at 9.17 GHz where the slave laser operates at its free-running frequency (Figure 63).

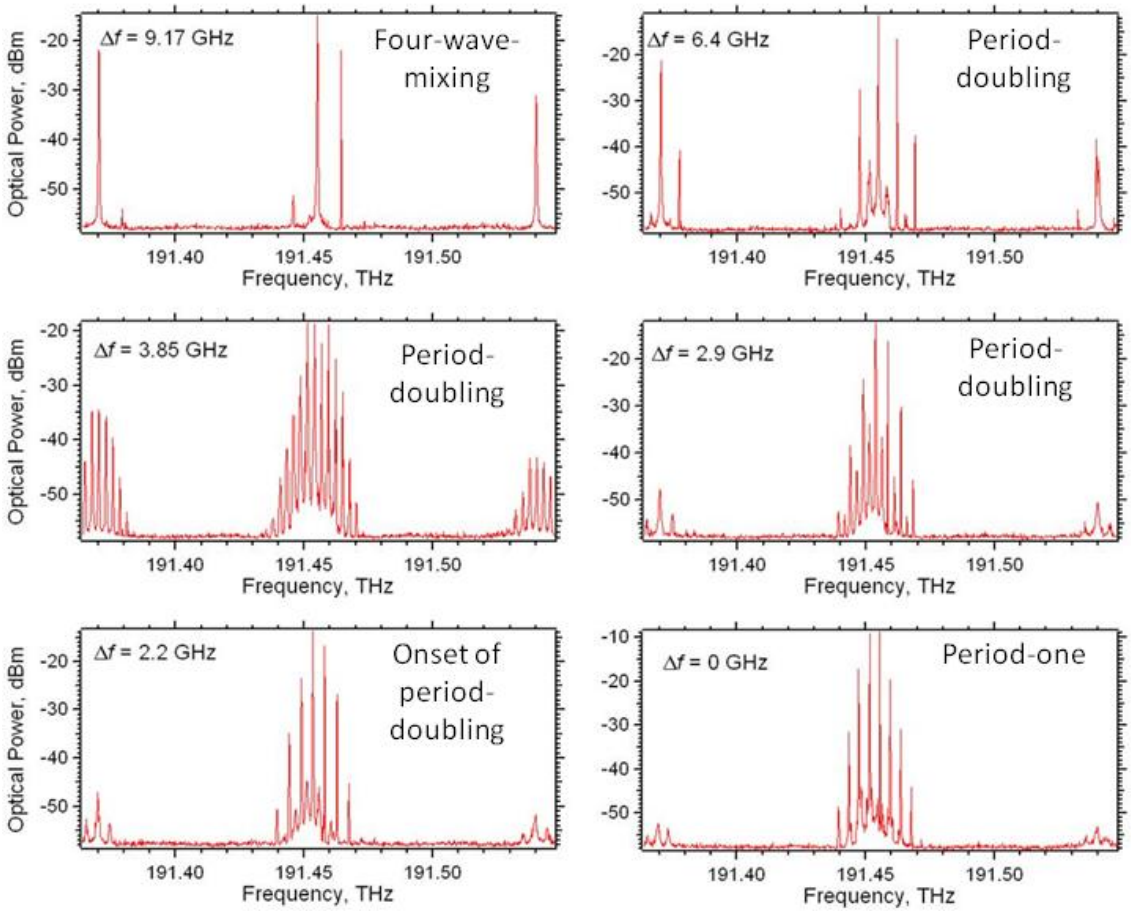

Figure 63. Positive frequency detuning series for a maximum injection strength of 14.2 GHz and a slave laser bias of 65 mA.

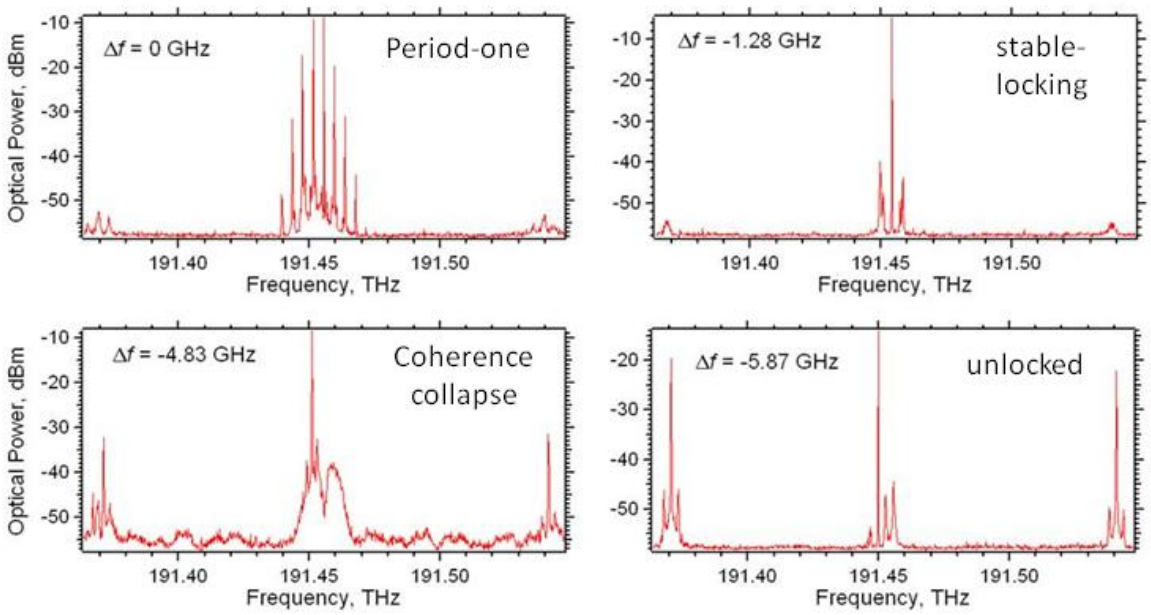

Figure 64. Negative frequency detuning series for a maximum injection strength of 14.2 GHz and a slave laser bias of 65 mA.

While the 65 mA and 85 mA stability maps are similar in nature, they differ in the injection strength needed to transition from period-one operation to stable injection-locking. This trend corresponds to expression (17) in reference [20] which states that the coupled system reaches the reverse-Hopf-bifurcation point and exhibits stable-locking for increased injected powers at a maximum injection strength, η_o, given by (112) for zero-detuning conditions.

$$\eta_{stable} = \left(\frac{P}{T} (\alpha^2 - 1) \right)^{1/2} = \frac{\Omega_r}{\sqrt{2}} (\alpha^2 - 1)^{1/2} \tag{112}$$

The expression illustrates that the threshold maximum injection strength to reach continued stable locking is directly proportional to the free-running relaxation oscillation frequency of the slave laser and proportional to the square root of the linewidth enhancement parameter in the limit of large α. The limitation of (112) is that it was

derived under various approximations, particularly the case where the nonlinear carrier relaxation rate was neglected.

Simulations of the quantum-dash laser at zero-detuning using the dimensionless rate equation model described in Chapter 3 for the 65 mA and 85 mA cases are given in Figure 65 and Figure 66, respectively. The theoretical results are in reasonable quantitative agreement with the experimental stability maps, where only regions of stable-locking and period-one oscillations are predicted at 65 mA, and a small window of period-doubling below η_o = 15 GHz followed by period-one oscillations and stable-locking are predicted at 85 mA.

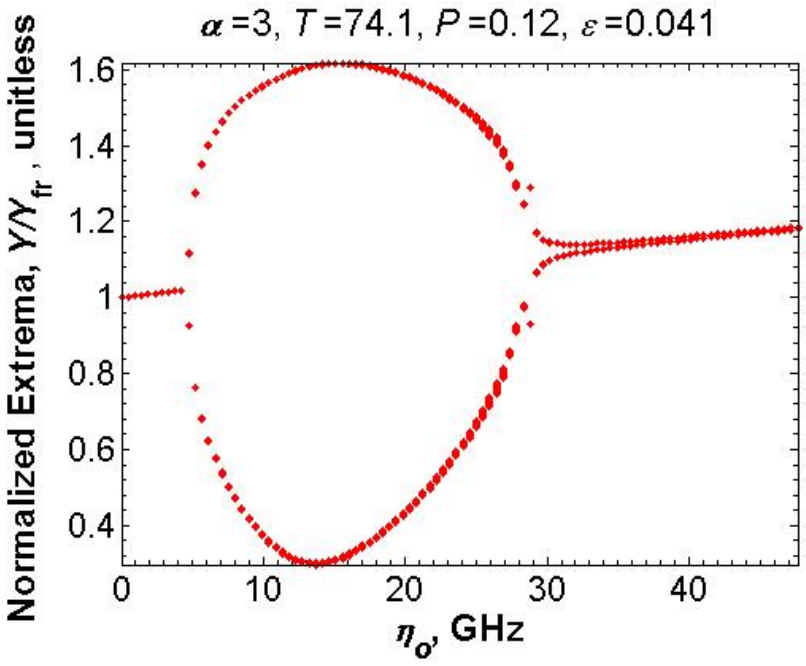

Figure 65. Theoretical simulation of the quantum-dash laser's dynamic response at 65 mA and zero-detuning.

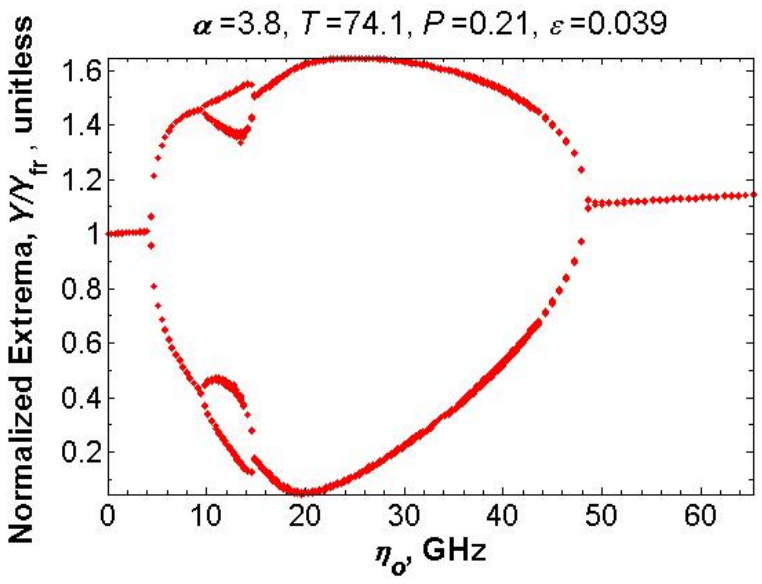

Figure 66. Theoretical simulation of the quantum-dash laser's dynamic response at 85 mA and zero-detuning.

The large period-one parameter space allows larger degrees of tunability to be reached, ideal for an optically-injected laser implemented as a tunable photonic oscillator. The tunability of the period-one resonance frequency, as measured by the spectral sidebands, for varied η_{ratio} and Δf values is illustrated in Figure 67. Specifically, Figure 67 shows that for the quantum-dash laser at a bias current of 65 mA under period-one operation, the resonance frequency (f_r) can be tuned from 4.02 GHz to 19.99 GHz, where the slave laser's free-running relaxation oscillation frequency is measured to be 3.1 GHz.

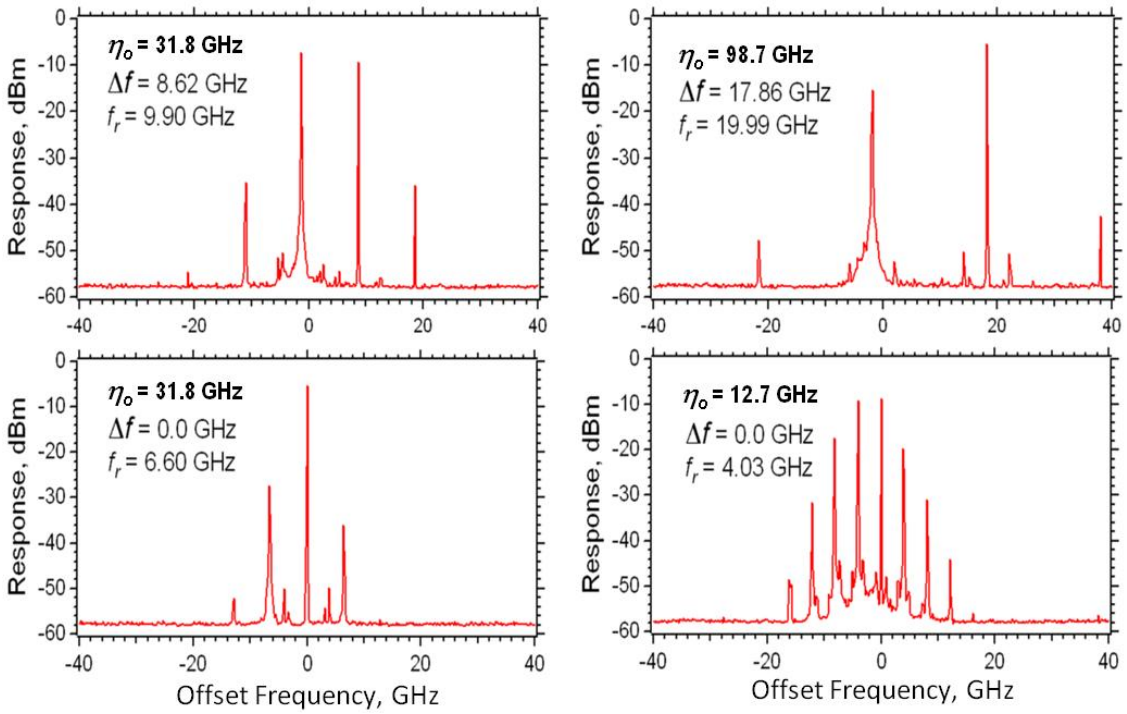

Figure 67. Optical spectra of the optically-injected quantum-dash slave biased at 65mA.

5.4. Approximation of the period-one resonance frequency at zero-detuning

In this section, the numerical approximation of the quantum-dash laser's period-one resonance frequency under zero-detuning conditions is discussed in reference to the stable solution to the microwave modulation response described in Chapter 2. As presented in Chapter 4, the quantum-dash nanostructure laser was shown to have relatively large nonlinear and spontaneous carrier relaxation rates when compared to quantum-well lasers. These increased rates are shown to enhance the coupled system's resonance frequency through interaction with the threshold gain shift induced in the slave laser, the linewidth enhancement parameter, and the phase offset. The novelty of this approach is that a stable solution is used to describe the period-one state, which is heavily

influenced by the nonlinear dynamics of the slave laser and not assumed to fall under steady-state approximations. This approach is shown to give strong agreement between measured and predicted period-one resonance frequencies.

Using expression (46) (page 29) and assuming that relatively weak injection strengths do not modify the slave laser's optical field from its free-running value (R_{FE} = 1) yields a resonance frequency of the coupled system given by (113). The function used to calculate the resonance frequency is applicable to all detuning conditions, given that the phase offset between the master and slave fields is known. The data presented in this section focuses on the zero-detuning conditions due to the phase-to-linewidth enhancement parameter relationship given by (14), which simplifies (113). Additionally, the zero-detuning case is especially attractive because both the master and slave lasers can be packaged with a reference wavelength locker to ensure frequency stability.

$$\Omega_r^2 = \Omega_{fr}^2 + \eta_o^2 + \gamma_s \gamma_{th} - \gamma_p (\eta_o \alpha \sin \theta_o - \frac{\gamma_{th}}{2}) \tag{113}$$

where Ω_r is the period-one resonance frequency and Ω_{fr} is the free-running relaxation oscillation frequency. This work uses (113) to calculate the period-one resonance frequency, whereas two commonly used approximations are given by (114) and (115) [9], [17].

$$\Omega_r^2 = \Omega_{fr}^2 + \eta_o^2 \tag{114}$$

$$\Omega_r^2 = \Omega_{fr}^2 + \eta_o^2 + \gamma_{th}\gamma_s \tag{115}$$

The key difference between (114) and (115) is the last term that accounts for the interaction between γ_{th} and γ_s. (113) accounts for the large nonlinear gain of the quantum-

dash laser through the nonlinear carrier relaxation rate γ_p, and its interaction with the slave laser linewidth enhancement parameter α, η_o, and phase offset between the master and slave θ_o.

Optical spectra of the injected slave laser in the period-one state and zero-detuning are shown in Figure 68, where the slave laser is biased at 70 mA. The resonance frequency in Figure 68 is measured by the spectral sidebands. Expression (113) is used to calculate the enhanced resonance frequency observed in Figure 68, and a strong agreement between experimental and the calculated value are reported (Figure 69). Using the free-running characterization results in Chapter 4, and by least-squares fitting the microwave modulation response at zero-detuning and the injection strength corresponding to the Hopf bifurcation, the linewidth enhancement parameter is found to be 3.2. This 3.2 value is in agreement with the values given in Table 10 (page 119) obtained by least-squares-fitting modulation response curves under strong injection conditions.

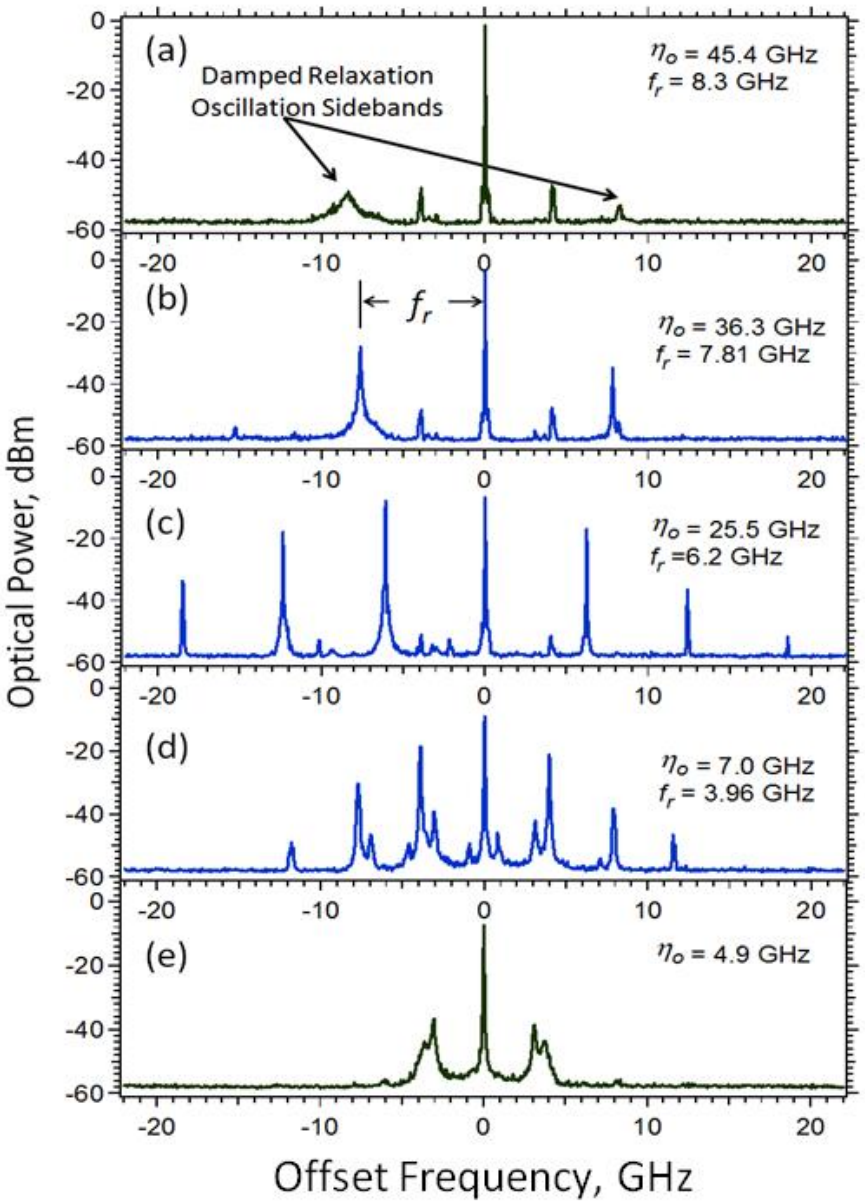

Figure 68. Optical spectra of the optically injected quantum-dash slave laser under a bias of 70 mA and zero-detuning showing the increase in resonance frequency with injection strength. f_r is the measured resonance frequency value. The spectra shown in blue are within the period-one operational region. The oscillations below -40 dBm are a result of residual feedback in the experimental setup.

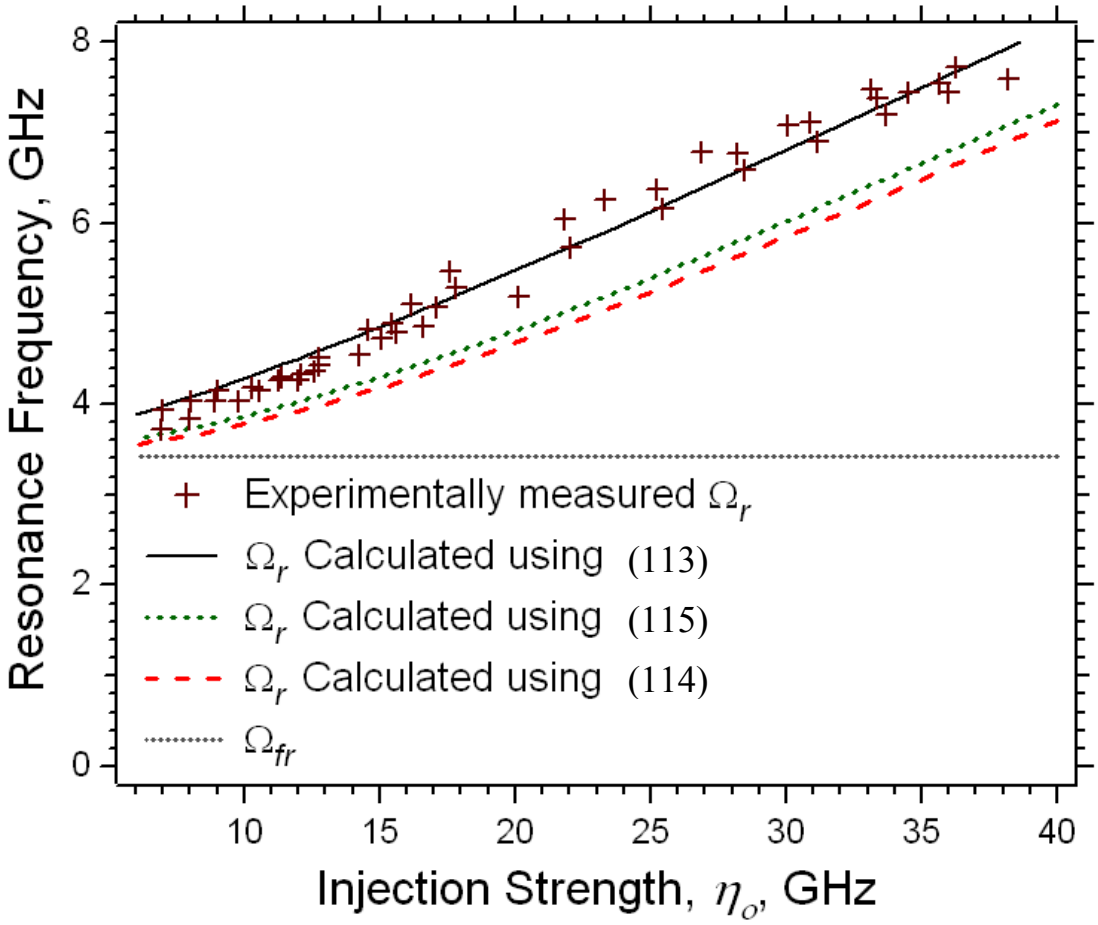

Figure 69. Measured and calculated period-one resonance frequency as a function of the injection strength for the quantum-dash slave laser at a bias current of 70 mA and zero-detuning. The resonance frequency was measured using the spectral sidebands as depicted in Figure 68.

The accuracy of (113) in predicting the period-one resonance frequency is illustrated in Figure 69, where the measured resonance frequency under zero-detuning is plotted with the values calculated using (114) and (115) as well. For the 70 mA slave bias case, the parameter values were $\Omega_{fr} = 21.6$ GHz, $\gamma_r = 9.8$ GHz, $\gamma_s = 4.5$ GHz, and $\alpha = 3.2$. γ_n and γ_p were calculated to be 1.34 GHz and 3.98 GHz, respectively. Using (113), the average error between experimental and calculated period-one resonance frequency is

3.0%, whereas the average error using the approximation in (114) was 12.5%. Using (115), which accounts for the threshold gain shift but neglects the nonlinear component, the average error is 10.1%. Although (113) is only exact at the reverse-Hopf-bifurcation point where the system operates under steady-state conditions, these results show that the resonance frequency of the undamped period-one oscillations trends with the solution derived under steady-state conditions and is a good approximation below the reverse Hopf bifurcation point.

Data sets corresponding to Figure 69 for other slave laser bias currents showed similar accuracy. For these other bias cases, γ_n and γ_p were adjusted based on the measured Ω_{fr} and γ_{fr} for the specific bias current under test. The corresponding linewidth enhancement parameter was extracted from the modulation response at the injection strengths corresponding to the reverse bifurcation point.

Chapter 6. Optically-Injected Quantum-Dot Lasers: Experimental Findings

In this chapter, the experimental findings covering the optically-injected quantum-dot laser are described and analyzed. First, the free-running characterization in section 4.1 is used to theoretically simulate the dynamic response (stable locking, period-one, period-doubling, or chaos) in the context of the normalized, dimensionless single-mode rate equations described in Chapter 3. This theoretical examination is compared with the collected experimental results. Specifically, the dynamic response is theoretically and experimentally examined under zero-detuned injection conditions for external injected power ratios ranging from 9 GHz to 75 GHz and slave current bias levels of 1.3X, 2X, and 2.6X threshold. The experimentally collected small-signal modulation response is theoretically examined at weak injection strengths using the modulation response transfer function derived in Chapter 2. Although experimentally limited by the resolution of the optical spectrum analyzer, the quantum-dot laser is observed to exhibit highly stable operation under optical-injection.

6.1. Optical spectral response under optical-injection at zero-detuning

The optical-injection experimental setup is illustrated in Figure 70. The master laser was a temperature-tunable 30 mW Fujitsu DFB quantum well laser at 1310-nm (model FLD3F7CZ) that had a polarization-maintaining (PM) fiber-coupled output. The high-resolution (10 pm / 1.75 GHz) optical spectrum analyzer (OSA) (Yokogawa AQ6319) and HP8722D vector network analyzer used in characterizing the free-running parameters were employed in the same fashion as previously to monitor the optical power spectra and small-signal S_{21} modulation response, respectively. A 3-port optical circulator

based on 1310-nm single mode PM fiber was used to connect the master and slave lasers and the test equipment with proper isolation. Experimentally, this fidelity of this work was limited by the resolution of the optical spectrum analyzer, as the 1.75 GHz resolution at ~1310-nm hampered the ability to observe weakly undamped relaxation oscillations at frequencies < 1.75 GHz from the locked mode.

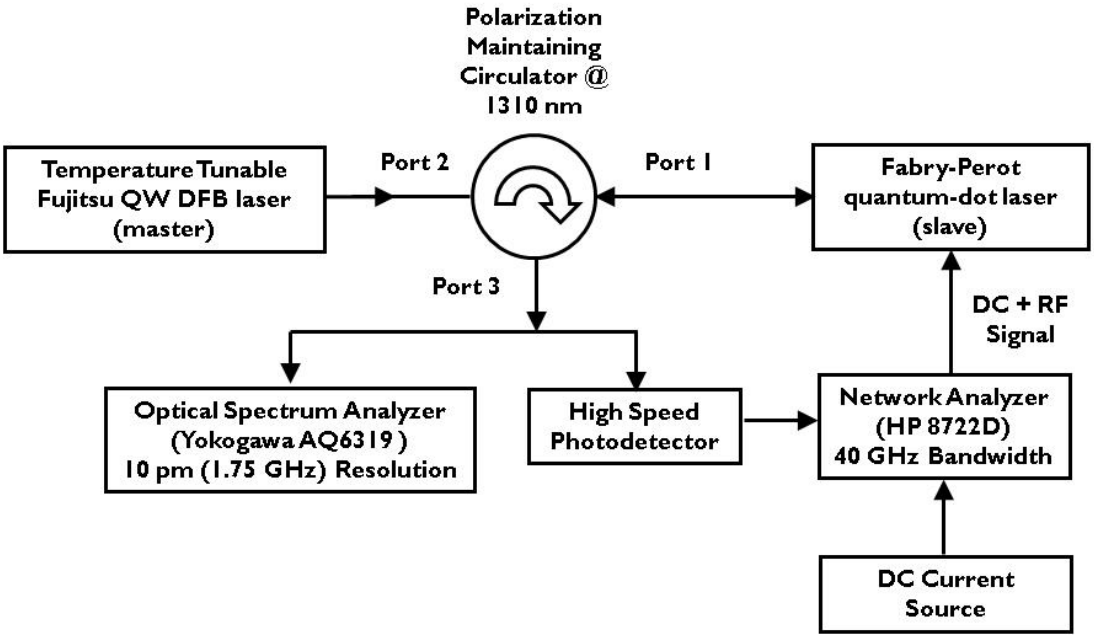

Figure 70. Experimental setup used to optically-inject the quantum-dot laser.

Using the free-running relaxation oscillation frequency and damping rate, photon decay rate, and spontaneous carrier relaxation rate, the optically-injected quantum-dot laser is simulated using the dimensionless rate equations derived in Chapter 3. Recall that in Chapter 3, sample bifurcation diagrams simulating the quantum-dash laser showed rich

nonlinear behavior under various bias conditions. The simulation results for the quantum-dot laser, shown in Figure 71, predict a highly stable response as the laser is subjected to increasing levels of injected power. The takeaway from Figure 71 is that under zero-detuning for both the 3.8 mA (2X threshold current) and 5 mA (2.6X threshold current), only stable-locking operation is expected due to the low linewidth enhancement parameter and significant nonlinear carrier relaxation rate. Although the stable behavior the quantum-dot laser has been previously described for optical feedback by O'Brien et al., the experimental results have not been compared in detail to numerical models that explicitly call out the dependence on non-linear gain for the optical feedback case [42].

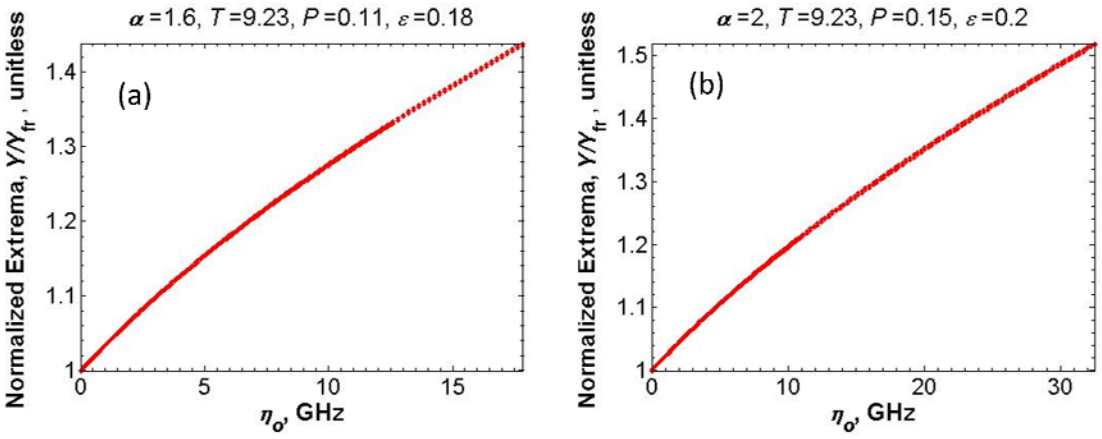

Figure 71. Bifurcation diagrams simulating the response under zero-detuning. The two cases correspond to respective P, T, and α-factor values for 3.8 mA(2X I_{th}), and 5 mA (2.6X I_{th}) bias conditions and illustrate the stability of the quantum-dot slave laser's operational behavior.

This high degree of stability in Figure 71 owes primarily to the small linewidth enhancement parameter value measured for the device. The stability is also impacted by

the large nonlinear carrier relaxation rate, γ_p, of the quantum-dot laser under test. Specifically, for the 3.8 mA case: γ_p = 2.75 GHz, γ_n = 1.65 GHz; for the 5 mA case: γ_p = 4.14 GHz, γ_n = 2.23 GHz.

The simulations in Chapter 3 showed that the nonlinear carrier relaxation rate suppressed periodic pulsations in the equilibrium condition. This ε parameter accounting for the impact of the nonlinear carrier relaxation rate in the dimensionless model, defined as $\varepsilon = \gamma_p\gamma_s/(\gamma_c\gamma_n)$, is relatively larger for the quantum-dot laser versus the quantum-dash laser. Essentially, the characteristic relaxation rates of the quantum-dot laser enhance the impact of the typically ignored nonlinear carrier relaxation rate. For comparison purposes, $\varepsilon \sim 0.04$ for the quantum-dash laser exhibits rich nonlinear dynamics (for larger linewidth enhancement parameters), while $\varepsilon \sim 0.2$ for the quantum-dot laser exhibits a high degree of stability (for smaller linewidth enhancement parameters) as simulated in Figure 71. While the stability of the laser under optical-injection is driven strongly by the linewidth enhancement parameter, its dependence on the nonlinear parameter described by ε strongly contributes to the stability of the quantum-dot device investigated here. The dependence on ε with respect to the device's stability is highlighted in the bifurcation diagrams in Figure 72, where the quantum-dot device is simulated at a bias current of 5 mA for a fictitious linewidth enhancement parameter of 4 and cases where the nonlinear carrier relaxation rate is and is not considered. The simulation where the nonlinear carrier relaxation rate is not considered (and hence $\varepsilon = 0$) predicts that a two-extrema solution indicative of period-one pulsations will occur for injection strengths ranging from 4 GHz to 68 GHz. As we shall see, this behavior is not observed experimentally.

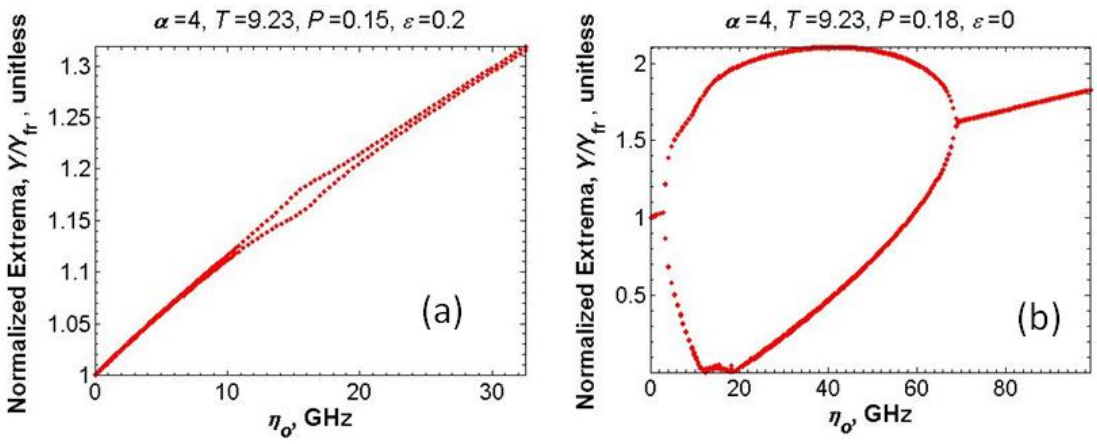

Figure 72. Bifurcation diagram for a linewidth enhancement parameter of 5 and relaxation rates based on a 5 mA bias current for the quantum-dot laser. (a) includes and (b) ignores the nonlinear carrier relaxation rate in the rate equations.

The second unique feature noted in simulating the quantum-dot laser is the extremely small *T*-term of 9.2. The *T*-term is given by γ_c/γ_s and is a fixed value for a given slave laser (i.e. not dependant on bias current); for this particular quantum-dot laser with HR-coated facets and a 300-µm cavity length, γ_c is relatively small and γ_s is relatively large compared to the quantum-dash laser. For comparison purposes, the *T*-term for the quantum-dash is ~74, and simulations found in the literature for quantum-well lasers using the dimensionless rate equation approach implemented here (where the impact of the nonlinear component is neglected) have a *T*-term of ~155 [17].

Experimentally, the quantum-dot laser was injected with strengths ranging from 9 GHz to 50 GHz at a bias current of 2.6X the threshold value (5 mA). The optical spectra for the 2.6X threshold bias current case at the onset of stable-locking are shown in Figure 73, where the maximum injection strength is calculated to be 14.8 GHz. Due to the single-mode nature of the dimensionless rate equation model derived in Chapter 3, a

discrepancy at low maximum injection strengths for the multi-mode slave under study is observed. The spectra in Figure 73(c) (30-nm span) shows only moderately suppressed Fabry-Perot modes away from the injected mode, where the side mode suppression ratio (SMSR) is measured to be 7 dB. In the 0.5-nm span shown in Figure 73(a), the small side-mode at ~1311.8-nm is believed to be a suppressed relaxation oscillation, where the SMSR is measured to be 44.8-dB.

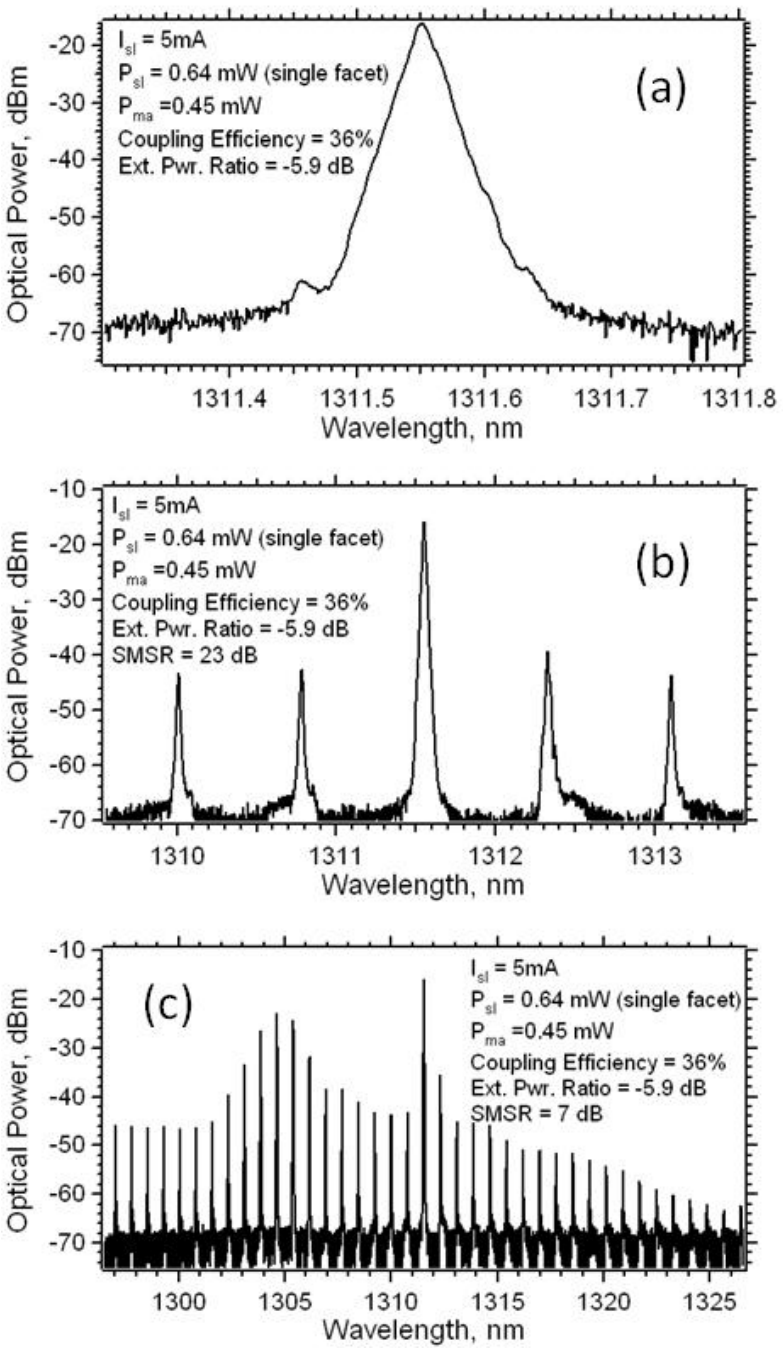

Figure 73. Experimental optical spectra for the quantum-dot laser under weak optical-injection at zero-detuning and a bias current of 5 mA. The maximum injection strength is 14.8 GHz for all three cases. The 0.5-nm span in (a) shows no observable undamped relaxation oscillations. The 4-nm span in (b) shows that the adjacent Fabry-Perot modes are not suppressed beyond 30 dB, the criteria for stable-locking. The 30-nm span in (c) shows that the Fabry Perot modes at ~1305-nm are minimally suppressed (7 dB).

The spectra in Figure 74 correspond to the experimentally observed onset of stable-locking, where the maximum injection strength is 17.4 GHz. The 0.5-nm span in Figure 74(a) shows no evidence of undamped relaxation oscillations, concluding that period-one operation is suppressed under zero-detuning conditions. As the maximum injection strength was increased up to 50 GHz, the Fabry-Perot side modes were more strongly suppressed. Experimental optical spectra collected at a slave laser bias current of 3.8 mA (2X I_{th}) showed similar results to those in Figure 73 and Figure 74 for the 5 mA slave bias current case (2.6X I_{th}). For the 3.8 mA bias current under external power ratios varied from 11 GHz to 90 GHz, unlocked behavior was observed at low maximum injection strengths followed by stable-locking as the injected power was increased; optical power spectra showing characteristics of undamped relaxation oscillations were not observed for the full range of external power ratios.

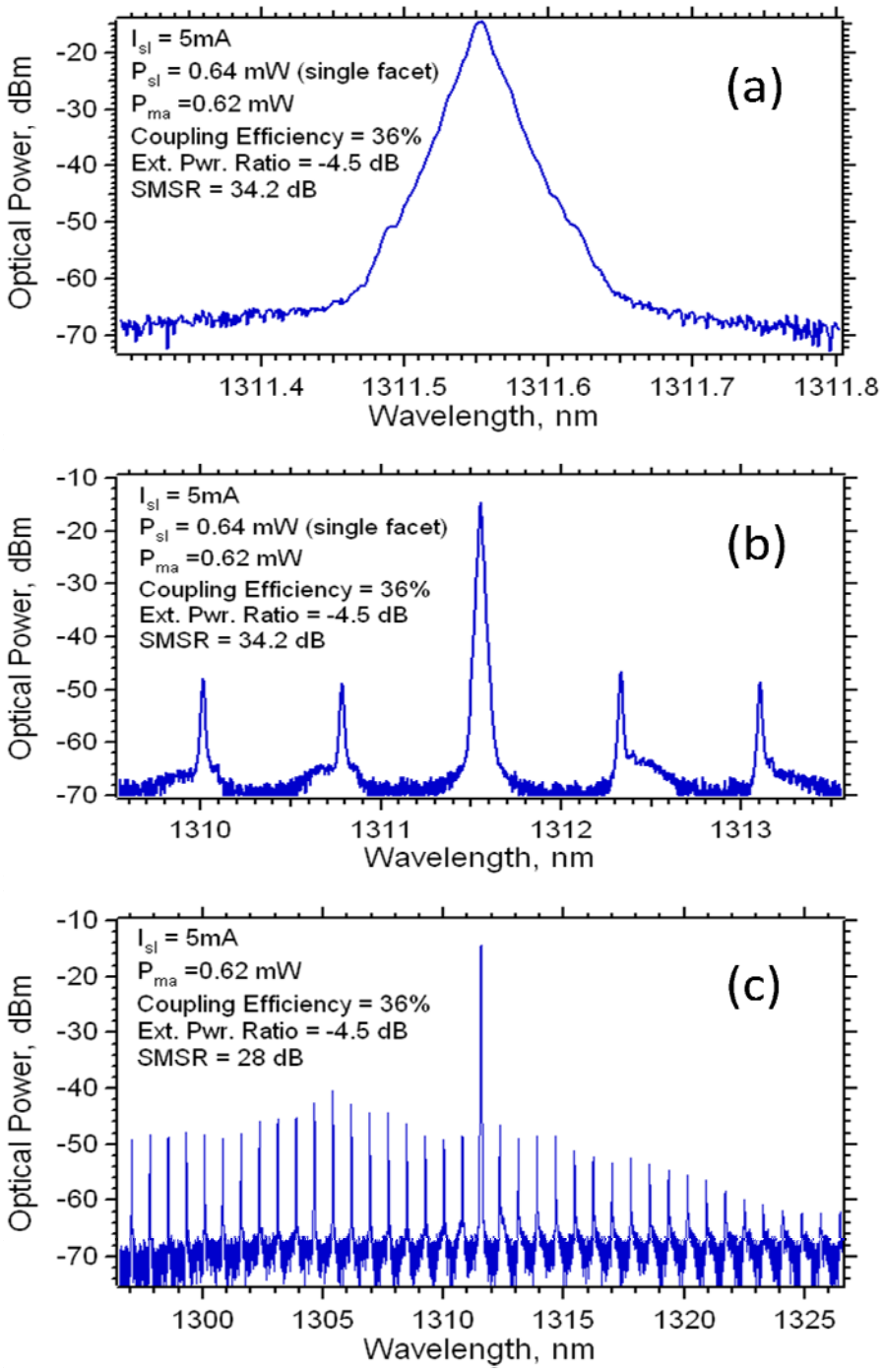

Figure 74. Experimental optical spectra for the quantum-dot laser under optical-injection at the onset of stable-locking at zero-detuning. The adjacent Fabry-Perot modes are suppressed beyond 30 dB, the criteria for stable locking; however, the 30-nm span shows that the distant Fabry-Perot modes are suppressed below the 30 dB threshold for stable-locking. The maximum injection strength is 17.4 GHz for all three cases. The wavelength spans are: (a) 0.5-nm; (b) 4-nm; and (c) 30-nm.

Although derived for the case where the nonlinear carrier relaxation rate is ignored, Erneux et al. and Gavrielides et al. introduce stability boundaries in terms of the *T*- and *P*- parameters and linewidth enhancement parameter [17], [20]. The analytical derivations of the expressions for steady-state locking (reverse-Hopf-bifurcation point) and Hopf-bifurcation boundaries are taken assuming a large *T*-parameter on the order of 100 – 1000. The applicability of the stability boundaries given by Erneux et al. is observed to be only an approximation for the slave laser analyzed in this work, as the *T*-parameter is calculated to be below 100 [17]. Expression (17) in Gavrielides et al. shows that the coupled system reaches the reverse-Hopf-bifurcation point and exhibits stable-locking for increased injected powers at an injection strength given by (116) [20].

$$\eta_{stable} = \left(\frac{P}{T} (\alpha^2 - 1) \right)^{1/2} = \frac{\Omega_{fr}}{\sqrt{2}} (\alpha^2 - 1)^{1/2} \tag{116}$$

From (116), the influence of the onset of stable-locking conditions is seen to be strongly dependent on the linewidth enhancement parameter, and conditions where the linewidth enhancement parameter is less than two will lead to sufficiently small threshold injection strengths for stable-locking making operation below this point difficult to observe experimentally. Gavrielides et al. also introduces an expression for a Hopf bifurcation line (ref. [20], expression (19)) describing the onset of unstable optical-injection (period-one, chaotic pulsations), which when zero-detuning is considered, reduces to (117).

$$\eta_{Hopf-Bifurcation} = \frac{(1+\alpha^2)^{1/2}}{(\alpha^2 - 1)} \left(\frac{(1+2P)^2}{T^2} \right)^{1/2} = \frac{(1+\alpha^2)^{1/2}}{(\alpha^2 - 1)} \gamma_{fr} \tag{117}$$

For cases of a sufficiently large γ_{fr} compared to Ω_{fr}, and small linewidth enhancement parameter, the $\eta_{Hopf\text{-}Bifurcation}$ value is greater than η_{stable}, resulting in the stable operation described by the single extrema electric field solution as simulated in illustrated in Figure 71. This particular case where $\eta_{stable} < \eta_{Hopf\text{-}Bifurcation}$ at zero-detuning is observed for the 3.8 mA case, where $\alpha = 1.6$, $\Omega_{fr} = 2\pi f_{fr} = 11.6$ GHz and $\gamma_{fr} = 11.9$ GHz. At a slave bias of 5 mA, this case ($\eta_{stable} < \eta_{Hopf\text{-}Bifurcation}$) is not met. The 5 mA forward and reverse bifurcation points equate to: $\eta_{Hopf\text{-}Bifurcation} = 10.4$ GHz and $\eta_{stable} = 16.7$ GHz, indicating that for a small range of injection strengths periodic pulsations will occur. The discrepancy between this conclusion and the bifurcation diagram in Figure 71 is believed to arise from the omission of the nonlinear parameter in (116) and (117), and from the initial approximations used in Gavrielides et al. to derive the expressions [20]. The significance of this particular approximation ($\eta_{stable} < \eta_{Hopf\text{-}Bifurcation}$) is an indicator that the highly damped nature of quantum-dot lasers are ideal for suppressing periodic pulsations leading to instabilities.

Next, the stability analysis illustrated in Figure 13, Chapter 2 based on the real part of the complex root of the polynomial function found in (57) at zero-detuning is implemented to theoretically investigate the quantum-dot laser's stability under optical-injection. The quantum-dot's stability is illustrated in Figure 75, where the impact of the slave laser linewidth enhancement parameter is emphasized. Negative values are a sign of stable-locking conditions and positive values are a sign of undamped oscillations indicative of unstable-locking. The conclusion from Figure 75 is that based on the free-running relaxation rates at 5 mA, only stable locking is predicted for linewidth enhancement parameters below 5 given the relatively large non-linear carrier relaxation

rate of the quantum-dot laser. The impact of the nonlinear carrier relaxation rate on modeling the stability of the optically-injected quantum-dot laser is illustrated in Figure 76. Both linewidth enhancement parameter cases in Figure 76 where the nonlinear carrier relaxation rate parameter is ignored predict that unstable operation will occur for a range of injection strengths. Stated in another way, the large nonlinear carrier relaxation rate of the quantum-dot laser suppresses unstable operation for fictitiously simulated increased linewidth enhancement parameter values. These results correspond to those based on the dimensionless rate equations illustrated in Figure 72.

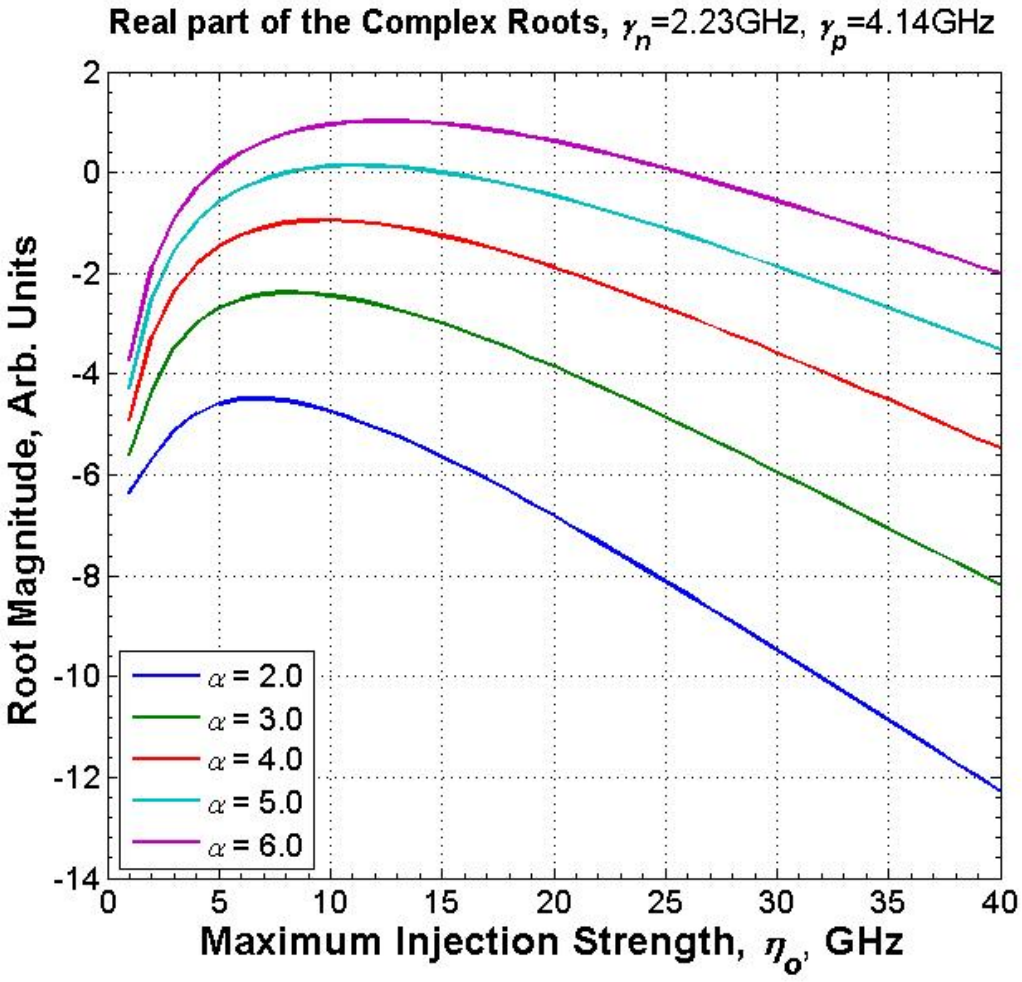

Figure 75. Quantum-dot stability analysis based on the real part of the complex roots of the polynomial function in (57) at zero-detuning emphasizing the impact of the slave laser linewidth enhancement parameter. Negative values are a sign of stable-locking conditions and positive values are a sign of undamped oscillations indicative of unstable-locking. The free-running quantum-dot laser values are for a bias current of 5 mA.

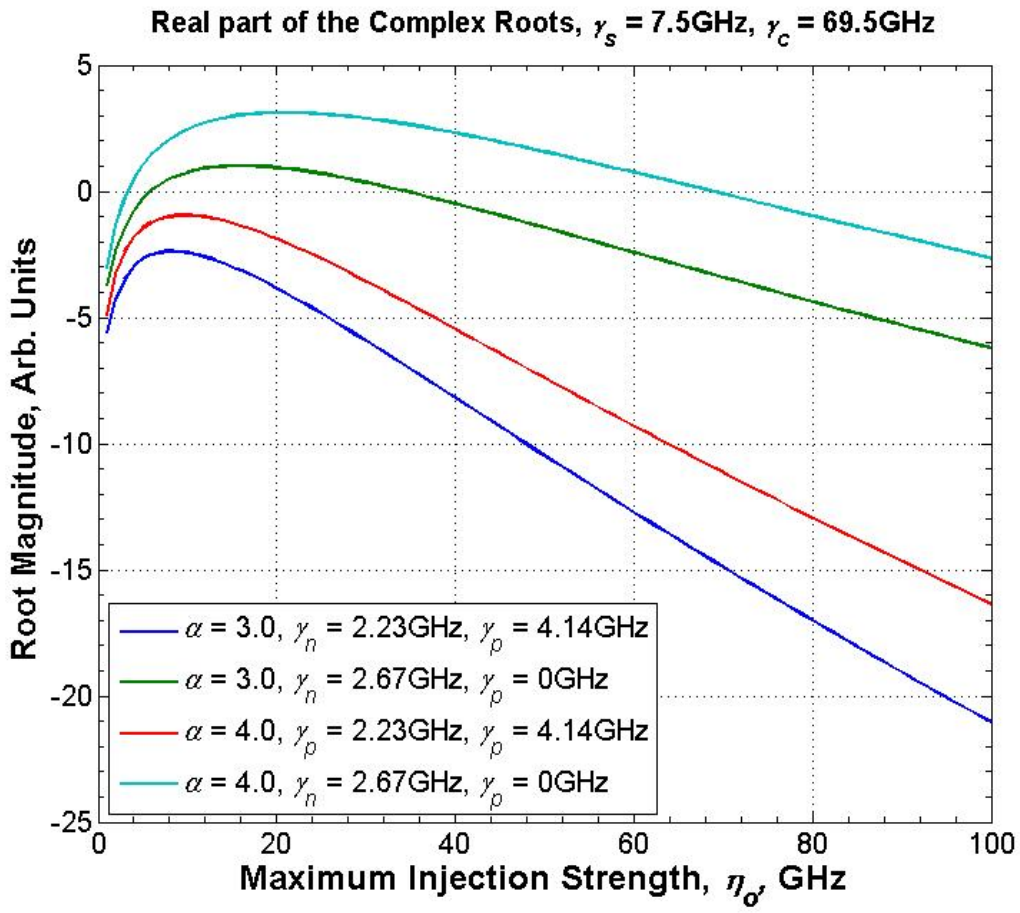

Figure 76. Impact of the nonlinear carrier relaxation rate on the predicted stability of the quantum-dot laser based on the real part of the complex roots of the polynomial function in (57) at zero-detuning.

6.2. Small-signal microwave modulation response

In this section, the experimentally collected small-signal modulation response is theoretically examined at weak injection strengths using the modulation response transfer function derived in Chapter 2. Figure 77 shows the normalized microwave modulation response where the slave laser is biased at 5 mA for injected master laser powers of 1.4 mW, 0.8 mW, and 0.5 mW under zero-detuning conditions. Figure 78 shows the

corresponding data without normalization and the associated least-square-fitting results for the modulation response curves using the transfer function in (118). Expression (118) is the equivalent of (51) with the second term in the denominator of (118) accounting for the parasitic RC and carrier transport effects; γ_t is the parasitic transport time.

$$\left|H(\omega)\right|^2 = \frac{(C/Z)^2(\omega^2+Z^2)}{(C-A\omega^2)^2+(B\omega-\omega^3)^2}\frac{1}{(1+(\omega/\gamma_t)^2)} \tag{118}$$

In Figure 78, the modulation efficiency is observed to decrease as the injected power is increased. The number of fitting parameters in the transfer function is reduced using the following: the phase-to-linewidth enhancement parameter constraint at zero-detuning given in (14); the phase-to-field enhancement factor relationship given in (34); and by holding the free-running relaxation rates given by γ_c, γ_s, γ_n, and γ_p constant (they are scaled under optical-injection using R_{FE}).

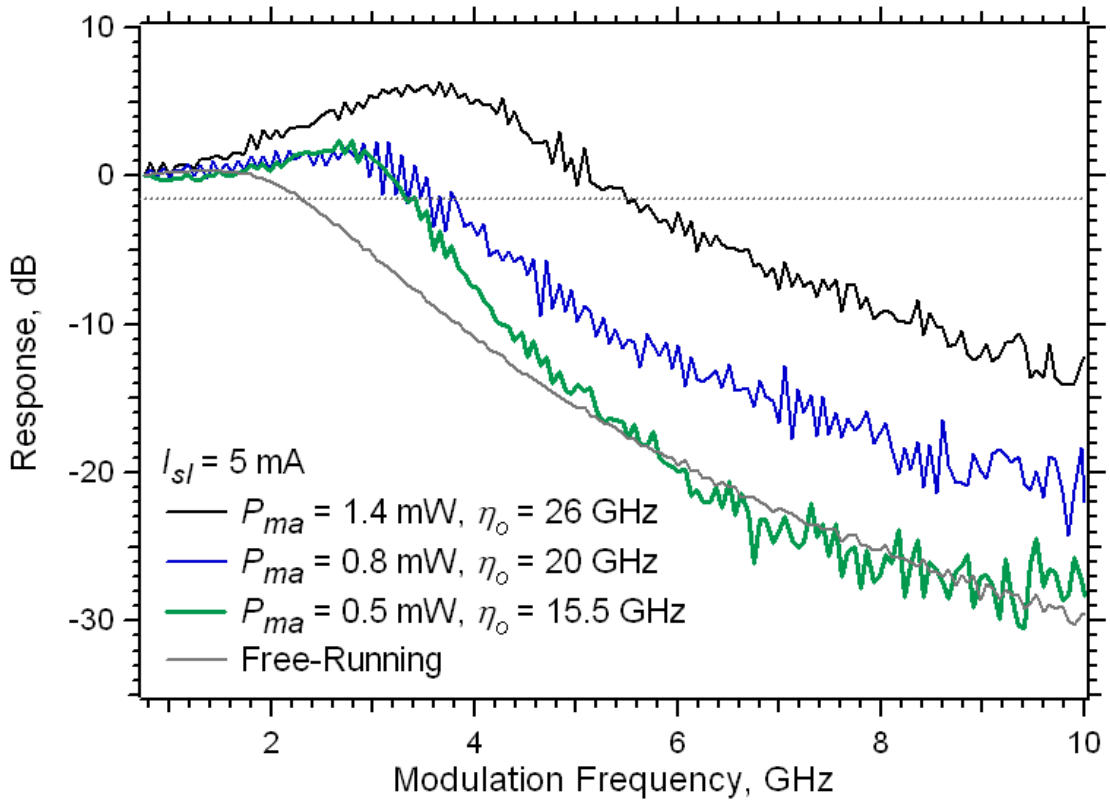

Figure 77. Normalized small-signal modulation response at zero-detuning.

The parameter values extracted by least-square-fitting the experimental data are shown in Table 16. The response curve for the 1.4 mW injected case could not be effectively least-square-fit with the zero-detuning phase-to-linewidth enhancement parameter constraint given in (14), and thus it was removed for this case. The fitting results for this curve show that the linewidth enhancement parameter dips extremely low. The linewidth enhancement parameter is found to decrease with increased injected powers based on the fitting results, a trend that was not observed in the linewidth enhancement parameter measurements based on the asymmetry of the stable-locking region. This result indicates that optical-injection can be used to manipulate the linewidth

enhancement parameter of the quantum-dot laser, a behavior that was not observed in the optically-injected quantum-dash laser.

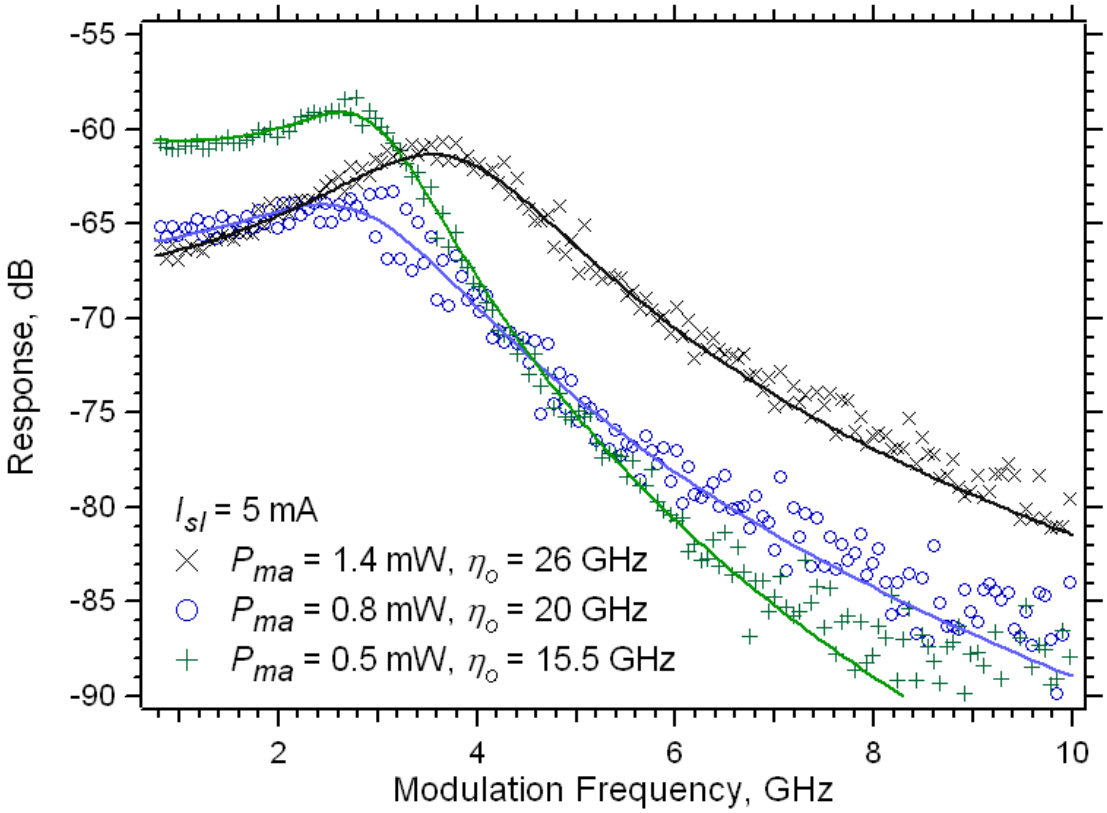

Figure 78. Small-signal modulation response at zero-detuning showing the least-square fitting results.

Table 16. Least-square-fitting results for the response curves in Figure 78.

P_{master} (mW)	Calculated η_o (GHz)	Least-Square-Fit η_o (GHz)	α	θ (rad)	γ_t (GHz)
0.5	15.5	9.6	2	-invTan(θ)	15
0.8	20	13	1.33	-invTan(θ)	58
1.4	26	20.8	0.167	-1.34	1000

A takeaway from the curve fitting results is the inaccuracy of the maximum injection strength, η_o, fitting the response curve versus the value calculated based on the internal cavity round trip time, facet reflectivity, and external power ratio. This discrepancy is attributed to inaccuracy in the measured coupling efficiency from the lensed fiber to the slave laser facet and/or inaccuracy in the facet reflectivity value. The emitting facet of the slave was HR-coated to have a reflectivity of 0.8. A small deviation in this value causes a relatively large variation in calculated injection strength. The high reflectivity of the injected slave facet is also noted to decrease the injected power efficiency according to (73).

Chapter 7. Conclusions and Future Work

7.1. Summary

In this work, the complete operation of optically-injected nanostructure lasers was investigated with emphasis on the contribution of their characteristically large nonlinear gain component. Explicitly accounting for the nonlinear gain of nanostructure lasers through the nonlinear carrier relaxation rate and nonlinear gain compression coefficient is found to enhance the capability of modeling optically-injected quantum-dash and quantum-dot Fabry-Perot devices.

First, a predictive model describing the small-signal microwave modulation response of the optically-injected nanostructure laser was derived and used to extract the operating parameters from experimentally collected modulation response curves for varied degrees of injection strength and frequency detuning levels. Under zero-detuning conditions, 3-dB bandwidth improvements greater than 3X were observed for the quantum-dash laser. Next, the novel small-signal modulation response function was used to least-squares-fit experimental data sets collected for varied quantum-dash slave laser bias conditions; the results showed that the quantum-dash laser's linewidth enhancement parameter varied less as a function of bias current conditions under zero-detuning than measured using the injection-locking technique discussed in section 4.2. The results also showed that the linewidth enhancement parameter varied minimally as the injection strength was increased; this finding was contrary to the linewidth enhancement parameter values reported in section 4.2 measured using the injection-locking technique, where α was observed to decrease as the injected power was increased. These finding are

concluded to arise from the injection-locking measurement technique's lack of dependence on the detuning frequency and thus the linewidth enhancement parameter's dependence on the detuning frequency.

Second, a dimensionless/normalized approach to theoretically evaluate the operational state (i.e. stable locking, period-one, period-doubling, or chaos) of an optically-injected nanostructure laser as a function of the injection strength and/or the detuning frequency for varied slave laser bias cases was described. The normalized model reformulated the rate equations describing optically-injected lasers into a dimensionless form that was advantageous compared with other methods due to its fundamental parameter scaling approach that facilitated the comparison of one laser to another. The model derived here is unique in that it includes the impact of the nonlinear carrier relaxation rate. The slave laser linewidth enhancement parameter and the nonlinear carrier relaxation rate are observed to have a strong impact on the level of stability exhibited by the optically-injected laser at low injected field ratios.

The operational stability map of the quantum-dash laser under optical-injection was observed to have a suitably large period-one parameter space; this behavior was concluded to be due to the relatively large nonlinear and spontaneous carrier relaxation rates and relatively small linewidth enhancement parameter. The resonance frequency of the optically-injected quantum-dash system in the period-one operational state was able to be enhanced over a wide range from 4 to 20 GHz. Additionally, the resonance frequency enhancement was well-approximated using the steady-state solution to the full rate equations derived with the novel small-signal modulation response function presented in this work. Overall, the large tunability of the undamped period-one

resonance suggests that the optically-injected quantum-dash slave laser operating at 1550-nm is applicable for photonic applications such as radio-over-fiber.

Lastly, it was found that the quantum-dot laser was highly stable under optical-injection. Contrary to the optically-injected quantum-dash laser, the optically-injected quantum-dot laser showed no signs of undamped relaxation oscillations as the injection strength and/or detuning frequency were varied; this highly stable finding indicated that the optically-injected quantum-dot laser is well-suited for implementation in wideband transmitters. One discrepancy between the theoretical predictions and experimental observations for the quantum-dot laser is the failure of the theoretical model to predict the unlocked operation in reference to adjacent Fabry-Perot modes at low injection strengths; this result shows the weakness of the single mode rate equations in modeling the complete operational space of a multi-mode slave laser.

7.2. Suggestions for Future Work

Previous works found in the literature have suspected that the slave laser linewidth enhancement parameter varies as a function of injection strength and/or detuning frequency [59]. This relationship cannot be determined using the injection-locking technique described in this work and thus it is suggested that FM/AM response ratio technique and/or time-resolved chirp measurements should be employed to fully understand the dependence of the linewidth enhancement parameter on the injection strength and detuning [7], [46]. Such an understanding would improve the applicability of the predictive tools derived in this work, as the linewidth enhancement parameter is theoretically predicted to have a strong impact on both the small-signal microwave

modulation response of an injection-locked laser and the nonlinear dynamics observed under weak injection strengths.

Next, noise measurements of the AM-to-FM conversion microwave signal would assist in determining the period-one oscillation state's capabilities as a tunable photonic oscillator. Bit error rate tests with the injection-locked quantum-dash and quantum-dot lasers would highlight the nanostructure lasers' potential for implementation in wideband transmitters.

Additionally, the injection-locked modulation response suffers a degraded modulation efficiency. The two-section gain-lever laser has been reported to improve modulation efficiency over the free-running single section laser [62]. These two findings open the possibility for an optically-injected two-section gain lever laser, where the bias characteristics of the gain lever device can be manipulated to yield an ideal slave laser to be optically-injected.

Lastly, this work combined with the optical-injection research over the past two decades shows that the optical-injection architecture is poised to transition from theory and lab-bench setups to packaged, engineered products for the market. The short-term step may be a dual butterfly packaged system with an optical-isolator in between the master and slave, reducing the size of the bench top footprint of the test setup and making headway towards a marketable design. The desired end result for the optical-injection architecture is a single-chip monolithic type design where the master and slave laser are butt-coupled to one another.

Chapter 8. References

[1] Kimura, T., "Coherent Optical Fiber Transmission," *IEEE Journal of Lightwave Technology*, LT-5(4), 414-428 (1987).

[2] Williamson, R. C., and Esman, R., "RF Photonics," *IEEE Journal of Lightwave Technology,* 26(9), 1145-1153 (2008).

[3] Seeds, A. J., "Microwave Photonics," *IEEE Transactions on Microwave Theory and Techniques*, 50(3), 877-887 (2002).

[4] Lester, L. F., Schaff, W. J., Offsey, S. D., Eastman, L. F., "High-speed Modulation of InGaAs – GaAs Strained-Layer Multiple-Quantum-Well Lasers Fabricated by Chemically Assisted Ion-Beam Etching," *IEEE Photonics Technology Letters*, 3(5), 403-405 (1991).

[5] Matsui, Y., Murai, H., Arahira, S., Kutsuzawa, S., and Ogawa, Y., "30 GHz bandwidth 1.55 μm strain-compensated InGaAlAs-InGaAsP MQW laser," *IEEE Photonics Technology Letters*, 9(1), 25-27 (1997).

[6] Fathpour, S., Mi, Z., and Bhattacharya, P., "High-speed quantum-dot lasers," *Journal of Physics D: Applied Physics*, 38, 2103-2111 (2005).

[7] Tucker, R., S., "High-Speed Modulation of Semiconductor lasers," *IEEE Journal of Lightwave Technology*, LT-3(6), 1180-1192 (1985).

[8] Su, H., Lester, L. F., "Dynamic properties of quantum-dot distributed feedback lasers: high speed, linewidth and chirp," *Journal of Physics D: Applied Physics*, 38, 2112-2118 (2005).

[9] Mogensen, F., Olesen, H., and Jacobsen, G., "Locking Conditions and Stability Properties for a Semiconductor Laser with External Light Injection," *IEEE Journal of Quantum Electronics*, 21(7), 784-793 (1985).

[10] Petitbon, I., Gallion, P., Debarge, G., and Ghabran, C., "Locking Bandwidth and Relaxation Oscillation of an Injection-Locked Semiconductor Laser," *IEEE Journal of Quantum Electronics*, 24(2), 148-154 (1988).

[11] Simpson, T. B., Liu, J. M., and Gavrielides, A., "Small-Signal Analysis of Modulation Characteristics in a Semiconductor Laser Subject to Strong Optical Injection," *IEEE Journal of Quantum Electronics*, 32(8), 1456-1468 (1996).

[12] Simpson, T. B., and Liu, J. M., "Enhanced Modulation Bandwidth in Injection-Locked Semiconductor Lasers," *IEEE Photonics Technology Letters*, 9(10), 1322-1324 (1997).

[13] Liu, J. M., Chen, H. F., Meng, X. J., and Simpson, T. B., "Modulation Bandwidth, Noise, and Stability of a Semiconductor Laser Subject to Strong Injection Locking," *IEEE Photonics Technology Letters*, 9(10), 1325-1327 (1997).

[14] Chan, S. C., Hwang, S. K., and Liu, J. M., "Period-one oscillation for photonic microwave transmission using an optically-injected semiconductor laser," *Optics Express*, 15(22), 14921-14933 (2007).

[15] Hwang, S. K., Chen, H. F., and Lin, C. Y., "All-optical frequency conversion using nonlinear dynamics of semiconductor lasers," *Optics Letters*, 34(6), 812-814 (2009).

[16] Liu, J. M., Applications of Nonlinear Dynamics. Berlin/ Heidelberg: Springer, 341-354 (2009).

[17] Erneux, T., Kovanis, V., Gavrielides, A., and Alsing, P. M., "Mechanism for period-doubling bifurcation in a semiconductor laser subject to optical injection," *Physical Rev. A*, 53(6), 4372-4380 (1996).

[18] Simpson, T. B., Liu, J. M., Gavrielides, A., Kovanis, V., and Alsing, P. M., "Period-doubling cascades and chaos in a semiconductor laser with optical injection," *Physical Rev. A*, 51, 5, 4181-4185 (1995).

[19] Simpson, T. B., "Mapping the nonlinear dynamics of a distributed feedback semiconductor laser subject to external optical injection," *Optics Communications*, 215, 135-151 (2003).

[20] Gavrielides, A., Kovanis, V., and Erneux, T., "Analytical stability boundaries for a semiconductor laser subject to optical injection," *Optics Communications*, 136, 253-256 (1997).

[21] Hwang, S. K., and Liu, J. M., "Dynamical characteristics of an optically-injected semiconductor laser," *Optics Communications*, 183, 195-205 (2000).

[22] Eriksson, S., "Dependence of the experimental stability diagram of an optically-injected laser on the laser current," *Optics Communications*, 210, 343-353 (2002).

[23] Pochet, M., Naderi, N. A., Terry, N., Kovanis, V., and Lester, L. F., "Dynamic behavior of an injection-locked quantum-dash Fabry-Perot laser at zero-detuning," *Optics Express*, 17(23), 20623-20630 (2009).

[24] Chrostowski, L., Faraji, B., Hofmann, W., Amann, M. C., Wieczorek, S., and Chow, W. W., "40 GHz Bandwidth and 64 GHz Resonance Frequency in Injection-Locked 1.55 μm VCSELs," *IEEE Journal of Selected Topics in Quantum Electronics*, 13(5), 1200-1208 (2007).

[25] Lau, E. K., Zhao, X., Sung, H. K., Parekh, D., Chang-Hasnain, C., and Wu, M. C., "Strong optical injection-locked semiconductor lasers demonstrating > 100-GHz resonance frequencies and 80-GHz intrinsic bandwidths," *Optics Express*, 16(9), 6609-6618 (2008).

[26] Hwang, S. K., Liu, J. M., and White, J. K., "Characteristics of Period-One Oscillations in Semiconductor Lasers Subject to Optical Injection," *IEEE Journal of Selected Topics in Quantum Electronics*, 10(5), 974-981 (2004).

[27] Pochet, M., Naderi, N. A., Kovanis, V., and Lester, L. F., "Optically-injected Quantum-dash Lasers at 1550 nm Employed as Highly Tunable Photonic Oscillators," Conference for Lasers and Electro-Optics, San Jose, Ca (2010).

[28] Pochet, M., Naderi, N. A., Li, Y., Kovanis, V., and Lester, L. F., "Tunable Photonic Oscillators Using Optically-injected Quantum-Dash Diode Lasers," *IEEE Photonics Technology Letters*, 22(11), 763-765 (2010).

[29] Nirmalathas, C., Lim, C., Novak, D., and Waterhouse, R. B., "Progress in Millimeter-Wave Fiber-Radio Networks," *Annals of Telecommunications*, 56(1-2), 27-28 (2001).

[30] Bimberg, D., Kirstaedter, N., Ledentsov, N. N., Alferov, Zh., I., Kop'ev, P. S., Ustinov, "InGaAs-GaAs Quantum-Dot Lasers", *IEEE Journal of Selected Topics in Quantum Electronics*, 3(2), 196-204 (1997).

[31] Bhattacharya, P., Klotzkin, D., Qasaimeh, O., Zhou, W., Krishna, S., Zhu, D., "High-Speed Modulation and Switching Characteristics of In(Ga)As-Al(Ga)As Self-Organized Quantum-Dot Lasers," *IEEE Journal of Selected Topics in Quantum Electronics*, 6(3), 426-438 (2000).

[32] Asada, M., Miyamoto, Y., Suematsu, Y., "Gain and the Threshold of Three-Dimensional Quantum-Box Lasers," *IEEE Journal of Quantum Electronics*, QE-22(9), 1915-1921 (1986).

[33] Newell, T. C., Bossert, D. J., Stintz, A., Fuchs, B., Malloy, K. J., and Lester, L. F., "Gain and Linewidth Enhancement Factor in InAs Quantum-Dot Laser Diodes," *IEEE Photonics Technology Letters*, 11(12), 1527-1529 (1999).

[34] Kondratko, P. K., Chuang, S. L., Walter, G., Chung,T., and Holonyak, N., Jr., "Observations of near-zero linewidth enhancement parameter in a quantum-well coupled quantum-dot laser," Applied Physics Letters, 83(23), 4818-4820 (2003).

[35] Coldren, L. A., and Corzine, S. W., *Diode Lasers and Photonic Integrated Circuits*, New York: John Wiley & Sons, Inc., 187-206 (1995).

[36] Murakami, A., Kawashima, K., and Atsuki, K., "Cavity Resonance Shift and Bandwidth Enhancement in Semiconductor Lasers with Strong Light Injection," *IEEE Journal of Quantum Electronics*, 39(10), 1196-1204 (2003).

[37] Liu, J. M., Photonic Devices, Cambridge: Cambridge University Press, 909-912 (2005)

[38] Lau, E. K., Sung, H. K., and Wu, M. C., "Frequency Response Enhancement of Optical-injectionLocked Lasers," *IEEE Journal of Quantum Electronics*, 44(1), 90-99 (2008).

[39] Lau, E. K., Wong, L. J., and Wu, M. C., "Enhanced Modulation Characteristics of Optical Injection-Locked Lasers: A Tutorial," *IEEE Journal of Selected Topics in Quantum Electronics*, 15(3), 618-633 (2009).

[40] Naderi, N. A., Pochet, M., Grillot, F., Terry, N., Kovanis, V., and Lester, L. F., "Modeling the Injection-Locked Behavior of a Quantum-dash Semiconductor Laser," *IEEE Journal of Selected Topics in Quantum Electronics*, 15(3), 563-571 (2009).

[41] Goulding, D., Hegarty, S. P., Rasskazov, O., Melnik, S., Hartnett, M., Greene, G., McInerney, J. G., Rachinskii, D., and Huyet, G., "Excitability in a Quantum-dot Semiconductor Laser with Optical Injection," *Physical Review Letters*, 98, 153903-1-153903-4 (2007).

[42] O'Brien, D., Hegarty, S. P., Huyet, G., McInerney, J. G., Kettler, T., Laemmlin, M., Bimberg, D., Ustinov, V. M., Zhukov, A. E., Mikhrin, S. S., and Kovsh, A. R., "Feedback sensitivity of 1.3μm InAs/GaAs quantum-dot lasers," *Electronic Letters*, 39, 1819-1820 (2003).

[43] Huyet, G., O'Brien, D., Hegarty, S. P., McInerney, J., Bimberg, D., Ribbat, C., Ustinov, V. M., Mikhrin, S. S., Kovsh, A. R., and Uskov, A. V., "Reduced sensitivity to external feedback in quantum-dot lasers," *Proceeding of the SPIE*, 5631(24), (2004)

[44] Liu, G., Jin, X., and Chuang, S. L., "Measurement of linewidth enhancement parameter of semiconductor lasers using an injection-locking technique," *IEEE Photonic Technology Letters*, 13(5), 430–432 (2001).

[45] Lau, E. K., "High-Speed Modulation of Optical Injection-Locked Semiconductor Lasers," *PhD Dissertation*, UC Berkeley (2006).

[46] Harder, C., Valhala, K., and Yariv, A., "Measurement of the linewidth enhancement parameter α of semiconductor lasers," *Applied Physics Letters*, 42(4), 328-330 (1983).

[47] Melnik, S., Huyet, G., and Uskov, A. V., "The linewidth enhancement parameter α of quantum-dot semiconductor lasers," *Optics Express*, 14(7), 2950-2955 (2006).

[48] Villafranca, A., Giuliani, G., Donati, S., and Garces, I., "Investigation on the linewidth enhancement parameter of multiple longitudinal mode semiconductor lasers," *Proceedings of the SPIE*, 6997, 699719.1-699719.8 (2008).

[49] Pochet, M., Naderi, N. A., Grillot, F., Terry, N., Kovanis, V., and Lester, L. F., "Methods for Improved 3-dB bandwidth in an Injection-Locked QDash Fabry Perot Laser @ 1550nm," *Conference for Lasers and Electro-Optics*, CTuQ4 (2009).

[50] Chrostowski, L., "Optical-injection Locking of Vertical Cavity Surface Emitting Lasers," *PhD Dissertation*, UC Berkeley (2004).

[51] Pochet, M., Naderi, N. A., Grillot, F., Terry, N., Kovanis, V., and Lester, L. F., "Modulation Response of an Injection Locked Quantum-Dash Fabry Perot Laser at 1550nm," *Proceedings of the SPIE*, 7211, 721107-1 – 721107-9 (2009).

[52] Murakami, A., "Phase Locking and Chaos Synchronization in Injection-Locked Semiconductor lasers," *IEEE Journal of Quantum Electronics*, 39(3), 438-447 (2003).

[53] Kovanis, V., Gavrielides, A., Simpson, T. B., and Liu, J. M., “Instabilities and chaos in optically-injected semiconductor lasers,” *Applied Physics Letters*, 67(19), 2780-2782 (1995).

[54] Wieczorek, S., Krauskopf, B., Simpson, T. B., and Lenstra, D., “The dynamical complexity of optically-injected semiconductor lasers,” *Physical Reports*, 416, 1-128 (2005).

[55] Bonatto, C., Gallas, J. A. C., “Accumulation horizons and period adding in optically-injected semiconductor lasers,” *Physical Review E*, 75, 055204-1 – 055204-4 (2007).

[56] Grillot, F., Naderi, N. A., Pochet, M., Lin, C. Y., and Lester, L. F., “Variation of the feedback sensitivity in a 1.55 μm InAs/InP quantum-dash Fabry–Perot semiconductor laser,” *Applied Physics Letters*, 93, 191108-1—191108-3 (2008).

[57] Wong, Y. C. A., Shore, K. A., “Influence of nonlinear gain on intrinsic bandwidth of quantum well and strained layer semiconductor lasers,” *IEE Proceedings-J*, 138(6), 413-419 (1991).

[58] Takahashi, T., Arakawa, Y., “Nonlinear Gain Effects in Quantum Well, Quantum-Well Wire, and Quantum Well Box Lasers,” *IEEE Journal of Quantum Electronics*, 27(6), 1824-1829 (1991).

[59] Nguyen, Q. T., Besnard, P., Vaudel, O., Shen, A., Duan, G. H., "Strong dependence of the Linewidth Enhancement Factor onto an externally injected optical signal for locked Fabry-Perot laser diodes," The Conference on Lasers and Electro-Optics- Europe (2009).

[60] Ukhanov, A. A., “Study of the Carrier-Induced Optical Properties in III-V Quantum Confined Laser Nano-Structures,” *PhD Dissertation*, The University of New Mexico (2004).

[61] Lin, C., and Mengel, F., "Reduction of frequency chirping and dynamic linewidth in high-speed directly-modulated semiconductor lasers by injection locking," *Electronics Letters*, 20, 1073-1075 (1984).

[62] Grillot, F., Naderi, N. A., Pochet, M., Lin, C. Y., Besnard, P., Dziak, C., Xin, Y. C., Kovanis, V., and Lester, L. F., "Tuning of the critical feedback level in 1.55-μm quantum-dash semiconductor laser diodes," *The Institution of Engineering and Technology,* 3(6), 242-247 (2009).

[63] Naderi, N., Li, Y., Dziak, C., Xin, Y. C., Kovanis, V., and Lester, L. F., "Quantum-dot gain-lever laser diode," *Conference Proceedings - Lasers and Electro-Optics Society Annual Meeting-LEOS,* 52-53 (2007).

Appendix A. Relevant Matlab Code

The following is used to call the small-signal modulation response and observe the impact of varied injection strengths and/or slave laser parameters:

```
5/27/10 2:52 PM  C:\Documents and Settings\Owner\Desktop\PTLPlot.m                1 of 2

clear;
clc;
clf;

% with this code, we can examine the effect of indivudual free-running
% parameters with increasing injected power at 0dt

endf = 20;

f = linspace(0, endf, 100);
DC1 = 0;

alpha = 3; %linewidth enhancement parameter

eta1 = 62; Pinj1 = 3.1; %injection strength and associated injected power
eta2 = 75; Pinj2 = 4.5;
eta3 = 87; Pinj3 = 6;
eta4 = 106; Pinj4 = 9;
eta5 = 123; Pinj5 = 12;
eta6 = 137; Pinj6 = 15;
eta7 = 146; Pinj7 = 17;

tauc = 0.012; % RC transport time
ep = 0.001; % nonlinear gain compression coefficient
gammat = 1/tauc;

%set various data strings to call with the function
data1 = [DC1 eta1 alpha tauc ep Pinj1];
data2 = [DC1 eta2 alpha tauc ep Pinj2];
data3 = [DC1 eta3 alpha tauc ep Pinj3];
data4 = [DC1 eta4 alpha tauc ep Pinj4];
data5 = [DC1 eta5 alpha tauc ep Pinj5];
data6 = [DC1 eta6 alpha tauc ep Pinj6];
data7 = [DC1 eta7 alpha tauc ep Pinj7];

PTL1 = my_PTL0dt(data1, f);
PTL2 = my_PTL0dt(data2, f);
PTL3 = my_PTL0dt(data3, f);
PTL4 = my_PTL0dt(data4, f);
PTL5 = my_PTL0dt(data5, f);
PTL6 = my_PTL0dt(data6, f);
PTL7 = my_PTL0dt(data7, f);

plot(f, PTL1, '--k', f, PTL2, '-b', f, PTL3,'r*', f, PTL4,'-.g',...
    f, PTL5, 'm--', f, PTL6,'k-', f, PTL7,'r-', f, (PTL1*0 - 3),'-k', 'Linewidth', 2)
xlabel('Modulation Frequency, GHz','FontSize',14);
ylabel('Modulation Response, dB','FontSize',14);
hold on;
box on;
grid on;
textString1 = ['\bf\it\alpha \rm =' num2str(alpha)...
    ',  \bf\it\gamma\it\bf_t \rm= ' num2str(gammat,2) 'GHz'];
```

The following is the small-signal response function:

5/27/10 2:52 PM C:\Documents and Settings\Owner\Desktop\my_PTL0dt.m 1 of 1

```
function FullModel = my_PTL0dt(param,f)

%Pass in the relevant parameters and their associated limits
DC =  param(1);
eta = param(2);
alpha = param(3);
tau_c = param(4);
ep = param(5);
Pinj = param(6);

%fixed free-running laser parameters for a given bias current
gamma_n = 1.12; %differential carrier relaxation rate
gamma_c = 333.3; %photon decay rate rate
gamma_p = 3.38; %nonlinear carrier relaxation rate
gamma_s = 4.5; %spontaneous carrier relaxation rate
Psl = 3.14; %free-running slave plower
kc = 85.7; %coupling coefficient

% phase to linewidth enhancement parameter relationship at zero-detuning
phi = -atan(alpha);

% scale the terms with injection strength
gamma_n = gamma_n.*(1 + ep*Psl)./(1 + ep*(Psl+ 0.7*Pinj));
gamma_p = gamma_p.*((1 + ep*Psl).^2)./((1 + ep*(Psl + 0.7*Pinj)).^2);

wr = sqrt(gamma_n*gamma_c + gamma_p*gamma_s);  % compute the emhanced
                                               % relaxation oscillation frequency
%cubic equation for solving Rfe based on injection strength
RfeExp = [wr^2 - 2*gamma_n*eta*cos(phi) -wr^2 ...
    (gamma_s*gamma_p*(eta^2)/(kc^2) - 2*gamma_s*eta*cos(phi))];
%pull out the max, real root
Rfe = max(roots(RfeExp));

% compute parametroc terms
gamma_th = 2.*(eta./Rfe)*cos(phi);
Z = -(eta./Rfe)*cos(phi) + (alpha*(eta./Rfe).*sin(phi));
A = gamma_s + gamma_p*(Rfe.^2) + gamma_n*(Rfe.^2) + gamma_th;
B = (eta./Rfe).^2 + gamma_c*gamma_n.*(Rfe.^2) + gamma_p*gamma_s.*(Rfe.^2)...
    + gamma_s.*gamma_th - alpha*gamma_p.*(Rfe.^2).*(eta./Rfe)*sin(phi)...
    + gamma_p.*(Rfe.^2).*(eta./Rfe)*cos(phi);
C = ((eta./Rfe).^2).*(gamma_n.*(Rfe.^2) + gamma_s) - Z.*...
    (gamma_n.*(Rfe.^2)*gamma_c + gamma_p.*(Rfe.^2)*gamma_s - gamma_n.*(Rfe.^2).*gamma_th);

numer = ((C/Z).^2).*(4*(pi^2)*f.^2 + Z.^2);
denom = ((C - A*4*(pi^2)*(f.^2)).^2) + ((B*2*(pi)*(f) - 8*(pi^3)*(f.^3)).^2);

denom_tauC = denom.*(1 + (2*pi*f*tau_c).^2);

FullModel = DC + 10*log10(numer./denom_tauC);
```

The following is used to least-squares-fit experimental data with the small-signal modulation response function on the previous page:

```
5/27/10 3:06 PM  C:\Documents and Settings\Owner\Desktop\QDashFit.m                1 of 1

clear;
clc;
clf;
%18.07 289
%load the experimental data (y-data only)
load nA80mW2.txt;
y = transpose(nA80mW2(10.289,1));
%create the corresponding frequency data
x = linspace(.8068, 18.07, 280);
% input the nominal injection strength calculated using externally measured
% master and slave powers
eta_nom = 51.8;

% input IC's in the order [dc eta alpha tauc Pinj]
initialConditions = [-58 eta_nom 3.5 0.015 0.06];
lb = [-65  eta_nom*0.95  0.1 0.0001 0.0001]; %set lower bounds
ub = [-47.0  eta_nom*1.08  8.0 0.04 0.01]; %set upper bounds

% call the least-squares-fit function using the custom function derived
[newParameters, error] = lsqcurvefit(@my_PTL0dt, initialConditions, x, y, lb, ub);
%generate a curve based on the least-squares-fit parameters extracted
y2 = my_PTL0dt(newParameters, x);

PW_x = transpose(x);
PW_y2 = transpose(y2);
PW_y = transpose(y);

plot(x,y, x, y2,'Linewidth', 2)
textString1 = [' DC = ' num2str(newParameters(1),2) 'dB  \eta_o = '...
    num2str(newParameters(2),3) ' GHz'];
textString2 = [' \alpha = '  num2str(newParameters(3),2),', \tau_c = '...
    num2str(newParameters(4),2)];
textString3 = [' error = ' num2str(error(1),3), ', \epsilon_p = '...
    num2str(newParameters(5),2),];
xlabel('Frequency, GHz','FontSize',13);
ylabel('Response, dB','FontSize',13);
hold on;
box on;
TITLE['QDash @ 0dt, 80mA','FontSize',13)
text(2, -62, textString1,'FontSize',13)
text(2, -66, textString2,'FontSize',13)
text(2, -69, textString3,'FontSize',13)
% text(1.2, -79, textString4,'FontSize',11)
grid on
axis tight
ylim([ 75  35])
```

Code for Figure 13 and Figure 14:


```
clear;
clc;
clf;

start = 1;
eta = start;
Y = 1;

%free-running slave laser damping rates
gamma_n = 1.34;
gamma_c = 333.3;
gamma_p = 3.98;
gamma_s = 4.5;

alpha = 3; %linewidth enhancement parameter

while eta < 151

%phase to linewidth enhancement parameter relationship
phi = -atan(alpha);

wr = sqrt(gamma_n*gamma_c + gamma_p*gamma_s);

%determine Rfe based on injection strength
P1 = gamma_n*eta*cos(phi);
P2 = -3*(wr^4) - 4*P1.^2;
P3 = 18*P1*(wr^4) + 54*gamma_s*eta*(wr^4)*cos(phi) + 16*(P1.^3);
S1 = 2*P1./(3*(wr^2));
s2num = -(2^(1/3)).*P2;
s2den = 3*(wr^2).*((P3 + sqrt(4*(P2.^3) + (P3.^2))).^(1/3));
S2 = s2num/s2den;
S3 = (1/((3*2^(1/3))*(wr^2))).*((P3 + sqrt(4*(P2.^3) + (P3.^2))).^(1/3));
Rfe = S1 + S2 + S3;

gamma_th = 2.*(eta./Rfe)*cos(phi);

Z = -(eta./Rfe).*cos(phi) + (alpha*(eta./Rfe).*sin(phi));
A = gamma_s + gamma_p*(Rfe.^2) + gamma_n*(Rfe.^2) + gamma_th;
B = (eta./Rfe).^2 + gamma_c*gamma_n.*(Rfe.^2) + gamma_p*gamma_s.*(Rfe.^2) + gamma_s.*gamma_th - alpha*gamma_p.*(Rfe.^2).*(eta./Rfe)*sin(phi)...
    + gamma_p.*Rfe.*(eta./Rfe)*cos(phi);
C = ((eta./Rfe).^2).*(gamma_n.*(Rfe.^2) + gamma_s) - Z.*(gamma_n.*(Rfe.^2)*gamma_c + gamma_p.*(Rfe.^2)*gamma_s - gamma_n.*(Rfe.^2).*gamma_th);
detl = [1 A B C];

detnum = [-1 +Z];
numroots = roots(detnum);

rdetl = roots(detl);
rdetltrans = transpose(rdetl);
rootl(Y) = abs(rdetltrans(:, 1));
rootlreal(Y) = real(rdetltrans(:, 1));
```

```
root1comp(Y) = imag(rdet1trans(:, 1));
root1full(Y) = rdet1trans(:, 1);
root2(Y) = abs(rdet1trans(:, 2));
root2real(Y) = real(rdet1trans(:, 2));
root2full(Y) = rdet1trans(:, 2);
root3(Y) = rdet1trans(:, 3);
root3comp(Y) = imag(rdet1trans(:, 3));

Zt(Y) = Z;

etax(Y) = eta;
etaxRfe(Y) = eta/Rfe;
plA(Y) = A;
sqB(Y) = sqrt(B);
cuC(Y) = C.^(1/3);

Y = Y + 1;
eta = eta + 1;
end

root1fulltra = transpose(root1full);

plot(etax, root1, etax, abs(root3), etax, -Zt, etax, etax, etax, etaxRfe, 'Linewidth', 2)
xlabel('Maximum Injection Strength, \it\bf\eta_o,\rm\bfGHz','FontSize',↙
16,'fontweight','b');
legend('Complex Roots', 'Real Root', 'Zero (-Z)', '\it\bf\eta_o',↙
'\it\bf\eta_o/\itR_F_E','Location','NorthWest")
ylabel('\bfAbsolute Value, GHz','FontSize',16);
title('\it\bf\alpha\rm\bf = 1, \it\bf\gamma_n \rm\bf= 1.34GHz, \it\bf\gamma_p \rm\bf= 3.98↙
GHz, \it\bf\gamma_s \rm\bf= 4.5GHz, \it\bf\gamma_c \rm\bf= 333.3GHz','FontSize',↙
15,'fontweight','b')
hold on;
box on;
grid on;
set(gca,'FontSize',14)
set(gca, 'xminortick', 'on','yminortick', 'on");
ylim([0 150])
```

Code for Figure 15:

```
5/28/10 10:55 AM  C:\Documents and Settings\Owner\Deskto...\PlotRealPolevsPhaseB.m   1 of 2

clear;
clc
clf;


gamma_n = 0.89;
gamma_c = 333.3;
gamma_p = 2.74;
gamma_s = 4.5;

alpha = 4.8;
eta = 98;

ep = 0.06;
Psl = 1.44;
Pinj = 4.5;

start = -pi/2;
phase = start;
Y = 1;

while  phase < -1.48

phi = phase;
wr = sqrt(gamma_n*gamma_c + gamma_p*gamma_s);

P1 = gamma_n*eta*cos(phi);
P2 = -3*(wr^4) - 4*P1.^2;
P3 = 18*P1*(wr^4) + 54*gamma_s*eta*(wr^4)*cos(phi) + 16*(P1.^3);
S1 = 2*P1./(3*(wr^2));
s2num = -(2^(1/3)).*P2;
s2den = 3*(wr^2).*((P3 + sqrt(4*(P2.^3) + (P3.^2))).^(1/3));
S2 = s2num/s2den;
S3 = (1/((3*2^(1/3))*(wr^2))).*((P3 + sqrt(4*(P2.^3) + (P3.^2))).^(1/3));
Rfe = S1 + S2 + S3;

gamma_n = gamma_n*(1 + ep*Psl)/(1 + ep*(Psl*Rfe^2 + Pinj));
gamma_p = gamma_p*((1 + ep*Psl)^2)/((1 + ep*(Psl*Rfe^2 + Pinj))^2);
gamma_th = 2.*(eta./Rfe)*cos(phi);

Z = -(eta./Rfe).*cos(phi) + (alpha*(eta./Rfe).*sin(phi));
A = gamma_s + gamma_p*(Rfe.^2) + gamma_n*(Rfe.^2) + gamma_th;
B = (eta./Rfe).^2 + gamma_c*gamma_n.*(Rfe.^2) + gamma_p*gamma_s.*(Rfe.^2) + gamma_s.↙
*gamma_th - alpha*gamma_p.*(Rfe.^2).*(eta./Rfe)*sin(phi)...
    + gamma_p.*Rfe.*(eta./Rfe)*cos(phi);
C = ((eta./Rfe).^2).*(gamma_n.*(Rfe.^2) + gamma_s) - Z.*(gamma_n.*(Rfe.^2)*gamma_c +↙
gamma_p.*(Rfe.^2)*gamma_s - gamma_n.*(Rfe.^2).*gamma_th);
detl = [1 A B C];

rdetl = roots(detl);
rdetltrans = transpose(rdetl);
rootl(Y) = abs(rdetltrans(:, 1));
```

```
root1real(Y) = real(rdetltrans(:, 1));
root1comp(Y) = imag(rdetltrans(:, 1));
root1full(Y) = rdetltrans(:, 1);
root2(Y) = abs(rdetltrans(:, 2));
root2real(Y) = real(rdetltrans(:, 2));
root2full(Y) = rdetltrans(:, 2);
root3(Y) = rdetltrans(:, 3);
root3comp(Y) = imag(rdetltrans(:, 3));
root3real(Y) = real(rdetltrans(:, 3));
Zt(Y) = Z;

phix(Y) = phase;
Rfex(Y) = Rfe;
Y = Y + 1;
phase = phase + 0.005;
end

subplot(2,1,1)
plot(phix, root2real,'Linewidth', 2)
xlabel('Stead-State Phase Offset, \it\theta_o, \rm\bfrad','FontSize',15,'fontweight','b');
%legend('Real Portion of Root 2','Location','SouthWest')
ylabel('\bfArbitrary Unit','FontSize',15);
title('Real Portion of the Complex Root, \it\alpha \rm= 3.0\bf, \it\eta_o\rm\bf =↙
100GHz','FontSize',15,'fontweight','b')
hold on;
box on;
grid on;
set(gca,'FontSize',15)
set(gca, 'xminortick', 'on','yminortick', 'on');
%xlim([-1.57 -1.45])

subplot(2,1,2)
plot(phix, Rfex,'Linewidth', 2)
title('\it\gamma_n \rm\bf= 1.34GHz, \it\gamma_p\rm\bf = 3.89GHz, \it\gamma_s\rm\bf = 4.5↙
GHz, \it\gamma_c\rm\bf = 333.3GHz','FontSize',15,'fontweight','b')
xlabel('Stead-State Phase Offset, \it\theta_o, \rm\bfrad','FontSize',15,'fontweight','b');
ylabel('\bfField Enhancement Factor, \itR_F_E','FontSize',15);
hold on;
box on;
grid on;
set(gca,'FontSize',15)
set(gca, 'xminortick', 'on','yminortick', 'on');
%xlim([-pi/2 -1.45])
%ylim([1 1.1])

Rfe2 = 1.075;
phi2 = -1.53;
delW = -(eta/Rfe2)*sqrt(1 + alpha^2)*sin(phi2 - atan(alpha))/2/pi
```

Code used to generate the bifurcation diagrams in Chapter 3:

This code was modified from an earlier version outlined by Nate Terry at AFRL/RYDP


```
%  The purpose of this code is to create a bifurcation diagram using the
%  normalized rate equations, where the nonlinear carrier relaxation rate
%  is accounted for in the rate equations.

clc;clear all;
close all;

%-----Initializes an array will all the values of eta
eta1=0.0000:.0005:0.009;
eta2=0.009:0.0005:0.06;
eta3=0.06:0.001:0.09;
etafull=cat(2,eta1,eta2,eta3);
%-----Initial Conditions
alpha = 3.0;  % linewidth enhancement factor
gammaN = 1.122; % differential carrier relaxation rate, GHz
gammaS = 4.5; % spontaneous carrier relaxation rate, GHz
gammaC = 300.3; % cavity decay rate, GHz, 1/tp, where tp = photon lifetime
gammaP = 3.378; % differential carrier relaxation rate, GHz
kc = 85.7;
ep = gammaP*gammaS/(gammaN*gammaC);
M = 0*gammaC/kc;
p=(1/2)*gammaN/gammaS;  % pumping level

T=gammaC/gammaS;  % ratio of carrier decay to photon decay

wr=sqrt(2*p*(1 + ep)/T)   % resonance frequency
dwfull=0.0; %-20:0.2:20.0; %normalized to relaxation oscillation
m=p*0.005; % modulation amplitude
Omega=2; % modulation frequency

%-- Variables
options = odeset('RelTol',1e-4,'AbsTol',1e-4,'MaxStep',.1); % define
                                                %options for ode solver
Einit=(sqrt(p)+.00001);
InitCond=[Einit 0 0];
h=waitbar(0,'Working, check back in a few');
count=0;
counttotal=length(etafull)*length(dwfull);
%-----Calculate the Electric field
count = 1;
dw=dwfull;
for n=0:length(etafull)-1

eta=etafull(n+1);
[t,E] = ode45(@InjectionModulator,[0 1100],InitCond,options,p,T,eta,alpha,dw,m,Omega,wr, ↙
ep,M);
lengthE=length(E(:,2));     % figure out how many data points are in E

ninetyE=ceil(.95*lengthE); % gets about 90% of the length
% to examine the bifuraction diagram for only the last 10% of the
% points on the E field--this is hopefully the stead state--it can be
% plotted individually using the commented code below to check
```

```
%-----Plot Electric field
%figure(1)
%plot(t(ninetyE:lengthE),abs(E(ninetyE:lengthE,2)))%
%legend('E1')
% --- Translate the eta used in the rate equations to that commonly used
% as given in the JSTQE and PTL manuscripts
        EtaVec(count) = eta;
        Elaverage = mean(abs(E(ninetyE:lengthE,1)));
etaPTL = eta*gammaC/sqrt(p)
%-----Identify Extrema
%--Local Max
Emax= localmaxmin(abs(E(ninetyE:lengthE,1)),'max');
% Ones in this list are locations of local maxima
% only want to examine the last 10% of E field

indmax=find(Emax(2:end-1));  % finds all the locations of the local maxima
maxlist=abs(E(ninetyE+indmax-1,1)); % calcs the value of the local maxima
%--Local Min
Emin= localmaxmin(abs(E(ninetyE:lengthE,1)),'min');
% Ones in this list are locations of local maxima
% only want to examine the last 10% of E field

indmin=find(Emin(2:end-1)); % finds all the locations of the local maxima
minlist=abs(E(ninetyE+indmin-1,1));  % calcs the value of the local maxima
Extrema{n+1}=cat(1,minlist,maxlist);  % makes master list of the extrema
        % the curley brackets indicate a cell array
%-----Plot the bifurcation diagram
%--only plot it if there are extrema to plot
    if isempty(Extrema{n+1})

    else
        figure(2)
        plot(etaPTL,(Extrema{n+1}/sqrt(p)),'r.') % plots the bifur diagram
        xlabel('\it\bf\eta_o\rm\bf, GHz','FontSize',17,'fontweight','b')
        ylabel('\bfNormalized Extrema, \itY/Y\rm_f_r ,\bf unitless','FontSize',↙
17,'fontweight','b')
        title(strcat('\it\alpha \rm=  ',num2str(alpha, 2), ', \itT \rm=  ', num2str(T,3),↙
', \itP \rm=  ' ,num2str(p,2), ', \it\epsilon \rm= ' , num2str(abs(ep),2)), 'FontSize',↙
17,'fontweight','b')
        set(gca,'FontSize',16)
        set(gca, 'xminortick', 'on','yminortick', 'on');
        axis tight
        hold on   % keeps the plot open so that the
        %  data from the next eta will also be considered
    end
end
close(h)
```

```
%  This code is the dimensionless normalized optical injection
%  rate equations

function dy=InjectionModulator(t,Y,p0,T,eta,alpha,dw,m,Omega,wr,ep,M)

%T is ratio of photon lifetime to carrier lifetime
%eta is the coupling strenght
%alpha is the linewidth enhancement factor
%dw is detuning
%m is modulation amplitude

dy=zeros(3,1);

dy(1) = Y(3)*Y(1) - (Y(1)/wr)*(ep*Y(1)*Y(1) - ep*p0 + (M^2)*(eta^2)) + (eta/wr)*cos(Y(2)
+dw*t);

dy(2) = (alpha)*Y(3) - (alpha*ep/wr)*(Y(1)*Y(1) - p0 + (M^2)*(eta^2)) - (eta/(Y(1)*wr))
*sin(Y(2)+dw*t) - dw/wr;

dy(3) = (1/(2*p0*(1 + ep)))*((p0+m*cos(Omega*t)) - wr*Y(3) - Y(1)*Y(1)*(1 + 2*wr*Y(3) -
2*ep*Y(1)*Y(1) + 2*ep*p0 - 2*ep*M*eta));
```

```
function [x,n]=localmaxmin(y,xn)
%LOCALMAXMIN(Y) Local Maxima and Minima.
% X = LOCALMAXMIN(Y) or LOCALMAXMIN(Y,'max') for vector Y returns a logical
% vector X the same size as Y such that Y(X) contains the local maxima in Y.
%
% N = LOCALMAXMIN(Y,'min') for vector Y returns a logical vector N the same
% size as Y such that Y(N) contains the local minima in Y.
%
% [X,N] = LOCALMAXMIN(Y) for vector Y returns logical vectors X and N such
% that Y(X) contains the local maxima and Y(N) contains the local minima.
%
% When Y is a matrix, outputs are logical array(s) the same size as Y, and
% the minima and/or maxima are computed down the rows of each column in Y.
%
% See also MAX, MIN.

% D.C. Hanselman, University of Maine, Orono, ME 04469
% MasteringMatlab@yahoo.com
% Mastering MATLAB 7
% 2006-03-08

mm=['min';'max'];
if nargin==1
   xn='max';
elseif nargin~=2
   error('localmaxmin:NotEnoughInputArguments',...
         'One or Two Input Arguments Required.')
end
if ~ischar(xn) || isempty(strcmp(xn,mm))
   error('localmaxmin:UnknownArgument','Unknown Second Input Argument.')
end
if ~isnumeric(y) || ~isreal(y)
   error('localmaxmin:IncorrectDataType','Y Must be Real Valued.')
end
ysiz=size(y);
isrow=ysiz(1)==1;  %% == tests to see if this is size 1 or not (i.e column or row)
if isrow % if row, convert to column for now
   y=y';
   ysiz(1)=ysiz(2);
   ysiz(2)=1;
end
if ysiz(1)<4
   error('localmaxmin:InsufficientData','Y Must Have at Least 4 Elements.')
end
x=false(ysiz);

sdiff=sign(diff(y));
zdiff=sdiff==0;     %% gives ones and zeros depending on whether sdiff=0
idz=find(sum(zdiff)); % columns where zero differences appear

if strcmp(xn,'min') || nargout==2   % get minima
                                    %% if the input argument on m file is
```

```
                                    %% xn, this function only looks for
                                    %% minima
    x(2:end-1,:)=diff(sdiff)==2;
    x(1,:)=sdiff(1,:)>0;
    x(end,:)=sdiff(end,:)<0;
    if any(sdiff)                   %% any checks if there are any non-zero values
       ir=1:ysiz(1);                %% a list of the columns
       for k=idx % handle columns with zero differences
          itmp=ir;                  %% uses list of columns
          itmp(sdiff(:,k))=[];
          if all(sdiff(:,k)==0) % entire column is flat
             x(:,k)=true;
          else
             tmp=diff(sign(diff(y(itmp,k))))==2; %% does derivative stay possitive
                                                 %% i.e. is 1 + 1 = 2
             x(itmp(tmp)+1,k)=true;              %% records location of everywhere
                                                 %% derivative stays
                                                 %% positive
             if sdiff(1,k)==0                    %% checks to see if endpoints are
                                                 %% zero
                nr=find(sdiff(:,k)>0,1);
                nf=find(sdiff(:,k)<0,1);
                if ~(isempty(nr)||isempty(nf))
                   x(1,k)=nr<nf;
                end
             end
             if sdiff(end,k)==0
                nr=find(sdiff(:,k)>0,1,'last');
                nf=find(sdiff(:,k)<0,1,'last');
                if ~(isempty(nr)||isempty(nf))
                   x(end,k)=nr<nf;
                end
             end
          end
       end
    end
    if isrow
       x=x.';
    end
    if nargout==2
       n=x;
    end
end
if strcmp(xn,'max') || nargout==2 % get maxima
    x=false(ysiz);
    x(2:end-1,:)=diff(sdiff)==-2;
    x(1,:)=sdiff(1,:)<0;
    x(end,:)=sdiff(end,:)>0;
    if any(sdiff)
       ir=1:ysiz(1);
       for k=idx % handle columns with zero differences
          itmp=ir;
```

```
        itmp(zdiff(:,k))=[];
        if all(sdiff(:,k)==0) % entire column is flat
           x(:,k)=true;
        else
           tmp=diff(sign(diff(y(itmp,k))))==-2;
           x(itmp(tmp)+1,k)=true;
           if sdiff(1,k)==0
              nr=find(sdiff(:,k)>0,1);
              nf=find(sdiff(:,k)<0,1);
              if ~(isempty(nr)||isempty(nf))
                 x(1,k)=nr>nf;
              end
           end
           if sdiff(end,k)==0
              nr=find(sdiff(:,k)>0,1,'last');
              nf=find(sdiff(:,k)<0,1,'last');
              if ~(isempty(nr)||isempty(nf))
                 x(end,k)=nr>nf;
              end
           end
        end
     end
  end
  if isrow
     x=x';
  end
end
```